Physical and numerical modelling of overtopping induced fluvial dikes breaching

Lydia Kheloui

École des Ponts ParisTech

Ph.D. THESIS
of École des Ponts ParisTech

Physical and numerical modeling of overtopping induced levee breaching

Doctoral school SIE

Fluid mechanics

CIFRE convention EDF R&D, ANRT N° 2018/1235
Prepared at the Saint-Venant Laboratory for Hydraulics et EDF RD LNHE, Chatou

LABORATOIRE D'HYDRAULIQUE SAINT-VENANT

EDF

Cifre

Defense expected on September 13^{th}, 2022, *by*

Lydia KHELOUI

Jury composition:

André, PAQUIER Dr, INRAE	*Rapporteur*
Sandra, SOARES FRAZAO Prof, Université catholique de Louvain	*Rapporteure*
Benjamin, DEWALS Prof, Université de Liège	*Examiner*
Jean-Robert, COURIVAUD Dr, EDF,CIH	*Examiner*
Kamal, EL KADI ABDERREZZAK Dr, EDF, R&D & LHSV	*Thesis director*
Sébastien, BOURBAN Dr, EDF, R&D & LHSV	*Guest*
Ismail, RIFAI Dr, Hydro-Québec	*Guest*

École des Ponts ParisTech

THÈSE DE DOCTORAT
de l'École des Ponts ParisTech

Modélisation physique et numérique de la rupture de digues fluviales soumises aux surverses

École doctorale Sciences Ingénierie et Environnement

Mécanique des fluides

Convention CIFRE EDF R&D, ANRT N° 2018/1235
Preparée au Laboratoire d'Hydraulique Saint-Venant et EDF R&D LNHE, Chatou

LABORATOIRE D'HYDRAULIQUE SAINT-VENANT

EDF

Cifre

Soutenance prévue pour le 13 Septembre 2022, par
Lydia KHELOUI

Composition du jury:

André, PAQUIER Dr, INRAE	*Rapporteur*
Sandra, SOARES FRAZAO Prof, Université catholique de Louvain	*Rapporteure*
Benjamin, DEWALS Prof, Université de Liège	*Examinateur*
Jean-Robert, COURIVAUD Dr, EDF,CIH	*Examinateur*
Kamal, EL KADI ABDERREZZAK Dr, EDF, R&D & LHSV	*Directeur de thèse*
Sébastien, BOURBAN Dr, EDF, R&D & LHSV	*Invité*
Ismail, RIFAI Dr, Hydro-Québec	*Invité*

Remerciements

"*On n'a jamais gagné une partie en abandonnant.*"– Xavier Tartakove

Ainsi la thèse fut une expérience laborieuse mais aussi très enrichissante et si c'était à refaire, je me réengagerai sans hésitation !

Évidemment, les travaux présentés dans ce manuscrit n'auraient pu aboutir sans le soutien et la contribution de nombreuses personnes, et je tiens à leur exprimer toute ma gratitude.

D'abord, je remercie chaleureusement mon directeur de thèse Kamal EL KADI ABDERREZZAK qui m'a fait confiance et permis de mener à bien ces travaux de thèse. Merci pour ton grand soutien et ton accompagnement tout au long de la thèse. Je tiens à mentionner ton savoir et ton expérience qui m'ont énormément apportée. Je tiens également à te remercier pour avoir attentivement relu et corrigé mon manuscrit. Pour ces raisons et bien d'autres, je te suis reconnaissante.

Je tiens ensuite à remercier Riadh ATA pour son encadrement en première partie de thèse, son soutien et tous ses conseils ainsi que Sébastien BOURBON pour son suivi en deuxième partie de thèse.

Un grand merci à mon jury de thèse, à commencer par son président Benjamin DEWALS, qui a suivi avec attention mes travaux de thèse et prodigué de précieux conseils lors des comités de suivi de thèse et des différentes réunions d'échange. Un grand merci à Sandra SOARES FRAZAO et André PAQUIER qui ont accepté de rapporter cette thèse, pour leur relecture attentive du manuscrit et leurs conseils avisés ainsi qu'aux autres membres du jury, Jean-Robert COURIVAUD et Ismail RIFAI. J'adresse des remerciements tout particuliers à Ismail RIFAI qui m'a accompagnée pour les premières expériences en laboratoire avec profilométrie laser.

J'adresse également mes remerciements à EDF R&D et l'ANRT dont le financement a permis la réalisation de ces travaux. Merci au Laboratoire d'Hydraulique Saint-Venant et à l'école doctorale des Ponts et chaussées qui ont accueilli cette thèse.
Merci à Vito BACCHI chef du projet MOISE qui a accueilli cette thèse et à Sofia M'JAHAD la cheffe de groupe P73 au département LNHE (EDF R&D) pour son accompagnement et ses encouragements en fin de thèse. Je voudrais également remercier l'équipe POMPHY et PHE du LNHE (EDF R&D) pour leurs contributions dans la partie expérimentale et numérique de la thèse, respectivement. Je remercie également tous mes collègues des groupes P73 et P74 et du LHSV (agents, doctorants, post-doctorants et stagiaires) qui, de près ou de loin, ont pu contribuer au bon déroulement de cette thèse

et avec qui j'ai partagé d'agréables moments de convivialité.

Évidemment, un énorme merci à mon Mari, mon meilleur ami, mon chéri et mon compagnon tant de chemin parcouru ensemble ! Merci d'avoir toujours cru en moi, d'avoir été là pour me soutenir et m'encourager. Tu as toujours eu les mots qu'il fallait pour me rassurer.

Je remercie également mes beaux parents, toute ma famille et mes amis pour leurs encouragements tout au long de la thèse !

Enfin, les mots me manquent pour exprimer ma gratitude envers mes parents ! je ne vous emercierais jamais assez de m'avoir élevée avec tant d'amour et transmis tant de valeurs. Merci pour votre soutien inconditionnel et d'avoir toujours cru en moi. Et à mes brillants frère et sœur Massyl et Marissa, je vous souhaite un très bel avenir et toute la réussite que vous méritez! Aussi, une pensée à Mirina partie trop tôt ...

Résumé

Les digues fluviales (*i.e.,* levées) sont d'importants ouvrages hydrauliques construits le long des rivières et des canaux pour protéger les zones inondables de la submersion. Cependant, de nombreux événements de rupture de digues ont été observés et les inondations qui en résultent se sont révélées être plus dévastatrices que des inondations naturelles. Ces ouvrages peuvent en effet subir plusieurs sollicitations entraînant la formation de brèches et leur expansion jusqu'à rupture de la digue. En particulier, sous l'effet de la surverse qui a été identifiée comme étant l'une des principales causes de rupture de digues fluviales. La modélisation numérique peut contribuer à la gestion du risque inondation et aider à améliorer la résilience des communautés face à cet aléa. Cependant, une prédiction précise de la dynamique de brèche est nécessaire pour estimer le débit de brèche et l'étendue des inondations qui en résulterait. Néanmoins, la modélisation de la formation de brèches dans les digues fluviales présente plusieurs défis, principalement liés à une compréhension limitée des processus physiques et leurs interactions complexes. De plus, les recherches ont pendant longtemps été consacrées au développement de modèles de rupture de barrages (digues frontales), qui ne sont pas adaptés à la simulation de la rupture d'ouvrages linéaires.

Les objectifs de ce travail de recherche sont, d'une part, d'améliorer nos connaissances sur les processus physiques associés à la rupture de digues fluviales par surverse et, d'autre part, d'améliorer la fiabilité des approches de modélisation actuelles. Dans un premier temps, des expériences ont été réalisées au Laboratoire National d'Hydraulique et d'Environnement (LNHE) d'EDF R&D et afin de clarifier les processus d'érosion d'une digue homogène non cohésive en présence d'un lit mobile dans le canal principal, les fondations de la digue et la plaine inondable. Le débit et la largeur du canal principal ont également été modifiés au cours des tests afin de mettre en évidence leur influence sur la progression de la brèche et le débit qui en résulte. Par la suite, des travaux numériques ont été menés en utilisant deux stratégies de modélisation différentes. D'une part, une approche de modélisation simplifiée qui a été développée dans le module hydrodynamique TELEMAC-2D du logiciel TELEMAC-MASCARET. À cet effet, plusieurs modèles de brèche ont été implémentés dans TELEMAC-2D, y compris des lois empiriques simples et des équations plus sophistiquées comme le modèle de brèche RUPRO développé à l'INRAE. D'autre part, une approche de modélisation détaillée a été étudiée en utilisant le module hydrodynamique (TELEMAC-2D) et le module morphodynamique (SISYPHE/GAIA). Dans ce contexte, de nouvelles équations de transport sédimentaire par charriage ont été mises en œuvre et la modélisation de la rupture de pente a été adaptée à l'état de l'art actuel. Les mesures en laboratoire et les données d'expériences terrain ont permis d'analyser les deux approches de modélisation et ont permis de fournir d'intéressantes indications pour de futures études sur des sites réels.

Mots-clés:

Digues fluviales, surverse, brèche, modélisation physique, modélisation numérique.

Abstract

Levees (*i.e.,*fluvial dikes) are important hydraulic structures built along rivers and channel banks to protect surrounding areas from inundations. However, several levee failure events were reported to bring exacerbated damages compared to natural floods. Indeed, these structures may experience several solicitations resulting in breach formation and expansion, overtopping being the most common cause of levee failure.

Numerical models can support flood risk management and improve populations' preparedness. However, an accurate prediction of breach dynamics and outflow discharge is essential to simulate possible inundations extent and corresponding flood maps. Nevertheless, levee breach modeling presents significant challenges related to complex physical processes and their poorly understood interactions. In addition, most past research efforts were dedicated to developing dam-breach (frontal dikes) failure models, which are not adapted to fluvial dike breaching.

The main goals of this research work are to improve the knowledge about the physical processes associated with overtopping induced levee failure on the one hand and increase the accuracy of actual modeling approaches on the other hand. First, experimental investigations were performed at the National Laboratory for Hydraulics and Environment (LNHE) of EDF R&D and aimed to clarify the erosion processes of a non-cohesive homogenous levee in the presence of a movable bed in the main channel, dike foundation, and floodplain. Main channel discharge and geometry were also varied through tests to highlight their influence on breach spacial progression and resulting discharge. Then, numerical investigations were conducted using two different modeling strategies. On the one hand, a simplified two-dimensional breach modeling approach was developed within the hydrodynamic module TELEMAC-2D of the open-source TELEMAC-MASCARET software. Various breach models were implemented in TELEMAC-2D, including simple empirical laws and more sophisticated equations like the RUPRO breach model developed at INRAE. On the other hand, a detailed physically-based approach was studied using the hydrodynamic module (TELEMAC-2D) and morphodynamic module (SISYPHE/GAIA). In this context, new sediment transport equations were implemented, and slope failure modeling was adjusted to the state of the art. Laboratory measurements and field experimental data helped analyze both modeling approaches and provided relevant indications to support actual field studies.

Keywords:

Fluvial dikes, levees, overtopping, breaching, physical modeling, numerical modeling.

Contents

List of Figures

List of Tables

Nomenclature

Roman symbols

B	Breach width	(m)
B_0	Initial breach width	(m)
B_f	Final breach width	(m)
d_{30}	Sediments grain sizes at which 30% sediments are finer	(m)
d_{50}	Sediments median diameter	(m)
d_{90}	Sediments grain sizes at which 90% sediments are finer	(m)
d_{50}	Sediment particle median diameter	(m)
E_{w1}	User defined breach widening rate at phase 1	(m/hr)
E_{w2}	User defined breach widening rate at phase 2	(m/hr)
F	Froude number	(-)
f_1	empirical factors for breach width,	(-)
f_1	empirical factors for breach width,	(-)
g	Gravity acceleration	(m/s^2)
H	Flow energy head	(m)
h	Flow depth	(m)
h_b	Average water depth in the breach channel for the RUPRO model	(m)
h_d	Dike initial height	(m)
h_w	height of water above final breach bottom, at notch location and at time of failure	(m)

K	Strickler coefficient	($m^{1/3}$/s)
k_d	Erodibility coefficent	(m^3/N-s)
l	Main channel width at the crest	(m)
L_{mc}	Main channel length	(m)
n	Manning coefficient	(s/$m^{1/3}$)
p	Sendiment porosity	(-)
P_w	Wetted perimeter in the RUPRO model	(m)
Q_b	Breach discharge	(m^3/s)
q_{bnew},q_y	Corrected bedload transport rate	(m^3/s)
Q_d	Drainage discharge	(m^3/s)
Q_i	Channel inflow discharge	(m^3/s)
Q_o	Channel dowstream discharge	(m^3/s)
$\mathbf{q_b}$	Volumetric sediment discharge	(m^3/s)
Q_s	Volumetric sediment discharge	(m^3/s)
q_u,q_v	Specific flow discharge in the x- and y-directions, respectively	(m^2/s)
q_x,q_y	Volumetric sediment discharge per unit width in the x- and y-directions, respectively	(m^2/s)
r	Local radius in Engelund's (1974) formula	(m)
R_H	Hydraulic radius	(m)
s	Sediment relative density	(-)
S_h	Source or sink term of fluid	(m/s)
S_0	Slope energy	(m/s^2)
S_f	Energy loss due to the bed and wall shear stresses	(m/s^2)
T	Coefficient for bedload transport direction correction	(-)
t	Time	(s)
T_1	Duration of breach widening phase 1	(s)
T_d	Deepening duration	(s)

T_f	Widening duration	(s)
$\mathbf{u}$	Flow velocity vector	(m/s)
u,v	Flow velocity in the x- and y-directions, respectively	(m/s)
u_c	critical flow velocity for the initiation of erosion of dike material ,	(m/s)
V_e	Erosion rate	(m/s)
w_b	Levee base width	(m)
l_{dc}	Crest width of the levee	(m)
z_b	Bed elevation	(m)
z_b	Bed elevation	(m)
z_{b0}	Initial elevation of the breach	(m)
z_{bmin}	Minimum bed elevation	(m)
z_{mean}	average water level in the main channel	(m)
z_w	Water surface elevation	(m)

Greek symbols

α	Multiplying coefficent of Meyer-Peter and Müller's formula	(-)
α_b	Bottom slope angle	(°)
β	Empirical coefficient of the Koch and Flokstra (1980) formula	(-)
β_2	Empirical coefficient of the Talmon et al. (1995) formula	(-)
δ	Angle between sediment transport and main flow direction	(°)
μ	Skin friction correction factor	(-)
ν	Velocity diffusivity	(m^2/s)
ϕ_{dep}	Deposited sediment repose angle	(°)
ϕ_{dry}	Dry sediment repose angle	(°)
Φ	Dimensionless sediment transport rate	(-)
ϕ_{wet}	Wet sediment repose angle	(°)

ψ	Angle between flow and slope directions	(°)
ρ	Water density	(kg/m^3)
ρ_s	Sediment density	(kg/m^3)
τ_b	Bed shear stress	(-)
$\tau^{\beta c}$	Adjusted critical Shields parameter (Soulsby, 1997)	(-)
τ_c	Critical shields parameter	(N/m^2)
θ_c^{ss}	Corrected dimensionless critical Shields parameter according to Soulsby (1997)	(-)
θ_c	Dimensionless critical Shields parameter	(-)
θ_c^{sm}	Dimensionless critical Shields parameter, modified by Smart (1984)	(-)

Introduction

Les digues fluviales ont pour vocation de protéger, contre les inondations, les populations établies aux abords des cours d'eau et leurs intérêts tels que des logements, terres agricoles et sites industriels parfois très sensibles. Cependant, ces ouvrages hydrauliques sont exposés aux aléas d'érosion et plus particulièrement au risque de rupture par surverse engendrant des inondations aggravées. La modélisation physique et numérique, de ce phénomène revêt d'un intérêt majeur pour l'anticipation, la gestion et la prévention du risque d'inondations dans les zones protégées. Mais les travaux sur la rupture de digues fluviales sont récents et les recherches pour comprendre ses mécanismes physiques et pour améliorer la fiabilité des modèles numériques demeurent nécessaires. L'objectif de ces travaux de thèse est, d'une part, d'enrichir les connaissances actuelles des processus physiques qui régissent la rupture de digues fluviales par surverse et, d'autre part, d'améliorer et de développer dans le système TELEMAC-MASCARET les stratégies de modélisation de ce phénomène dans le but de présenter un modèle fiable et adapté aux applications terrain.

General context

Flooding is a dangerous global hazard threatening populations' lives and assets worldwide (Fig.1). Among the various causes of flooding, heavy rainfall events and melting snows may cause surface floods in poor drainage lands or fluvial floods when rivers' water supply increases. On the other hand, hurricanes and extreme tidal conditions can carry seawater onshore and induce coastal floods. Such events resulted in unmitigated damages during the last century, with socio-economic effects (e.g., high potential of human fatalities, spread of diseases due to contaminated water, destruction of properties and infrastructures) and environmental effects such as the destruction of ecosystems. Data reported by Tellman et al. (2020) highlighted an increase of 24% in the proportion of people exposed to the risk of flooding between 2000 and 2015. Furthermore, Figure 2 shows the prediction of a continuous increase in flood exposure by 2030. In addition, Hirabayashi et al. (2013) presented results of 11 climate models for the year 2100 that predicted an aggravation of flood frequency and magnitude due to climate change, massive urbanization, and increasing population demographics in flood-prone areas.

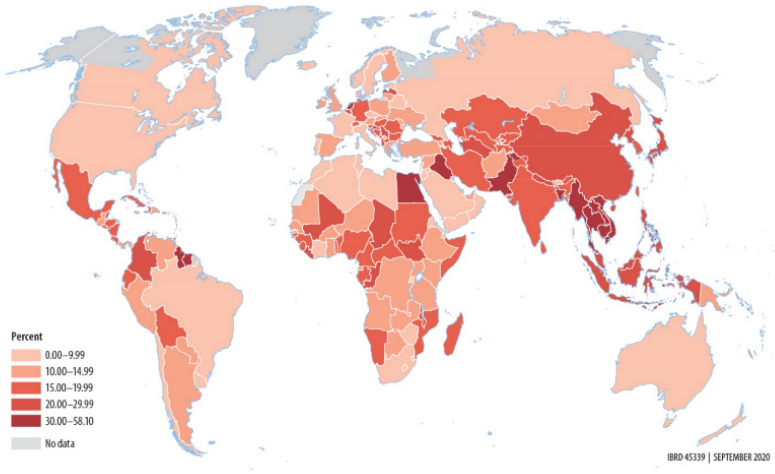

Figure 1: Relative population exposure to moderate or high risk inundation at country level by (Rentschler and Salhab (2020)).

In France, flooding is the primary natural hazard faced by territories (Fig.3): 17 million inhabitants are exposed to flooding by overflowing rivers, and 1.4 million are at risk of coastal submersion. Including urban run-off in cities makes the proportion of communes exposed to flood risk unto 70% (source: European Center for Flood Risk Prevention CEPRI). Over the last few decades, severe flood episodes caused significant socio-economic losses. Revealing the inadequacy of existing protections against this risk, some communities were not even prepared for such events. In France, nine thousand kilometers of dikes were built along rivers and coastlines to protect lowland areas against the risk of flooding. However, several levee failure events (Fig.4) were reported to bring exacerbated

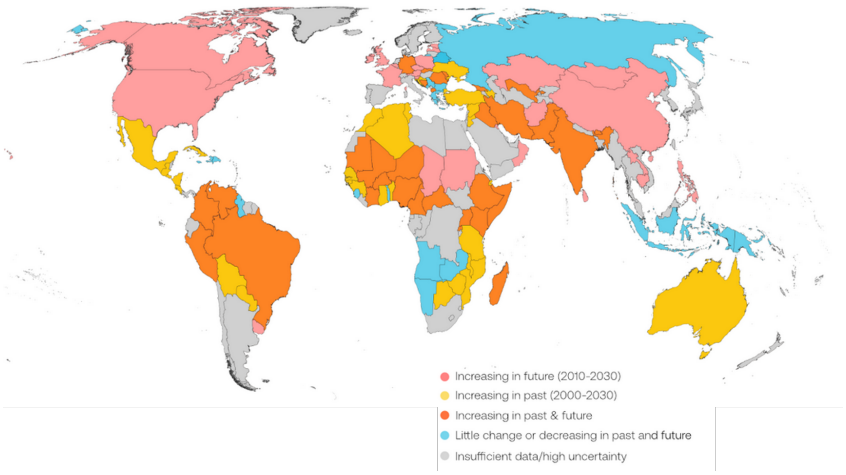

Figure 2: Changes in proportion of population exposed to floods observed by satellite 2000-2015 and expected by 2030 according to climate models (Tellman et al. (2020)).

damages in comparison with natural floods (Charrier (2015)). Indeed, these structures may experience several solicitations resulting in surface and internal erosion-induced breaching. Overtopping has been identified as the main cause of surface erosin and failure of levees Fry et al. (2012), Vorogushyn et al. (2010). Overtopping ocurs if the river discharge exceeds the design value of the dike or, broadly, if the water level exceeds the levee crest or the flow overtops a weak dike segment. The levee system can also deteriorate due to natural aging (first levees were built in the 12^{th} century), lack or inadequate maintenance, and construction errors Orlandini et al. (2015).

The French legislation has emitted numerous decrees and laws, and set up several plans to improve flood risk management, among which:

- Plans for flood hazard prevention (PPRNi);
- Plan for flood risk management;
- 2003 circulaire on levee safety;
- 2007 decree with classified rules for hydraulic structures safety;
- "Digues" decree in 2015 which clarifies the responsibilities of dike owners and managers.

In recent years, levee failure issue has received renewed attention among territories, especially since 2018 when the State modified laws regarding the organization of aquatic environments' management and flood prevention with the GEMAPI (gestion des milieux aquatiques et la prévention des inondations) regulation. The latter responsibilities were devolved to the local authorities, including the inspection, maintenance and development of flood defense structures. In addition, the French legislation requires breach failure and flood risks analysis to be carried out. These studies can be tough to perform for complex and extensive levee systems, sometimes undocumented due to the lack of structural data.

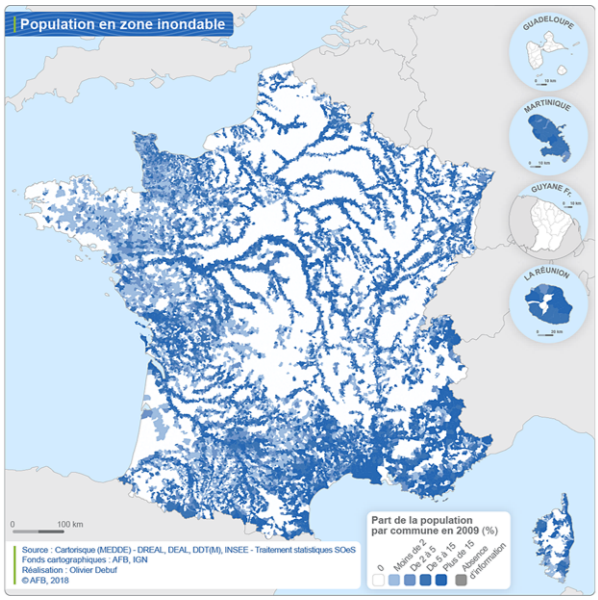

Figure 3: Proportion of population exposed to floods in France (www.eaufrance.fr).

Figure 4: Examples of levee failure cases: (a) Levee breach near Hamburg in 2011 (www.floodfactor.com), (b) Levee failure on the Elbe river in 2013 (Jüpner (2015)), (c) Levee breach along the Arkansas river in 2019 (www.detroitnews.com), (d) Levee failure along the Saône-et-Loire in 2021 (www.lejsl.com).

Research needs and objectives

Using numerical tools in simulating flood propagation can help improve populations' preparedness and prevent significant damages. Therefore, it is crucial to use adequate approaches and modeling strategies to achieve accurate estimations of breach growth rate and outflow discharge. The latter is a key parameter for predicting possible flood extent and impact due to levee breaching under overtopping flows. Levee failure modeling presents significant challenges as breaching physical processes and their interactions are complex and poorly understood. In addition, most of past research efforts were dedicated to developing dam-breach (frontal dikes) failure models, which are not adapted to fluvial dike breaching. There is a clear need for a better understanding and description of the levee breaching process. This can be achieved through experimental investigations that provide the necessary information to improve existing numerical breach models. As mentioned previously, there is a primary need to improve the knowledge about the physical processes associated with levee breaching on the one hand, and increase the accuracy of actual modeling approaches on the other hand. The main goals of the research conducted during this thesis align closely with those needs and include both experimental and numerical investigations of overtopping induced levee breaching.

- **Laboratory experiments:** Rifai (2018) provided a detailed description of the levee breaching process through extensive laboratory experiments of overtopping-induced levee failure under various conditions. Detailed monitoring of breach dynamics was performed thanks to the non-intrusive Laser Profilometry Technique (Rifai et al. (2020a)). However, most presented configurations were characterized by a rigid bottom in the main channel and floodplain. In the present work, laboratory experiments are proposed to assess the effect of bottom mobility in both main channel and floodplain for various inflow discharges and main channel sizes.
- **Numerical modeling:** the primary objective of this part is to work on two typical breach modeling strategies. First, a simplified two-dimensional modeling approach is developed within the hydrodynamic module TELEMAC-2D of the open-source TELEMAC-MASCARET code. Then a detailed physically-based approach, coupling hydrodynamic (TELEMAC-2D) and morphodynamic (SISYPHE/GAIA) processes, is investigated. Laboratory experiments are employed to validate improvements in the latter approach, and field experiments data help confront both modeling approaches. Finally, relevant indications and lessons are highlighted to support actual field studies.

Organization of the Manuscript

This manuscript includes five chapters. Chapter 1 focuses on understanding common levees' functions and failure mechanisms and establishes state of art for experimental and numerical levee breach modeling. Chapter 2 is dedicated to laboratory experiments of overtopping induced levee failure where a movable bed was used in the main channel and floodplain. Main channel size and

inflow discharge are varied through tests, and their influence on the breaching process is studied. Chapter 3 presents the simplified modeling approach developed in TELEMAC-2D and analyses its capabilities to model field experiments. Chapter 4 provides a complete evaluation of the detailed modeling approach using laboratory and field-scale experimental data. Finally, Chapter 5 concludes this manuscript by summarizing the key findings of the present research work. It establishes the pros and cons of the presented modeling approaches in terms of accuracy and usability for flood prediction aims and offers suggestions for future work.

Chapter 1

Literature review

Après une description des différents types de digues fluviales, de leurs fonctions ainsi que des différentes causes et mécanismes à l'origine d'une rupture. Un état de l'art des travaux de modélisation physique et numérique de la formation de brèches dans les digues fluviales soumises aux surverses est dressé dans ce chapitre. Les principaux apports scientifiques des expériences en laboratoire et sur le terrain sont rappelés suivis d'une description détaillée des différentes approches de modélisation numérique allant des modèles empiriques aux modèles hydromorphodynamiques détaillés en passant par des modèles hybrides alliant une représentation basée sur la physique des processus hydrodynamiques et une modélisation simplifiée de la formation de brèche.

1.1 Levees: types and functions

Hydraulic structures are commonly installed on rivers and coastlines for water storage, power generation, irrigation of agricultural lands, and protection from rising water levels. Levees, also known as fluvial dikes or flood banks, are important hydraulic structures constructed adjacent (*i.e.* , parallel) to rivers and artificial waterways and part of flood protection systems that resemble several structures such as drainage systems, gates, culverts, and storm sewers. Levees are raised above the natural bed elevation using earth materials for the primary function of flood risk mitigation to allow urbanization and human activity in flood prone areas. Unlike dams (*i.e.* frontal) that are mainly used to retain and store water, levees can be very long (several kilometers) with a limited height. Besides engineering works, levees can also form naturally through sedimentation processes on river banks and landslides; this usually happens after a flood event when sediments deposit and increase bed elevation along rivers. However, natural levees do not offer sufficient protection against flood risk. Figure 1.1 shows the cross-section geometry of a simple flood defense levee and its different design characteristics (base width W_B, crest width W_c, dike height h_L, side slopes m_p and m_f) that may vary considerably from a location to another and define the limits of the levee's protection level. Design constraint parameters are usually calculated based on historical and actual data to ensure the stability of the structure and its ability to contain floodwater for a specific anticipated range of river discharge and water levels. Additional aspects are also considered and include available land space, type of foundation soil, local ecosystems, and climate.

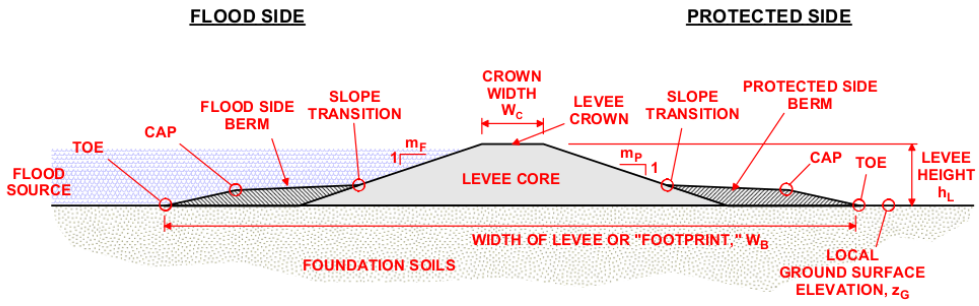

Figure 1.1: Illustration of a typical flood defense levee cross-section (Saucier et al. (2009)).

Existing embankments can be classified into earth-fill structures built of clay, silt, sand and gravel material or non-earth-fill structures that are built of concrete or masonry (Fredlund and Rahardjo (1993)). In the same way, one can classify levees based on their composition (Foster and Spannagle (2020)):

- **Earth-fill levees** that are made by compaction of cohesive or non-cohesive material with a large variety of sediment sizes and properties such as clay, sand, and gravel. One can make the

distinction between homogeneous embankments built with a single material type (generally extracted locally) and layered or zoned levees which are made with different material layers or zones (Fig.1.2).

- **Non-earthfill levees** are more recent and also more sophisticated and engineered. In addition to earth material, it includes structural elements such as concrete cut-off or T-walls and other reinforcing elements (Fig.1.2).
- **Historical levees** built in early times by our ancestors, their composition is very complex and was adjusted several times in different ways over time. It shows several layers of materials that were most likely extracted locally with a variable composition along the longitudinal direction. Most of them were improved using new materials and techniques to satisfy actual needs.

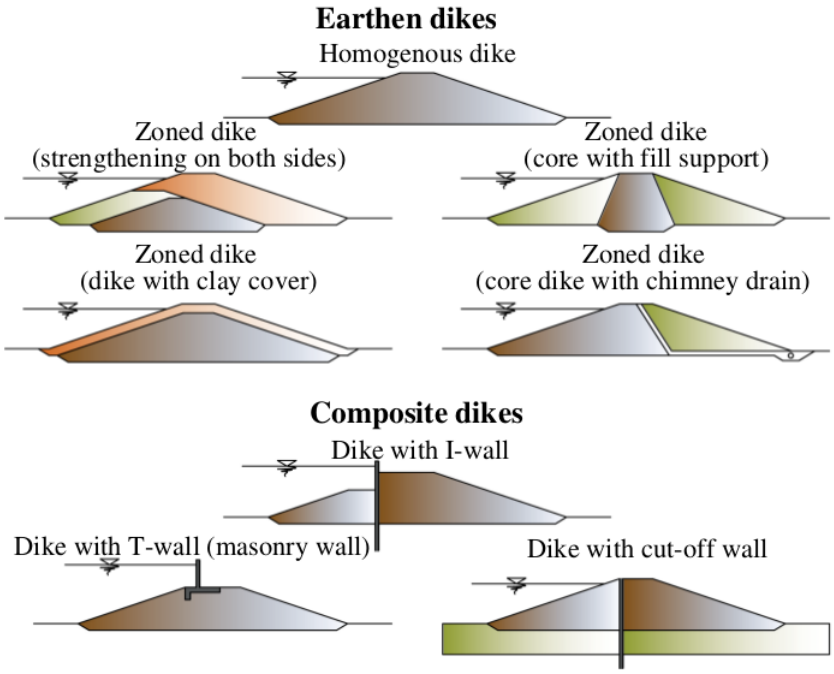

Figure 1.2: Cross-section illustration for homogeneous, zoned and composite levees (Danka and Zhang (2015))

Levees can also be differentiated based on their primary function and flood defense mechanisms (Sharp et al. (2013)): (i) levees preventing floods by water retention; (ii): channeling levees that divert the floodwater from critical areas and (iii): levees allowing controlled water discharges at a specific location to protect critical areas from inundations. One should note that a single levee can encapsulate several functions in the framework of flood resilience. As leveed areas attract populations and industrial assets, other uses were developed on modern levees that integrate secondary functions,

such as transport facilities (roads and railways) integrated on the dike crown for space optimization, noise control, or simply used as recreational spaces near waterways.

1.2 Levee breaching: causes and mechanisms

1.2.1 Definition of levee breaching

Before addressing the leading causes and mechanisms of levee breaching, one can define a breach as damages in the levee structure that results in a loss of its primary flood protection function. Depending on the solicitation inducing levee failure (*i.e.* , breaching), we may observe a decrease in levee's protection level (crest height) or water passing through a hole dug in the body of the levee. In both cases, a breach will start at a given location and progress by different mechanisms until levee collapse and uncontrolled release of water in protected areas. The floodplains behind these structures are then exposed to an aggravated flood wave with higher velocities, and water levels than natural inundations would cause in the absence of flood banks (Michelazzo et al. (2015)). Several levee failure accidents were reported and resulted in life and property losses (*e.g.,* , New Orleans flood (2005), Mississippi flood (2008), Elbe river flood (2002 and 2013), and Enza River (Italy) in December 2017).

1.2.2 Levee breach initiating factors

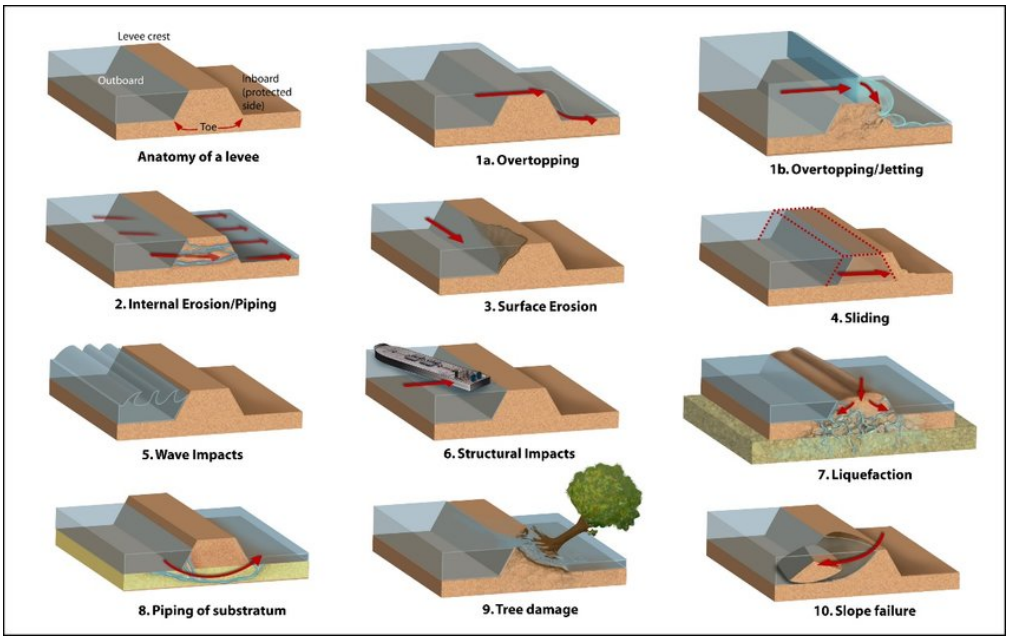

Figure 1.3: Illustration of different failure situations (Kheirkhah Gildeh et al. (2019))

The breaching process can be triggered by different phenomena (Fig. 1.3), among which:

- **Technical and structural issues** : For levees to fulfill their primary function, technical studies are made *a priori* to define conception parameters. However, inadequate geotechnical design, construction malfunctions, and use of inadequate materials in the levee are not uncommon (Sharp et al. (2013)). For example, non-cohesive soils are eroded relatively fast, whereas cohesive embankments show a higher resistance to surface erosion (Morris (2000)). On the other hand, levee components may experience natural aging and lose their properties, especially when combined with a lack of inefficient maintenance work. In these cases, the vulnerable levee comes with a higher failure probability.

- **External solicitations** : environmental factors and solicitations such as human and animal activity or hydrological events may weaken the levee and initiate its failure. High water levels and discharges may induce levee overtopping during extreme hydro-meteorological events and trigger the breaching process by surface erosion. An ineffective drainage system can also allow seepage flows in the levee foundation or core and cause internal erosion of the structure. Burrowing animals were also found responsible for piping-induced earthen levee failure (Orlandini et al. (2015), Sofia et al. (2017)), while vegetation promotes levee failure by instability. On the other hand, levee vulnerability increases in specific regions with seismic activity.

1.2.3 Levee breach mechanisms

Failure mechanisms, also called failure paths, are the physical processes resulting from initiating events and inducing levee breaching and failure. They were extensively described in the International Levee Handbook (Sharp et al. (2013)) and reported by several studies (Kakinuma and Shimizu (2014), Michelazzo et al. (2015), Morris et al. (2009), Rifai (2018)). Several mechanisms may occur during breach opening and are mainly related to hydraulic loads, permeability, and erodibility of levee material. The failure is usually progressive for earthen levees and abrupt for concrete structures. The most common failure mechanisms were widely reported in the literature and included three main categories: (i) surface erosion, (ii) internal erosion, and (iii) instability. The separation between them is not sharp as they can take action one after another during the same failure event. Each of these mechanisms can lead to failure in different ways as follows :

- **Surface erosion from the land side** is a direct consequence of levee overtopping (the main cause for levee failure as identified in (Danka and Zhang (2015), Fry et al. (2012)) and its soil erodibility. When flood protection structures face extreme loads or in the presence of weak spots along a levee (Saucier et al. (2009)), the water flows over the dike crest on the back slope towards the floodplain (Fig. 1.4). The flow velocity intensifies as it spills over levee's relatively high back slope, and removes material from the levee as the exerted shear stress exceeds levee soil cohesion forces and resistance. AS reported by Zhu (2006) and Orendorff et al. (2013) surface erosion is different based on the levee soil composition. Non-cohesive homogeneous

levees show a gradual lowering of the levee and erosion around a fixed rotation point (Fig. 1.5), while cohesive embankments erosion is more complex and consists in cutting the back slope with the formation of steps and cascades (Fig. 1.5). Once initiated, the erosion results in a breach progressing from the back slope of the levee (dry side or land side) towards the levee crest and will then deepen and widen due to hydraulic loads through the breach channel.

- **Surface erosion from the water side** can happen without the presence of overtopping flows. The interaction between the parallel flow field in the waterway and levee material is the driving process in this case. The strong turbulent flow applies sufficient shear stress on the levee surface leading to soil detachment. It may induce erosion of the levee front slope and core or scour the dike toe and foundations (Fig. 1.6).

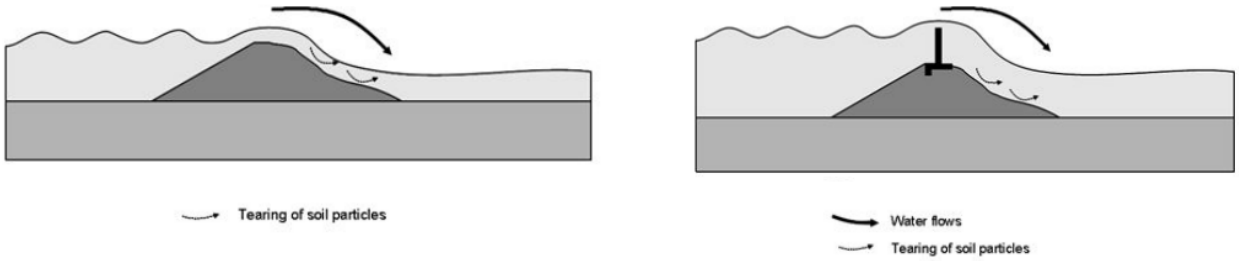

Figure 1.4: Illustration of surface erosion from the land side (Sharp et al. (2013)).

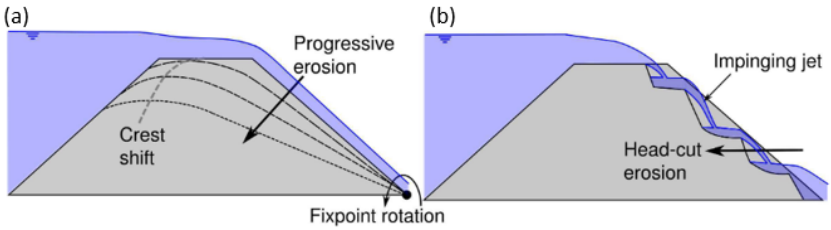

Figure 1.5: (a) Illustration of surface erosion for non-cohesive embankments and (b) head-cut erosion for cohesive embankments (Volz (2013)).

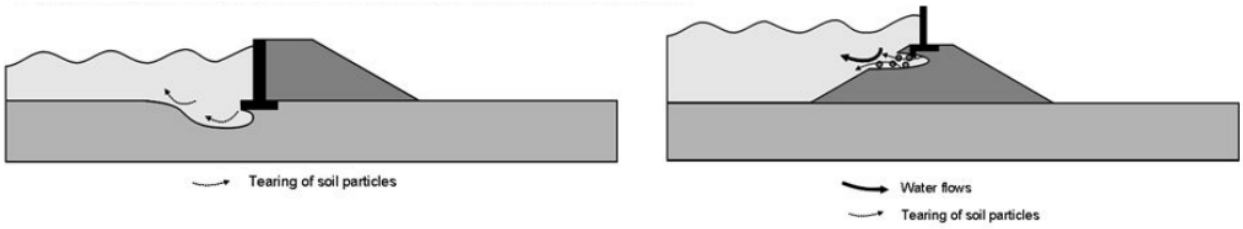

Figure 1.6: Illustration of surface erosion from the water side (Sharp et al. (2013)).

- **Internal backward erosion** is caused by damaging seepage flows removing material from

the dike core and foundation. Starting from the seepage outflow spot and moving backwards. As a result, the levee fails, and material boils are usually observed (Fig. 1.7).

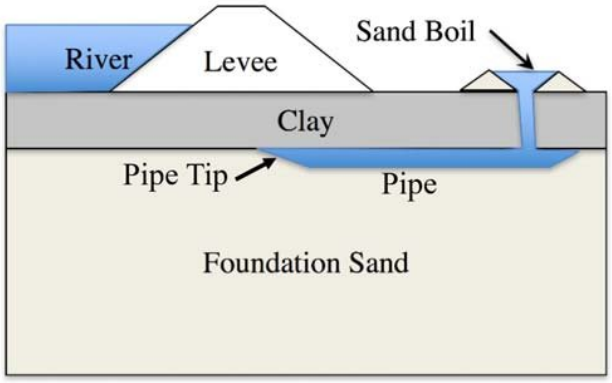

Figure 1.7: Illustration of backward erosion (Orlando, Florida, 2019Montalvo-Bartolomei and Robbins Orlando, Florida, 2019 Orlando, Florida, 2019).

- **Internal erosion by suffusion** also results from seepage flow, but it is characterized by the preferenced erosion of fine particles, which increases space between coarser ones and weakens the structure (Fig. 1.8).

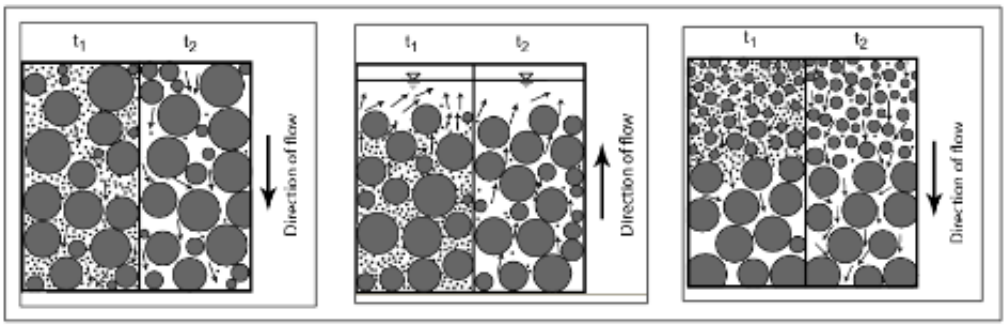

Figure 1.8: Illustration of suffusion (Riha et al. (2019)).

- **Internal contact erosion** occurs when the interface between fine and coarse material is parallel to seepage flow and induces migration of fine material towards the coarse layer (Fig. 1.9).

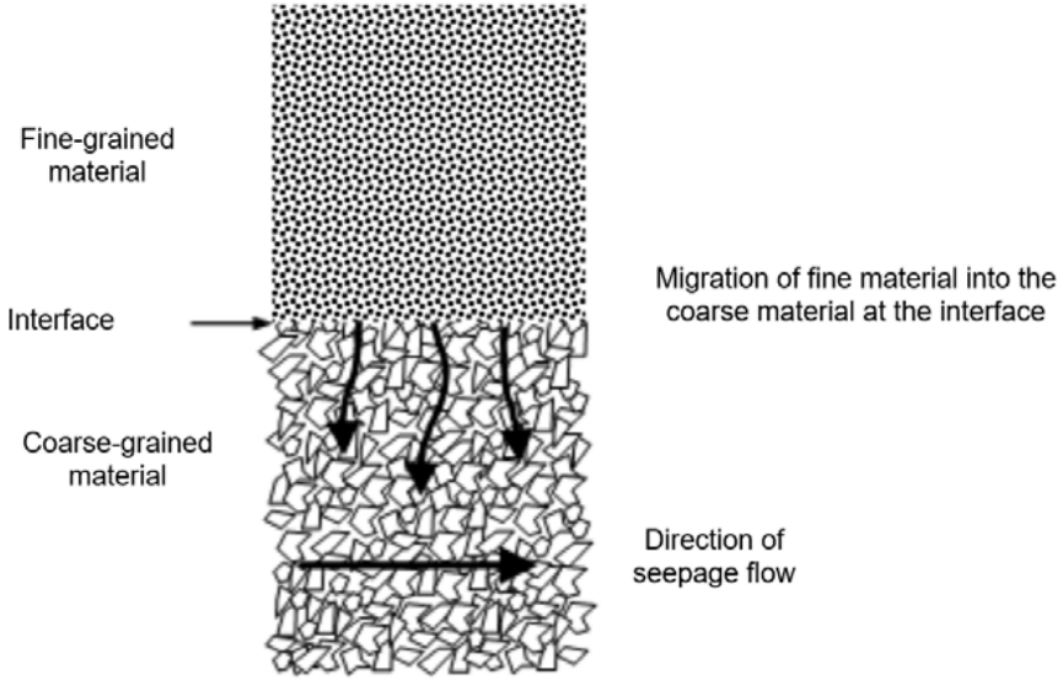

Figure 1.9: Illustration of contact erosion (ICOLD (2015)).

- **Internal concentrated leak erosion** results from water flowing through the levee core or foundation in an existing space of crack. The levee material is then eroded and removed from concentrated leak walls (Fig. 1.10).

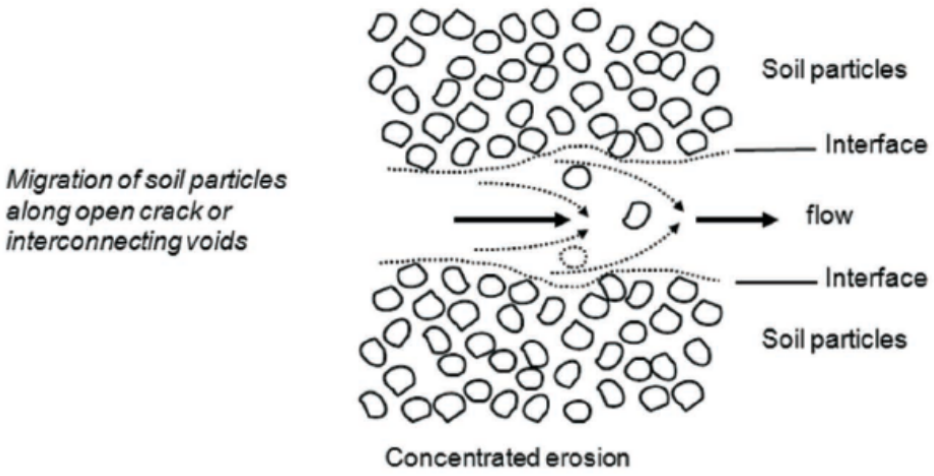

Figure 1.10: Illustration of concentrated leak erosion (Sharp et al. (2013)).

- **Slope sliding** starts when breach side walls become too steep and unstable blocks of levee material slide on the front or back slope of the structure. It results from important external

forces such as gravity which overcome cohesion or friction forces between soil particles. The sliding occurs discontinuously can be superficial, rotational, earthflow, spread or translational (Fig. 1.11).

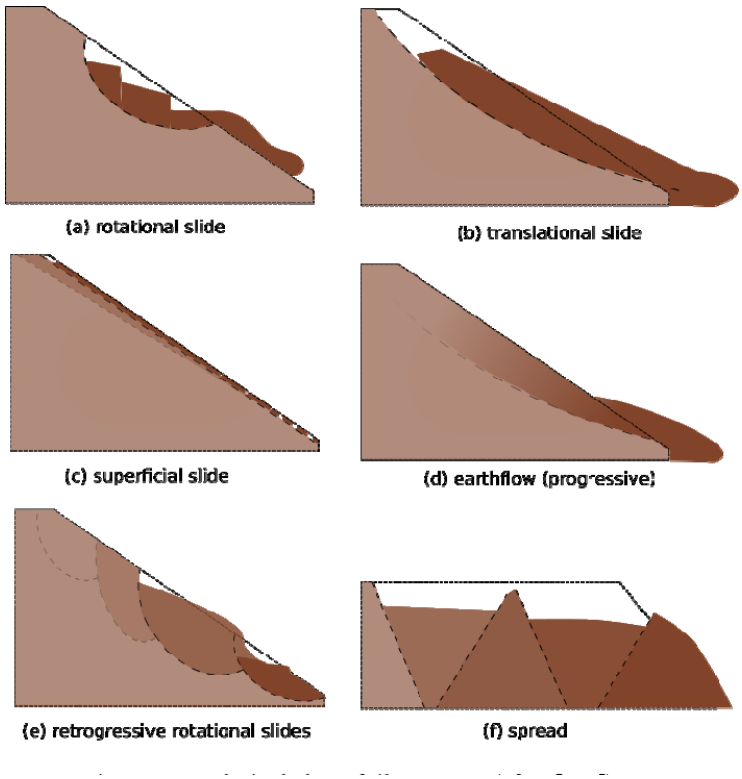

Figure 1.11: Illustration of slope sliding failure (Vardon (2017)).

1.3 Physical modeling of levee failure due to overtopping

Important research efforts addressed embankment dam failure mechanisms (Amaral et al. (2019, 2020), Coleman et al. (2002), Dhiman and Patra (2020), Morris et al. (2009), Morris (2000)). However, these structures are built across the river channel with a perpendicular approach flow while levees are parallel to the water field. In the following, the focus will be made on studies reporting lateral levee breach that was quite different from frontal structures failure (ASCE/EWRI task committee (2011)). A distinction will also be made between laboratory and field scale investigations, levee material, and failure mechanisms.

1.3.1 Field experiments

Kakinuma et al. (2013) reported full-scale experiments of side-overflow levee breaching in Chiyoda test channel (Fig. 1.12), the largest river experimental facility in Japan built on Tokachi River, Hokkaido. Levee failure tests triggered by overtopping were conducted for various channel inflow

discharges, dike soil composition, and geometry, as well as the location of initial breach. They measured water levels discharges and monitored breach expansion with acceleration sensors placed at specific locations in the dike body to detect material collapse. The main physical processes of levee breaching were clarified through four stages : (i) initial dike breaching stage, with surface erosion of levee's back slope and its top; (ii) onset of widening, with symmetrical lateral expansion towards the upstream and downstream directions; (iii) acceleration of widening, after breakage start rapid breach expansion in the downstream direction and increased breach outflow with a peak are observed; (vi) slower widening stage mainly in the downstream direction where the flow is constricted with material deposition at the upstream side. Levees with high fine sediment content and wider crest width showed slower breach initiation, while tests with increased inflow discharge showed higher breach widening rates.

Peeters et al. (2014) presented results from a field scale experiments of overflow dike breaching on the Scheldt river in Flanders (Belgium). The erosion of cohesive dikes was described in five stages: (i) removal of the embankment cover layer and onset of head-cut erosion; (ii) Head-cut progression with scour and mass failure processes; (iii) dike crest flattening and breach deepening under supercritical flow conditions; (vi) breach widening with critical flow conditions; (v) subcritical flow conditions and breach lateral progression . However, the initiation stage could not be properly be differentiated because of the existing steep slopes and established head-cut erosion. Early progression stages were characterized by head-cut migration while final breach stages were driven by the breach side-slopes failure.

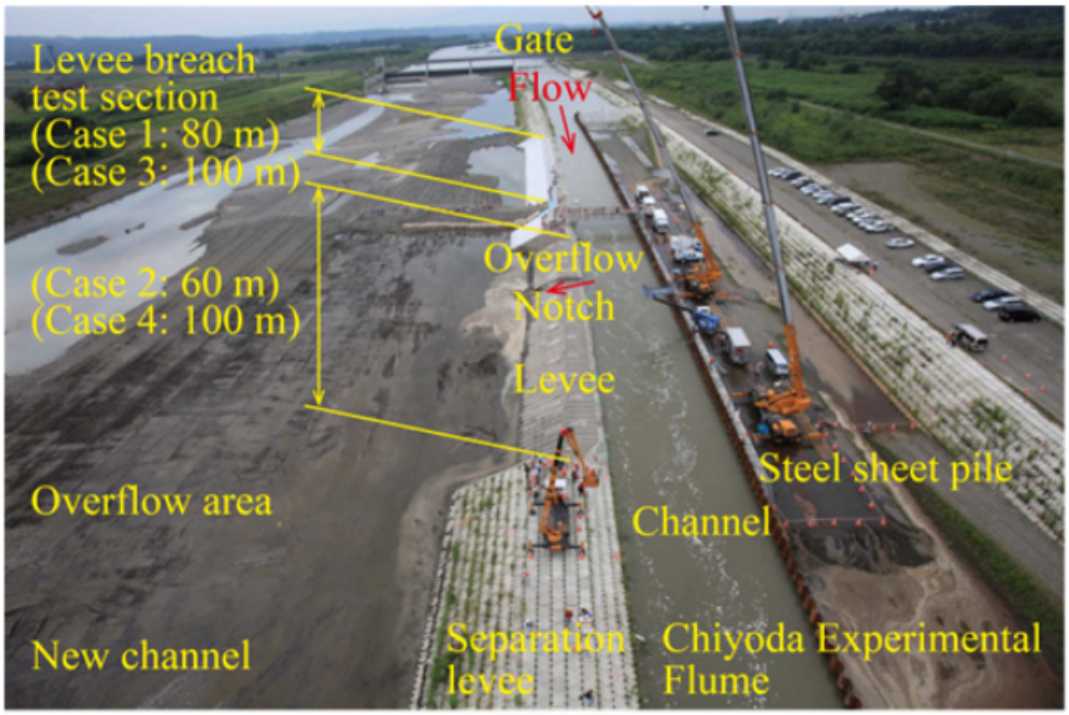

Figure 1.12: Chiyoda experimental flume (Tobita et al. (2014)).

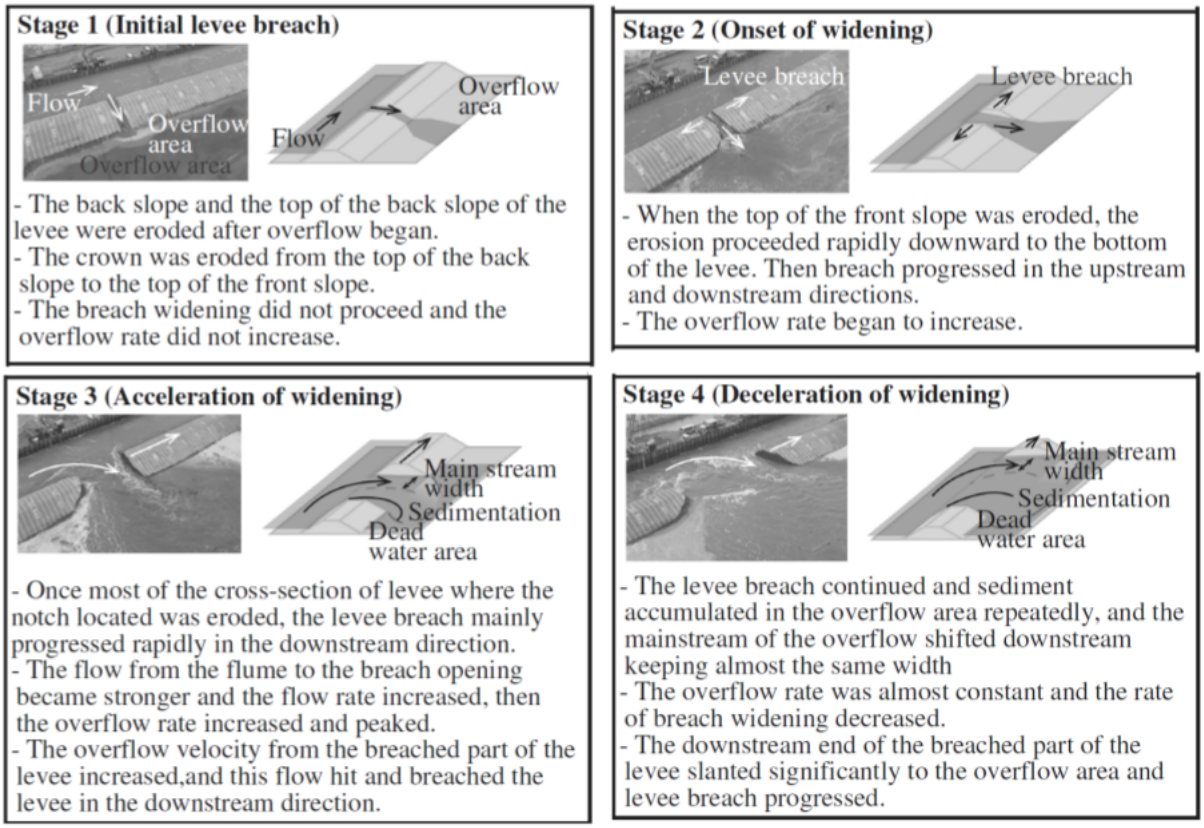

Figure 1.13: Levee breach stages description by Kakinuma and Shimizu (2014).

1.3.2 Laboratory experiments

Existing experiments included pure hydrodynamic investigations where the focus was made on breach flow patterns, such as Roger et al. (2009) who performed laboratory experiments to study the main patterns of the flow field resulting from a sudden levee breach. A pneumatically driven gate mimics instantaneous and complete levee failure with a parallel approach flow. Several configurations were studied, varying breach width and main channel inflow discharge. Resulting breach discharges and water levels at steady state were used to evaluate hydrodynamic numerical models. Al-Hafidh et al. (2022) conducted laboratory experiments with varying main channel inflow discharge, floodplain area, breach location length. Measurements focused on water level evolution in the main channel in the context of flood management with engineered levee breaches design.

Further studies aimed to understand the levee failure process with both measurements of the flow field and breach morphodynamics. Islam (2012) performed laboratory experiments of overtopping induced levee breach. Six configurations were investigated with cohesive and non-cohesive dikes and different bed levels in the main channel. The measurements included water levels and breach discharges. Three-dimensional dike reconstructions were also obtained using continuous monitoring of breach evolution with laser sensors. The results demonstrated that the breaching process

was different from frontal embankment with an asymmetrical breaching towards the downstream direction. The increase in breach dynamics was also correlated with higher inflow discharges or higher bed levels in the main channel.

Other authors, such as Yu et al. (2013), performed overtopping dike breach tests in a U-bend channel for sand and colt levees. The authors tested 12 configurations and found out that : (i) a higher head difference between upstream (channel side) and downstream (floodplain) of the levee was associated with higher breach growth rates; (ii) higher inflow discharges in the main channel induced larger final breach and (iii) using sediments with a higher diameter results in rapid breaching at the early stage of the failure process. Similar conclusion were made by Bhattarai et al. (2015) who presented an interesting study where the effect of levee material size on lateral breach expansion was presented through a series of laboratory experiments triggering homogeneous levee failure by overtopping flows. The authors concluded that increasing sediment median diameter induces quick levee collapse due to important saturation of the dike. Further investigations by Wei et al. (2016) used the same setup as Yu et al. (2013) to describe cohesive dikes failure under overtopping and reported three main stages : (i) the initial stage driven by surface erosion on the dike back slope along with scouring erosion at the structures' toe; (ii) the head-cut migration stage, by surface erosion lowering the levee crest and eroding slope walls along with jet scour at dike toe and (iii) the breach widening stage due to breach side slopes erosion due to the shear stress exerted by the flow passing through breach channel followed by slope failure of unstable masses above the flow field. The authors also mentioned the importance of factors increasing soil cohesion (soil composition, compaction, water content) as they afford a better resistance to erosion. Charrier (2015) also investigated the failure mechanisms of cohesive levees with a non-erodible bed in the main channel and floodplain. He performed five laboratory experiments to study flow patterns for various inflow discharges, different clay contents in the levee and different compaction methods.

Levee failure tests performed by Michelazzo et al. (2015) were first performed in a fixed bed configuration to study the impact of a lateral side weir flow on the main channel hydrodynamic features. Particle tracking velocimetry measurement showed an increase in the upstream Froude number in the main channel for longer side weirs, and three-dimensional flow structures were observed in the flow separations area. Starting from de Marchi's hypothesis for zero-height side weirs, Michelazzo et al. (2015), based on his experimental study outcomes, proposed a breach equilibrium flow model. Michelazzo et al. (2015) had also performed dike breach experiments with erodible sandy dikes and channel bed. Data analysis displayed the presence of a steady final equilibrium state when the difference between upstream (channel side) and downstream (floodplain side) hydrodynamic head is close to zero. As observed previously by Yu et al. (2013), the final breach width was also correlated to the main channel inflow discharge, and an interesting test case was performed to see the evolution and interaction between two adjacent breaches. The downstream breach showed a greater erosion rate, but they showed the same final width once the final steady-state was achieved. Elalfy et al. (2018) presented experiments of lateral flow through a fixed trapezoidal breach with various inflow discharges. Measurements were used to validate a two-dimensional hydrodynamic model,

and additional experiments with an erodible dike were performed to evaluate a coupled hydro-morphodynamic model. Experiments also reported the characteristic asymmetrical breach expansion from the downstream side. This aspect is commonly reported from all levee failure experiments with a parallel approach flow (Fig. 1.14).

Further laboratory experiments were presented by Rifai (2018) including a large number of laboratory experiments of overtopping induced levee failure. Two modular experimental models were constructed, and a set of fifty-four tests were performed with easy access to data Rifai et al. (2019). Measurements included water levels, flow discharges, and a detailed breach monitoring through the non-intrusive Laser Profilometry Technique Rifai et al. (2020b). Test series with different experimental conditions highlighted critical influencing factors on the breaching process. The first tests were performed with homogeneous sandy dikes and a rigid bed in the main channel and floodplain. The effects of main channel inflow discharge, main channel size, and floodplain confinement were analyzed. It was found that : (i) higher inflow discharges induced fast breach opening and higher breach dimensions and outflow; (ii) floodplain confinement resulted in lower flow velocities and thus reduced the breach erosion downstream; and (iii) an increase in channel width show lower breach outflow to inflow ratios. Tests on dike composition displayed a slight effect of fine material on breach outflow, but a noticeable change was reported in the breaching process.

Recently, Schmitz et al. (2021) conducted laboratory experiments to investigate the effect of dike geometry on levee breaching. The normalized unit dike volume was used to indicate the overall geometric parameters. Geometric parameters seemed to slightly affect the advanced breach stage compared to early breach development. In the latter stage, strong dikes (with higher normalized unit dike volume) were more resistant to erosion with less occurrence of a peak in breach outflow discharge.

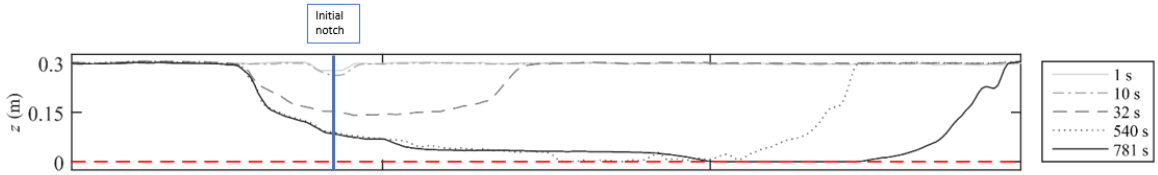

Figure 1.14: Breach longitudinal profiles at the dike crest highlighting the non-symmetrical lateral expansion (Rifai (2018)).

1.4 Numerical modeling of levee breaching

Since 1980s, numerical models are widely used to support flood risk management and increase community preparedness. The accurate prediction of the levee breaching processes and breach discharge is essential in elaborating flood maps and evacuation plans. Once validated and calibrated, numerical models help investigating several scenarios, with the main advantage of being less constraining in time and cost than physical models. Numerical modeling offers the possibility of investigating the

influence of several parameters, which could help plan maintenance work or solutions to mitigate levee failure flood risk. In the past years, various numerical approaches and models were developed to predict embankment failure, but only a few were dedicated to levee breaching. These models have to include the most important processes underpinning fluvial dike breaching due to overtopping flows, such as mixed flow regimes, surface erosion, slope failure, strong sediment transport and associated morphological changes (Dazzi et al. (2019), Onda et al. (2019), Rifai et al. (2017b)). The diverse modeling approaches offer different advantages, including the ease of use, time efficiency and precision. In the following sections, models will be described and categorized according to their degree of detail or simplification as empirical, simplified or detailed multidimensional physically-based models ASCE/EWRI task committee (2011).

1.4.1 Non-discretized empirical models

Empirical models are simple regression equations statistically derived from experimental and historical embankment failure data analysis. These equations do not account for the detailed breaching process and evolution in time. However, they can be used to provide critical parameters such as the ultimate breach width, side slope, peak outflow, and failure time while ignoring the final breach depth (Froehlichl (1995), Jandora and Říha (2008), Singh (1996), Walder and O'Connor (1997), Xu and Zhang (2009). Existing models were developed based on data from dam (frontal embankments) failure events (Wu et al. (2011)) and usually predict the peak discharge as a function of the reservoir water level and volume (Pierce et al. (2010), Singh (1996), USBR (1982)). Their applicability to compute levee breach discharge remains questionable as the parallel incident flow towards the breach zone and its interaction with erosion processes are pretty complex and evolve gradually in time through distinct phases (Michelazzo et al. (2015), Rifai (2018)). Other studies focused on the estimation of breach width and presented breach with to depth ratios going from 2 to 4 with a possibility to reach a ratio of 10 for long levees (Saucier et al. (2009)). MacDonald and Langridge-Monopolis. (1984) and Von Thun and Gillette (1990) studied embankment dams breaching and presented a simple equation to estimate ultimate breach width as a function of the reservoir water height. Nagy (2006) processed a large number of data sets related to historical levee failure events and recent ones in Hungary and highlighted parameters influencing final breach width, among which we can mention: river discharge, head acting on the levee, geotechnical properties of the levee and its geometry. Nagy (2006) also provided an equation for final breach width depending on the hydraulic head in front of the levee. Few equations were developed to compute the breach time-varying width, and the most straightforward way would be a time-dependent linear equation. For example, USBR (1988) proposed a linear progression in time for breach width based on twenty-one dam failure cases with a growth rate of 91 m/hr and no distinctions regarding embankment composition or failure mechanism. While the model developed by Von Thun and Gillette (1990) includes two different equations to adjust breach growth rate according to embankment material composition. He derived upper and lower bounds for widening coefficients corresponding to non-cohesive and cohesive levees, re-

spectively. Verheij (2002) also differentiated highly erodible from resistant dams with two different equations based on field and laboratory data sets. Compared to simple linear widening equations (USBR (1988), Von Thun and Gillette (1990), this model has the advantage of estimating breach dynamics with a high widening rate at the beginning of the process (of the order of 0.33 m/hr for non-cohesive levees), which then decreases in as the breach width increases similar to experimental observations (Elalfy et al. (2018), Rifai (2018)). Verheij and Van der Knaap (2003) improved the previous formulations by including the effect of the water level difference across the levee (between river and floodplain sides) at the breach location and the critical flow velocity to initiate erosion of the dike material was also introduced to account for soil composition. This model offers the advantage of reproducing a staged breaching process with a high widening rate at the beginning when the water level difference across the levee is very high, followed by a slower stage as the latter parameter decreases. Finally, this model, compared to simple equations where the breach expansion is not limited, a allows breach to reach equilibrium as the water level difference approaches zero. The latter equations did not indicate breach cross-sectional shape or vertical erosion rates. The empirical model proposed by Froehlich (2008) can also be used to mimic a staged failure process based on the concept of Brunner (2002) who proposed a sine-curve breach progression with a slow opening at the initiation of the breach, which is then accelerated and followed by another slow phase close to the end of breach development. Froehlich (2008) proposed three different variants to approximate both lateral and vertical breach opening. Each of the three models assumes that a breach begins to form at the top and grows into a trapezoidal shape with time. In this model, Froehlich (2008) also introduced a coefficient to separate overtopping induced breaching from piping induced failure cases. Recently, Zomorodi (2020) selected fifty-five reliable data sets of fluvial dike breaching experiments and recent river levee failure events in the United States, France, Italy, Germany, Belgium, Dutch-Belgian border, China, and Japan. The author derived empirical equations and curves to predict breach final width and erosion rate for cohesive and non-cohesive dikes and provided equations to approximate breach peak discharge. The use of purely empirical models can be appreciated for their simplicity and time efficiency to provide predictions and recommendations to support flood management in a short time. However, the potential uncertainties related to such models can be very high (Danka and Zhang (2015)). Most of them relied on mixed data from frontal and lateral embankment and only a few distinguished failure mechanisms. In addition, models approximating breach peak discharge might not be adapted for levee failure cases a varying water surface level develops in the main channel and changes the head influences breach progression and outflow (Peeters et al. (2016)).

1.4.2 Simplified physically-based models

Simplified physically-based models represent an interesting alternative with reasonable computational requirements and a hybrid approach between the complexity of detailed-physically based models and the lack of accuracy in empirical equations. These models solve equations related to the

flow in one or two dimensions and integrate the breaching process based on simplifying assumptions and empirical equations (*e.g.,* erosion rate formula, broad-crested/weir equation for computing the breach outflow discharge). Therefore, users may need to specify some input parameters (*e.g.,* breach location, breach start time, breaching duration, erosion rates, final breach width, and depth, side-slope, critical velocity, or shear stress required to initiate detachment for the dike material, and erodibility coefficient) and assumptions to simplify the problem (*e.g.,* prismatic symmetrical breach shapes such as trapezoidal, triangular and parabolic, one-dimensional quasi-steady flow in the breach channel). This approach is employed in various models such as the 1D RUPRO breach model Paquier and Béraud (2010) that takes breach location and final dimensions as input parameters and computes breach width and depth at each time step based on the estimated sediment discharge by Meyer-Peter and Müller (1948) formula with the assumption of a rectangular breach section while breach outflow is estimated using Bernoulli equation. West et al. (2018) published a comprehensive review of existing models, among which: the Hydrologic Engineering Center River Analysis System (HEC-RAS) (USACE (2011)) allows the user to model embankment failure by predefined information related to the breaching process, including breach geometry and equations describing its progression; the AREBA model presented by Van Damme (2012) that simulates overtopping and slope failure of homogeneous and composite embankments. The user defines breach opening parameters, and breach outflow is computed with a weir formula; A more sophisticated model was developed by Wu (2013, 2016), the DL BREACH model offers the possibility to simulate both cohesive and non-cohesive embankments failure and includes some physical processes such as scour erosion and slope failure. The model can also estimate the probability of failure using Monte Carlo simulations and model two-way coastal levee breaches. However, breach expansion must be defined by the user *a priori*. Most of the existing simplified physically-based models were dedicated to earthen dams; few attempts have been made to assess their applicability to fluvial dikes. According to Risher and Gibson (2016), these models perform best during initial, rapid fluvial breach widening but may diverge when tailwater impacts breach flow. Vacondio et al. (2016) simulated the 2014 levee failure event on the Seccheria river in Italy using the 2D shallow water equation to compute flow variables while the breaching process was represented by a geometric approach with predefined breach location, shape, expansion duration, and final dimensions. Recently, Tadesse and Fröhle (2020) modeled the 1996 Awash river levee breach in Ethiopia using the 2D hydrodynamic numerical model TELEMAC-2D and its parametric breach module and analyzed the influence of user input parameters on the resulting flood. Indeed, assumptions regarding breach failure time, geometry, and erosion rate come with non-negligible uncertainties (Zhong et al. (2017)). However, when rapid flood risk assessment simulations are required, these models may be beneficial because of their low computational cost and ease of use.

1.4.3 Detailed physically-based models

Detailed physically-based models solve two or three-dimensional physically-based equations describing the motion of the fluid, sediment transport processes (suspension, bedload, or saltation), and geotechnical processes. Several studies applied this approach to simulate dam and frontal dike failure, Volz (2013) presented the BASEMENT model to simulate the overtopping induced failure of non-cohesive embankments with various soil composition configurations. The model uses the two-dimensional (2D) shallow water equations for the flow field with empirical equations to compute suspended and bedload sediment transport and performs slope failure through a geometrical algorithm. Wang and Bowles (2006) modeled a field-scale dam breach experiment. The model only allowed surface erosion simulation through an erosion rate formula, and a 3D slope stability analysis module was developed. Recently, Onda et al. (2019) developed a 3D multiphase Reynolds-averaged Navier–Stokes (RANS) model to simulate both overtopping and seepage flow. The model provided promising results but was only tested on laboratory experiments with frontal embankments configurations. Few studies have applied detailed hydro-morphodynamic models in fluvial dike breaching scenarios induced by flow overtopping, making model-data comparisons generally on integral parameters (*e.g.,* breach outflow hydrograph, ultimate breach width) rather than on the 3D evolving breach geometry. For example, Faeh (2007) used a 2D morphodynamic model considering side stability and both bedload and suspended load to simulate the levee breach expansion in the Elbe River. The model was validated against the breach outflow hydrograph only; no model-data comparison was provided on the breach geometry evolution. Kakinuma and Shimizu (2014) simulated field-scale, non-cohesive levee breaching tests using the 2D morphodynamic model Nays 2D which was modified to incorporate bedload transport and slope stability formulations derived from the experimental results. The model failed in capturing the early stage of the dike breaching but successfully reproduced the breached volume during the widening stage. Dou et al. (2014) simulated curved fluvial dike breaching due to overtopping using a non-equilibrium total sediment transport model and reported model-data comparisons for the final breach width only. Elalfy et al. (2018) applied a 2D morphodynamic model in which a new source term was included in the sediment-mass-conservation equation to account for slumping failure. The model reasonably reproduced the breach characteristics (*i.e.* breach-shape evolution and breach hydrograph). Recently, Dazzi et al. (2019) proposed a 2D code coupled with a physically-based erosion model and a bank failure module. Deposition of sediments is not included assuming that the eroded material is washed away by the flow. This assumption disagrees with laboratory and field observations (Islam (2012), Kakinuma et al. (2013), Rifai et al. (2017b, 2018)). The model presented by Dazzi et al. (2019) was applied to a field-scale non-cohesive dike breach experiment. The breaching process was not captured in detail, but the outflow hydrograph, the final breach width, and asymmetry (regarding the initial notch position) were fairly replicated. Detailed physically-based models can accurately represent the hydrodynamic and physical processes of breach expansion in fluvial dikes induced by flow overtopping. However, the use of these models is still complex and requires high computational run times. Studies also showed the importance of a good calibration to provide reliable results, and the choice of some em-

pirical coefficients may highly influence model predictions. Finally, some geotechnical aspects of the breaching process are in general poorly described in numerical models.

1.5 Conclusion and scientific questions

The literature review presented above reflects a large choice of modeling approaches to simulate levee breaching. Each category presents advantages and shortcomings. Detailed physically-based models can provide more accurate simulations of the hydrodynamic and physical process of breach expansion in fluvial dikes. However, such models require a good calibration and include empirical equations to model-specific features with user-defined empirical coefficients. One of the primary objectives of the present work is to provide guidance for the best model choices in the particular case of levee breaching and risk assessment studies. Various breach models are implemented in TELEMAC-2D, the hydrodynamic module of the TELEMAC-MASCARET code, in the framework of a simplified physically-based modeling approach. Developments included empirical laws and the RUPRO breach model by Paquier and Béraud (2010). These models are evaluated against a detailed physically-based modeling approach coupling TELEMAC-2D and the TELEMAC-MASCARET morphodynamic module GAIA with an improved slope failure module. On the other hand, laboratory experiments are performed following the investigations carried out by Rifai (2018). Experiments of overtopping induced levee failure are performed, and investigations focus on the influence of a movable bed in the main channel, dike foundation, and floodplain on the breaching mechanisms.

Chapter 2

Experimental investigation of overtopping induced levee failure with a movable channel and floodplain bottom

Les processus physiques liés à la rupture de digues fluviales ne sont aujourd'hui que partiellement élucidés et nécessitent davantage de données expérimentales ou de cas réels afin d'améliorer notre compréhension des interactions complexes entre l'écoulement et l'ouvrage de protection. Ces données servent aussi à nourrir les modèles numériques et améliorer leur prédictivité. Dans ce chapitre, nous réalisons des expériences à échelle laboratoire de rupture d'une digue fluviale par surverse. La digue est construite en sable homogène et une couche de sable érodable est mise en place dans le canal principal, la plaine d'inondation et les fondations de la digue. Un suivi détaillé dans le temps de l'évolution 3D de la brèche est réalisé grâce à la technique de Profilomètre Laser. La largeur du canal principal ainsi que le débit d'entrée sont variés au fil des expériences afin d'élucider leur influence sur la dynamique de la brèche.

The work presented in this chapter is in preparation for submission to the *Water Resources Research* journal, entiteled *Experimental investigation of bed erodibility effect on overtopping induced levee breaching.*

Lydia KHELOUI[1,2] , Vincent Schmitz[3], Ismail Rifai[4], Benjamin Dewals[3], Kamal El Kadi Abderrezzak[1,2]
[1]EDF RD LNHE - National Laboratory of Hydraulics and Environment (Chatou, France)
[2]Saint-Venant Hydraulics Laboratory (Chatou, France)
[3]Research Group of Hydraulics in Environmental and Civil Engineering (HECE), University of Liège, Liège, Belgium.
[4]Hydro-Québec, Montréal, Canada.
Corresponding author: lydia.kheloui@edf.fr

2.1 Introduction

Hydraulic numerical models are widely used to support the design and maintenance of flood protection structures, predict flood maps, and elaborate evacuation plans. In the case of levee (i.e., fluvial dike) breaching and consequent inundations, severe socio-economic damages can be caused to communities and activities established in protected areas (Sharp et al. (2013)). Various failure causes are reported in the literature (Vannucchi et al. (2014)), such as structural defaults, animal burrows, liquefaction, seepage, and overtopping, which is the most common breach initiating factor. In Europe, floods have resulted in 700 fatalities and a loss of more than 25 billion euros since 2000 (Ventini et al. (2021)) while the number of extreme floods is constantly increasing (Özer et al. (2016)). Therefore, the accurate prediction of breach outflow and dynamics is critical to improve flood resilience and preparedness and requires a good understanding of the main dike failure mechanisms and their implementation in numerical models. Breach initiation and expansion due to overtopping flows involve rapid and complex physical processes, making measurements and data collection difficult in real failure events. In addition, the experimental research on understanding the breaching process was mainly dedicated to frontal embankments (i.e., dams) (Ahadiyan et al. (2022), Cestero et al. (2015), Müller et al. (2016), Pickert et al. (2011)); thus, poor information on fluvial dike failure is available. However, an increased number of laboratory investigations described fluvial dike breaching processes during the last decade. A global database called International Levee Performance Database (ILPD) was also developed (Özer et al. (2020)) to describe levee failure processes from the analysis of 1500 cases. Those research efforts clarified the main features of levee failure mechanisms, which are relatively different from frontal embankments (Resio et al. (2009), Saucier et al. (2009), Zomorodi (2020)), because of the parallel flow field in the main channel and the dimensions on levees which are longer in flow direction. Hydrodynamic investigations preformed by Michelazzo (2014) highlighted characteristics of the flow in the main channel in the presence of a lateral weir, such as complex 3D flow structures in the vicinity of the breach, an increase in the lateral discharge and channel Froude number for longer weirs, an increased transversal velocity and a decrease in longitudinal velocity along the weir. Experiments with an erodible levee and channel bottom (Islam (2018), Michelazzo (2014)) were also performed and elucidated breach expansion in river dikes and erosion in the main channel and floodplain. They reported a continued opening in the lateral direction after maximum breach depth was completed, and an asymmetrical breach widening leaning toward the downstream direction. The same features were also observed in field-scale experiments presented by Kakinuma and Shimizu (2014), Kakinuma et al. (2013), that described erosion in the main channel upstream the breach opening and deposition of the material in the floodplain. Kakinuma et al. (2013) also varied dike geometry and dike composition in their experiments, showing that addition of fine-particle into gravel and sand levees resulted in a slower initiation of the breaching process followed by a higher lateral erosion rate. A slower breach initiation was also observed with a wider levee crest. Wu et al. (2017) carried out investigations on the non-symmetrical overtopping induced breaching process and provided asymmetry coefficients (downstream breach width to upstream breach width

ratio) for both cohesive and non-cohesive levees ranging between 2.9-3.3 and 2.2-2.6, respectively. The laboratory experiments of overtopping induced levee failure presented by Rifai (2018) included a set of fifty-four tests with an open-access to collected data (Rifai et al. (2019)). This work provided the following main outcomes : (i) increasing the main channel inflow discharge results in faster breach opening and longer breaches with higher discharges; (ii) floodplain confinement slows the flow through the breach channel and thus reduces its erosion; and (iii) a lower breach discharge to channel inflow ratios is measured for wider flumes. Recently, Schmitz et al. (2021) varied geometric levee parameters, which impacted the second stage of breach development. Levees with high normalized unit volume showed a greater resistance to erosion and an absence of a peak in breach discharge. To the best of our knowledge, the effect of channel and floodplain erodibility, was not clearly isolated in existing fluvial dike breaching experiments (Islam (2018), Kakinuma et al. (2013), Michelazzo (2014)). Aiming to improve the understanding of channel and floodplain erodibility effect on levee failure mechanisms, eight laboratory experiments were performed on the laboratory setup used by Rifai (2018). Tests included variation of the inflow discharge and the main channel width and were then compared to equivalent tests from Rifai (2018) with rigid channel and floodplain beds.

This chapter is organized as follows: in Section 2.2, a description of the experimental setup, measurements, and test program is given. The general results are presented in Section 2.3, followed by a discussion in Section 2.4. Conclusions are drawn in Section 2.5.

2.2 Laboratory facility

2.2.1 Laboratory setup

The Laboratory investigations were performed at the National Laboratory for Hydraulics and Environment (LNHE) of EDF-R&D using the experimental set-up presented by Rifai et al. (2019). It consisted of a main channel of l = 15.5 m long with a L_d = 7 m long side opening toward a 1 × 7 m floodplain (Fig. 2.1). The main channel width l could be modified using wood panels; four values were tested: 1 m, 1.4 m, 1.8 m, and 2.25 m. The main channel and floodplain were separated with a longitudinal sand dike of trapezoidal shape, with h_d = 0.3 m high, l_{dc} = 0.1 m wide crest and inner and outer face slopes of S_i = S_o = 1:2 (V:H). The sand was uniform, with a median diameter d_{50} = 1 mm, a density ρ_s = 2470 kg/m^3, a bulk density ρ_b= 1556 kg/m^3 and a porosity p = 0.37. The bottom of the main channel and floodplain, along with the dike foundation, was at the same level and consisted of a 0.1 m erodible sand layer. To ensure dike stability and avoid seepage failure, a drainage system was placed at the dike bottom, and a 0.02 m deep, 0.1 m wide initial notch was cut at 2.5 m from the upstream end of the dike crest to trigger overtopping. A perforated plane located at the downstream end regulated the outflow so that, for a given inflow discharge Q_i, the required water level was reached in the main channel to allow dike overtopping at notch location. In the tests reported hereafter, a constant inflow discharge Q_i was used, and the flow across the breach

was discharged freely from the floodplain without any storage change or tailwater effects.

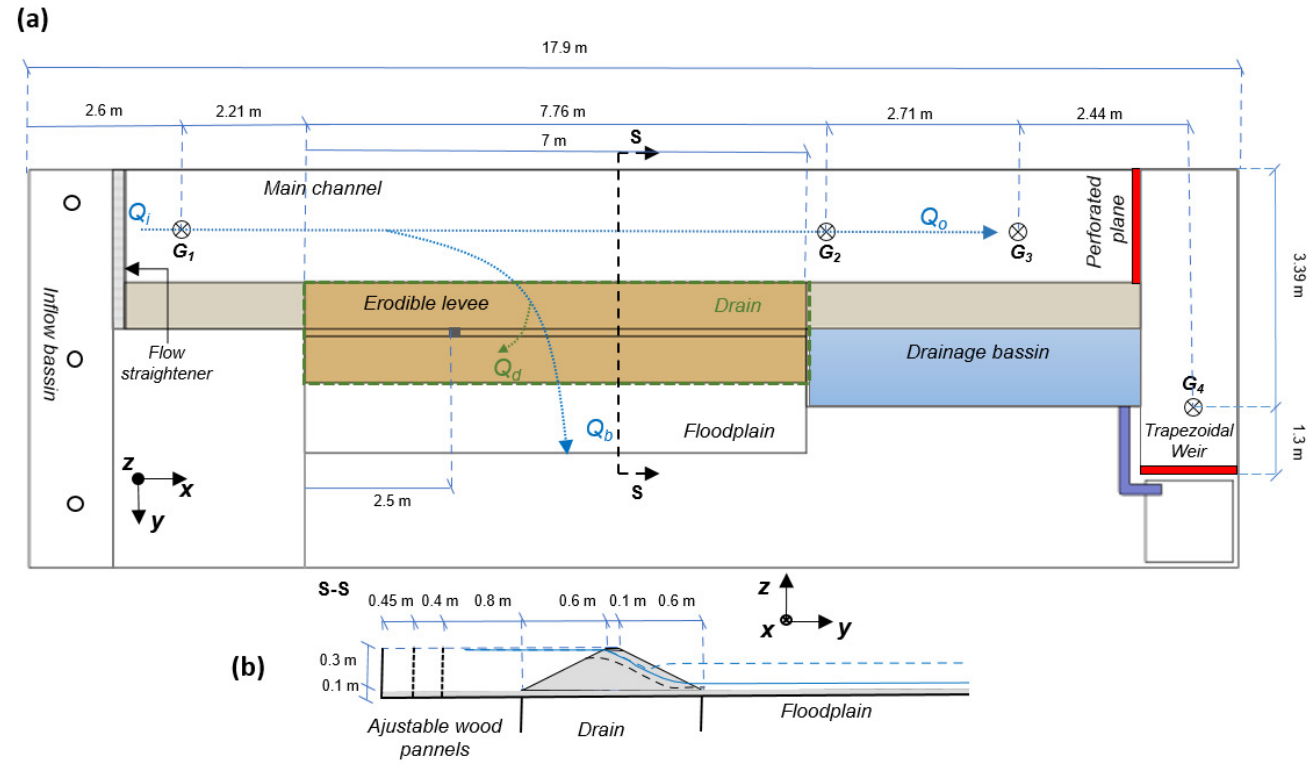

Figure 2.1: (a) Plan sketch of the experimental setup, and (b) channel cross-sectional profile (cut S-S). Q_i, Q_b, Q_d and Q_o are inflow discharge, breach discharge, drainage discharge and main channel outflow discharge, respectively. G_i denotes gauge stations.

2.2.2 Test program and measurements

Experiments consisted in provoking the overtopping of the main channel flow over the dike crest at a designated spot (i.e. initial notch) and observing subsequent dike erosion and breach expansion. Eight tests conducted at the National Laboratory of Hydraulics and Environment of EDF-R&D with a movable bed configuration in the main channel and floodplain. A 0.1 m layer of homogeneous sand (d_{50} = 1 mm) was installed in the main channel and floodplain, over which the 0.3 m high levee was built. Investigations of the breaching process were performed under different configurations. As shown in Table 2.1, the test program included experiments with variable main channel widths and inflow discharges. The 'E' symbol stands for Tests with and erodible bed in main channel and floodplain while 'NE' refers to experiments performed by Rifai et al. (2019) where erosion was allowed for the levee only. To simplify results analysis, tests are generally referred to as small or high main channel inlet Froude numbers with 'SF' and 'HF' notations.

Water surface levels were continuously recorded with ultrasonic sensors at different locations from G_1 to G_4 as shown in Fig.2.1. In the main channel, water levels were measured upstream the

Test ID	Q_i (m^3/s)	l (m)	$F(-)$	$l/h_d(-)$	Data source
1E	0.058	1.4	0.116 (SF)	4.67	This study
1NE	0.054	1.4	0.108 (SF)	4.67	Test 33 Rifai et al. (2019)
2E	0.094	1.4	0.188 (HF)	4.67	This study
2NE	0.092	1.4	0.184 (HF)	4.67	Test 35 Rifai et al. (2019)
3E	0.074	1.8	0.105 (SF)	6	This study
3NE	0.072	1.8	0.102 (SF)	6	Test 36 Rifai et al. (2019)
4E	0.100	1.8	0.142 (HF)	6	This study
4NE	0.125	1.8	0.177 (HF)	6	Test 39 Rifai et al. (2019)
5E	0.121	1.8	0.171 (HF)	6	This study
6E	0.130	1.8	0.185 (HF)	6	This study
7E	0.098	2.25	0.105 (SF)	7.5	This study
7NE	0.098	2.25	0.105 (SF)	7.5	Test 40 Rifai et al. (2019)
8E	0.160	2.25	0.171 (HF)	7.5	This study
8NE	0.160	2.25	0.171 (HF)	7.5	Test 45 Rifai et al. (2019)

Table 2.1: Test program (NE stands for tests with a rigid bed in main channel and floodplain).

levee at G_1 and downstream the levee at G_2 and G_3. The water level measured at a trapezoidal weir (G_4) was used to determine the main channel outflow discharge Q_o, while the inflow discharge Q_i was directly measured with an electromagnetic flowmeter. The drainage discharge Q_d was calculated as a function water level variation in the main channel. Finally, the breach discharge Q_b was computed based on the mass balance in the main channel Rifai et al. (2017a). For more details on the monitoring of water levels and flow discharges, readers may refer to Rifai et al. (2018, 2019, 2021).

The 3-D breach evolution was monitored by a non-intrusive Laser Profilometry Technique (LPT) consisting of laser sheet projection on the dike (emitted by a laser line projector Z-Laser Z30M18S3-F-640-LP75) Rifai (2018), Rifai et al. (2017a). The recording was performed by a digital camera set on a full HD resolution (1920 × 1080 pixels) at 60 frames per second. Two laser projectors, fixed to an automated sliding rail system, were used to cover the full 7 m dike length. The 3-D reconstruction algorithm of the dike geometry includes an optical distortion correction module and a refraction correction module for submerged dike portions. Further details on the breach geometry reconstruction are given by Rifai et al. (2020a).

2.3 Results

In this section, data from our experiments with an erodible bed over the entire test channel are analyzed to understand breach growth and its specific features when varying geometric or hydrodynamic test conditions. The origin of the longitudinal axis x is set at the upstream end of the breach and for the vertical axis z at the level of the erodible sand layer in the main channel and floodplain (10 cm above the rigid bed).

2.3.1 Breach spatial and temporal growth

Features of overtopping induced levee breaching are described in this section through the temporal analysis of spatial breach expansion, flow rates, and water level measurements. The main physical processes being qualitatively similar for all tests, results in this section rely on data collected for Test 2E (Table. 2.1) only. For more clarity, the time frame start was adjusted to fit the beginning of overtopping at the initial notch location and results analysis was limited to the first 500 seconds. The water level measurements and calculated flow rates were also processed with a Savitzky and Golay (1964) filter to improve their quality.

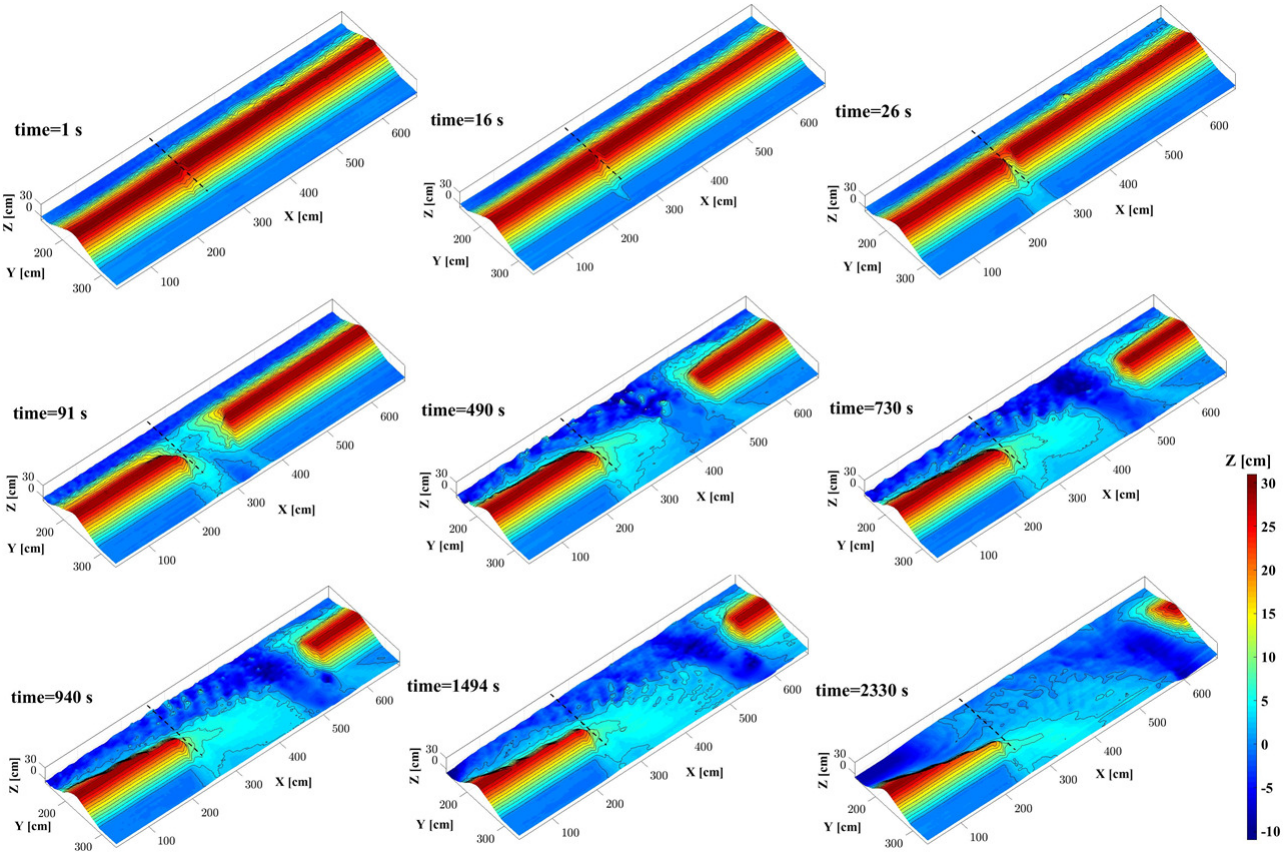

Figure 2.2: 3D reconstructed breach evolution for Test 2E. Dashed lines indicate position of the initial notch center (x=2.55 m).

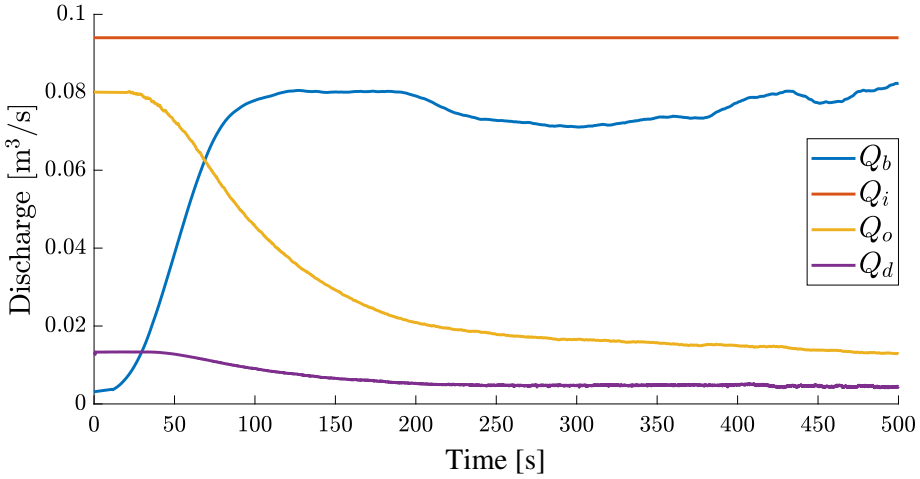

Figure 2.3: Discharges recorded during Test 2E (l = 1.4 m; Q_i = 0.094 m^3/s).

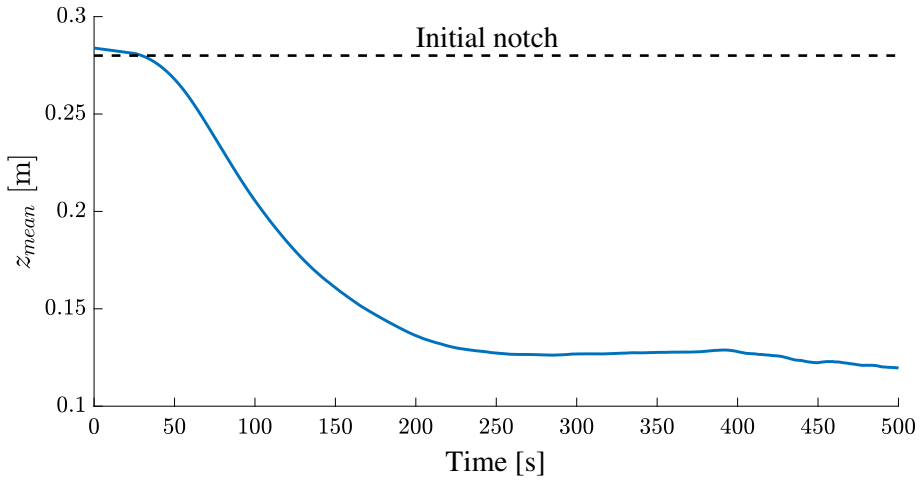

Figure 2.4: Mean water level in the main channel recorded during Test 2E (l = 1.4 m; Q_i = 0.094 m^3/s).

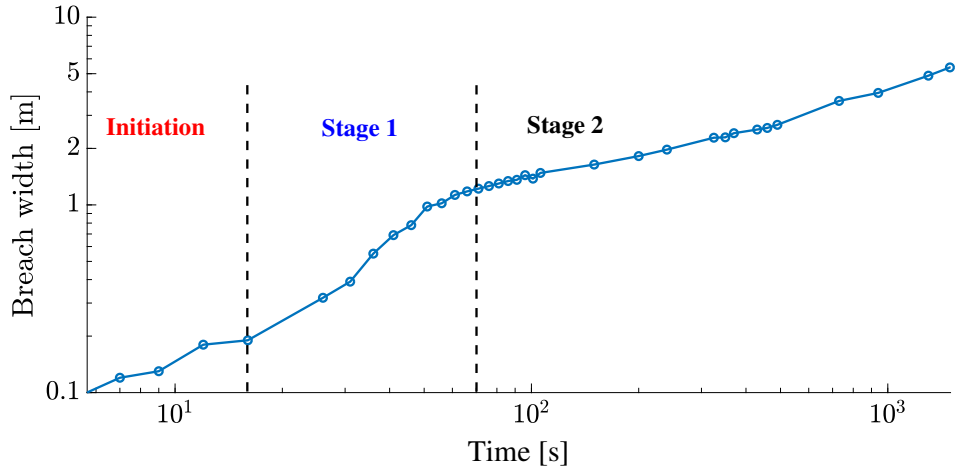

Figure 2.5: Breach width temporal evolution measured at the center of the dike crest during Test 2E (l = 1.4 m; Q_i = 0.094 m^3/s).

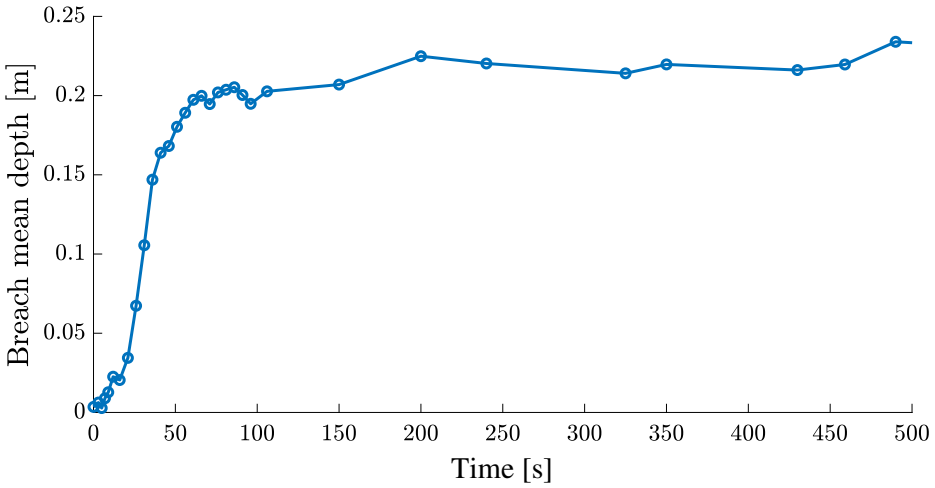

Figure 2.6: Breach mean depth measured at the center of the dike crest during Test 2E (l = 1.4 m; Q_i = 0.094 m^3/s).

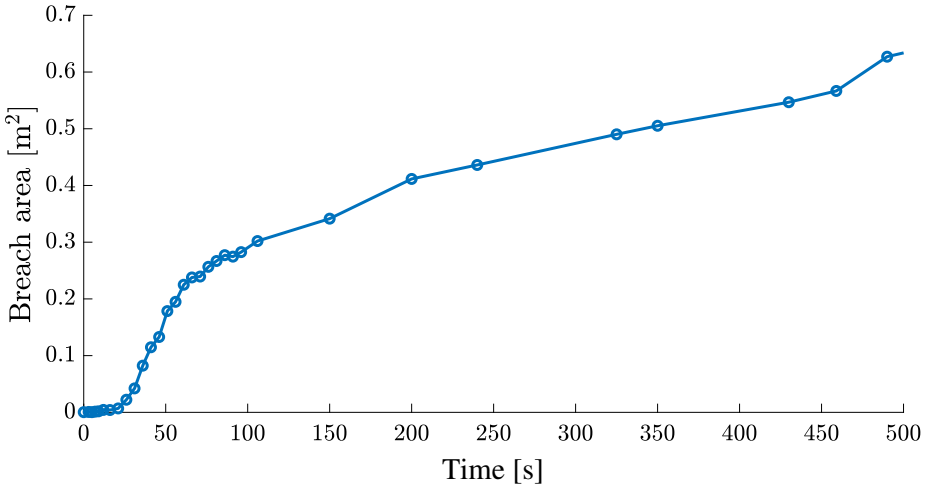

Figure 2.7: Breach area measured at the center of the dike crest during Test 2E (l = 1.4 m; Q_i = 0.094 m^3/s).

As reported in previous research by Kakinuma et al. (2013), Michelazzo (2014), Rifai et al. (2017b), Schmitz et al. (2021), Visser (1998), Yu et al. (2013), breach expansion is a gradual process characterized by different phases. In the present work, the breaching process starts when the water level in the main channel exceeds the levee crest at a notch location, it is then characterized by a three-stages expansion. Breach initiation (Stage 0 from the moment overflow starts at 0 seconds to 16 seconds) is a complex step as it is highly influenced by experimental conditions such as notch dimensions, channel inflow, water levels in the main channel, and the levee drainage system. Figure 2.2 shows three-dimensional reconstructions of the levee as measured by the Laser Profilometry Technique and the chronological progression of breach shape. The overflow progresses towards the floodplain with high flow velocities and induces material erosion at the back slope of the dike (time = 16 sec-

onds). when retrograde erosion reaches the crest and the top of the front slope, the vertical erosion and symmetrical lateral expansion of the breach downstream and upstream the initial notch location start. In Figures 2.3 and 2.4 a slight variation of the main channel water level can be observed and Figures 2.5, 2.6 and 2.7 show that breach width, mean depth and longitudinal section area increase quite slowly and breach discharge remains relatively small.

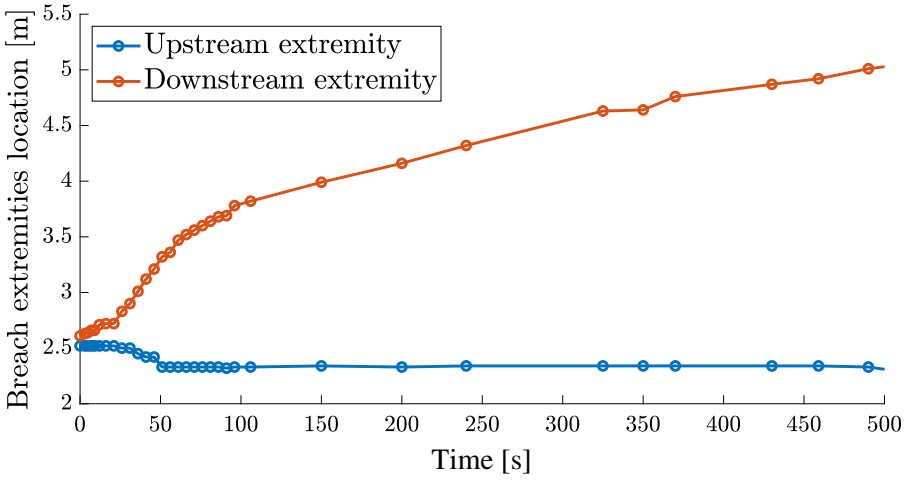

Figure 2.8: Measured positions of breach extremities along the longitudinal axis at the center of the dike crest for Test 2E (l = 1.4 m; Q_i = 0.094 m^3/s).

After the early breaching phase, a fast deepening and widening of the breach in a complex 3D shape occur in Stage 1 (from 6 seconds to 71 seconds), with an hourglass shaped breach channel as shown in Figure 2.2) . As a greater breach section is offered to convey the flow from the main channel to the floodplain, breach discharge increases rapidly and reaches a maximum value corresponding to 85% of the main channel inflow discharge for Test 2E. As a result, the main channel water level and outflow discharge drop quickly (Figures 2.4 and 2.5). Breach morphodynamics, at this stage, is driven by two main processes; surface erosion and unstable sand block failure. The material is then transported by the flow stream as bedload. After breach depth reaches dike foundations, it can be seen in Figures 2.8 and 2.9 showing breach extremities position and breach section evolution on the center axis of levee crest, that the breach no longer expands symmetrically. Instead, the breach preferentially widens towards the dike's downstream end due to the main channel's lateral incident flow. As mentioned by Michelazzo (2014) in his investigations including surface velocity measurements, the breach flow deviation angle increases along the breach towards the downstream section of the breach resulting in a breach that widens mainly downstream.

During Stage 2 (from 71 s until test end), the breach discharge converges to an equilibrium state around its maximum value, and the average water level in the main channel stabilizes at a minimum value. Breach expansion rate decreases (Figures 2.5, 2.7 and 2.6) and mainly occurs at the downstream extremity of the breach as shown in Figure 2.9. On the other hand, the upstream portion of the dike is eroded at the toe from by the parallel flow in the main channel. Indeed, the water depth

in the upstream part of the main channel stabilizes at its minimum value and the flow velocities increase. As a result, the upstream end of the breach displays a slight evolution with several episodes of unstable sand blocks failure. The longitudinal breach section evolution in Figure 2.9 highlights the vertical expansion of the breach through the dike foundation downstream from the notch location where flow velocities are important. At the same time, sediments eroded in the upstream portion of the main channel bed, and the levee collapsed material from the channel side are deposited in the upstream part of breach section which become shallower. This aspect was also reported in similar experiments by Michelazzo (2014) and field scale experiments performed by Kakinuma et al. (2013). We can also observe in the 3D reconstructions (Figure 2.2) a channel in the breach area that indicates the breach outflow mainstream location with a lower bed elevation. This channel is then shifting along the longitudinal axis in flow direction from [250:350] cm at 91 seconds to [400:500] cm at 490 seconds, [450:550] cm at 730 seconds. It keeps moving downstream with a relatively constant width until [600:700] cm at the end of the experiment.

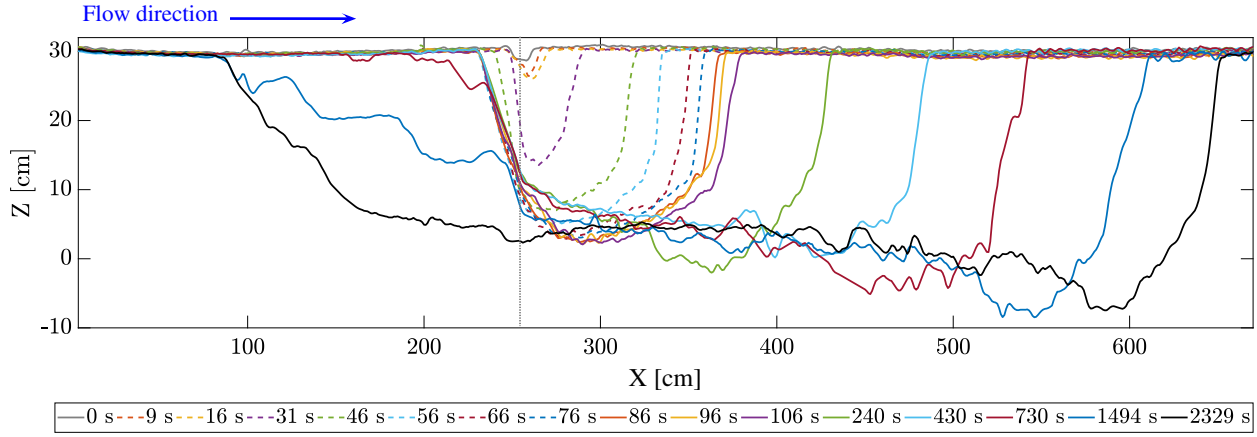

Figure 2.9: Longitudinal breach profile evolution for Test 2E at the crest center. Doted vertical line indicates position of the initial notch center (x=2.55 m).

2.3.2 Influence of channel inflow discharge

To assess the influence of the initial Froude number in the main channel on breach growth experiments 3E, 4E, 5E, and 6E were performed with a constant main channel width (1.8 m) and a variable inflow discharge. Tests 1E, 2E and 7E, 8E with a main channel width of 1.4 m and 2.25 m, respectively, may also be analyzed in that context. Figures 2.10 and 2.11 show breach discharges and breach discharge to main channel inflow ratios variation in time for Tests 3E, 4E, 5E and 6E with characteristic main channel width 1.8 m. Breach outflow is directly impacted by the increase in main channel input discharge. As displayed in Figure 2.12 there is a quasi-linear augmentation of the breach peak discharge with the augmentation of main channel inflow. However, Figure 2.11

shows that increasing the inlet Froude number reduces breach discharge to main channel inflow ratios. Hence, a smaller portion of the flow deviates towards the breach opening when the longitudinal flow velocities are higher in the main channel.

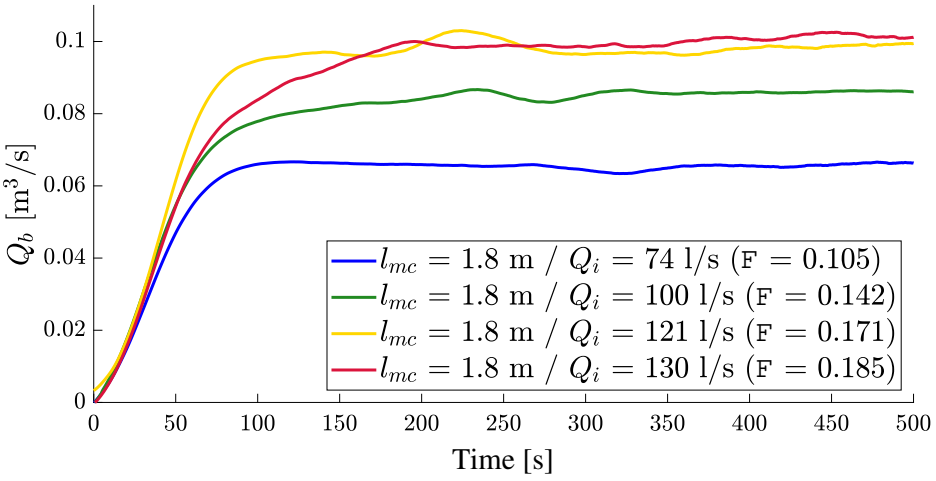

Figure 2.10: Impact of the Froude number on the breach discharge (experiments 3E, 4E, 5E and 6E).

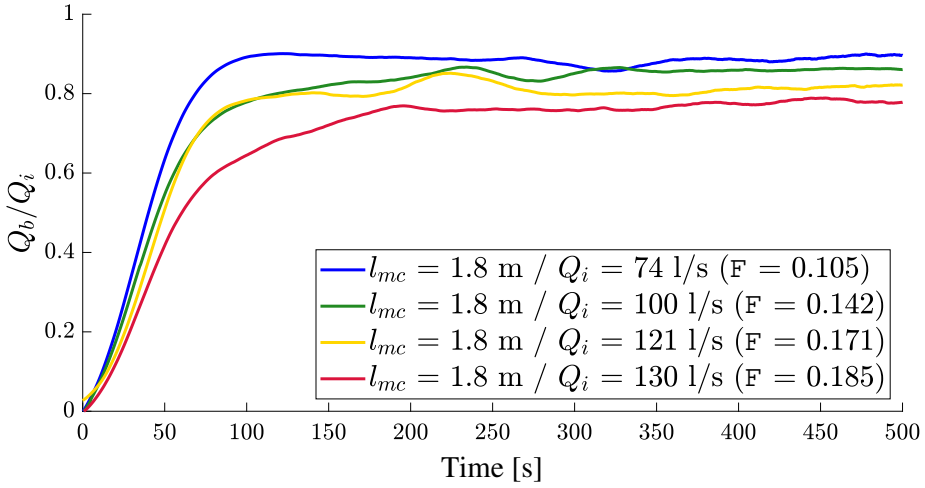

Figure 2.11: Impact of the Froude number on the non-dimensional breach discharge (experiments 3E, 4E, 5E and 6E).

The instantaneous mean channel water level variations illustrated in Figure 2.13 are not significantly impacted by the inflow discharge during breach initiation, except for Test 5E, where breach initiation was delayed and required higher overflow depths. This is, on the one hand, assumed due to the initial notch cut that is handmaid for each case and can thus vary and be shallower for some tests. On the other hand, dike compaction was reported in the literature by Al-Riffai (2014) to play an essential role in breach growth, and initiation especially for cohesive embankments and small grain size sediments with the presence of a time lag between breach outflow hydrographs corre-

sponding to configurations with a different dike compaction or drainage discharge. Additionally, Winz (2012) demonstrated a significant impact of material compaction in his experiments for non-cohesive sediments with d_{50}= 2.5 mm. High compaction levels resulted in delayed breaching. Main channel water levels (Figure 2.13) started decreasing during the first stage with higher speeds for lower Froude numbers experiments, which also stabilized at lower values during Stage 2. These observations agree with breach discharge behavior, as bigger portions of the main channel flow are conveyed through the breach opening when lower main channel input discharges are used.

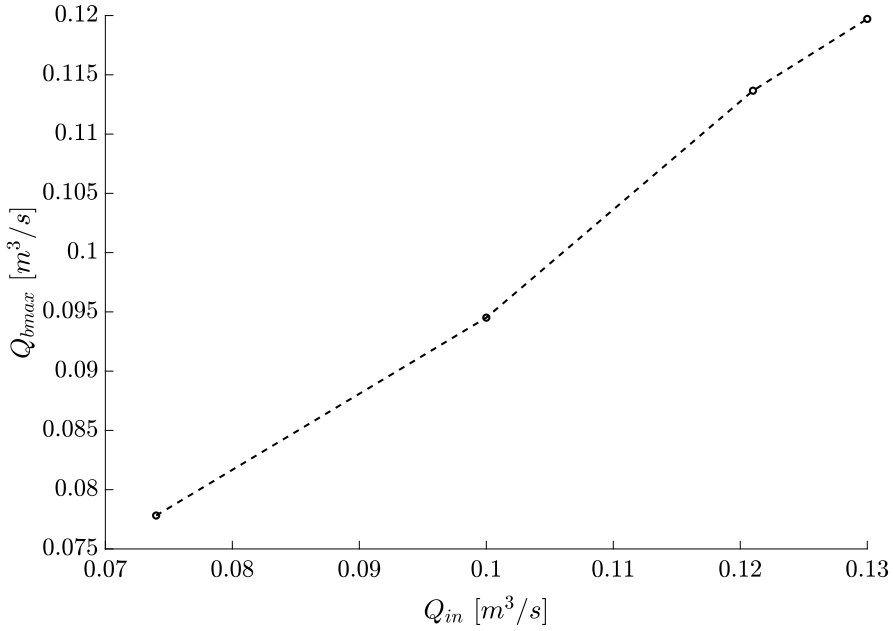

Figure 2.12: Maximum breach discharge as a function of main channel input discharge for experiments 3E, 4E, 5E and 6E

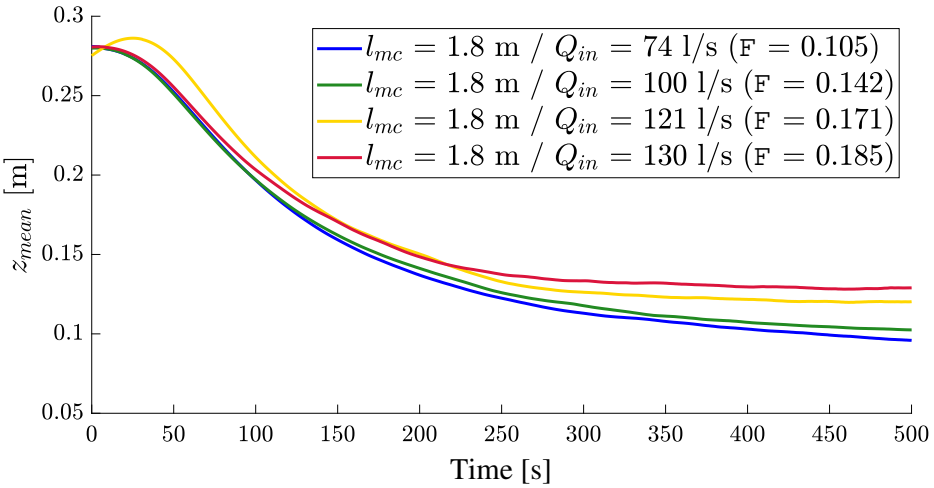

Figure 2.13: Impact of the Froude number on the mean water level in the main channel (experiments 3E, 4E, 5E and 6E).

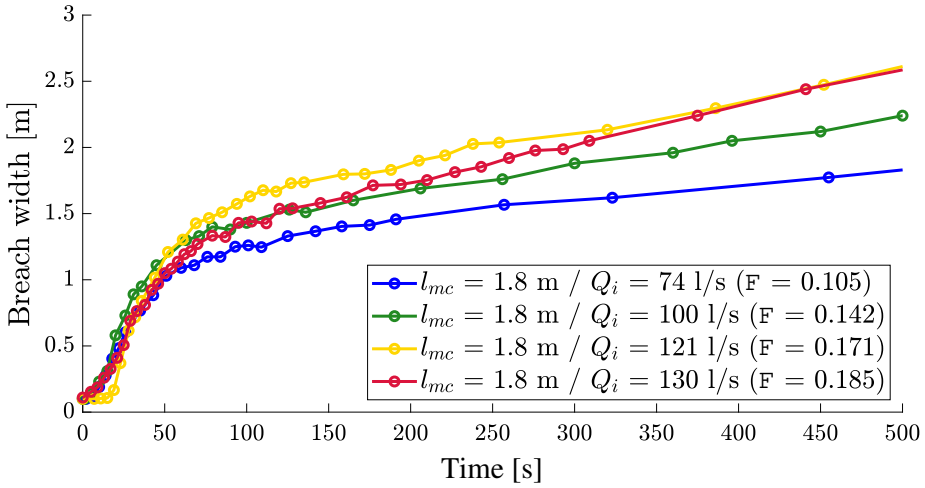

Figure 2.14: Impact of the Froude number on the breach width (experiments 3E, 4E, 5E and 6E).

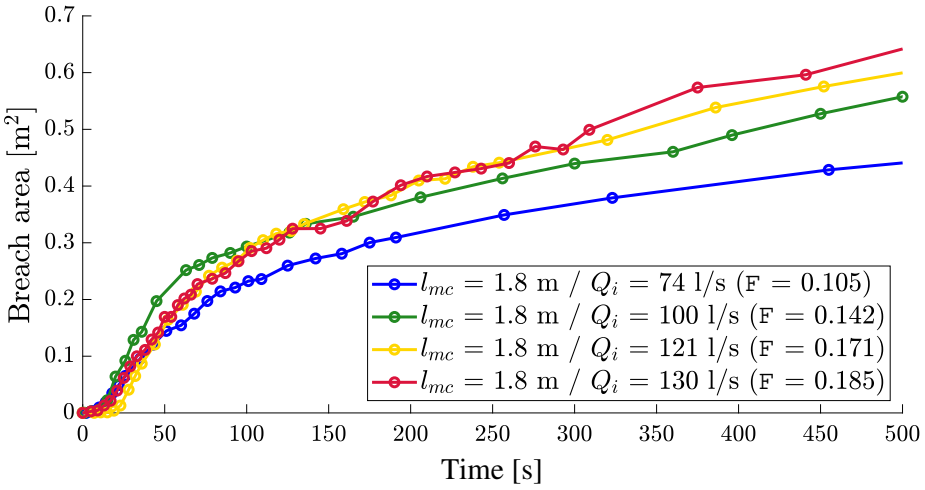

Figure 2.15: Impact of the Froude number on the breach cross area (experiments 3E, 4E, 5E and 6E).

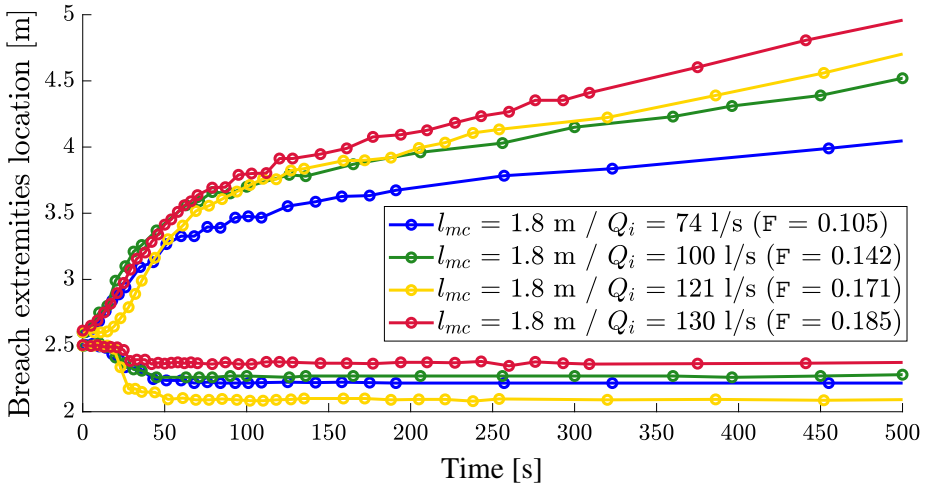

Figure 2.16: Impact of the Froude number on the breach extremities location (experiments 3E, 4E, 5E and 6E, the notch center is located at x = 2.55 m).

Looking at breach growth dynamics highlights two main features. First, breach top width analysis shows a smoother transition between Stage 1 and Stage 2 for Tests 5E and 6E compared to 3E and 4E, for which Stage 1 duration is shorter with a clearly marked transition to the quasi-stabilization Stage 2. In addition, wider breaches (Figure 2.14) and larger breach sections (Figure 2.15) are result from experiments with higher inflow discharges and higher breach discharges. The latter feature, was also observed in analogous field scale experiments by Kakinuma et al. (2013). Second, the detailed analysis of breach lateral expansion at the crest center line in Figure 2.16, shows that the upstream breach extremity expands more when decreasing the main channel inlet Froude number. This effect is due to the breach discharge deviation angle in respect to the lateral stream in the main channel; the flow stream through the breach leans towards the downstream end in experiments with higher main channel input discharges inducing a significant erosion at the downstream breach extremity. Similar observations were reported in experiments by Rifai et al. (2017b) performed with a rigid bed in the main channel and floodplain. The author also reported a more acute breach discharge deflection angles when increasing main channel inflow discharge.

The average breach depth over the crest longitudinal section in Figure 2.17 does not bring much information on the deepening of the breach when varying main channel input discharge. Figure 2.18 illustrate the longitudinal breach profile at the crest center for tests with a main channel width of 1.8 m at 100 s and 450 s. At 100s, the comparison of breach profiles displays deeper breaches for increasing main channel initial Froude numbers and comforts previous observations regarding lateral breach expansion. Further in the breaching process at 450 s it can be seen the breach flow channel is not only narrower in tests with higher main channel input discharges but also leans more towards the downstream end of the breach. Here again, Test results 5E did not follow the same trend as other experiments.

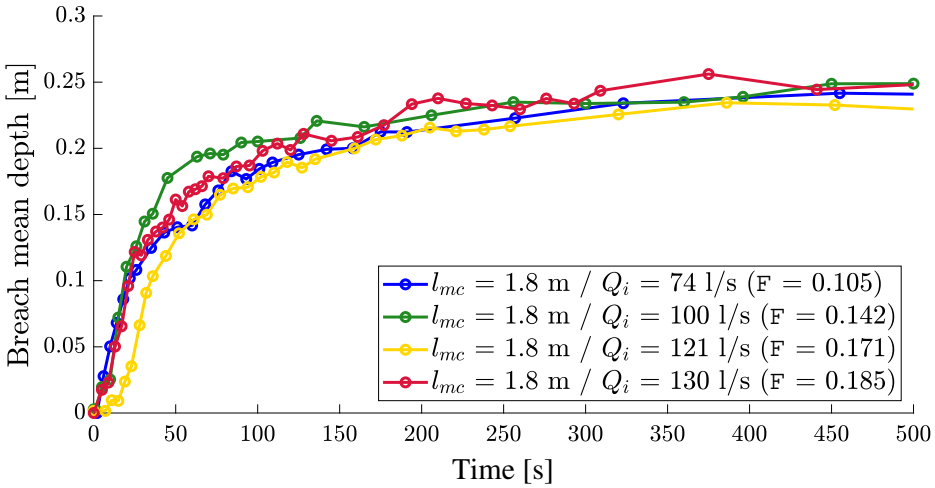

Figure 2.17: Impact of the Froude number on the breach mean depth (experiments 3E, 4E, 5E and 6E).

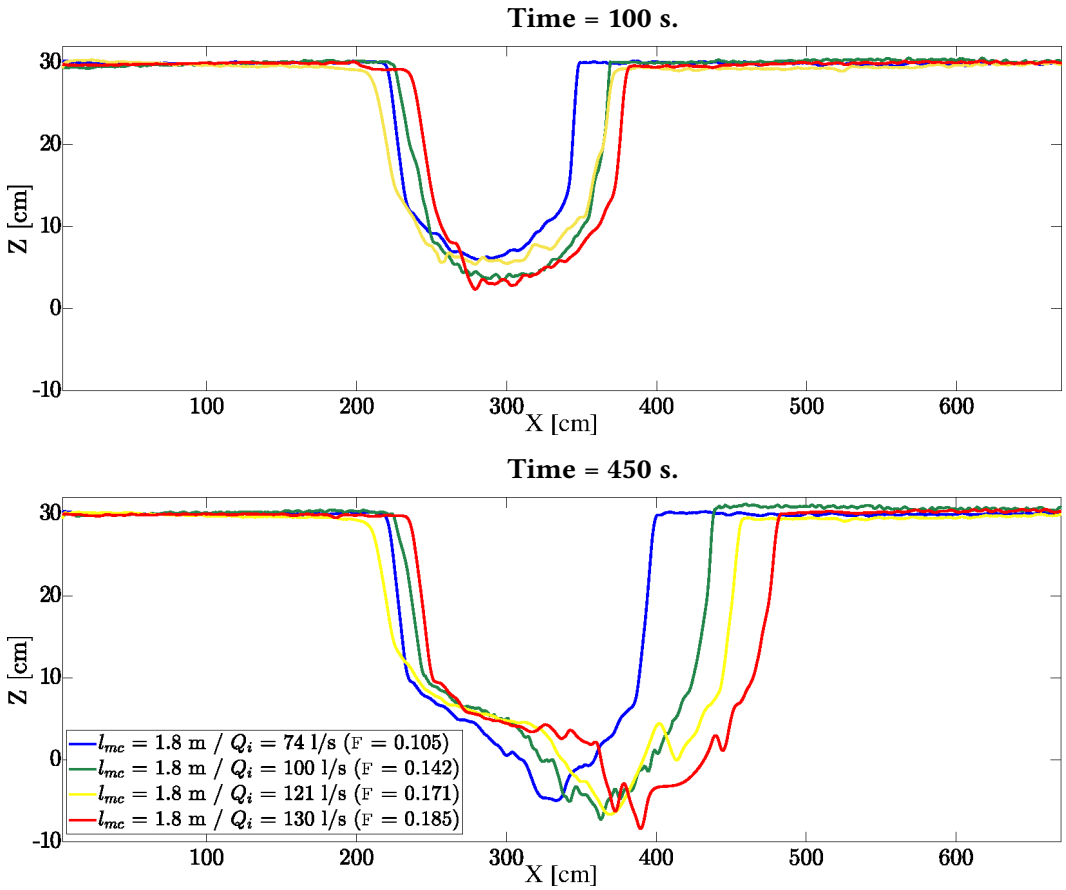

Figure 2.18: Breach longitudinal profile at the crest center for experiments 3E, 4E, 5E and 6E.

2.3.3 Influence of the main channel width

In order to study the influence of the main channel width on breach characteristics, experiments 1E, 2E, 3E, 4E, 5E, 6E, 7E, and 8E were performed, varying the main channel widths (1.4, 1.8, and 2.25 m). The main channel input discharge was also adjusted to set equivalent Froude numbers at the beginning of the experiments. The results are then presented in two groups: tests with small initial Froude numbers and high initial Froude numbers in the main channel. During the first stage, the breach discharge to channel inflow ratio increases fast in each case to reach a maximum value as shown in Figures 2.19 and 2.20. For both small and high Froude test series, a decrease in the maximum flow portion that deviates towards the breach is observed when increasing the main channel width. Experiments 1E and 2E performed with a smaller main channel width (1.4 m) are characterized by the formation of a peak after the rapid increase, which does not appear for experiments with wider test channels. In addition, a slower increase in breach outflow and a slower drop in the main channel average water level are observed when the test channel width is increased (Figures 2.21 2.22). In the second stage, the breach discharge to main channel inflow ratios stabilize close to their maximum value in most cases while it slightly decreases after the peak for Tests 1E and 2E (l=1.4 m).

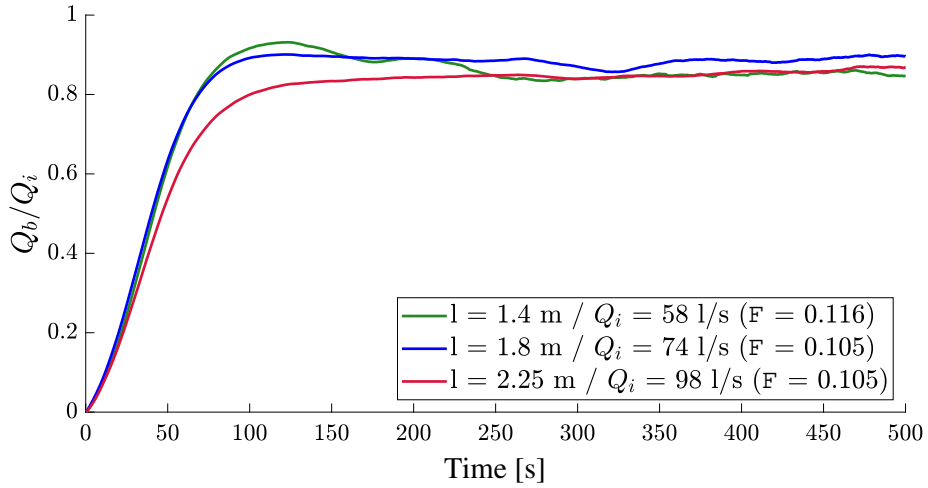

Figure 2.19: Impact of the channel width on the non-dimensional breach discharge (experiments 1E, 3E and 7E).

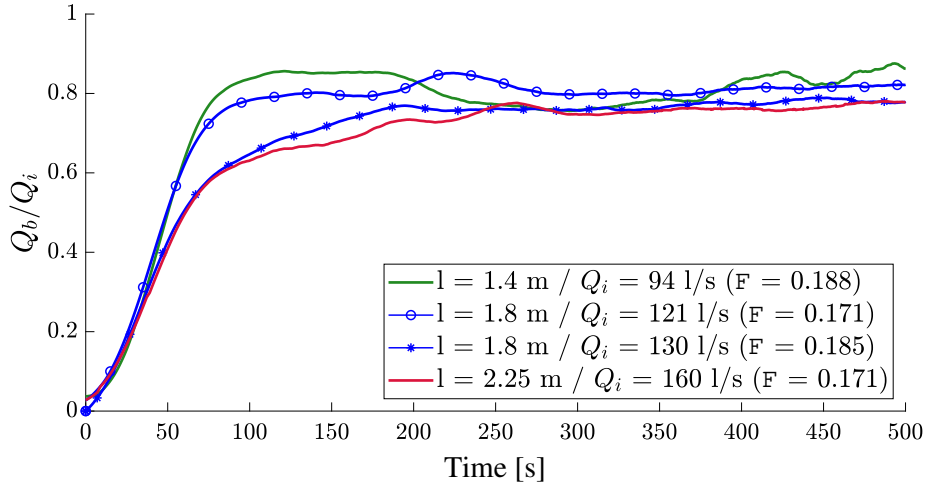

Figure 2.20: Impact of the channel width on the non-dimensional breach discharge (experiments 2E, 4E, 5E and 8E).

The comparison of experiments with equivalent inlet Froude numbers but different main channel widths (Test 3E with l=1.8 m and Test 7E with l=2.25 m; Test 2E with l=1.4 m and Test 6E with l=1.8 m; Test 5E with l=1.8 m and Test 8E with l=2.25 m), shows that main channel width changes flow deviation towards the breach. A wider channel leads to a smaller breach discharge to main channel outflow ratio. However, this ratio decreased for tests 1E and 2E during the second stage, which is rather supposed to be related to the high inlet Froude numbers used for these experiments. This results in higher horizontal velocities in the main channel. Thus, a smaller part of the main channel stream is conveyed to the breach, as found in section 2.3.2.

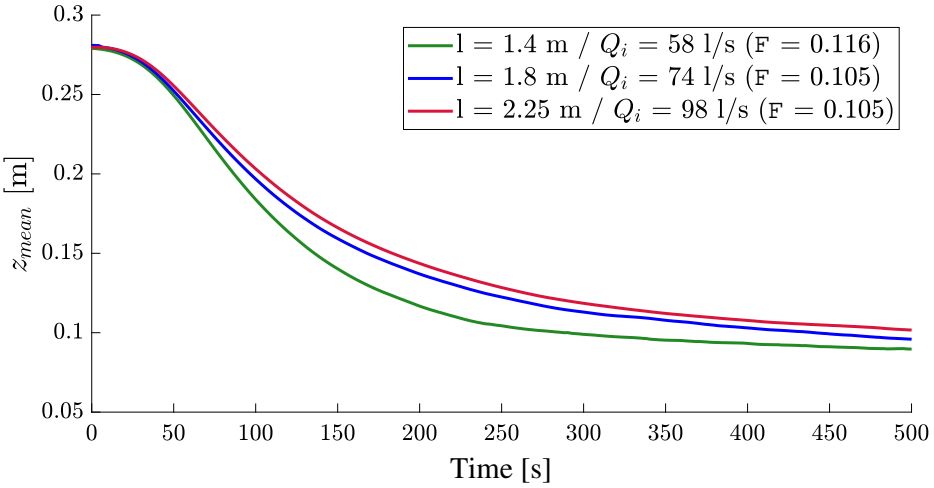

Figure 2.21: Impact of the channel width on the mean water level in the main channel (experiments 1E, 3E and 7E).

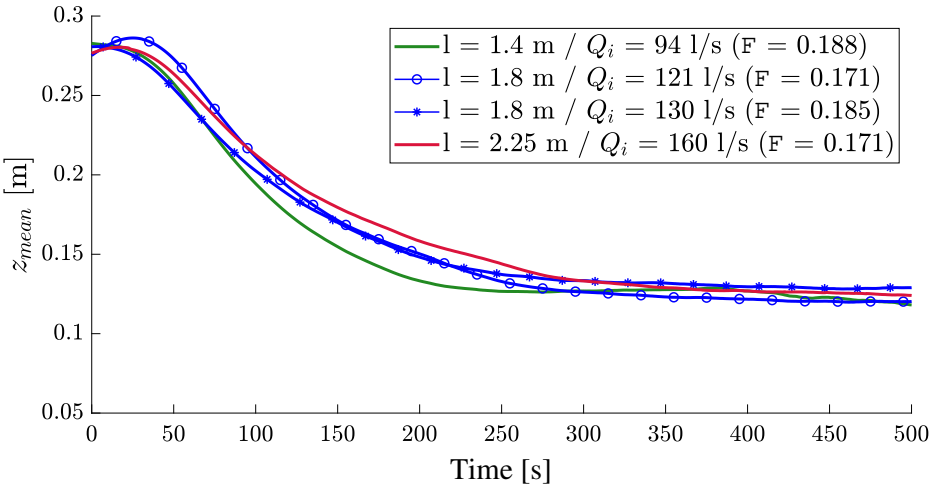

Figure 2.22: Impact of the channel width on the mean water level in the main channel (experiments 2E, 4E, 5E and 8E).

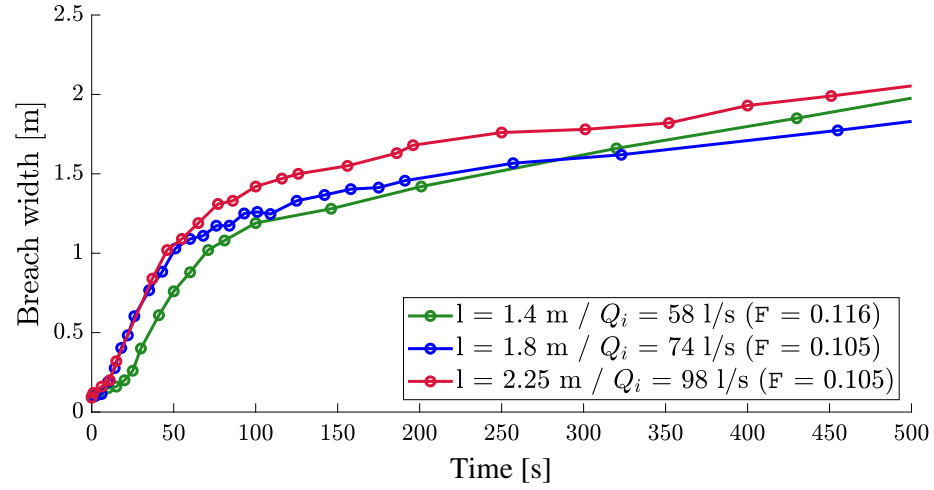

Figure 2.23: Impact of the channel width on breach width (experiments 1E, 3E and 7E).

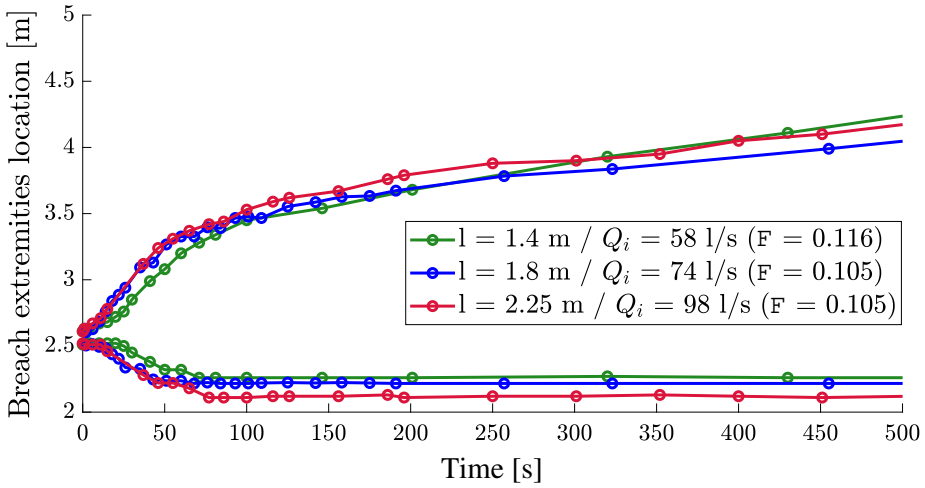

Figure 2.24: Impact of the channel width on the breach expansion (experiments 1E, 3E and 7E).

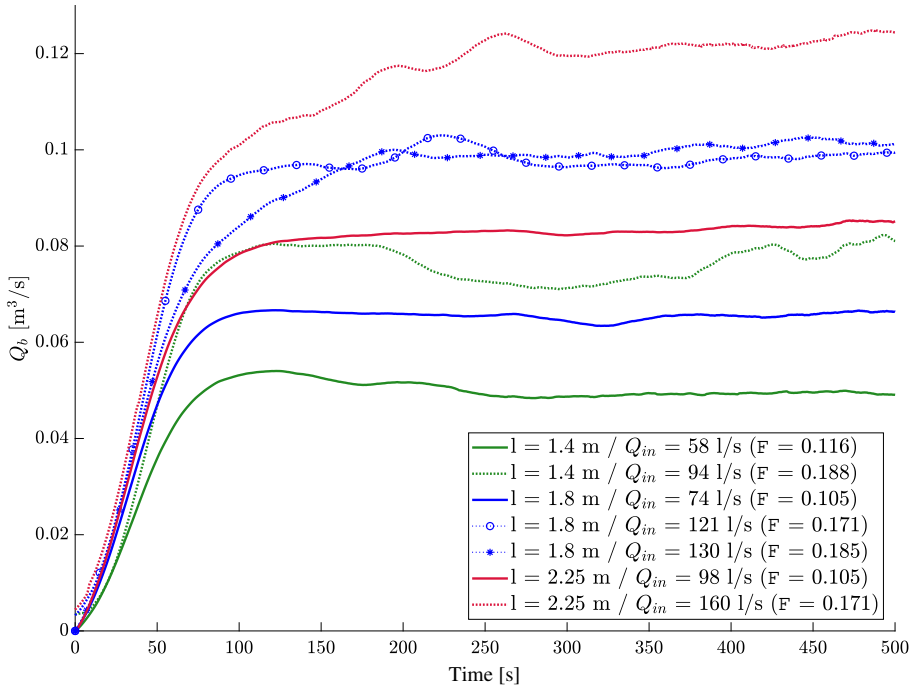

Figure 2.25: Impact of the channel width on the breach discharge (erodible bed).

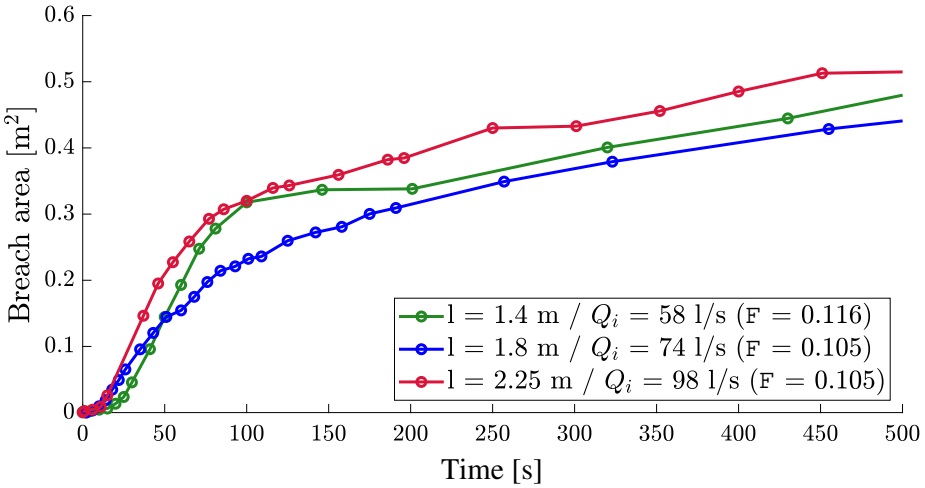

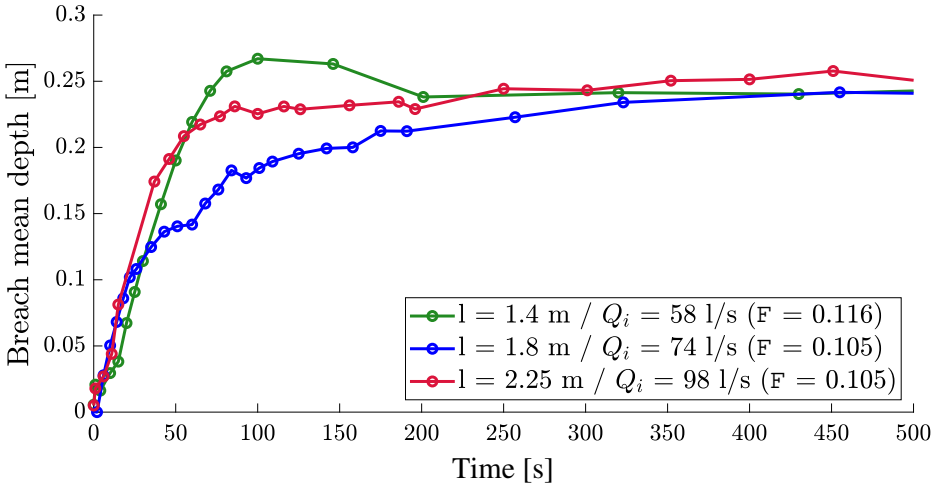

Figure 2.27: Impact of the channel width on breach mean depth (experiments 1E, 3E and 7E).

Figures 2.23 and 2.24 illustrate the main channel width influence on the lateral breach opening for experiments with low inflow intensities. Breach widening during Stage 1 is very similar for cases with main channel widths of 1.8 and 2.25 m, while experiment 1E with a tighter main channel and a slightly higher initial Froude number has a slower breach lateral expansion. In Stage 2, breach width For smaller channels is less than in wider channel cases. This effect seems to be a direct consequence of the breach outflow discharge that was higher for experiments with wider channels (Figure 2.25). Indeed, the main channel inflow discharge had to be increased for the latter cases in order to reach the desired inlet Froude numbers. Breach section area in Figure 2.26 and average depth in Figure 2.27 at the crest center, during the first 50 seconds, follow the same trend with a smaller longitudinal breach section and depth for smaller main channel widths. These observations are comforted by the longitudinal breach profiles at 25 seconds in Figure 2.28. However, at 100 seconds (Figure 2.28), the breach deepened faster for Test 1E, which was carried out with a higher inlet Froude number in comparison to Tests 3E and 7E. In addition, at 1115 seconds Figure 2.28 shows that for Test 1E, breach widening leans more towards the downstream end of the breach. As it has been seen in section 2.3.2, this is instead due to the impact of the inlet Froude number that was relatively higher for Test 1E.

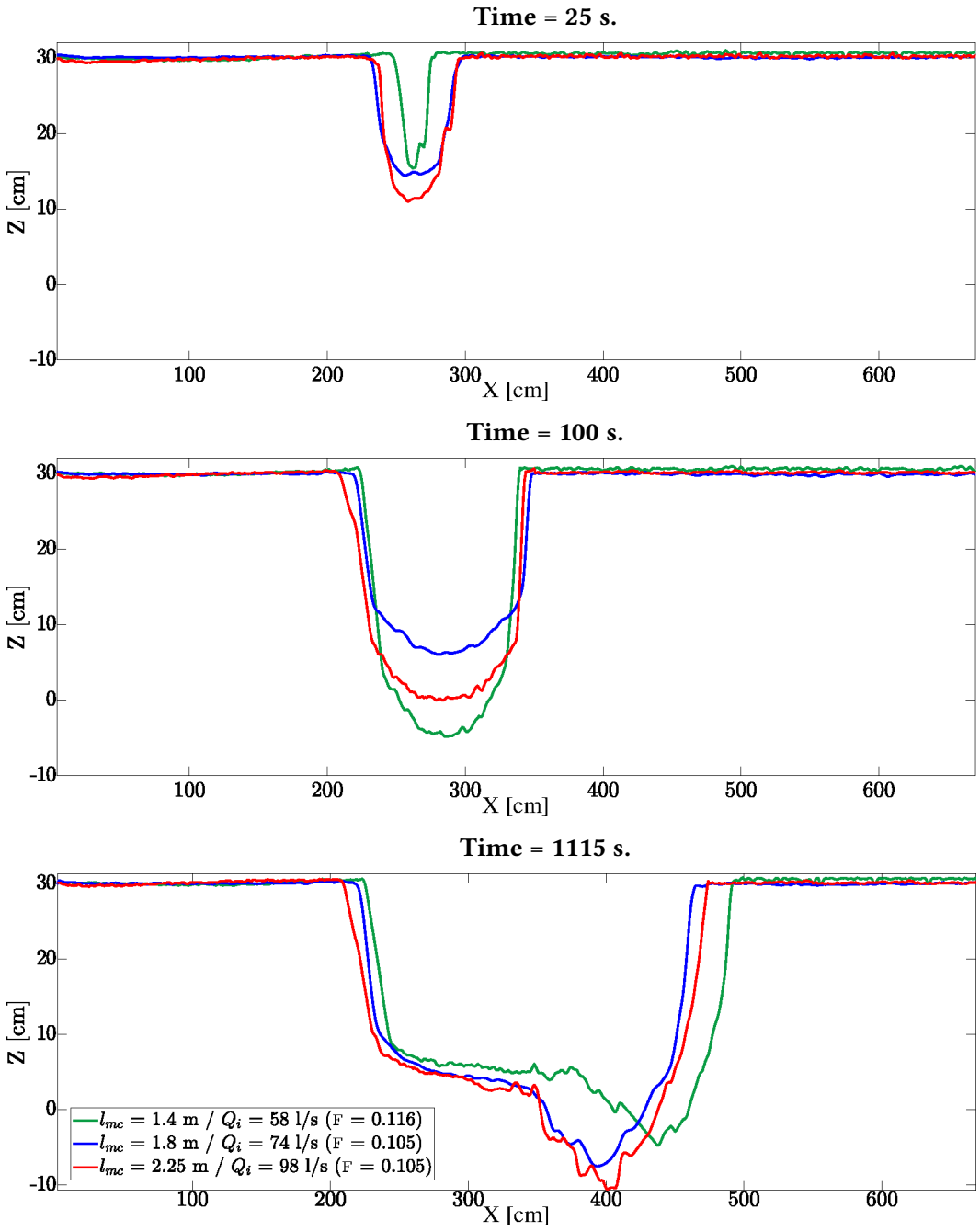

Figure 2.28: Breach longitudinal profile at the crest center (experiments 1E, 3E and 7E).

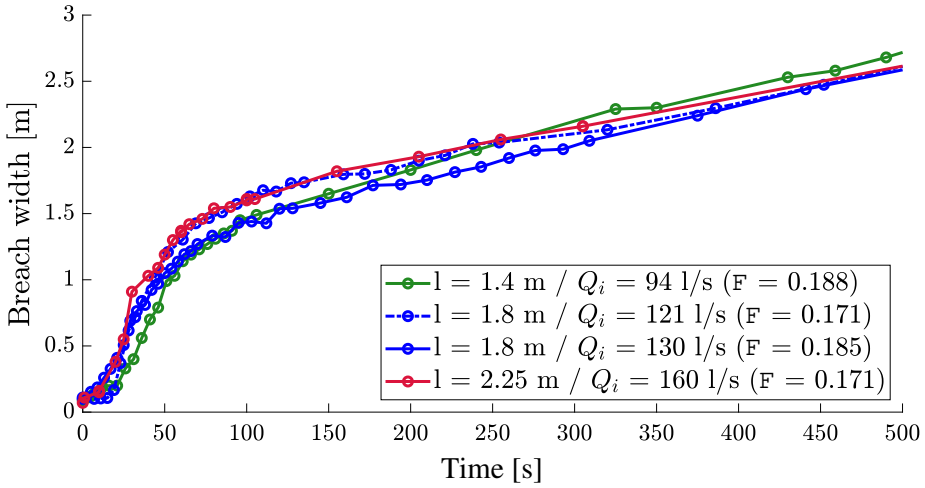

Figure 2.29: Impact of the channel width on breach width (experiments 2E, 4E, 5E and 8E).

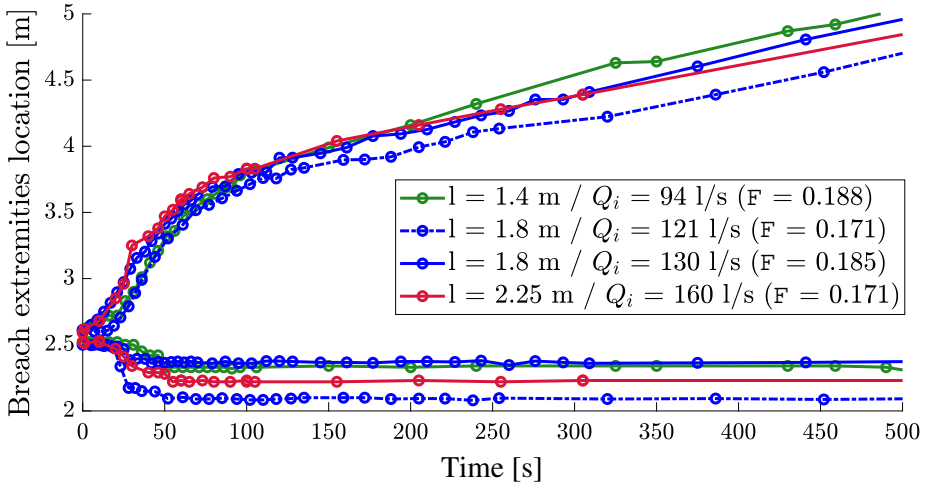

Figure 2.30: Impact of the channel width on the breach expansion (experiments 2E, 4E, 5E and 8E).

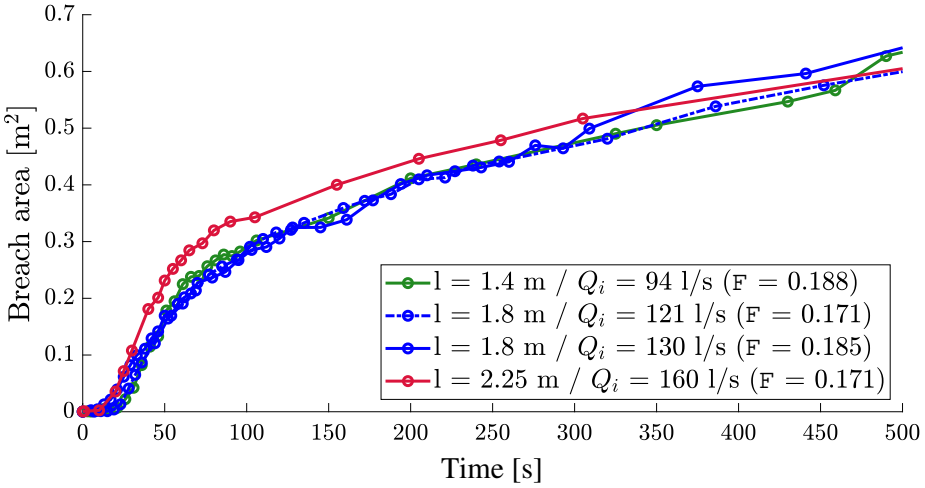

Figure 2.31: Impact of the channel width on the breach cross area (experiments 2E, 4E, 5E and 8E).

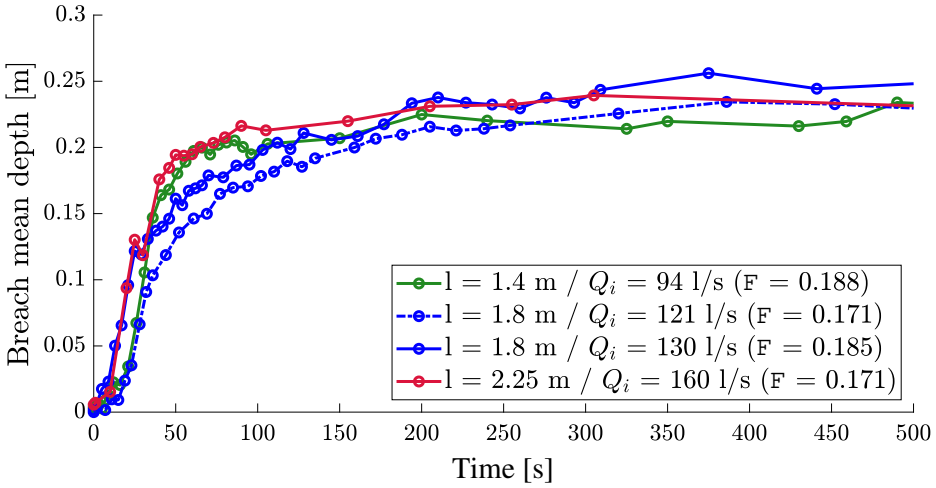

Figure 2.32: Impact of the channel width on breach mean depth (experiments 2E, 4E, 5E and 8E).

Tests from the high inlet Froude number series 'HF' also show the same trend as for small inlet Froude numbers with a greater breach width for cases with bigger main channel widths (Figures 2.29 and 2.30). The average breach area at the crest center is overall higher for Test 8E (l=2.25 m) but remains very similar for other tests (Figure 2.31). The mean depth of the breach section at the crest center line does not display a uniform influence of main channel width over time (Figure 2.32). As it is relatively lower for Test 5E (l=1.8 m) in comparison to Test 8E (l=2.25 m), both performed with very close inlet Froude numbers. In Test 2E, where the main channel is tighter (l=1.4 m), a slower deepening is noted in the early breaching phase compared to Test 6E (l=1.8 m). This effect can also be seen at 25 seconds in Figure 2.33, while later in the breaching process at 50 seconds (Figure 2.33) the adverse effect is observed. Finally, at 1035 seconds, we notice that the breach is shallower for Test 8E and tilts more towards the downstream extremity of the dike for Tests 2E and 6E performed with a higher inlet Froude.

The overall effect of the main channel width on the breaching process can not be clearly seen in experiments with high inlet Froude numbers, while its influence on breach hydrographs agrees with results from small inlet Froude numbers experiments. Generally, it can be said that breach characteristics are more sensitive to the variation of main channel inflow discharge than the main channel width.

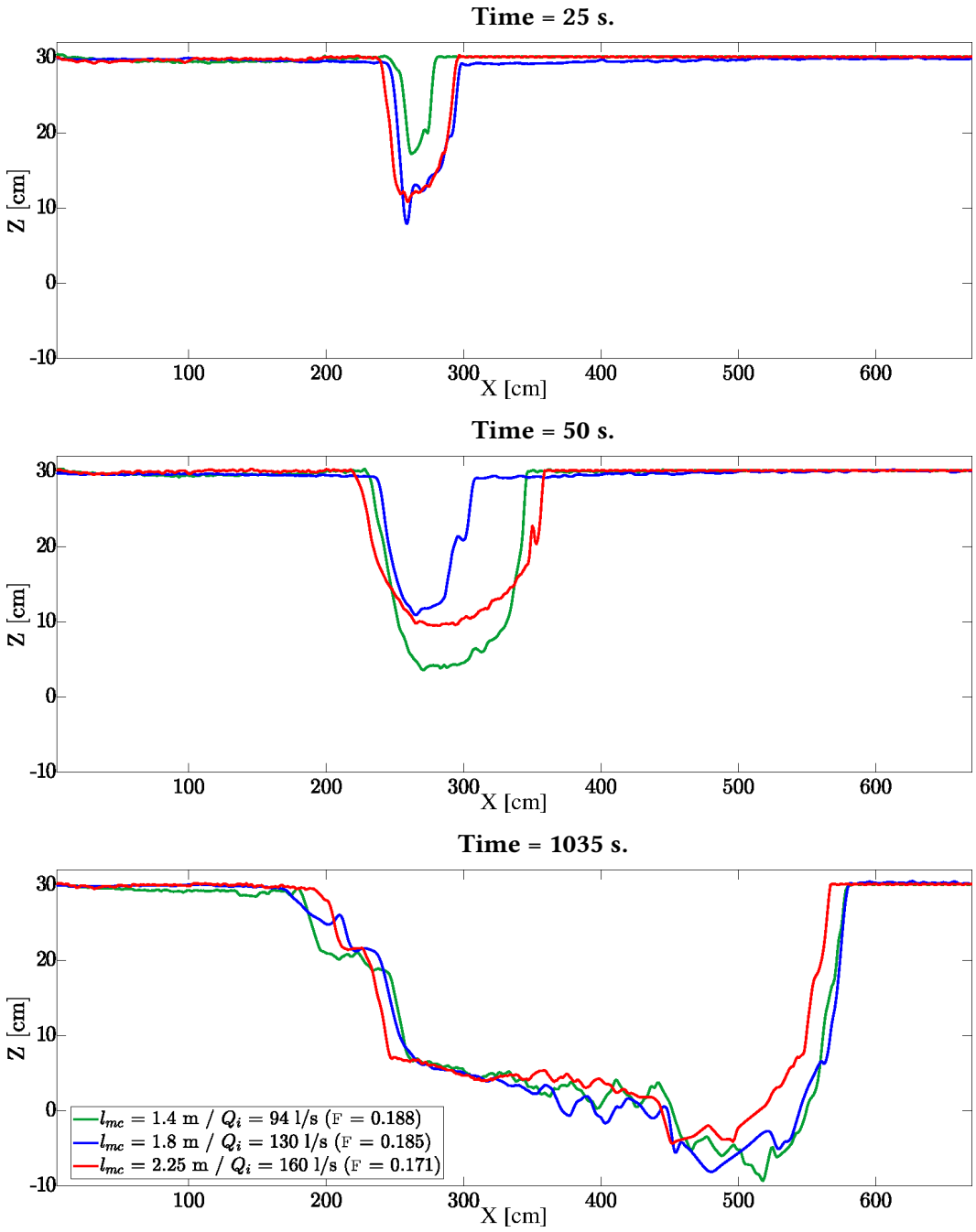

Figure 2.33: Breach longitudinal profile at the crest center (experiments 2E, 4E, 5E and 8E).

2.4 Discussion

Several features of the breaching process were highlighted in section 2.3 including the effect of hydrodynamic and geometric parameters on breach characteristics. This section aims to verify the similarities and differences between previous experiments by Rifai et al. (2019) with a non-movable bed in the main channel and floodplain and equivalent configurations from the present work with

an erodible sand layer in the test channel and floodplain.

Figures 2.34 and 2.35 represent the evolution of the breach hydrograph to main channel inflow ratio for both series of experiments with small and high inlet Froude numbers. Regarding Tests with a non-erodible bed in the main channel and floodplain 'NE', experiments with a movable sand layer have higher ratios and breach discharges (Figures 2.36 and 2.37), especially during Stage 2. In addition, Figures 2.34 and 2.36 display the formation of a peak during the rapid increase stage in breach discharge for tests with small inlet Froude numbers and rigid beds in the main channel and flood plain. The instantaneous mean channel water level variations in the main channel (Figures 2.38 and 2.39) are in agreement with breach discharge observations with a relatively faster drop in average water levels for cases where erosion is allowed in the main channel and floodplain. In addition, the latter experiments are also characterized by an earlier stabilization of the main channel average water level at smaller values. This effect results from the combined higher breach discharge and bed erosion in the main channel, mainly in the upstream part, as shown in section 2.3.1.

Results in Figures 2.41 and 2.45 highlight differences in breach width at the center of the dike crest between rigid and erodible bottom Tests for both small and high inlet Froude numbers. Although the overall breach dynamics are very similar with the initiation, rapid increase, and stabilization stages, and a preferential widening in the direction of the main channel flow (Figures 2.40 and 2.44), the breach is clearly wider in erodible bed cases. For the latter experiments, results also show that the longitudinal breach section area (Figures 2.42 and 2.46) is larger than in rigid bottom tests where erosion of the dike foundation was not allowed. This led to shallower breaches with smaller values of breach mean depth, as displayed in Figures 2.43 and 2.47. It is also interesting to note that the overall ranking of the cases results in respect to their main channel width remains the same for erodible and rigid bottom cases.

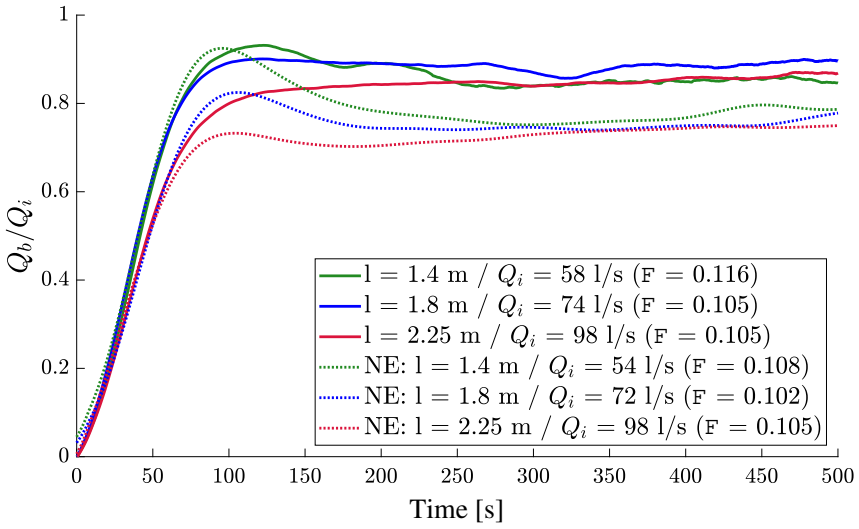

Figure 2.34: Impact of the bed erodibility on the non-dimensional breach discharge (experiments 1E, 3E and 7E).

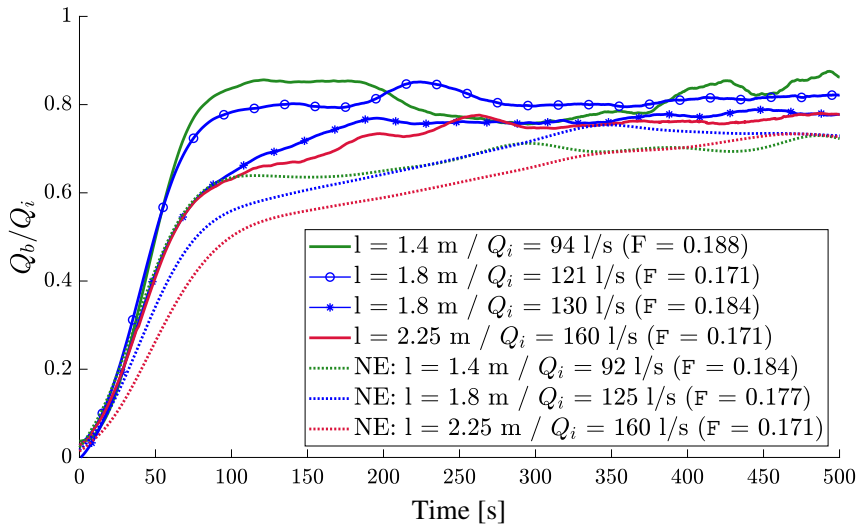

Figure 2.35: Impact of the bed erodibility on the non-dimensional breach discharge(experiments 2E, 4E, 5E and 8E).

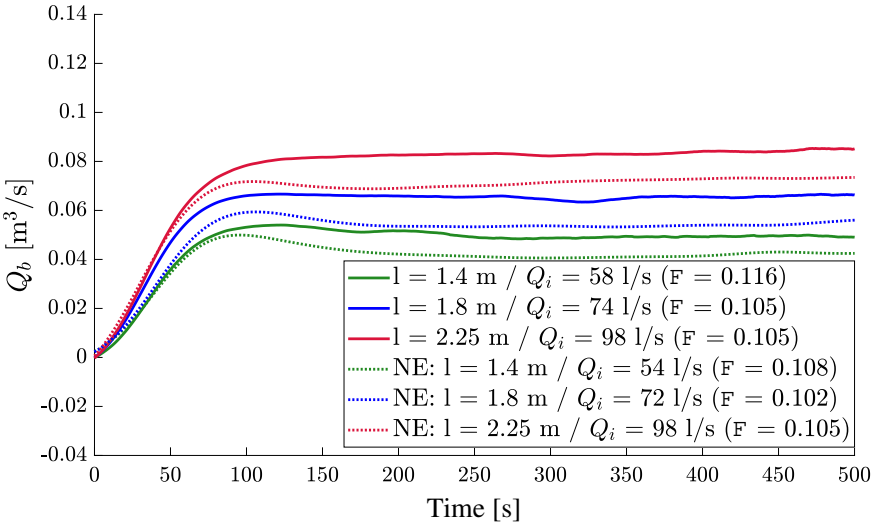

Figure 2.36: Impact of the bed erodibility on the breach discharge (experiments 1E, 3E and 7E).

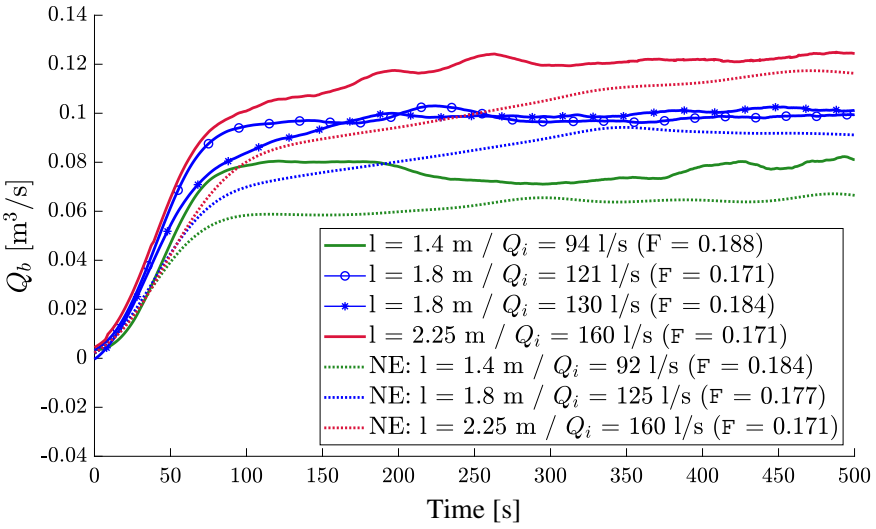

Figure 2.37: Impact of the bed erodibility on the breach discharge (experiments 2E, 4E, 5E and 8E).

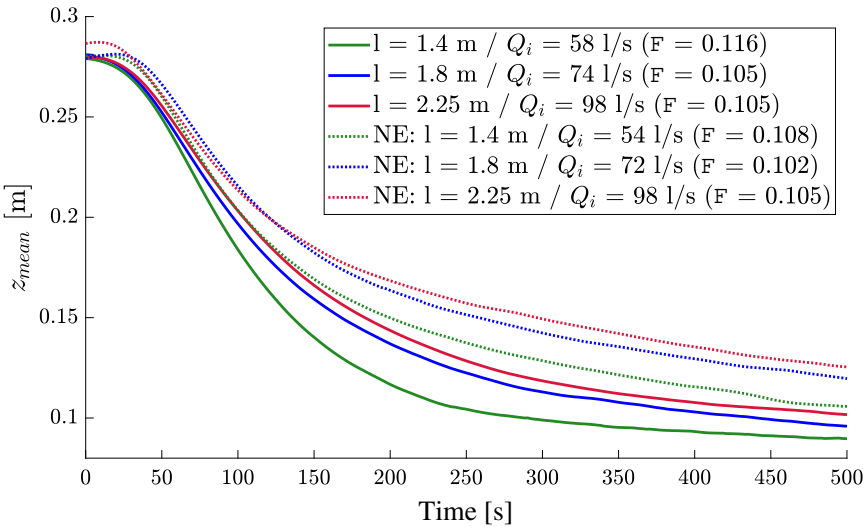

Figure 2.38: Impact of the bed erodibility on the water level in the main channel (experiments 1E, 3E and 7E).

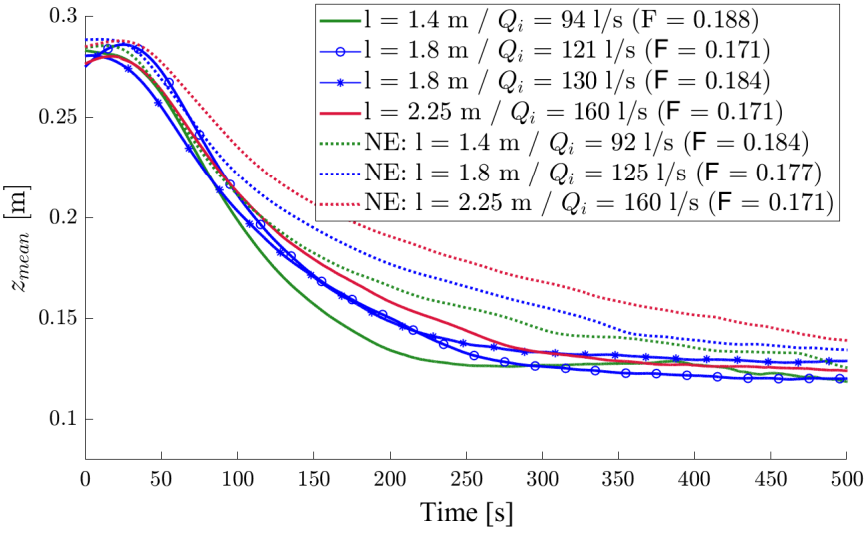

Figure 2.39: Impact of the bed erodibility on the water level in the main channel(experiments 2E, 4E, 5E and 8E).

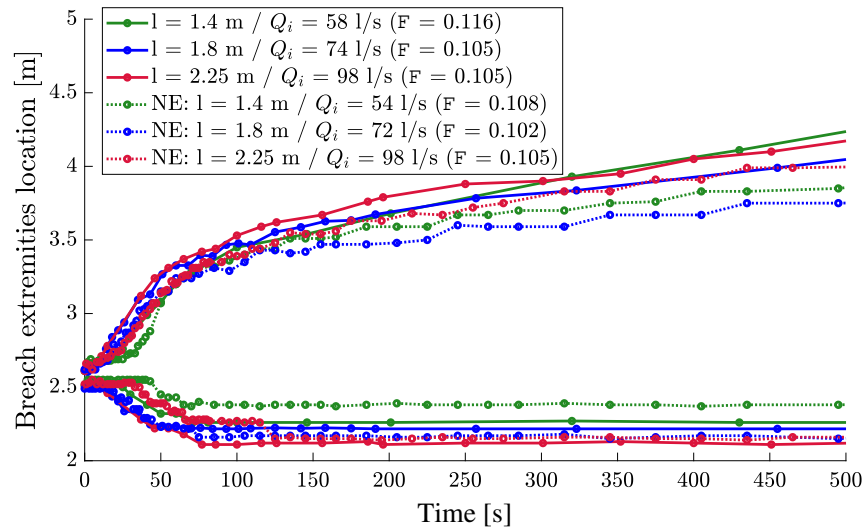

Figure 2.40: Impact of the bed erodibility on the breach expansion (experiments 1E, 3E and 7E).

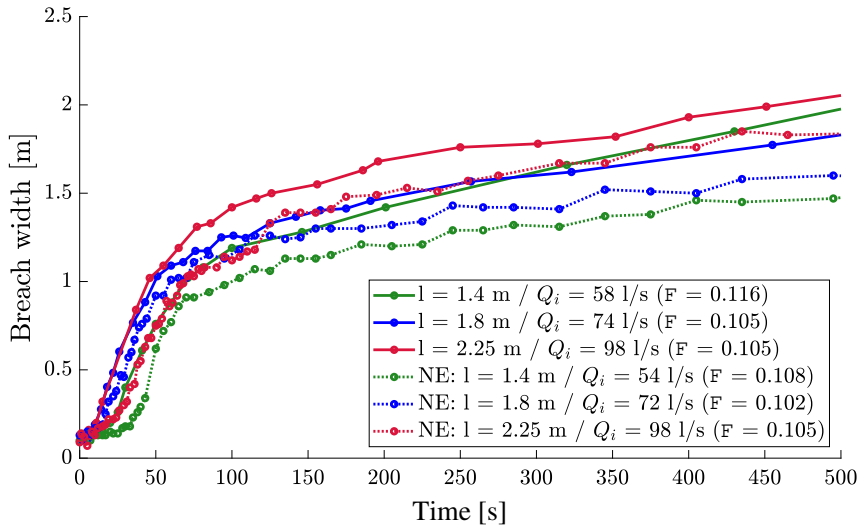

Figure 2.41: Impact of the bed erodibility on breach width (experiments 1E, 3E and 7E).

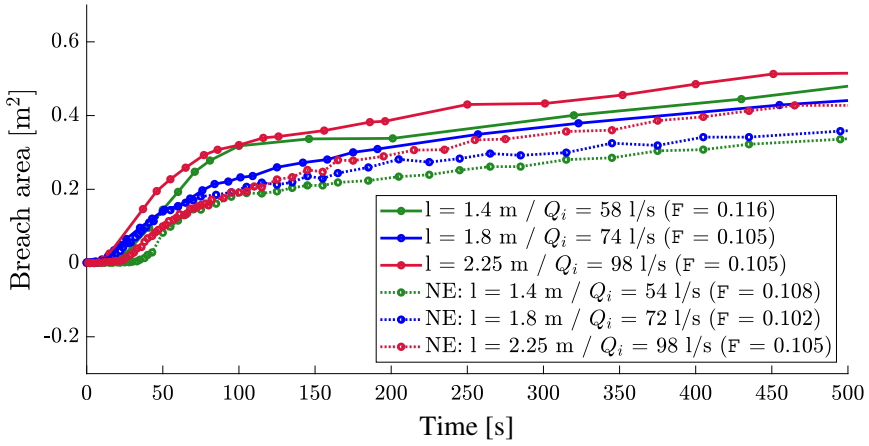

Figure 2.42: Impact of bed erodibility on the breach cross area (experiments 1E, 3E and 7E).

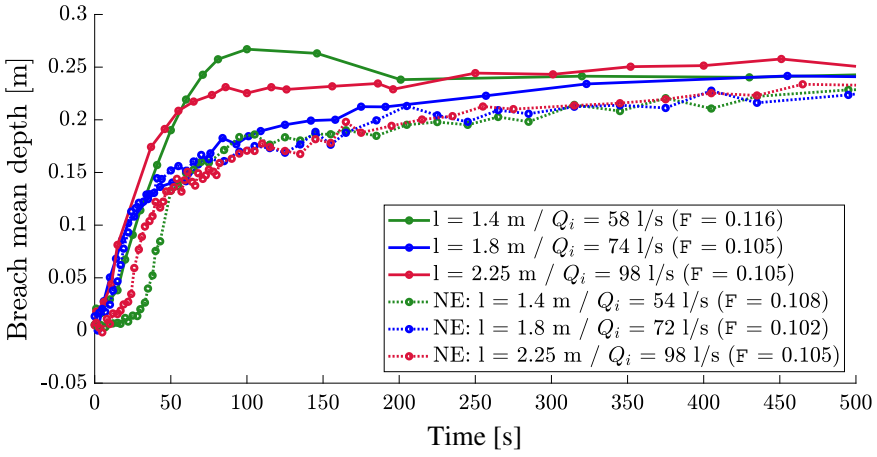

Figure 2.43: Impact of the bed erodibility on breach mean depth (experiments 1E, 3E and 7E).

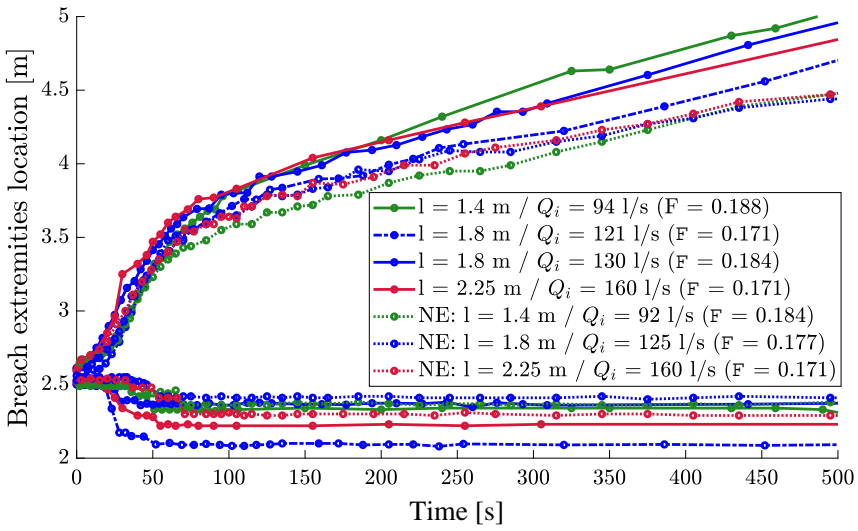

Figure 2.44: Impact of the bed erodibility on the breach expansion (experiments 2E, 4E, 5E and 8E).

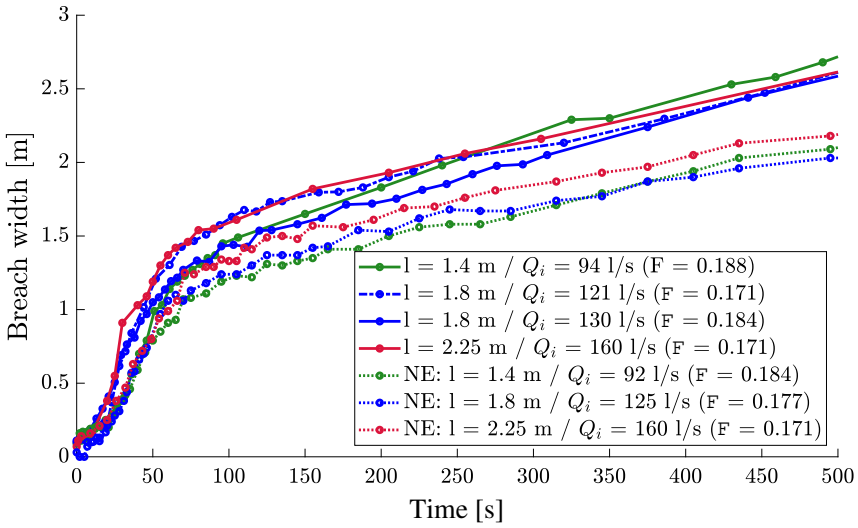

Figure 2.45: Impact of the bed erodibility on breach width (experiments 2E, 4E, 5E and 8E).

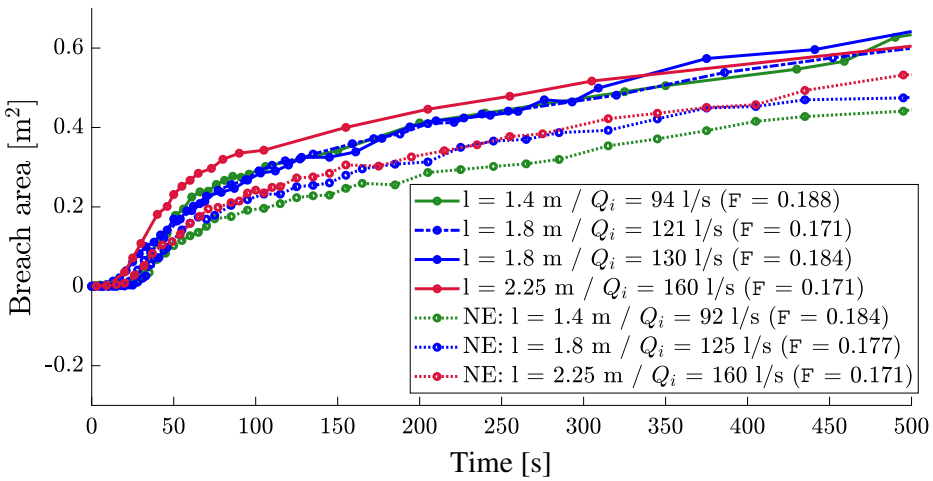

Figure 2.46: Impact of the bed erodibility on the breach cross area (experiments 2E, 4E, 5E and 8E).

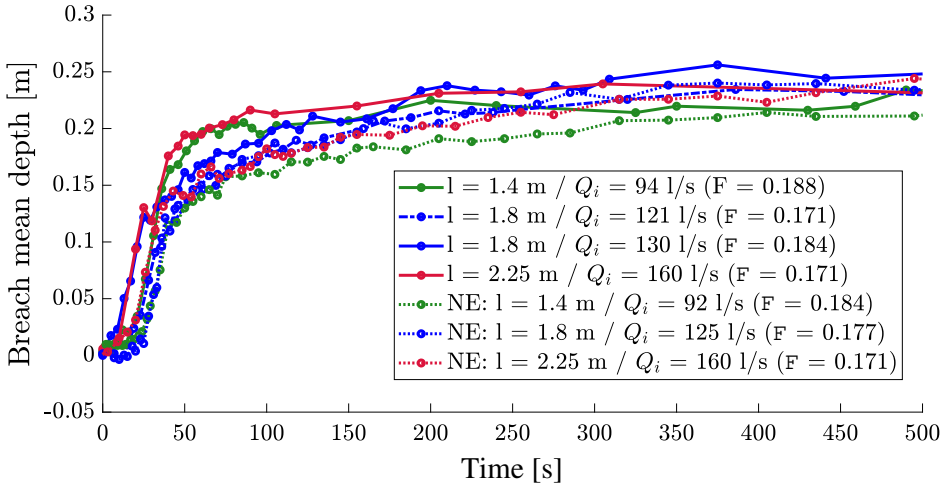

Figure 2.47: Impact of the bed erodibility on breach mean depth (experiments 2E, 4E, 5E and 8E).

2.5 Conclusion

This experimental work aimed to understand in detail the breach growth mechanisms of non-cohesive levees due to overtopping in the presence of an erodible bed in the main channel, dike foundation, and floodplain. For that purpose, a series of experiments were performed at the National Laboratory for Hydraulics and Environment (LNHE) of EDF-R&D using the experimental set-up presented by Rifai (2018) and following the same procedure. Results analysis provided information regarding the influence of the main channel input discharge and main channel width on the spatial and temporal breach expansion. Data from previous experiments with a rigid bottom by Rifai et al. (2019) were then employed to investigate the impact of bed erosion in the main channel, dike foundation, and floodplain of the breaching process. The qualitative comparisons of hydrodynamic and morphodynamic breach characteristics in different experimental configurations highlighted the following key tendencies :

- The main channel inflow discharge had an apparent effect on the breaching process. Breach discharge linearly increased with the augmentation of main channel inflow. As expected, this effect resulted in wider and deeper breaches. In addition, the flow stream through the breach channel leans more towards the downstream end of the breach for high inlet Froude numbers. For the latter configurations, breach extremities were, therefore, more eroded in the downstream direction compared to cases with small inlet Froude numbers, while the adverse effect was observed at the upstream end of the breach.

- The influence of the main channel width on breach dynamics was not as striking as that of the inlet Froude number. However, it was shown that wider main channels led to smaller breach discharge to main channel inflow ratios. In addition, the small inlet Froude number test series showed a peak formation in breach discharge for cases with tighter main channels.

- The three-staged breach dynamics were relatively the same in erodible and rigid bottom cases. In addition, the influence of the inlet Froude number and main channel width remained the same for both configurations. However, allowing erosion in the main channel and dike foundation induced higher breach discharge with larger breaches in both lateral and vertical dimensions.

Finally, the data collected in the presented experiments can be used for numerical breach models validation. It may also help evaluate their accuracy with the information provided on expected trends in breach characteristics under various configurations.

Chapter 3

Simplified physically-based approach for side-overflow levee breaching

Prédire l'étendue des inondations dues à la rupture de digues fluviales est d'un intérêt majeur pour améliorer de la résilience des populations face à cet aléa. Cependant, la fiabilité de cette prédiction nécessite en amont une estimation précise de la dynamique de et l'hydrogramme de brèche. Dans ce chapitre, différentes formulations empiriques décrivant la dynamique d'ouverture d'une brèche sont implémentées dans le module de brèche du code hydrodynamique bidimensionnel TELEMAC-2D, dans le cadre d'une approche de modélisation simplifiée. Les données provenant d'expériences de terrain de rupture de digues fluviales par surverse sont utilisées pour valider et évaluer les résultats numériques. Une analyse plus approfondie des modèles de brèche est mise en place pour identifier l'influence des paramètres d'entrée spécifiques de chaque modèle sur l'hydrogramme de brèche.

3.1 Introduction

As climate heat intensifies, the occurrence of extreme meteorological phenomena is expected to rise along with the risk of natural hazards (IPCC (2014), Madsen et al. (2014)). In this context, flood events related to levee breaching are a major concern worldwide, as populations living in flood-prone areas are continuously increasing due to the well-known "levee effect" (Aerts et al. (2018), Di Baldassarre et al. (2018b)), which makes the risk of important fatalities and property destruction even greater (OCDE (2015)). Therefore, inundations induced by levee breaching must be carefully analyzed and predicted to avoid the severe economic, social, and environmental damages they may cause.

Fluvial levees (i.e., fluvial dikes) are important defense structures built along river and channel banks as part of the flood prevention efforts against inundations. Most of them are composed of erodible material ranging from cohesive to non-cohesive materials, whose characteristics are generally poorly known. Insufficient maintenance, construction or rehabilitation deficiency, wildlife activity (e.g., animal burrows) (Di Baldassarre et al. (2018a), Orlandini et al. (2015)), as well as exposure to frequent hydrological events (Apel et al. (2009), Hui et al. (2016)) increase levee vulnerability. Failure and breaching cases reported in history show that external (i.e., surface) erosion by overflow is the most common mechanism (ASCE/EWRI task committee (2011), Danka and Zhang (2015), Flynn et al., West et al. (2018), Özer et al. (2020)). Overtopping occurs when water level or flow discharge increase in rivers (or channels) and exceed the levee designed capacity. A large number of laboratory studies on the breaching of earthen embankments exist where the structure is transversal (i.e. frontal) to the flow direction (Al-Riffai (2014), Coleman et al. (2002), Frank (2016), Morris et al. (2007), Pickert et al. (2011), Schmocker and Hager (2012), Zhou et al. (2019)). However, breach formation in fluvial dikes is a complex phenomenon and differs from that of a dam embankment. Indeed, this configuration does not encompass all specificities of fluvial dikes, such as the parallel flow velocity along the dike, the non-uniform distribution of the flow unit discharge through the breach, the three-dimensional (3D) flow structures developing in the near field of the breach (Michelazzo et al. (2015), Roger et al. (2009)) and the asymmetric evolution of the breach geometry (Rifai et al. (2017b)). Fluvial dikes have gained recently in interest through experimental modeling (e.g. Islam (2012); Kakinuma and Shimizu (2014); Bhattarai et al. (2015); Tabrizi et al. (2015); Elalfy et al. (2018);Michelazzo et al. (2018); Rifai et al. (2018, 2021)), thus improving our knowledge of the physical processes whilst providing sound data sets to enhance the accuracy of numerical models simulating the breaching process (Rifai et al. (2019)). A review of the existing laboratory studies on fluvial dikes is given by Rifai et al. (2017b) and Schmitz et al. (2021).

In the numerical modeling framework, the primary task is the accurate prediction of breach evolution and outflow hydrograph. For this purpose, several approaches have been proposed, which can be divided into three main categories based on the details included in the treatment of the breach and flow processes (ASCE/EWRI task committee (2011): parametric, simplified or detailed multi-dimensional physically-based breach models. Parametric models are simple regression equations, generally in dimensional form, calculating the breach peak discharge, ultimate side slope and width,

and opening duration. These equations were derived from statistical analysis of reported historical failure events, without distinguishing failure modes, soil material properties, and frontal embankments from levees, and ignoring the backwater effects near the breach location. Such models are straightforward to use and cost-efficient, although most of them do not describe neither the final breach depth (nor the time evolution of the breach geometry and resulting hydrograph Froehlich (2008), Froehlichl (1995), Jandora and Říha (2008), Singh (1996), Walder and O'Connor (1997), Xu and Zhang (2009). Few equations compute the breach time varying width (e.g., MacDonald and Langridge-Monopolis. (1984); Von Thun and Gillette (1990); Verheij (2002)) and consider the effect of embankment erodibility Peeters et al. (2016). The gradual opening of the levee breach has been integrated within 1D and 2D hydrodynamic models following empirical laws, since the assumptions of instantaneous breaching is not realistic. The evolving topography of the breach is assumed prismatic in shape that widens and deepens from the crest of the dike to the ground elevation (e.g. Vorogushyn et al. (2010); Vacondio et al. (2016); Shustikova (2020); Ferrari et al. (2020)). The breach parameters are often the number of breaches, locations, initial breach width, rates of widening and deepening, final breach width, final breach level, and breach duration. Simplified physically-based models, such as CastorDigue Paquier and Béraud (2010), HR BREACH Morris et al. (2009), WinDam Visser (1998) and DLBreach Wu (2016), simulate the temporal variation of the breach geometry and outflow hydrograph by taking into account some physical processes (i.e. erosion, deposition, head cut migration, soil mechanics). Some of these models make a distinction between the erosion processes of non-cohesive and cohesive soils, but contain empirical formulas (e.g. erosion rate formula, broad-crested/weir equation for computing the breach outflow discharge), support many assumptions to simplify the problem (e.g. prismatic symmetrical breach shapes such as trapezoidal, triangular and parabolic, 1-D quasi-steady flow in the breach channel), and have different input parameters (e.g. final breach width and depth, breach side slope, critical velocity or shear stress required to initiate detachment for the dike material, erodibility coefficient) and boundary conditions Peeters et al. (2016). Simplified physically based models are mainly dedicated to earthen dams; few attempts have been made to assess their applicability to fluvial dikes. According to Risher and Gibson (2016), these models perform best during initial, rapid fluvial breach widening, but may diverge when tailwater impacts breach flow. Simplified physically based approaches have been integrated into 1D or 2D hydrodynamic models, solving the flow equations in the main channel and floodplain, whereas the dike breaching is handled by a simplified physically based module Paquier and Recking (2004). A review of existing simplified physically based models is given by ASCE/EWRI task committee (2011) and Al-Riffai (2014) and Danka and Zhang (2015). Detailed physically based models (i.e. hydromorphodynamic models) simulate the breach formation by discretizing and solving the flow and sediment transport governing equations using a computational mesh of the domain (main channel, dike, and floodplain). The governing equations are generally 1D or 2D shallow water equations for hydrodynamic, convection diffusion equation for suspended load, and Exner equation for bed changes, completed with empirical formulations for deposition, erosion and bedload transport capacity rates and in some models with a side operator for dike and breach slope failure (e.g., Dazzi et al.

(2019), Dou et al. (2014), Elalfy et al. (2018), Faeh (2007), Kakinuma and Shimizu (2014)). Detailed physically based models are expected to give more accurate predictions of breach characteristics than simplified physically based models. However, they require various input parameters, reliable data for accurate calibration and validation of the model, and long simulation times when the model are applied to large areas.

To our best knowledge, no study has been completed to assess the suitability of existing empirical laws and simplified physically based approaches for the gradual levee breach expansion within a 2D numerical hydraulic modeling of flood propagation. For this purpose, we implemented a set of empirical laws describing the gradual opening of the levee breach and we integrated an adapted version of a simplified physically based model proposed by Paquier and Recking (2004) into the open source 2D depth averaged hydraulic model TELEMAC-2D. Existing laboratory experimental cases of levee breaching have been simulated and numerical results have been compared to measured data.

The chapter is organized as follows: Section 3.2 describes the hydraulic model TELEMAC2D and its BREACH module. In Section 3.3, two large-scale levee breach experimental cases performed by Kakinuma et al. (2013) are shortly presented. In Section 3.4, performance of the implemented breach modeling approaches is assessed by simulating numerically the laboratory experiments. Section 3.5 is an overall discussion of the numerical results along a sensitivity analysis to various input parameters. This is followed by concluding remarks and recommendations in Section 3.6.

3.2 Model description

The open-source TELEMAC-MASCARET system (www.opentelemac.org) offers an extensive range of solvers mainly dedicated to the study of environmental processes in fluvial and maritime hydraulics. In the present work, the two-dimensional shallow-water code TELEMAC-2D is combined with its BREACH module to describe overtopping induced levee failure. Sediment transport is not simulated and the breaching process is integrated through the gradual update of levee's topography by the BREACH module (Fig.3.1).

3.2.1 Hydrodynamic component

Disregarding the Coriolis, wind and viscous forces, and assuming a hydrostatic pressure with an incompressible flow and negligible vertical velocity, TELEMAC-2D solves the two-dimensional Saint-Venant equations written in conservative and vector form as :

$$\frac{\partial \mathbf{U}}{\partial t} + \frac{\partial \mathbf{E}}{\partial x} + \frac{\partial \mathbf{G}}{\partial y} = \mathbf{S} \tag{3.1}$$

Where t is time; (x, y) are Cartesian coordinates; $\mathbf{U} = [h, hu, hv]^{\mathrm{T}}$ is the vector of conservative variables, with h denoting flow depth, u and v are x- and y- components of the velocity vector; $\mathbf{E} = [hu, hu^2 + \frac{gh^2}{2}, huv]^{\mathrm{T}}$ and $\mathbf{G} = [hv, huv, hv^2 + \frac{gh^2}{2}]^{\mathrm{T}}$ are the flux vector functions in the

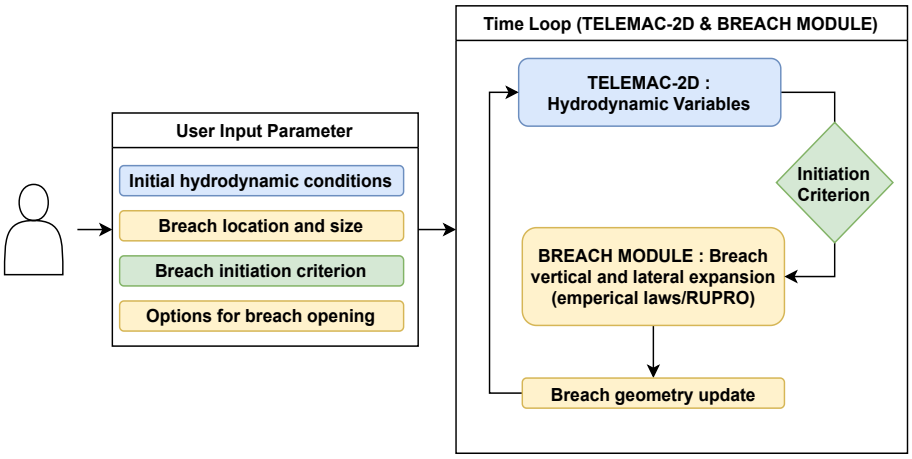

Figure 3.1: Diagram of the simplified physically based approach for levee breach modeling in TELEMAC-2D.

x- and y- directions respectively, with g the gravitational acceleration; and $\mathbf{S} = \mathbf{S_0} + \mathbf{S_f}$, with $\mathbf{S_0} = [0, -gh\frac{\partial z_b}{\partial x}, -gh\frac{\partial z_b}{\partial y}]^{\mathrm{T}}$ is the slope energy and $\mathbf{S_f} = [0, -gn^2u\frac{(u^2+v^2)^{1/2}}{h^{1/3}}, -gn^2v\frac{(u^2+v^2)^{1/2}}{h^{1/3}}]^{\mathrm{T}}$ the energy loss due to the bed and wall shear stresses, where z_b is bed elevation and n is Manning roughness. In this study, the numerical solution of Equation 3.1 was computed with the finite element method, where advection of water depth and velocity were performed using the mass-conservative PSI scheme (Positive Streamwise Implicit) and NERD scheme (N-Edge-based Residual Distributive), respectively. The zero-equation constant eddy viscosity model was employed for turbulence closure with a constant velocity diffusivity of 0.001 $\mathrm{m^2 s^{-1}}$ over the computational domain.

3.2.2 Breach component

The breach module estimates levee failure based on simplifying assumptions and a set of user input parameters. First, the breach location is specified with a polygon created from the coordinates of a polyline along the levee crest and dike base width. Then breach formation criterion can be selected among three options : (i) a specific initiation time, (ii) a threshold value for the average overflow water level above the entire breach location previously defined, or (iii) a threshold water level at a specific node. Finally, the user can choose to model breach opening in two different ways : (i) breach expansion is performed by lowering the breach bottom level for the complete breach zone (i.e., breach final width is reached instantaneously and vertical erosion is gradual), or (ii) both breach widening and deepening are performed gradually. For this latter option, we newly implemented selected models describing breach development. These approaches include both empirical equations from the literature, which are derived through the regression analysis of data from historical embankment failures, and a more advanced breach model developed by Paquier and Recking (2004). Depending on the breach modeling approach, information needed *a priori* may vary from final breach dimensions, breach expansion rate, breach opening duration, or other empirical parameters. It should be noted that breach widening is, by default, symmetrical upstream and downstream

of the initial notch location with a rectangular breach cross-sectional profile. Nevertheless, other configurations are studied in this chapter with a non-symmetrical breach widening and a different breach shape according to the Froehlich (2008) model.

3.2.3 Empirical breach models

3.2.3.1 Linear breach growth laws

Current state-of-the-art on overtopping induced levee failure shows that the breaching process is progressive (non-instantaneous) Morris et al. (2009), Rifai et al. (2017b), Wu and Li (2017), and the simplest way to describe breach expansion would be a time-dependent linear equation. Once initiated, a breach grows over time at a user-defined uniform rate to reach its ultimate dimensions. Recommendations for the choice of growth, *i.e.* erosion, rates can be found in the literature. For example, USBR (1988) recommended a single breach widening rate of 91 m/hr for embankment dams (Eq.3.2).

$$B(t) = 91t + B_0 \qquad \text{for} \qquad t \leq T_f \tag{3.2}$$

where t is time in hours (after the breach initiation), B the breach width in meters, B_0 the initial breach width in meters and T_f total duration of the breach expansion. Resio et al. (2009) reported that the rate of breach widening ranges between 9 m/hr for erosion-resistant soils (cohesive levees) and 60 m/hr for erodible alluvial material (sand and gravel soils). The widening rate can rarely reach 300 m/hr for very erodible dikes. Experimental investigations, both at laboratory (Michelazzo (2014); Rifai (2018); Elalfy et al. (2018)) and field Shimada et al. (2009) scales, pointed that the breaching process is divided into two main stages:

- First phase : the breach develops very fast with both deepening and lateral widening promoted by the increasing overtopping flow depth and velocity over the dike.
- Second phase : the breach development is slowed down by the decrease in main channel free surface. The lateral expansion of the breach is mainly due to mass slumping failure towards channel flow direction (*i.e.* downstream breach expansion).

Therefore to mimic the real breach widening, another option is to split the process into two main phases (Eqs. 3.3a and 3.3b), where the breach width grows quickly in the first phase, and then slows down toward the end of the development time:

$$B(t) = E_{w1}t + B_0 \qquad \text{for} \qquad t \leq T_1 \tag{3.3a}$$

$$B(t) = E_{w1}T_1 + E_{w2}(t - T_1) + B_0 \qquad \text{for} \qquad T_1 \leq t \leq T_f \tag{3.3b}$$

where T_1 is the duration of phase 1 in hours and E_{w1} and E_{w2} are user-prescribed breach growth rates (m/hr) for phase 1 and 2, respectively.

3.2.3.2 Von Thun and Gillette (1990) equation

The model developed by Von Thun and Gillette (1990) includes two different equations for breach widening in the case of low and high erodibility soils. The coefficients derived for these cases are actually upper and lower bounds for the value to be taken according to the studied case.
For erodible dikes (i.e. non-cohesive dikes), the law reads as:

$$B(t) = (4h_w + 61)t + B_0 \qquad \text{for} \qquad t \leq T_f \tag{3.4}$$

For cohesive levees the law reads as:

$$B(t) = 4h_w t + B_0 \qquad \text{for} \qquad t \leq T_f \tag{3.5}$$

where h_w is the height of water above final breach bottom, at notch location and at time of failure in meters.

3.2.3.3 Verheij (2002) equation

Based on field and laboratory data sets, simple relationships between breach width B and time for sand and clay levees were provided by Verheij (2002). The advantage of these laws is their approximation of breach dynamics with a high widening rate at the beginning of the process (of the order of 0.33 m/hr for non-cohesive levees), which then decreases in a as the breach width increases.
For sand levees (i.e. non-cohesive dikes), the equation is:

$$B(t) = 37.2t^{0.51} + B_0 \qquad \text{for} \qquad t \leq T_f \tag{3.6}$$

For clay levees (i.e. cohesive dikes), the law reads as:

$$B(t) = 13.4t^{0.5} + B_0 \qquad \text{for} \qquad t \leq T_f \tag{3.7}$$

3.2.3.4 Verheij and Van der Knaap (2003) equation

Verheij and Van der Knaap (2003) improved the previous formulations by including the effect of the difference in water levels at both sides of the dike at the breach location, and the critical flow velocity for the initiation erosion of the dike material. The empirical equation reads as:

$$\begin{cases} B(t) = f_1 \frac{(g^{0.5}\Delta H^{1.5})}{u_c} log(1 + \frac{f_2 g}{u_c} t) + B_0 & \text{for} \qquad t \leq T_f \\ \Delta H = h_{up} - h_{down} \end{cases} \tag{3.8}$$

with u_c the critical flow velocity for the initiation of erosion of dike material (m/s), f_1 and f_2 are empirical factors for breach width, and ΔH (m) denotes the difference in water level between the upstream (channel) and downstream (floodplain) sides of the breach.

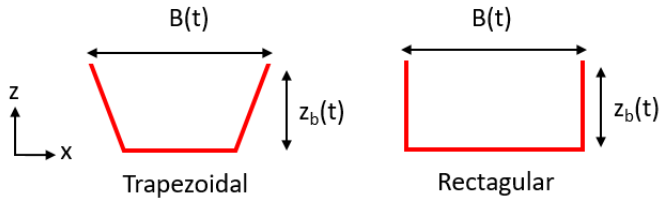

Figure 3.2: Sketch of the simplified longitudinal breach profile.

Experiments by Dou et al. (2014) highlighted a strong correlation between the water head both in the main channel and floodplain with breach outflow and dynamics. Therefore, in the implemented version within TELEMAC-2D, we consider the difference of water head instead of water level with h_{up} the hydraulic head upstream of the breach (channel side) and h_{down} the hydraulic head downstream of the breach (floodplain side). This term allows a natural balance, meaning that breach width stabilizes when the hydraulic head difference is close to zero. The user is not expected to give final breach width to run the model. Default values and ranges have been proposed for f_1 and f_2 (Table 3.1). Table 3.2 shows characteristic values of the critical velocity u_c for the surface erosion according to the dike material.

Parameter	Default	Range
f_1 (-)	1.3	0.5-5
f_2 (-)	0.04	0.01-1

Table 3.1: Default and range of values for coefficients f_1 and f_2 according to Verheij and Van der Knaap (2003).

Type of Soil	u_c (m/s)
Grass, good	7
Grass, moderate	5
Clay, good	1.0
Clay with 60% sand	0.80
Good clay with less structure	0.70
Good clay, heavily structured	0.60
Bad clay	0.40
Sand with 17% silt	0.23
Sand with 10% silt	0.20
Sand with 0% silt	0.16

Table 3.2: Strength characteristics of various soil types according to Verheij and Van der Knaap (2003).

3.2.3.5 Vertical breach expansion

Levees are generally very long with a limited height in comparison to dams. Therefore, levee breach depth is achieved early in the breakage process before the width reaches its ultimate dimension (Morris (2009); Wahl and Lentz (2012); Rifai (2018)). When the breach bottom reaches the foundation of the dike or an erodible layer, no further deepening of the breach is possible and lateral widening is controlling the breach expansion until its stabilization (i.e. fully formed breach and erosion is stopped). The empirical models described above focused on breach widening and no indication was given for breach deepening. In the present modeling approach, the time-evolution of the breach invert elevation is simulated according to the following a single linear-time progression law:

$$z_b(t) = z_{b0} - (z_{b0} - z_{bmin})\frac{t}{T_d} \qquad \text{for} \qquad t \leq T_d \tag{3.9}$$

with z_{bmin} the breach minimum bottom (elevation of the dike foundation, main channel bottom or of a rigid layer), z_{b0} the initial elevation of breach invert and T_d is the required duration to reach z_{bmin} in hours. The breach minimum bottom level z_{bmin} is reached in a shorter period than lateral expansion till ultimate breach width. In the present work, the duration T_d is taken by default 10 times smaller than the total duration of the breach lateral expansion T_f. The influence of this parameter is further investigated in this research work.

3.2.3.6 Froehlich (2008) model (adapted)

The empirical model proposed by Froehlich (2008) comprises three breach evolution variants to approximate breach widening and deepening. Each of the three models assumes that a breach begins to form at the top and grows with time into a trapezoidal shape. In this model, Froehlich (2008) used the concept of Brunner (2002) who proposed a sine-curve time breach progression (instead of the standard linear time evolution), reflecting slower growth at the start; then acceleration followed by another slow phase close to the end of breach development. The longitudinal cross-sectional profile of the breach is trapezoidal. In TELEMAC-2D, an adapted version is implemented for two-dimensional simulations. The time-evolution of the breach top width is computed as:

$$\begin{cases} B(t) = \beta(t)(B_f - B_0) + B_0 & \text{for} \qquad t \leq T_f \\ \beta(t) = \frac{1}{2}\{1 + sin[\pi(\frac{t}{T_f} - \frac{1}{2})]\} \end{cases} \tag{3.10}$$

and B_f as the final top width of the breach in meters. The breach bottom elevation evolves as:

$$\begin{cases} z_b(t) = z_{b0} - \beta_1(t)(z_{b0} - z_{bmin}) & \text{for} \qquad t \leq T_d \\ \beta_1(t) = \frac{1}{2}\{1 + sin[\pi(\frac{t}{T_d} - \frac{1}{2})]\} \end{cases} \tag{3.11}$$

3.2.4 RUPRO breach model

In the framework of semi-physical modeling techniques, the simplified one-dimensional breach model RUPRO Paquier (2007) allows estimating breach expansion and discharge hydrograph for overtopping and piping embankment failures. It takes breach location and shape (rectangular for overtopping and circular for piping) as input parameters and applies simplifying assumptions to calculate the breach flow. First, average hydrodynamic variables through breach cross-section are computed with Bernoulli's equation between the average water level in the main channel and critical flow depth on the floodplain side, with the linear head loss estimated with the Manning-Strickler formula. Sediment discharge is then calculated using the Meyer-Peter and Müller (1948) empirical formula (Eq.3.12) for bedload or using the linear excess shear stress formula (Eq. 3.15) that estimates the bed erosion rate.

3.2.4.1 Hydrodynamic variables

The main difference between the original RUPRO model and its implementation in TELEMAC-2D is that the breach section is explicitly defined in the computational mesh with some simplifications related to its time-evolution, such as the assumption of a rectangular cross-section. The use of Bernoulli's equation is thus not necessary here. First, a reference section is chosen to carry out the hydrodynamic calculations at the center of the dike crest. Breach outflow Q_b is computed through the longitudinal breach section along with the average water depth in the breach channel h_b, wetted perimeter P_w, and wetted surface S_w that are required to estimate the sediment discharge.

3.2.4.2 Sediment discharge: Meyer-Peter and Müller (1948) formula

$$\begin{cases} Q_s = \frac{\alpha P_w}{g(\rho_s - \rho)\sqrt{\rho}}(\tau_b - \tau_c)^{3/2} & \text{for} \qquad \tau_b > \tau_c \\ Q_s = 0 \qquad \text{for} \qquad \tau_b \leq \tau_c \end{cases} \tag{3.12}$$

where Q_s is sediment discharge in (m^3/s); P_w (m) is the wetted perimeter on which sediment transport is active ($P_w(t) = 2h_b(t) + B(t)$) ; τ_b is the bed shear stress in (Pa) and τ_c the critical shear stress to initiate sediment transport in (Pa) calculated as follows:

$$\begin{cases} \tau_b = g\rho J R_H \\ \tau_c = 0.047 g(\rho_s - \rho) d_{50} \end{cases} \tag{3.13}$$

where ρ the density of water in (kg/m^3); ρ_s the density of sediment (kg/m^3); R_H the hydraulic radius in (m) corresponding to the ratio of wetted surface to wetted perimeter; d_{50} is the embankment material median diameter in (m); α is the dimensionless Meyer-Peter and Müller (1948) empirical coefficient with a default value of 8; 0.047 the dimensionless Shields Shields (1936) parameter as suggested by Meyer-Peter and Müller (1948) and J the energy slope calculated using Manning-

Strickler formula as follows :

$$J = \frac{Q^2}{K^2 S_w^2 R_H^{4/3}} \tag{3.14}$$

With K the Strickler coefficient in ($m^{1/3}s^{-1}$).

3.2.4.3 Sediment discharge: linear erosion formula

Sediment discharge can also be estimated proportional to the effective shear stress in excess of the critical shear stress using the linear erosion formula Walder and O'Connor (1997) :

$$\begin{cases} Q_s = ALMP_w K_d(\tau_b - \tau_c) & \text{for} \quad \tau_b > \tau_c \\ Q_s = 0 \quad \text{for} \quad \tau_b \leq \tau_c \end{cases} \tag{3.15}$$

with ALM the transverse length of the breach channel, K_d the erodibility coefficient in (m/(s Pa)) that depends on levee material characteristics such as the size of the sediments, and the water content, soil permeability, and compaction energy used for construction Fell et al. (2013), Hanson and Hunt (2007). The erodibility coefficient can be measured on different scales using various methods such as hole erosion tests and submerged jet tests. Otherwise, one can refer to the literature to select reasonable values of K_d. Hanson et al. (2010) provided minimum and maximum values for the erodibility coefficient according to the embankment's clay content and compaction energy, while Wu (2013) provided an equation estimating K_d in (m/(h Pa)) as a function of the soil dry specific weight γ_d, water specific weight γ and clay content $c_{\%}$ as follows:

$$K_d = \frac{0.063\gamma}{\gamma_d} exp[-0.121 c_{\%}^{0.406} (\frac{\gamma_d}{\gamma})^{3.1}] \tag{3.16}$$

3.2.4.4 Erosion rate and update of breach dimensions

The erosion rate is estimated from the sediment discharge distributed on the breach surface active for sediment transport as follows :

$$V_e = \frac{Q_s}{(1-p)S_{breach}} \tag{3.17}$$

with V_e the erosion rate in (m/s); p the levee soil porosity, and S_{breach} is the surface of breach sides and bottom. RUPRO breach model was extensively validated against experimental data, and other physically-based models during CADAM Paquier (2001), and IMPACT Paquier and Recking (2004) projects. Here we integrated an adapted two-dimensional version of this model in the breach module of TELEMAC-2D (Fig.3.1). Hydrodynamic variables are computed with TELEMAC-2D, and Bernoulli's equation is thus not used. Their average values are calculated on the breach section at crest level and are then used to estimate sediment discharge and breach lateral ($2\times V_e$) and vertical (V_e) erosion rates. Once initiated by overtopping, Paquier (2007) tested four different options to

model breach expansion:

- Option 1 (original model): consists of two main steps after breach initiation (Step 1). Step 2, where the breach can only deepen until its final bed elevation is reached. Then, lateral expansion of the breach starts in Step 3.
- Option 2 (IMPACT): this version was tested during the IMPACT project and consists of two main steps after breach initiation (Step 1). However, Step 2 allows both lateral and vertical breach expansion. When the breach final bed elevation is reached, Step 3 starts with breach widening only.
- Option 3 (modified wetted perimeter P_w in Step 3): this version models Step 2 in the same way as the original version and limits the wet perimeter in step 3, where only widening is permitted to twice the water depth in the breach channel.
- Option 4 (reduction of wall shear stress and modified wetted perimeter P_w in Step 3): in addition to the limitation of the wetted perimeter in Step 3, the lateral shear stress applied on breach side walls is also reduced. For that, the ratio of lateral shear stress to bottom shear stress (R_τ) estimated by Knight and Hamed (1984) from his laboratory experiments in a rectangular channel is used and computed as follows:

$$\begin{cases} R_\tau = 1 & \text{for} \quad h_b > 0.5B \\ R_\tau = 0.6 + \frac{h_b}{0.83B} & \text{for} \quad h_b < 0.083B \\ R_\tau = 1.06 - \frac{0.03B}{h_b} & \text{for} \quad 0.083B < h_b < 0.5B \end{cases} \tag{3.18}$$

where h_b is the average water depth in the breach channel in (m) and B the breach width in (m).

3.3 Field scale experiments modeling

Full-scale experiments of side-overflow levee breaching presented by Kakinuma et al. (2013) were employed to validate and compare the newly implemented breach modeling approaches. These tests were carried out in the Chiyoda test channel (Fig.3.3), which is the largest river experimental facility in Japan (Fig.3.3) built on Tokachi River, Hokkaido. The levee failure was triggered by overtopping, and the influence of channel inflow discharge, dike soil composition, and dike geometry on the breaching process was investigated. In this study, test cases 2 and 4 were considered as described in Figure 3.5 and Table 3.3 with a 8 m wide main channel and a longitudinal bed slope of 1/500, approximately. The levee was built along the right side of the main channel toward a 80 m wide floodplain. The length of its erodible part varied from 60 m to 100 m for cases 2 and 4, respectively. The levee's height was 3 m for both tests with a crown width of 3 m and side slopes equal to 1:2 (V:H), except for Case 4 where the levee was built larger with a 6 m wide crest. Soil composition comprised non-cohesive sand and gravel fractions.

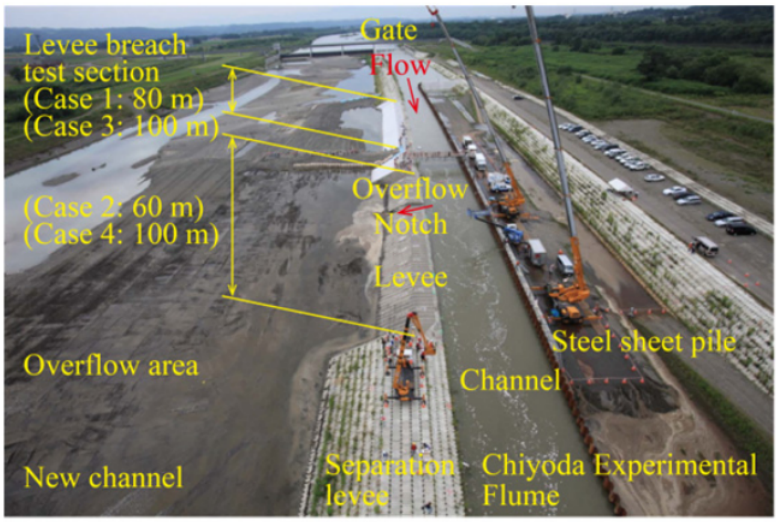

Figure 3.3: Chiyoda test channel facility and specifications from Kakinuma et al. (2013).

In order to control breach initiation by overtopping, a trapezoidal-shaped notch was carved 20 m far from the upstream end of the erodible dike portion. The notch was 0.5 m deep, 3 m wide at the crest, and 1 m wide at the bottom, and the main channel inflow discharge was gradually increased as shown in Figure 3.4 to reach the required water level for overtopping. Measurement data included breach outflow hydrographs, water levels, and levee-breaching process estimated from acceleration sensors observations. Further information on these experiments can be found in Kakinuma et al. (2013).

3.3.1 Computational domain and parameters

The 2D computational domain was discretized into structured triangular elements with an edge of 0.5 m as recommended by Kakinuma and Shimizu (2014) and Dazzi et al. (2019). Boundary conditions (Fig.3.5) consisted in imposing the measured inflow discharge at the main channel inlet (Fig.3.4) and a rating curve at the downstream end to achieve the required water level in the main channel and trigger levee overtopping at the notch location. A supercritical outflow with free water depth and velocity was set in the floodplain, and a solid boundary was imposed elsewhere. The Strickler coefficient was adjusted for each case to achieve the required water level in the main channel and trigger levee overtopping at the notch location. A constant velocity diffusivity (molecular viscosity + turbulent viscosity) of 10^{-3} ($m^2\ s^{-1}$) was applied for turbulence closure. The time step was set to 0.1 s, and the conjugate gradient solver was employed with an accuracy of 10^{-6}. The mass-conservative PSI scheme and NERD scheme were used for water depth and velocity advection. Figure 3.6 shows a good agreement between the computed and measured water level temporal change at notch location in cases 4 and 2 before breaching for Strickler coefficients of 43 and 38 ($m^{1/3}s^{-1}$), respectively. Minor discrepancies can be noticed but are believed to be related to the assumption of a non-movable bed

in the main channel and floodplain. More accurate calibration of the hydrodynamic model would require the use of water depth by calculating the balance of the water level and the evolving bed level in time. However, the latter information was only available before and after the breaching test.

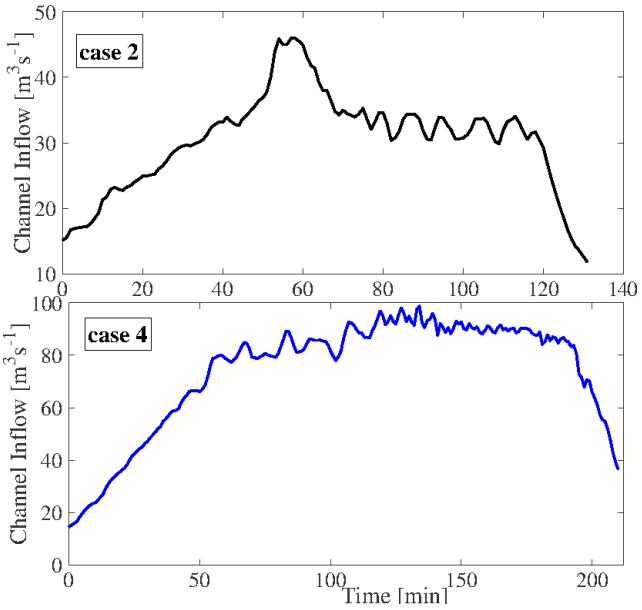

Figure 3.4: Measured inflow discharge for the test cases 2 and 4.

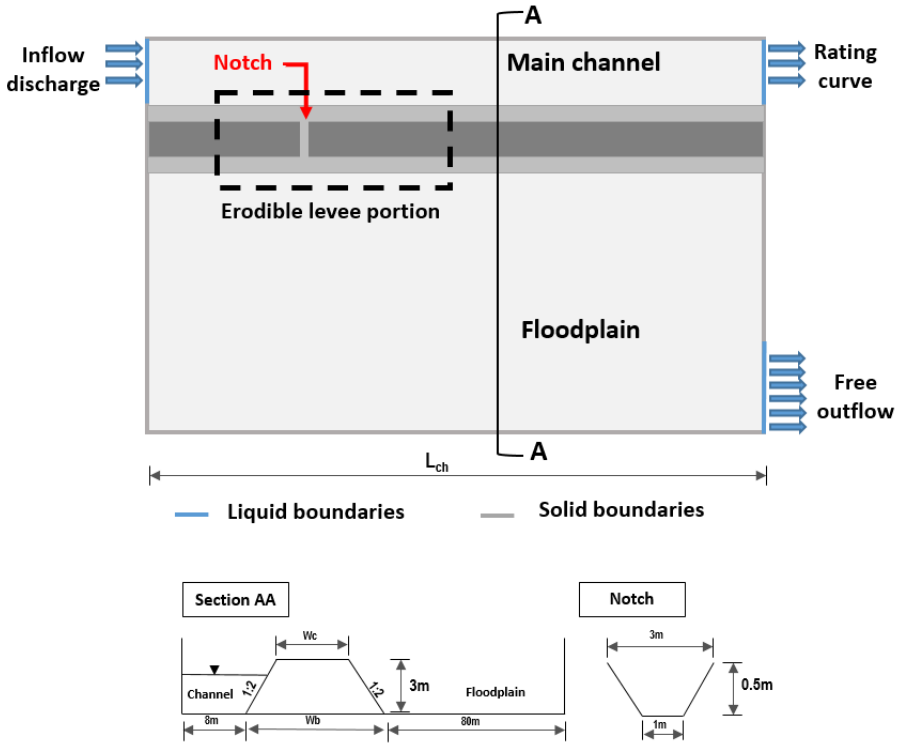

Figure 3.5: Sketch of field experiments setup and model boundary conditions.

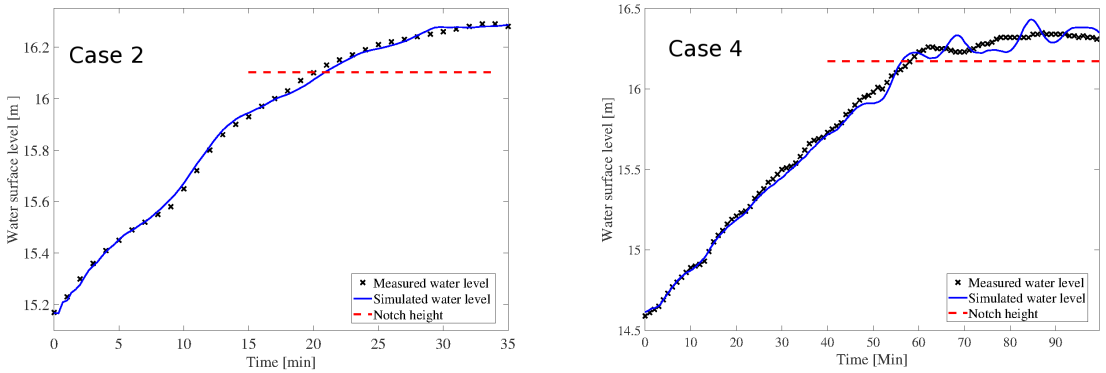

Figure 3.6: Comparison between measured and computed water level evolution at notch location, before breaching.

Case	d_{50} (mm)	W_c (m)	W_b (m)
2	4.9	3	15
4	0.74	6	18

Table 3.3: Description of field test cases.

3.4 Results and parametric analysis

Assumptions about the initiation and rate of levee breaching in the proposed semi-physical approach are expected to impact breach hydrograph prediction, which is a crucial parameter for flood risk management. It can influence the estimated arrival time, velocity, and depth of flooding in the protected area. In this section, performances of the breach models presented above are highlighted, and the capacity of some parameters used in this approach to affect the resulting breach discharge is discussed. Most of the simulations in this section were carried out by setting the model's user-defined parameters from experimental observations. For the Verheij and Van der Knaap (2003) and RUPRO models, a natural equilibrium is expected to rise when the water head difference upstream and downstream the levee tends to zero for the Verheij and Van der Knaap (2003) model or when the actual shear stress is lower than the critical shear stress required to initiate sediment motion for the RUPRO model. However, the dimensions of the computational domain being limited the same breach width limitation was used for all simulations. Finally, vertical breach expansion was not allowed in the dike foundation in coherence with the non-movable bed assumption in the main channel and floodplain.

3.4.1 Case 4

For experimental Case 4 a start time of 105 min was defined to initiate breach opening (except for the RUPRO model that does not require this information). The initial breach width was set equal to the notch top width (B_0 =3 m), and a final breach width of 75 m was predefined as a criterion to stop breach widening.

3.4.1.1 User-defined linear widening rate

A short sensitivity analysis was performed for the user-defined linear expansion equation (both simple and dual-stages) to assess the effect of the breach growth rate on simulated breach discharge. Thus, different values of erosion rate were tested as shown in Table 3.4. First, a simple time-dependent breach width growth law was considered (WL1, WL2, WL3, USBR in Table 3.4). Then, a dual-staged breach widening formula was defined with two different erosion rates and T_1 = 45 min (WLD in Table 3.4).

Run	E_{W1} (m/hr)	E_{W2} (m/hr)	NRMSE on breach width	NRMSE on breach outflow
WL1	50	50	16.2%	5.5%
WL2	65	65	7.2%	7.5%
WL3	80	80	4.6%	12.8%
USBR (1988)	91	91	7%	15.6%
WLD	65	30	8.8 %	6.7%

Table 3.4: Linear growth law simulations of Case 4 and resulting Normalized Root-Mean-Square Error on breach width and discharge.

The resulting breach discharge and width time series are presented in Figures 3.7 and 3.8, and compared with experimental data for a qualitative assessment of model performance. The rapid increase in breach discharge, followed by a quasi-stabilization step around a maximum value close to 70 m^3/s before dropping at the test end (due to the limitation of channel inflow discharge at the test end, as shown in Figure 3.4) is well reproduced by the simplified modeling approaches. However, the results display a higher simulated amplitude of breach discharge with USBR (1988) formula while it was underestimated for run WL1 performed with a lateral erosion rate of 50 (m/h). A higher breach width increases the breach section offered to convey the flow and thus induces greater breach discharges.

Performances are evaluated quantitatively; for each of the simulated growth rates. Normalized Root-Mean-Square Error (NRMSE) values for breach width and discharge are compared in Table 3.4. The best agreement for breach width is achieved for run WL3 while run WLD performed better on breach discharge (run WL1 displayed the lowest deviation on breach discharge magnitude, but it was less conservative). For the tested range of lateral erosion rates, breach width evolved differently

but did not significantly impact predicted breach outflow. The latter parameter only varies slightly when the user-defined widening rates remain within a reasonable range. Finally, simulation with E_w = 65 (m/hr) seems to be a good compromise as it is more conservative than the run WL1 and showed reasonable values of NRMSE.

It should also be noted that the change in breach erosion rate during stage 2 has a limited influence on breach discharge as shown in run WLD, using two phases of breach widening slightly improved breach discharge estimation.

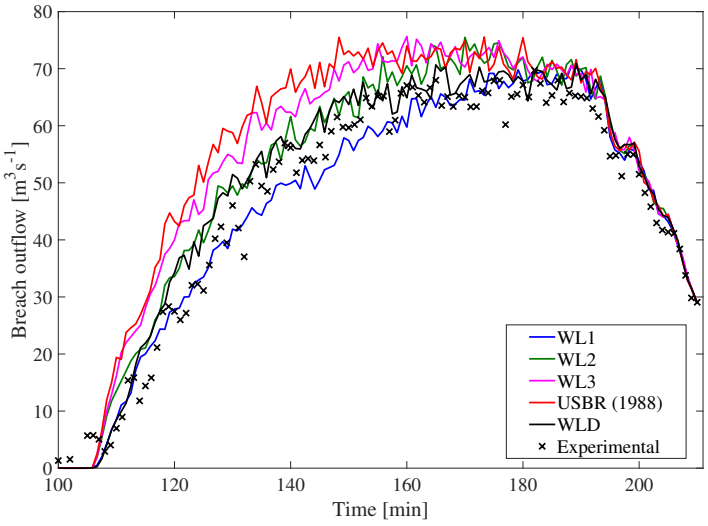

Figure 3.7: Measured and computed time-evolution of breach discharge with the linear breach expansion laws.

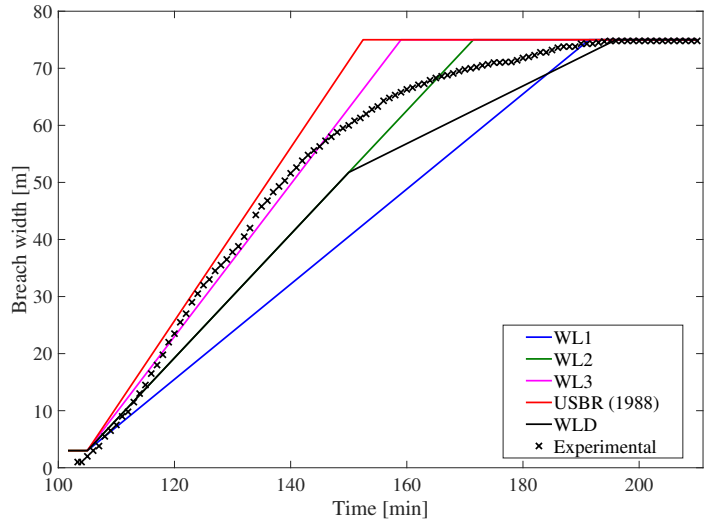

Figure 3.8: Measured and computed time-evolution of breach width with the linear breach expansion laws.

Run	h_w (m)
VG1	Fixed value of h_w (t_{start}, notch location)
VG2	Time changing value h_w (t, notch location)
VG3	Time changing value h_w (t, average value over breach width)
VG4	Time changing value h_w (t, maximum value over total breach width)

Table 3.5: Case 4 simulations with the Von Thun and Gillette (1990) model.

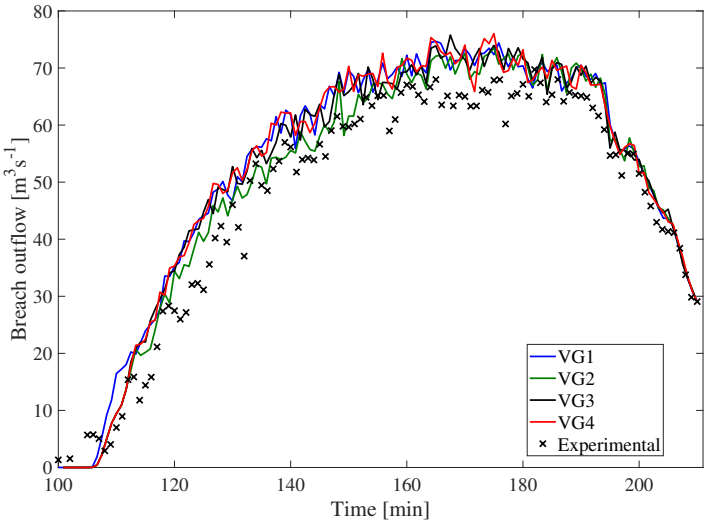

Figure 3.9: Measured and computed time-evolution of breach discharges with the Von Thun and Gillette (1990) law.

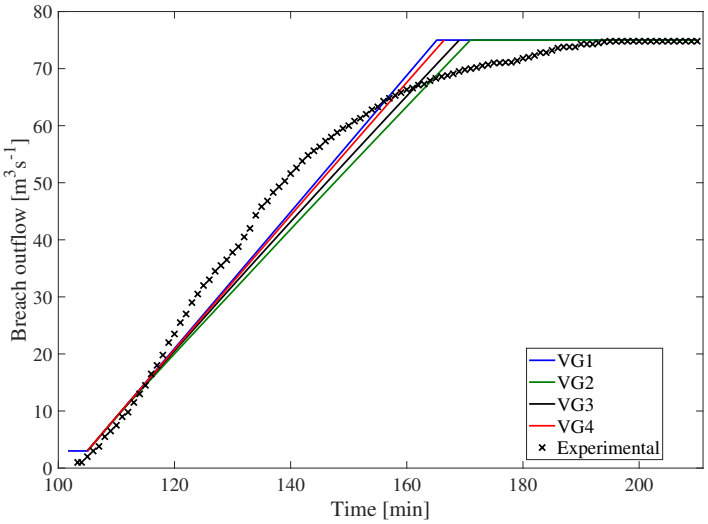

Figure 3.10: Measured and computed time-evolution of breach width with the Von Thun and Gillette (1990) law.

3.4.1.2 Breach model by Von Thun and Gillette (1990)

The Von Thun and Gillette (1990) model was developed from historical dam failure data. It describes breach width as a function of time and water height above the final breach bottom at failure time. For levees, the water supply is not limited and could be unsteady, so considering the water level corresponding to failure time is questionable. In addition, these parametric equations are generally employed in non-discretized models, and considering a uniform water depth in the main channel seems to be adapted only for dams and reservoirs.

In the case of fluvial dikes with a lateral incident flow, water depth can vary along breach location. Therefore we conducted four different simulations (Table 3.5) where the water depth in the breach widening equation was calculated differently. First, we considered the original formulation as a reference run VG1. Then, we analyzed the effect of adjustments in the definition of the parameter h_w on results accuracy. Simulations VG2, VG3, and VG4 were performed with time-varying water depth at notch location, averaged or by taking its maximum value along total breach width, respectively.

Resulting breach discharge and width for all runs are compared in Figures 3.9 and 3.10 and show that all four methods provided reasonable and conservative results for breach discharge In addition, no significant difference can be observed between the performed simulations with different methods for the water depth term in the Von Thun and Gillette (1990) model.

3.4.1.3 Breach model by Verheij (2002)

The equations for breach lateral opening presented by Verheij (2002) are expected to be more accurate for fluvial dikes as they result in a very high enlargement rate at the beginning of the process, which decreases as the breach width grows. However, Figures 3.12 and 3.11 show that breach width and discharge were poorly modeled with the Verheij (2002) model for the tested prototype Case 4. Breach width was first overestimated during the initiation stage, then the model computed a slower erosion process of the breach, and its width values remained lower than experimental data. Therefore, the model fell short of capturing the maximum breach discharge value and resulted in a global NRMSE over test duration of 29.6% for breach width and 12.4% for breach discharge.

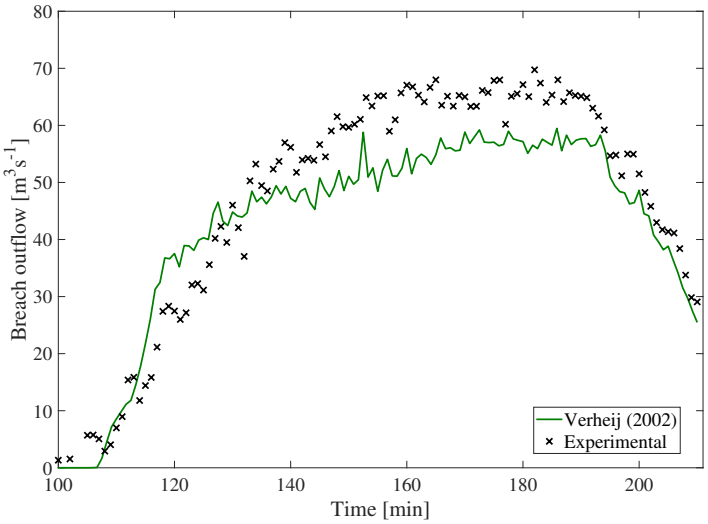

Figure 3.11: Measured and computed breach discharges with the Verheij (2002) law.

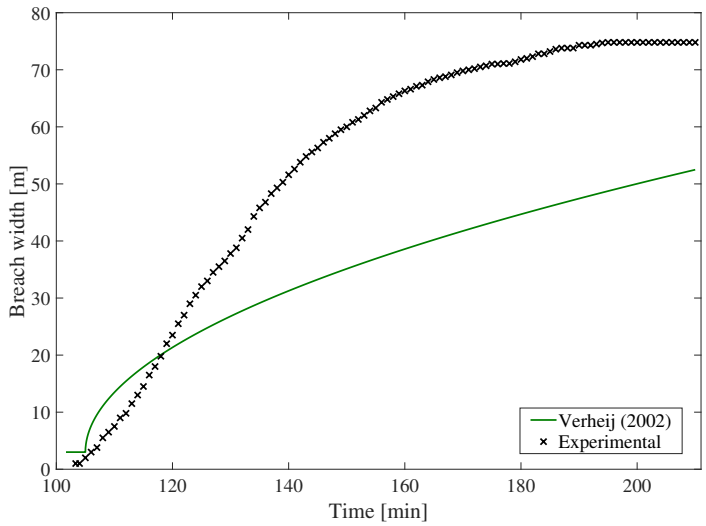

Figure 3.12: Measured and computed time-evolution of breach width with the Verheij (2002) law.

3.4.1.4 Breach model by Verheij and Van der Knaap (2003)

For the Verheij and Van der Knaap (2003) formulation, the critical erosion velocity u_c was set to 0.23 (m/s), as proposed by authors in Table 3.1 for sandy dikes with silt soil fractions and default values were taken for f_1 (=1.3) and f_2 (= 0.04). Because the breach deepened faster than it widened, and because this model does not require a user-input breach final width or widening duration, the time for the final breach bottom to be reached T_d was limited to 5 min (approximated value from measurements). In addition, a sensitivity analysis was carried out on the influence of breach width empirical parameters f_1 and f_2 and the critical erosion velocity u_c .

Run	ΔH	f_1	f_2	u_c	NRMSE on breach width	NRMSE on breach outflow
VR1	Average ($h_{up} - h_{down}$)	1.3	0.04	0.23	52.9%	34.2%
VR2	Max ($h_{up} - h_{down}$)	1.3	0.04	0.23	47.4%	28.5%
VR3	Average ($H_{up} - H_{down}$)	1.3	0.04	0.23	41.8%	23.6%
VR4	Max ($H_{up} - H_{down}$)	1.3	0.04	0.23	30.1%	12.5%

Table 3.6: Case 4 simulation parameters for Verheij and Van der Knaap (2003) formula.

The model was first tested in its original formulation considering water level difference upstream (channel side) and downstream (floodplain side) of the dike. A comparison was made in simulations VR1 and VR2 between two different methods to compute this difference. First, we considered the average value of the computed water level differences between the main channel and floodplain side (VR1). In the second run, the maximum value is used (VR2). For the last simulations (VR3 and VR4), we employed the hydraulic head instead of the water level to account for the effect of the approaching lateral river flow momentum.

In the same way, the results for simulations with the average and maximum hydraulic head difference values (VR3 and VR4) were compared. One can see in Figures 3.13 and 3.14 that both the choice of hydraulic variable (water level and hydraulic head) and computation method of the difference term (maximum or average value) may impact result quality. Estimated breach opening and discharge were improved in run VR2 and run VR4 compared to tests VR1 and VR3, respectively. Using the hydraulic head (VR3 and VR4) instead of water level (VR1 and VR2) has proven to induce lower NRMSE values and increase the accuracy of simulated breach dynamics and discharge. As demonstrated, the equation with the maximum value of hydraulic head difference was integrated into the Breach component of TELEMAC-2D to best estimate breach evolution and discharge.

Run	ΔH	f_1	f_2	u_c	NRMSE on breach width	NRMSE on breach outflow
VR4	Max ($H_{up} - H_{down}$)	1.3	0.04	0.23	30.13%	12.5%
VR4P1	Max ($H_{up} - H_{down}$)	1.95	0.04	0.23	11.8%	7.7%
VR4P2	Max ($H_{up} - H_{down}$)	1.3	0.06	0.23	16.9%	8.3%
VR4P3	Max ($H_{up} - H_{down}$)	1.3	0.04	0.21	24.1%	8.1%
VR4P4	Max ($H_{up} - H_{down}$)	1.3	0.04	0.20	19.7%	7.4%

Table 3.7: Case 4 simulation parameters with the modified Verheij and Van der Knaap (2003) formula.

The additional simulations presented in Table 3.7 were performed to investigate the influence of breach width empirical parameters f_1 and $f2$. Since default values resulted in a lower breach width and discharge than experimental measurements, two simulations were performed by increasing f_1 and f_2 (150% of default values) in run VRP1 and VRP2, respectively. Figures 3.15 and 3.16 highlight an improved prediction of breach characteristics when increasing f_1 or f_2. These user-defined pa-

rameters can be calibrated to simulate cases with different levee material compositions. Additional simulations VR4P3 and VR4P4 varying u_c were also performed. Since silt content of levee material in Case 4 is 14.9%, the actual u_c range between 0.2 and 0.23 according to Table 3.2. Tests VR4P3 and VR4P4 show a clear improvement in the predicted breach width and discharge (Figures 3.17 and 3.18). As expected, decreasing the critical erosion velocity increases estimated breach erosion rates and thus results in higher breach discharges approaching the values measured in experiments. For Case 4, increasing f_1 in run VRP1 achieved the best agreement with measured breach width and hydrograph as it was more conservative than test VR4P4. One can also notice that estimated breach width is more sensitive to changes in f_1 and f_2 than u_c values.

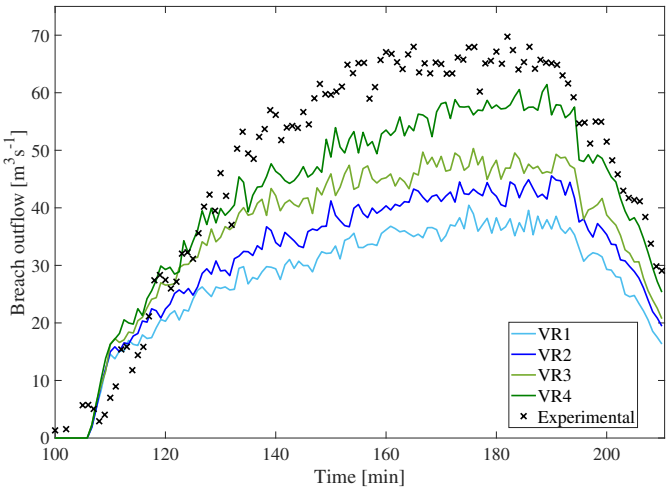

Figure 3.13: Measured and computed breach discharges with the Verheij and Van der Knaap (2003) law.

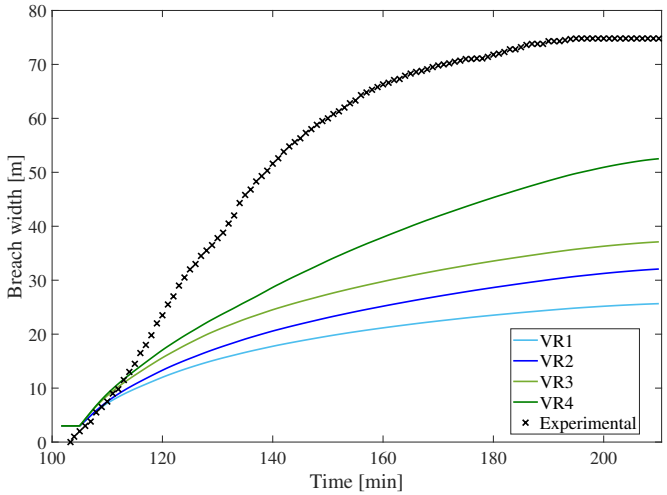

Figure 3.14: Measured and computed time-evolution of breach width with the Verheij and Van der Knaap (2003) law.

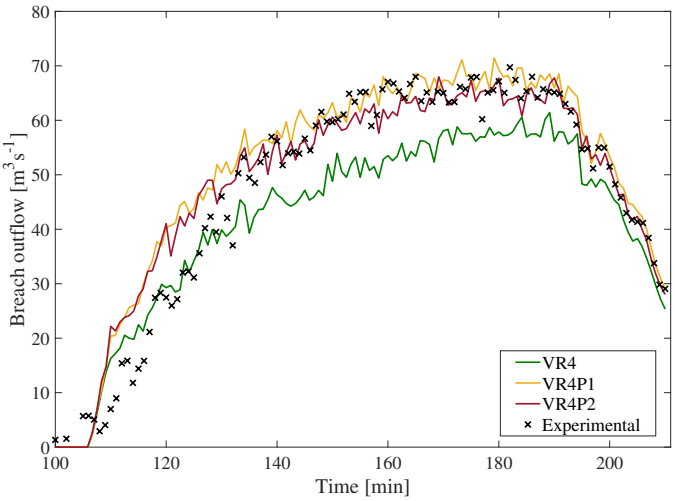

Figure 3.15: Measured and computed time-evolution of breach discharge with the modified Verheij and Van der Knaap (2003) formula varying of f_1 and f_2.

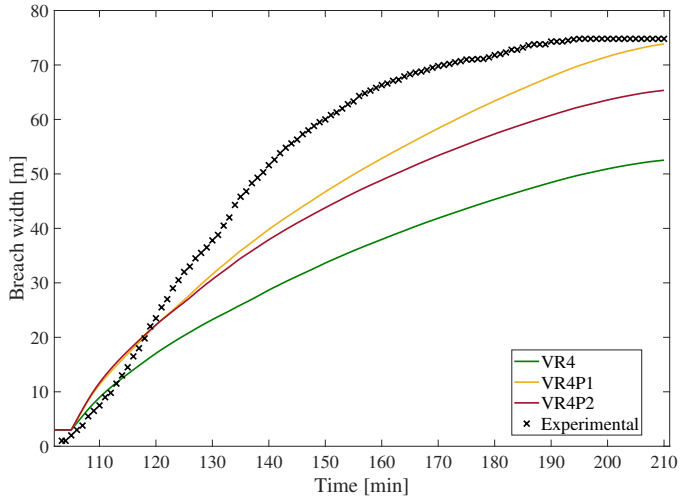

Figure 3.16: Measured and computed time-evolution of breach width with the Verheij and Van der Knaap (2003) formula varying of f_1 and f_2.

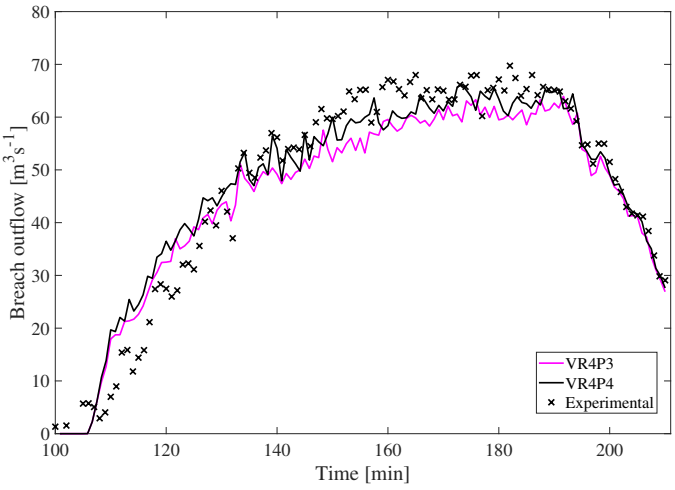

Figure 3.17: Measured and computed breach discharges with Verheij and Van der Knaap (2003) model varying u_c.

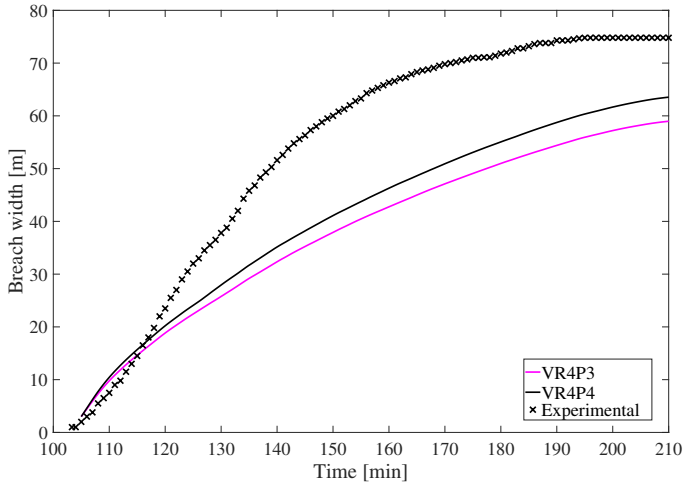

Figure 3.18: Measured and computed time-evolution of breach width with the Verheij and Van der Knaap (2003) formula varying u_c.

3.4.1.5 Breach model by Froehlich (2008)

For the Froehlich (2008) model, a first run was performed with a lateral expansion period equal to that observed experimentally for the breach to reach its ultimate width (90 min after the initiation time). As shown in Figures 3.19 and 3.20, this value did not achieve a good concordance between simulated and measured breach width and discharge. Indeed, the computed widening rate was slow, and breach outflow rapid increase was not captured. Therefore, we conducted two additional simulations (Table 3.8) with T_f adjusted as 75 min and 45 min.

In Figure 3.19, simulation with T_f = 45 min leads to a better estimation of breach widening and more a conservative breach outflow hydrograph. Finally, Figure 3.21 illustrates the time evolution of the trapezoidal-like shaped longitudinal breach section at the crest center line (y = 89 m) for T_f = 45 min.

T_f (min)	NRMSE on breach width	NRMSE on breach outflow
90	19.1%	16.1%
75	10.3%	8.7%
45	10.3%	8.7%

Table 3.8: Case 4 simulation parameters with the Froehlich (2008) model and resulting NRMSE values.

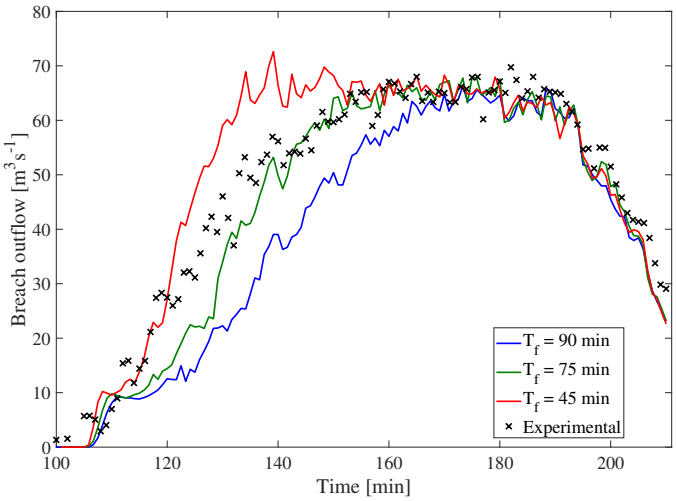

Figure 3.19: Measured and computed time-evolution of breach discharge with Froehlich (2008) model.

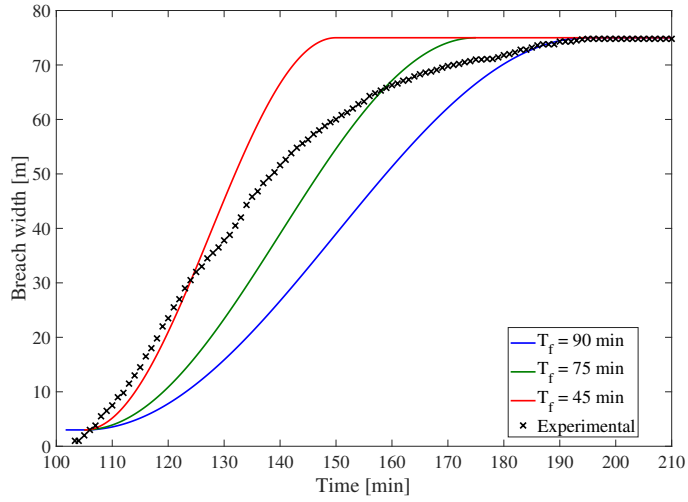

Figure 3.20: Measured and computed time-evolution of breach width with Froehlich (2008) model.

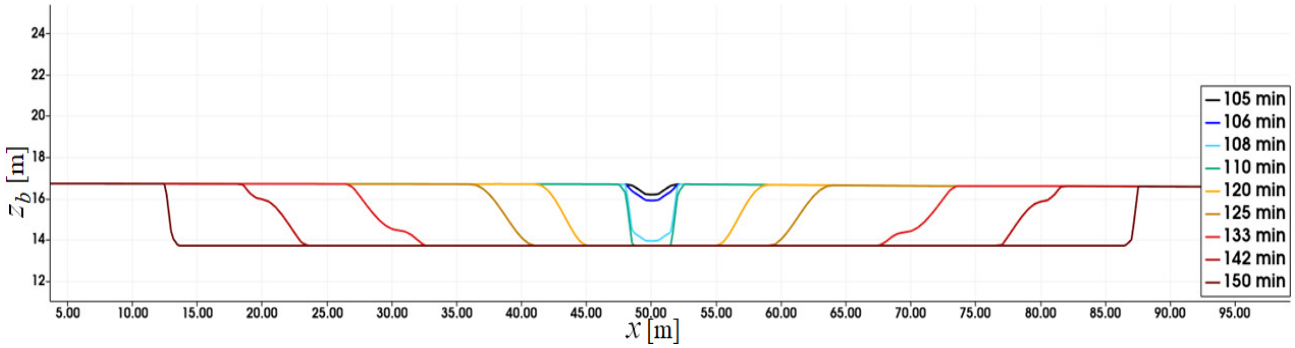

Figure 3.21: Longitudinal breach profile at the crest level (y=89 m) computed with Froehlich (2008) model for T_f = 45 min.

3.4.1.6 Influence of breach asymmetrical widening

Experimental research on levee failure highlighted critical differences between longitudinal and frontal embankments breaching. Field and laboratory investigations (Kakinuma et al. (2013); Michelazzo (2014); Rifai (2018); Elalfy et al. (2018)) reported a specific feature of levee breach dynamics that consists in an asymmetrical lateral breakage. Due to the parallel approaching flow in the main channel, the levee breach mainly expands towards the downstream edge of the breach (Figure 3.22). Implementing additional features and physical processes in numerical breach models can help improve their accuracy but can also bring additional uncertainties since the user defines additional parameters. Therefore, the impact of breach asymmetry on resulting breach discharge is investigated in this section.

For the sake of simplicity, USBR (1988) (only implies time variation of the breach expansion) and Verheij and Van der Knaap (2003) (includes hydraulic head in the main channel along breach location) breach models are considered here to perform additional simulations with a non-symmetrical breach widening where 4% of breach width is distributed upstream notch location and 96% downstream as reported in Kakinuma et al. (2013).

Results presented in Figure 3.23 show a very light impact of breach asymmetry on the resulting breach outflow hydrograph. However, this conclusion can only apply for the latter test case and parametric breach models with a simple floodplain configuration and a uniform bed with low bed slopes in the longitudinal direction. Rifai et al. (2017a) reported the critical influence of tailwater on the breach discharge; one can expect a significant influence of breach asymmetry for cases with a non-uniform floodplain bed level impacting the flow through the breach channel in the presence of tailwater, for example.

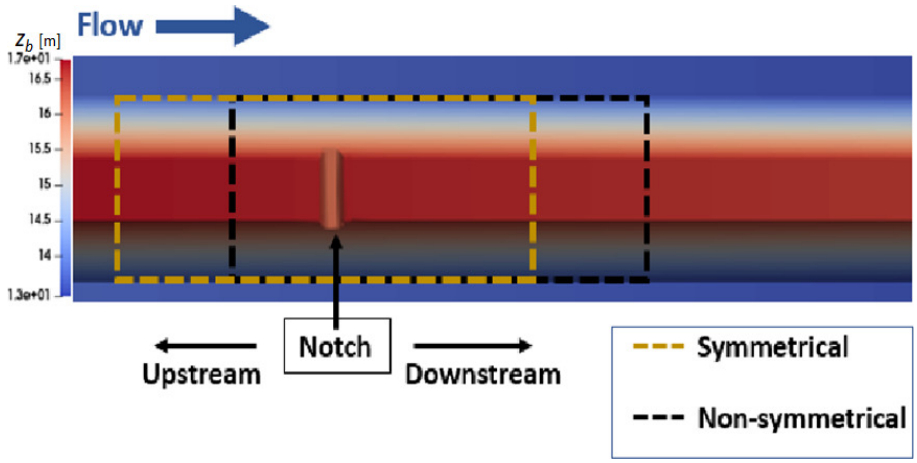

Figure 3.22: Definition of the erodible breach zone for symmetrical and non-symmetrical configurations.

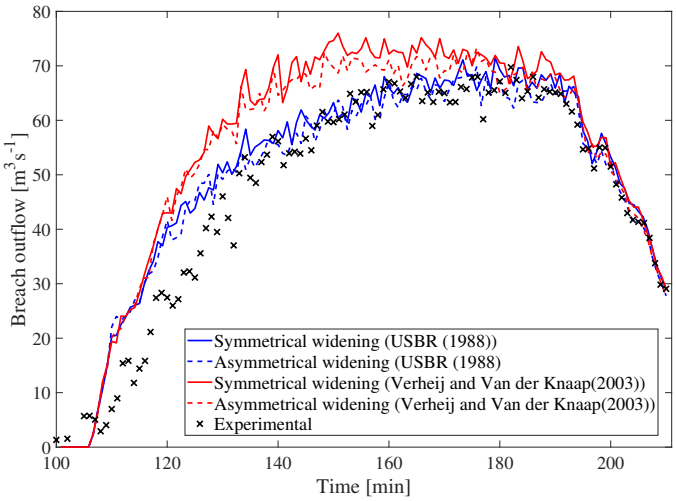

Figure 3.23: Influence of the asymmetrical breach lateral erosion on breach discharge.

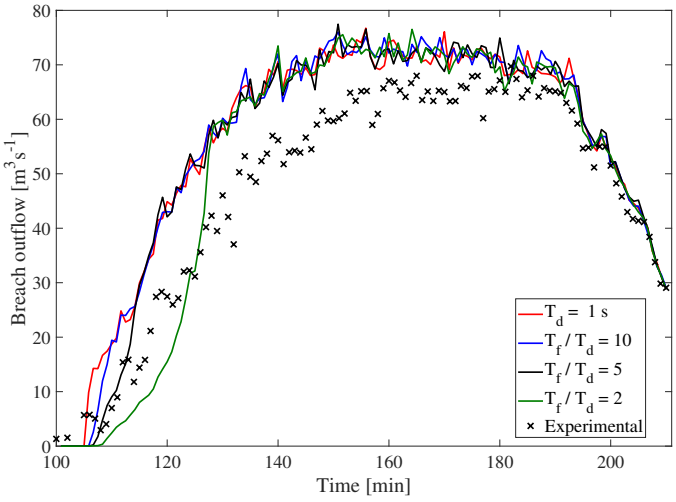

Figure 3.24: Influence of the vertical erosion rate on breach discharge (USBR (1988) formula).

3.4.1.7 Influence of breach vertical erosion

Most empirical breach models describe the lateral erosion rate, which is deemed to be the evolution of breach top width (Zomorodi (2020)), while breach deepening is often considered instantaneous. One can therefore question the influence of the breach vertical erosion rate on the predicted breach discharge. Additional tests are presented here with the USBR (1988) formula for lateral erosion and a variable deepening duration. Figure 3.24 shows that overestimating the breach deepening period can significantly impact the estimated breach discharge as it influences the breach section offered to convey the flow. However, the results remain accurate for a reasonable breach widening period to breach vertical erosion between 10 and 5 for Case 4 with USBR (1988) formula. In addition, considering a quasi-instantaneous breach, vertical erosion seems an interesting alternative. It results

in good predictions of breach discharge. It exempts the user from calibrating T_d as the ratio of (T_f/T_d) equal to 10 adopted in the results section was only validated in the context of this study.

3.4.1.8 RUPRO model

In this section, capabilities of the RUPRO breach model Paquier (2007) implemented in TELEMAC-2D to estimate breach width and discharge are investigated. The linear erosion law (Eq. 3.15) is used to compare the four different options of RUPRO (cf Section 3.2.4): RUP1 for Option 1, RUP2 for Option 2, RUP3 for Option 3, and RUP4 for Option 4). Table 3.9 summarizes the configurations simulated, while changing options and values of the erodibility coefficient (60, 80, 100 and 120 (cm^3/(s Pa))). A non-symmetrical breach widening was used where 4% of breach width is distributed upstream of the notch location and 96% downstream of the notch as measured by Kakinuma et al. (2013).

Run	K_d (cm^3/(s Pa))	Option	NRMSE on breach width	NRMSE on breach outflow
RUP1A	60	1	15.5%	11.3%
RUP1B	80	1	9.8%	11.6%
RUP1C	100	1	19%	23%
RUP1D	120	1	28.9%	23.53%
RUP2A	60	2	21.1%	17.7%
RUP2B	80	3	11.8%	11.3%
RUP2C	100	4	12.53%	14.81%
RUP2D	120	4	19.9%	22.5%
RUP3A	60	2	64.7%	53.3%
RUP3B	80	3	60.8%	47.5%
RUP3C	100	3	56.84%	41.5%
RUP3D	120	4	53.2%	35.7%
RUP4A	60	2	60.8%	55%
RUP4B	80	3	64.9%	49.6%
RUP4C	100	3	57.4%	44.8%
RUP4D	120	4	54.3%	40.7%

Table 3.9: Case 4 simulation parameters for different options of the RUPRO model and resulting NRMSE values (All numerical runs were performed with an asymmetrical widening) .

First, RUP1 is used to compare the results with different widening configurations (Table 3.10). In test "RUP1B-symmetrical", the breach widens symmetrically upstream and downstream notch location. For the computation "RUP1B-asymmetrical," a non-symmetrical breach widening was used where 4% of breach width is distributed upstream notch location and 96% downstream the notch as measured by Kakinuma et al. (2013), and simulation "RUP1B-downstream" where the breach only

widens downstream the notch. The erodibility coefficient K_d was set to 80 (cm^3/(s Pa)) based on simulations performed by Dazzi et al. (2019) of Case 4 using a 2D hydro-morphodynamic model showing that breach width and discharge were best predicted for K_d = 80 (cm^3/(s Pa)).

Run	K_d (cm^3/(s Pa))	Option	NRMSE on breach width	NRMSE on breach outflow
RUP1B-symmetrical	80	1	10.6%	10.9%
RUP1B-asymmetrical	80	1	9.8%	11.6%
RUP1B-downstream	80	1	9.8%	11.8%

Table 3.10: Simulations with the Option 1 of RUPRO model and different widening configurations.

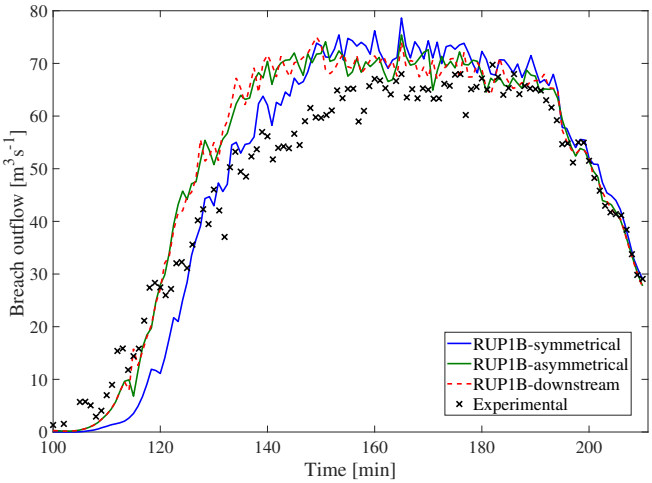

Figure 3.25: Influence of the widening configuration on breach discharge with Option 1 of RUPRO model and $K_d = 80$ (cm^3/(s Pa)).

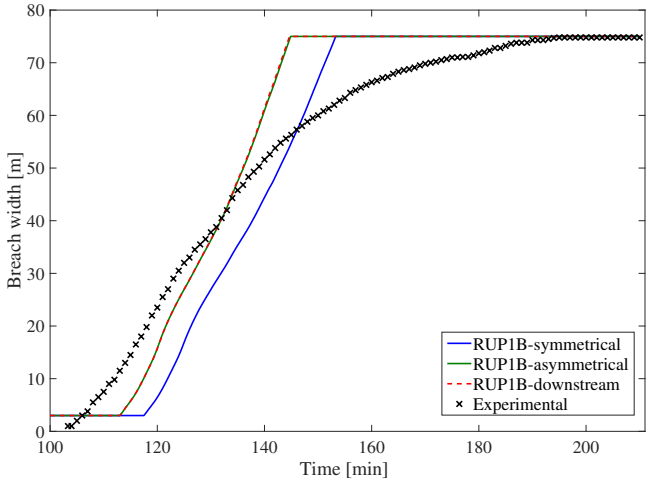

Figure 3.26: Influence of widening configuration on breach width of RUPRO Option 1, K_d= 80 (cm^3/(s Pa)).

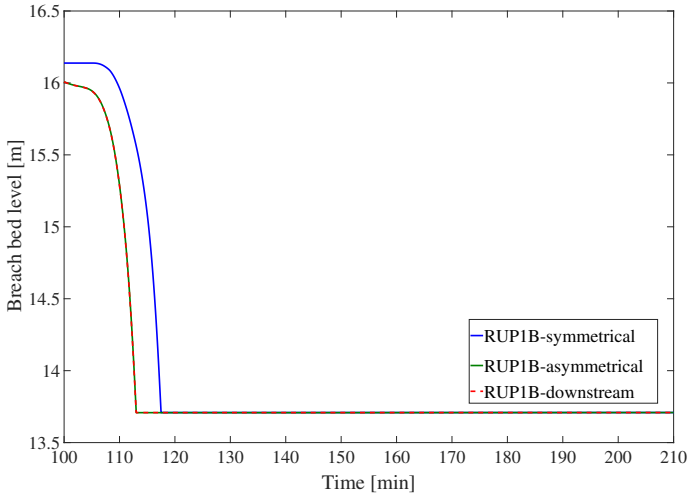

Figure 3.27: Influence of widening configuration on breach bed level of RUPRO model and K_d= 80 (cm^3/(s Pa)).

Figures 3.25, 3.26 and 3.27 highlight the impact of breach widening configuration on estimated breach hydrograph and dimensions. Unlike previous empirical breach models, different results were observed between symmetrical and non-symmetrical lateral breach opening with higher estimated breach dimensions and outflow discharge for the latter configuration. Therefore, the assumption of a symmetrical breach widening is questionable invalid for the RUPRO model. In addition, we performed a test using the simplification stating that breach widens only in the downstream direction "RUP1A-downstream", which resulted in equivalent results to the non-symmetrical configuration.

In the absence of information about the positions of breach extremities and ratios of upstream to downstream breach width, the results above state that assuming that the breach only expands downstream from the notch is a better approximation than the symmetrical widening. In the following sensitivity analysis we performed all tests with an asymmetrical breach widening.

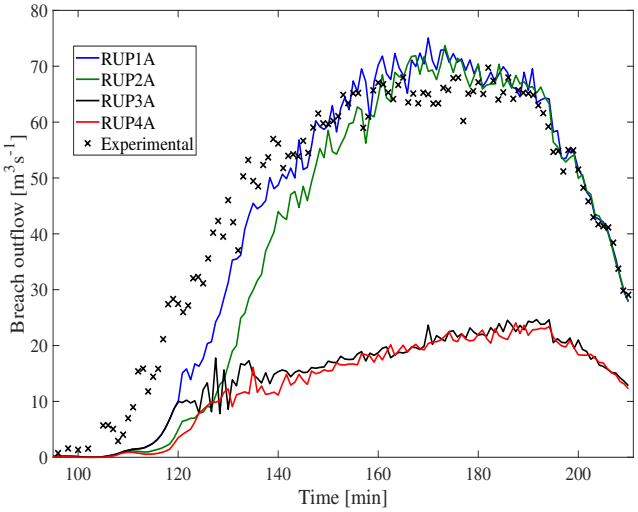

Figure 3.28: Comparison of computed breach discharge for different RUPRO model options and $K_d = 60$ (cm^3/(s Pa)).

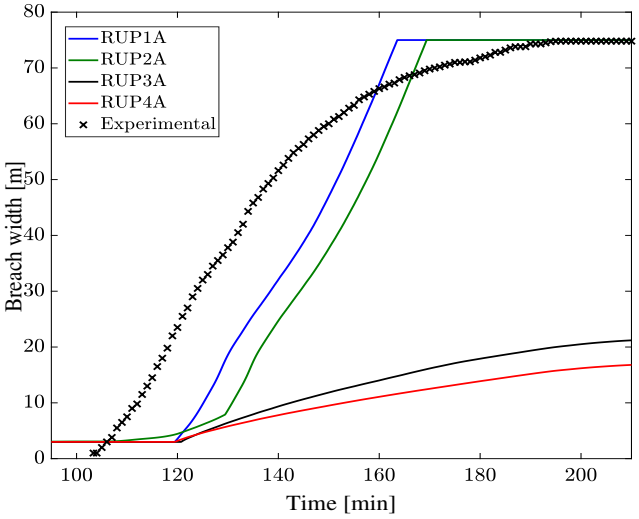

Figure 3.29: Comparison of computed breach width for different RUPRO model options and $K_d = 60$ (cm^3/(s Pa)).

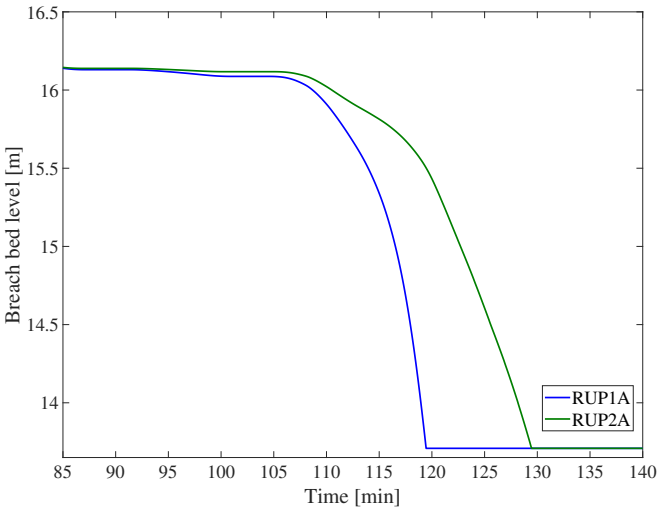

Figure 3.30: Comparison of computed bed level for different RUPRO model options and $K_d = 60$ (cm^3/(s Pa)).

The influence of the erodibility coefficient K_d was also investigated. Hanson et al. (2010) provided a table of erodibility coefficient values according to material compaction and clay fraction. Knowing that for Case 4, the levee only contained 4.4% of clay, K_d values range from 50 to 800 (cm^3/(s Pa)), increasing from highly compacted structures to embankments with low compaction. Here we vary the value of the erodibility coefficient K_d through numerical runs between 60 and 120 (cm^3/(s Pa)).

Figures 3.28, 3.29, 3.30, 3.31, 3.32, 3.33, 3.34, 3.35, 3.36, 3.37, 3.38 and 3.39 display the estimated breach discharge, width and bed level for different erodibility coefficients K_d values tested with the four different RUPRO model options presented in Section 4.2. For the sake of simplicity, breach bed level is not presented for options 3 and 4 since Step 2 (deepening step) was identical to that in option 1. All four options exhibit a critical sensitivity to the erodibility coefficient K_d; increasing this parameter shortens breach opening start time. It also leads to higher breach widening and deepening rates and thus increased breach discharge.

The results also highlight critical differences between the various model options. One can clearly state that applying a reduction of the wetted perimeter in option 3 or both reducing P_w and the lateral shear stress in option 4, during Step 3 induces under-estimated breach widths and outflow discharges. In addition, increasing the erodibility coefficient did not allow significant improvements in predictions of options 3 and 4.

Options 1 and 2 perform significantly better in estimating breaching start time, widening rate, and outflow discharge. However, allowing both vertical and lateral breach opening during Step 2 in option 2 led to lower widening and deepening rates than in option 1. In the latter option, assuming that the computed sediment discharges in Step 2 and Step 3 are independently eroded from the breach bottom surface and lateral walls resulted in higher erosion rates than option 2. With the latter option, the sediment discharge is split between the base and lateral faces of the breach resulting in lower erosion rates. Therefore, the breach deepens fast in Step 2 of option 1 and offers a more extensive section to convey breach discharge. The breach outflow discharge increases fast and induces a higher hydrodynamic forcing, resulting in higher sediment discharges and widening rates in Step 3.

Finally, the best fit is obtained with the original version of the RUPRO model and K_d = 80 (cm^3/(s Pa)), which combines low NRMSE values, a well-predicted initiation time, and a conservative prediction of breach discharge.

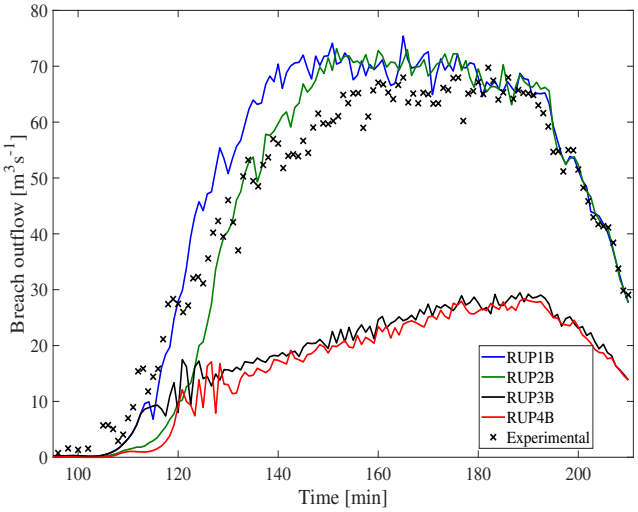

Figure 3.31: Comparison of computed breach discharge for different RUPRO model options and $K_d = 80$ (cm^3/(s Pa)).

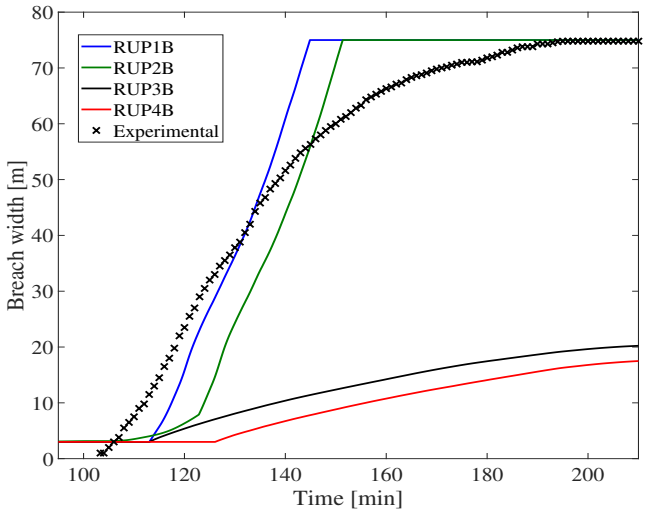

Figure 3.32: Comparison of computed breach width for different RUPRO model options and $K_d = 80$ (cm^3/(s Pa)).

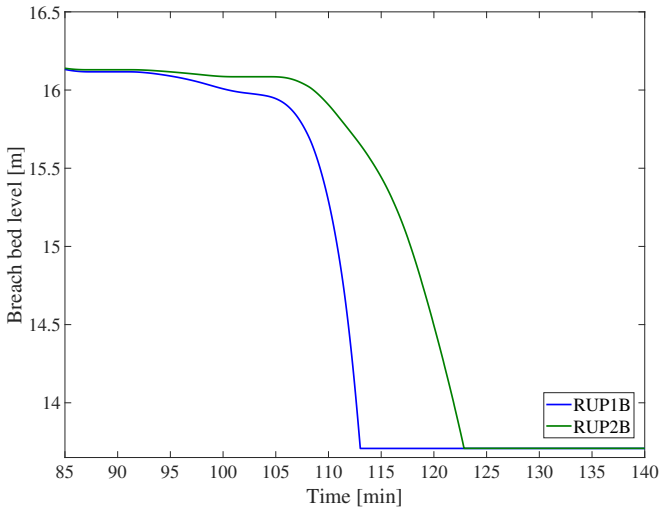

Figure 3.33: Comparison of computed bed level for different RUPRO model options and $K_d = 80$ (cm^3/(s Pa)).

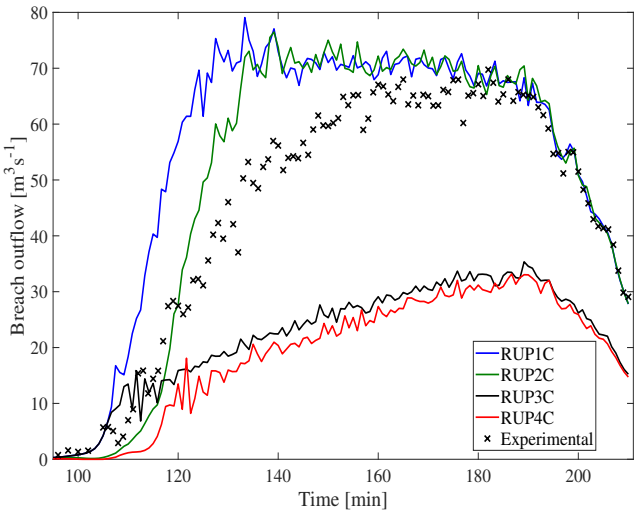

Figure 3.34: Comparison of computed breach discharge for different RUPRO model options for $K_d =$ 100 (cm^3/(s Pa)).

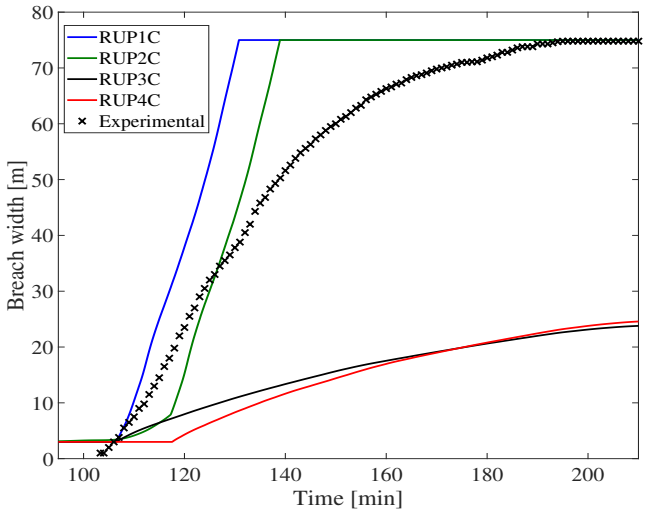

Figure 3.35: Comparison of computed breach width for different RUPRO model options and $K_d =$ 100 (cm^3/(s Pa)).

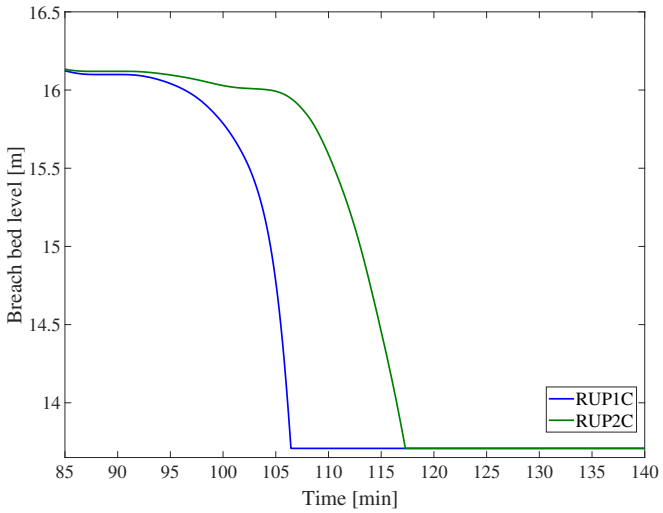

Figure 3.36: Comparison of computed breach width and bed level for different RUPRO model options and $K_d = 100$ (cm^3/(s Pa)).

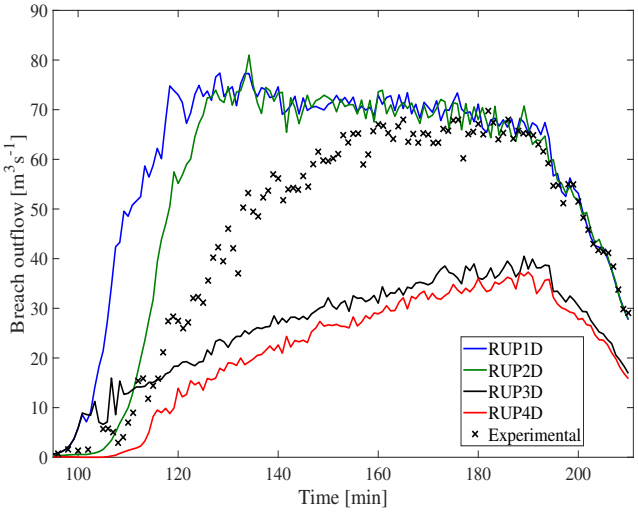

Figure 3.37: Comparison of the computed breach discharge for different RUPRO model options and $K_d = 120$ (cm^3/(s Pa)).

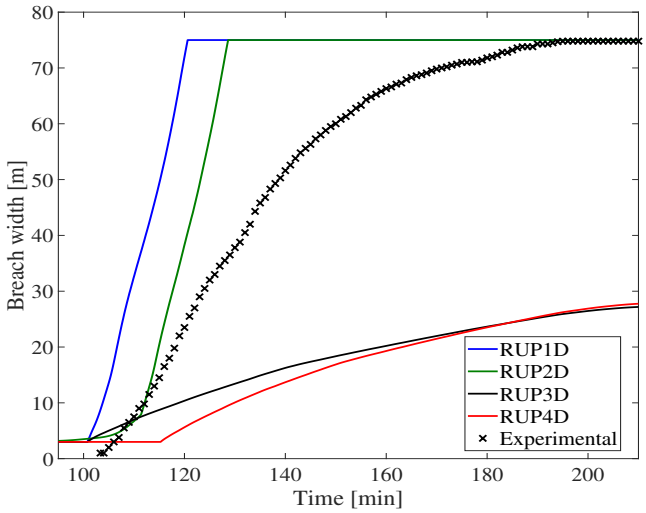

Figure 3.38: Comparison of computed breach width for different RUPRO model options and $K_d = 120$ (cm^3/(s Pa)).

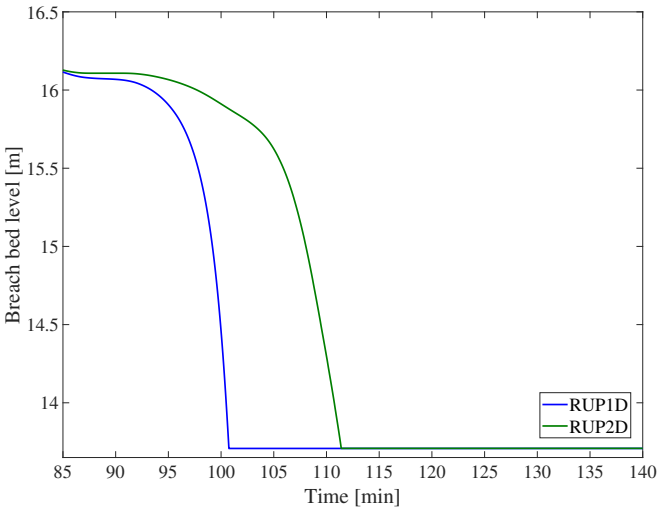

Figure 3.39: Comparison of computed breach bed level for different RUPRO model options and $K_d = 120$ (cm^3/(s Pa)).

The influence of the erodibility coefficient K_d was also investigated. Hanson et al. (2010) provided a table of erodibility coefficient values according to material compaction and clay fraction. Knowing that for Case 4, the levee only contained 4.4% of clay, K_d values range from 50 to 800 (cm^3/(s Pa)), increasing from highly compacted structures to embankments with low compaction. Here we vary the value of the erodibility coefficient K_d through numerical runs between 60 and 120 (cm^3/(s Pa)). Figures 3.28, 3.29, 3.30, 3.31, 3.32, 3.33, 3.34, 3.35, 3.36, 3.37, 3.38 and 3.39 display the estimated breach discharge, width and bed level for different erodibility coefficients K_d values tested with the four different RUPRO model options presented in Section 3.2.4. For the sake of simplicity breach, bed level is not presented for options 3 and 4 since Step 2 (deepening step) was identical to that in option 1. All four options exhibit a critical sensitivity to the erodibility coefficient K_d; increasing this parameter shortens breach opening start time. It also leads to higher breach widening and deepening rates and thus increased breach discharge.

The results also highlight critical differences between the various model options. One can clearly state that applying a reduction of the wetted perimeter in option 3 or both reducing P_w and the lateral shear stress in option 4, during Step 3 induces under-estimated breach widths and outflow discharges. In addition, increasing the erodibility coefficient did not allow significant improvements in predictions of options 3 and 4. Options 1 and 2 perform significantly better in estimating breaching start time, widening rate, and outflow discharge. However, allowing both vertical and lateral breach opening during Step 2 in option 2 led to lower widening and deepening rates than in option 1. In the latter option, assuming that the computed sediment discharges in Step 2 and Step 3 are independently eroded from the breach bottom surface and lateral walls resulted in higher erosion rates than option 2. With the latter option, the sediment discharge is split between the base and lateral faces of the breach resulting in lower erosion rates. Therefore, the breach deepens fast in Step 2 of option 1 and offers a more extensive section to convey breach discharge. The breach outflow discharge increases fast and induces a higher hydrodynamic forcing, resulting in higher sediment discharges and widening rates in Step 3. Finally, the best fit is obtained with the original version of the RUPRO model and K_d = 80 (cm^3/(s Pa)), which combines low NRMSE values, a well-predicted initiation time, and a conservative prediction of breach discharge.

3.4.2 Case 2

Simulations of experimental Case 4 provided interesting information about the different breach models and how their parameters can impact predicted breach characteristics. In this section simulations of the experimental Case 2 are presented including a sensitivity analysis to discuss the conclusions drawn from the analysis of the numerical predictions for the experimental Case 4.

The first series of simulations aimed to set the vertical erosion duration for models that only provide breach widening information and the configuration for breach widening (symmetrical or non-symmetrical). For that purpose, a constant lateral erosion rate (91 m/h according the the USBR (1988) formula) is used, the start time is defined at 41 min, initial breach width is set equal to the

notch top width (B_0 =3 m), and a final breach width of 30 m is predefined as a criterion to stop breach widening.

Figure 3.40 compares estimated breach discharge for a breach vertical opening duration T_d of 1 second (assuming a quasi-instantaneous breach deepening) and in the case of a T_f/T_d ratio equal to 10. One can see that only a slight difference is observed between the two simulations comforting observations in section 3.4.1.7. Therefore, a quasi-instantaneous breach vertical opening can be a good approximation, especially for empirical models requiring a user input vertical erosion duration.

In agreement with results for Case 4 presented in Section 3.4.1.6, Figure 3.41 confirms that the breach discharge predicted for a symmetrical breach widening is similar to that calculated in the case of an asymmetrical configuration for empirical breach equations. Although the symmetrical breach widening assumption did not impact breach discharge for simple empirical laws, the parametric analysis for Case 4 highlighted its apparent impact on the RUPRO model results. Therefore, an asymmetrical breach widening (7% upstream from the initial notch and 93% downstream) is considered for all models, including the RUPRO model. Thus, we set a quasi-instantaneous breach deepening in the simulations presented hereafter with the linear erosion laws, the Verheij (2002) model, and the Verheij and Van der Knaap (2003) model.

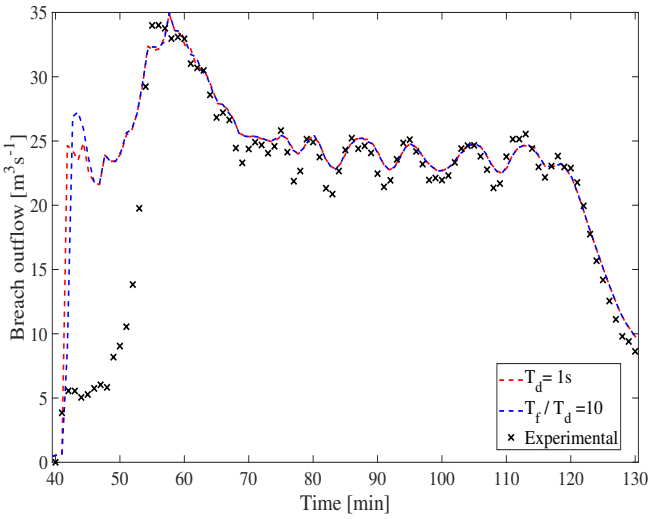

Figure 3.40: Influence of the vertical erosion rate on breach discharge (USBR (1988) formula).

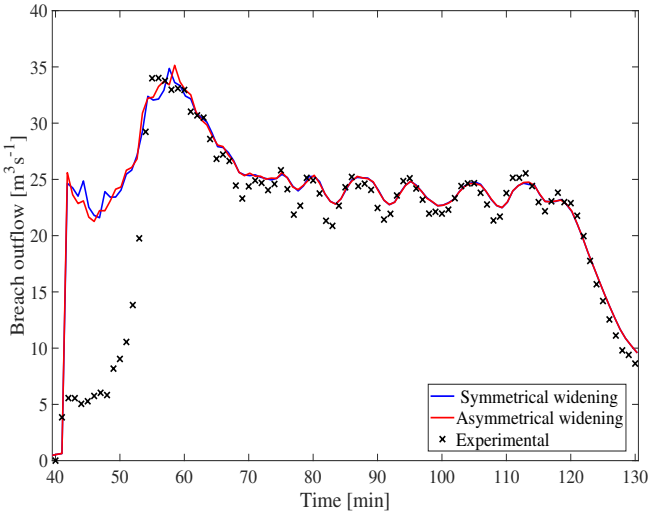

Figure 3.41: Influence of the lateral erosion configuration on breach discharge (USBR (1988) formula).

3.4.2.1 Linear widening rate

In this section we compare simulations of levee breach experiment Case 2 following a linear widening law and different erosion rates including the USBR (1988) model and Von Thun and Gillette (1990) model with h_w considered constant and set to its at the time of failure, as shown in Table 3.11.

Run	E_{W1} (m/hr)	E_{W2} (m/hr)	NRMSE breach width	NRMSE breach outflow
WL1	35	35	7.8%	14.3%
WL2	45	45	11.4%	14.8%
WL3	55	55	15.6%	15.4%
WLD	45	9	7.4%	14.8%
Von Thun and Gillette (1990)	Eq. 3.4	3.4	15.6%	11.9%
USBR (1988)	91	91	25.5%	17.1%

Table 3.11: Linear growth law simulation parameters of Case 2.

Figures 3.42 and 3.43 compares the numerical results with the observed time series of breach width and discharge. All tests predicted breach hydrographs with reasonable accuracy and NRMSE values ranging between 14% and 17%. However, a rapid increase in breach discharge, followed by a peak, was obtained in the numerical simulations while not observed in experiments. This artifact can be ascribed to the overestimated breach width in the early breaching stage. The peak in

the experimental breach hydrograph was captured in numerical simulations. The amplitude of the computed peak increases for runs with higher erosion rates.

One should note that, although breach width was overestimated in all runs (except run WL1), the amplitude of breach outflow peak is slightly underestimated for runs WL2, WL3, and WLD, probably due to the simplifying assumptions of the 2-D hydrodynamic model and precision of experimental measurements. Additionally, using a different widening rate during breach stage 2 results in a very similar breach hydrograph to that simulated with a single erosion rate for the whole duration of the breaching process.

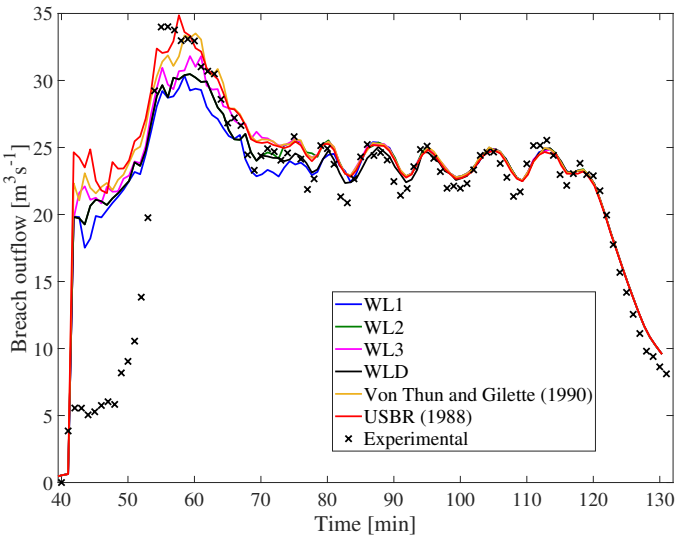

Figure 3.42: Comparison of computed breach discharges with linear erosion equations.

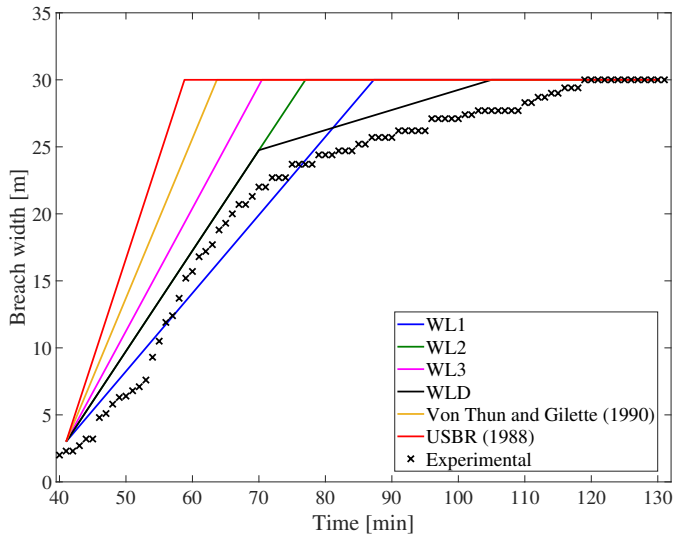

Figure 3.43: Comparison of computed breach widths with linear erosion equations.

3.4.2.2 Breach model by Verheij (2002)

In contrast to the observations made in Case 4, the Verheij (2002) model provided satisfactory predictions for Case 2 (Figures 3.44 and 3.45) with a NRMSE value on breach discharge of 17.8% and 21.3% on breach width. A first artificial peak was also observed in this simulation for breach discharge. It was higher than previous runs with the linear erosion models, which can be explained by a much higher computed breach width at the beginning of the process with the Verheij (2002) model.

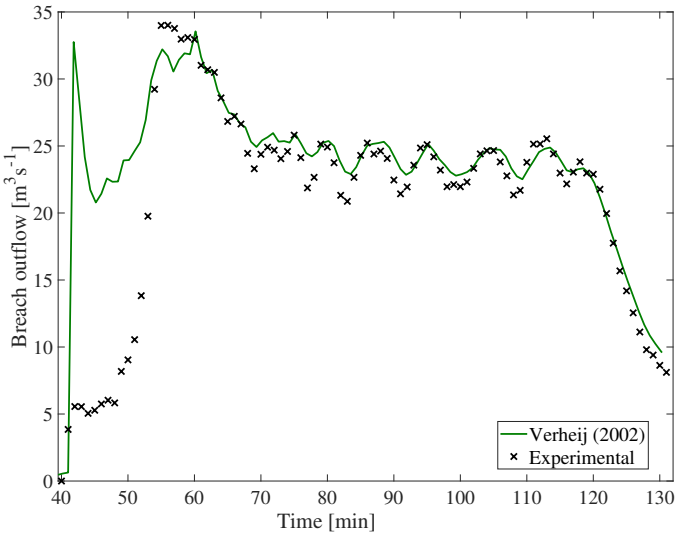

Figure 3.44: Comparison of measured and computed breach discharges with the Verheij (2002).

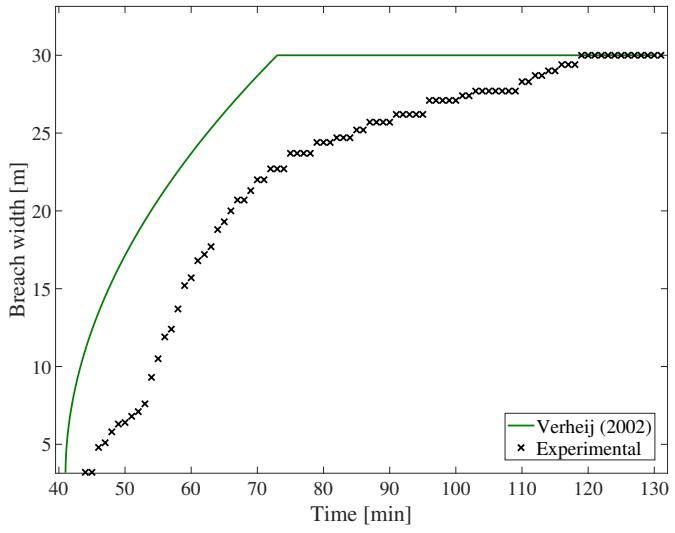

Figure 3.45: Comparison of measured and computed breach widths with the Verheij (2002).

3.4.2.3 Breach model by Verheij and Van der Knaap (2003)

Figures 3.46 and 3.47 compares the Verheij and Van der Knaap (2003) model simulations VR1 and VR2 with a difference in water level and water head, respectively. Recall that simulations for Case 4 showed a significant improvement when using the water head with respect to the original formulation with the water level. Surprisingly, the model behavior is similar for both configurations, with a slightly higher widening rate in run VR2. The difference observed between Case 4 and Case 2 could be explained by the low inflow discharge in Case 2 that results in lower velocities in the main channel. Therefore, the estimated breach width with the original version and the one using the hydraulic head were very similar in the first breaching stage. However, in the second stage, breach width was higher in run VR2 due to the flow acceleration in the main channel in the upstream and breach zones, as shown in experimental investigations resulting in higher hydraulic head values. As observed for the linear widening laws, the difference in breach width during the second breaching stage did not influence breach discharge.

Run	ΔH	f_1	f_2	u_c	NRMSE on breach width	NRMSE on breach outflow
VR1	Max $(h_{up} - h_{down})$	1.3	0.04	0.16	7.7%	16.2%
VR2	Max $(H_{up} - H_{down})$	1.3	0.04	0.16	9.3%	16.1%

Table 3.12: Case 2 simulation parameters with the Verheij and Van der Knaap (2003) formula.

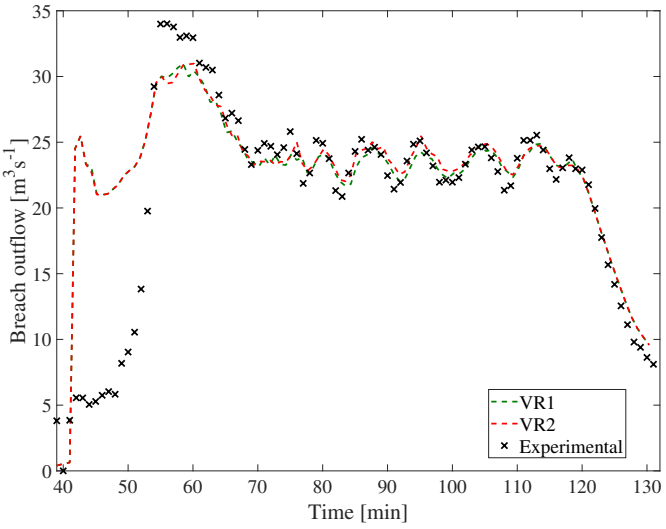

Figure 3.46: Comparison of computed breach discharges the Verheij and Van der Knaap (2003) formula.

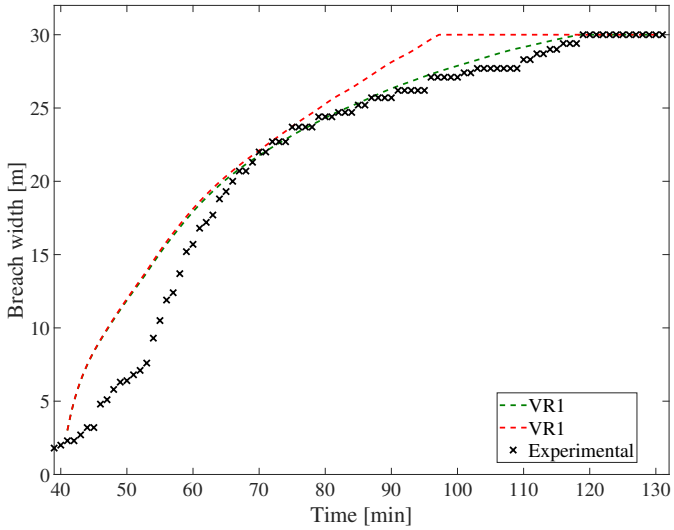

Figure 3.47: Comparison of computed breach widths the Verheij and Van der Knaap (2003) formula.

3.4.2.4 Breach model by Froehlichl (2008)

Simulation with the Froehlichl (2008) model included a first run with a lateral expansion period equal to that required for the breach to reach its ultimate width in the experiment (78 min after the initiation time) and a test with a reduced T_f of 50% as in Case 4, decreasing T_f by 50% achieved the best fit with measured breach width and discharge. A similar parametric analysis is performed for Case 2, the first run was performed using the duration observed in experiments, then in the second run we decreased T_f by 50% as shown in Table 3.13.

T_f (min)	NRMSE on breach width	NRMSE on breach outflow
78	20.4%	12%
39	10.8%	10.4%

Table 3.13: Case 2 simulation parameters with the Froehlich (2008) model and resulting NRMSE values.

Figures 3.48 and 3.49 display the dependence between estimated breach parameters and the parameter T_f of the Froehlich (2008) model. Decreasing the experimental value of T_f by 50% appears to be necessary as for Case 4 to achieve reasonable predictions. One can also note that the first artificial peak in breach discharge observed with previous empirical models is significantly reduced with the Froehlich (2008) model and T_f=39 minutes that offers a better fit between computed and measured breach width in the first stage of levee breaching.

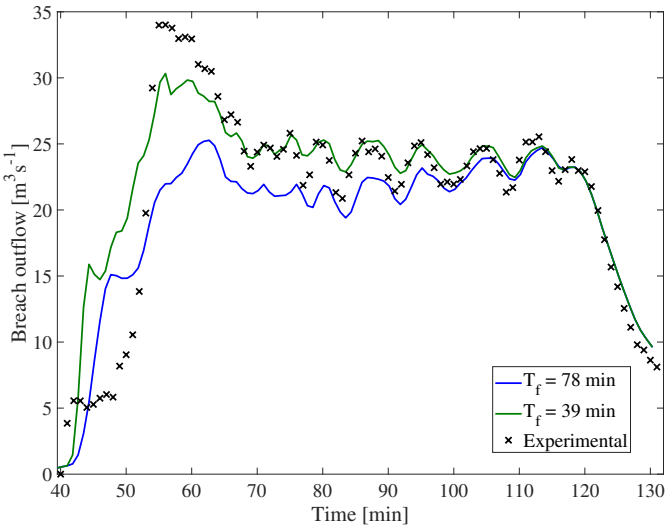

Figure 3.48: Comparison of computed breach discharges with Froehlich (2008) model for different T_f values.

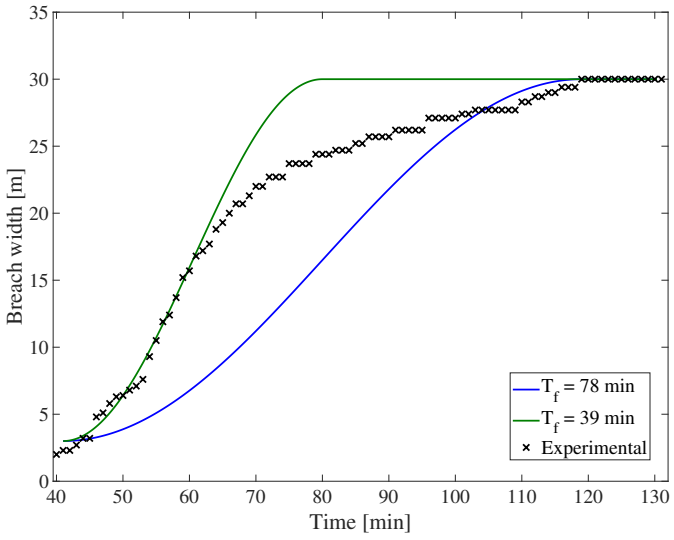

Figure 3.49: Comparison of computed breach widths with Froehlich (2008) model for different T_f values.

3.4.2.5 RUPRO model

The different numerical tests performed for Case 2 with the RUPRO model are summarized in Table 3.14. Both the influences of the erodibility coefficients and RUPRO model options are investigated. In Case 2 the clay content of the levee was similar to Case 4 and represented a fraction of 4.4%. Therefore, equal erodibility coefficient K_d values were tested for both cases, ranging from 60 and 120 (cm^3/(s Pa)). Breach widening was considered asymmetrical with 3% of the total width distributed

upstream from the initial notch and 97% downstream.

Run	K_d (cm^3/(s Pa))	Option	NRMSE on breach discharge	NRMSE on breach width
RUP1A	60	1	11.5%	12.2%
RUP1B	80	1	14.9%	26.8%
RUP1C	100	1	17.1%	30.7%
RUP1D	120	1	18.2%	33.6%
RUP2A	60	2	7.2%	17.6%
RUP2B	80	3	12.1%	24.1%
RUP2C	100	4	15%	28.5%
RUP2D	120	4	17.2%	31.7%
RUP3A	60	2	11.5%	32.9%
RUP3B	80	3	13.1%	25.7%
RUP3C	100	3	14.4%	20.3%
RUP3D	120	4	14.7%	16.1%
RUP4A	60	2	11.2%	29.3%
RUP4B	80	3	12.8%	21.6%
RUP4C	100	3	14%	15.8 %
RUP4D	120	4	14.6%	11.7%

Table 3.14: Case 2 simulation parameters for different options of the RUPRO model and resulting NRMSE values .

Figures 3.50, 3.51, 3.52, 3.53, 3.54, 3.55, 3.56, 3.57, 3.58, 3.59, 3.60 and 3.61 present the resulting breach discharge, width and bed level for the different options of the RUPRO model and varying erodibility coefficients K_d values. As explained for Case 4, breach bed level is not presented for options 3 and 4 since Step 2 (deepening step) was identical to that in option 1. Looking at the results, we first observe that breach width and depth are very sensitive to the RUPRO model options and erodibility coefficient K_d values while breach discharge is less impacted and remains reasonably estimated. Figures of breach discharge also confirm that first artificial peak observed in some numerical results is due to the overestimated breach width at the beginning of the failure process. As observed for Case 4 options 1 and 2 tend to overestimate breach width while it is rather underestimated in options 3 and 4 with the reduction of the wetted perimeter P_w and the lateral shear stress during Step 3. However, breach width values remain closer to the measured values while the results differed strongly for Case 4 with options 3 and 4. An explanation may be that the breach base and lateral walls surface is lower for Case 2 in which levee dimensions were different from that of Case 4, so the reduction of the wetted perimeter had a limited impact. Finally, options 1 and 2 predicted more conservative breach discharge values and the best estimations were obtained with the original version of the RUPRO model and K_d = 80 (cm^3/(s Pa)), which combines low NRMSE values, a well-predicted initiation time, and a conservative prediction of breach discharge.

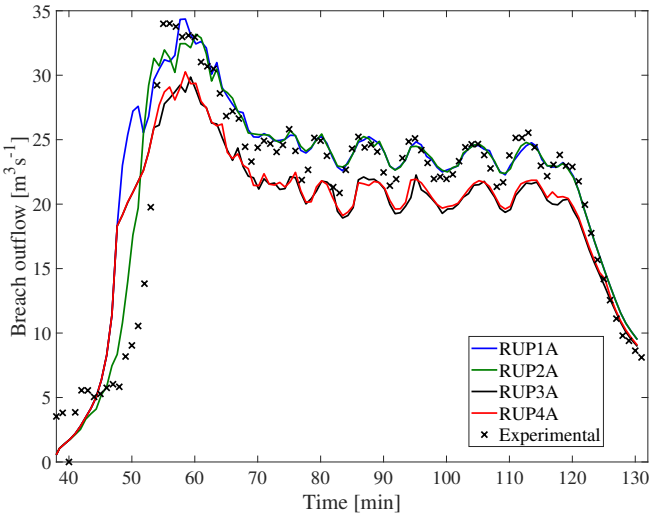

Figure 3.50: Comparison of computed breach discharge for different RUPRO model options for $K_d = 60$ (cm^3/(s Pa)) (Case 2).

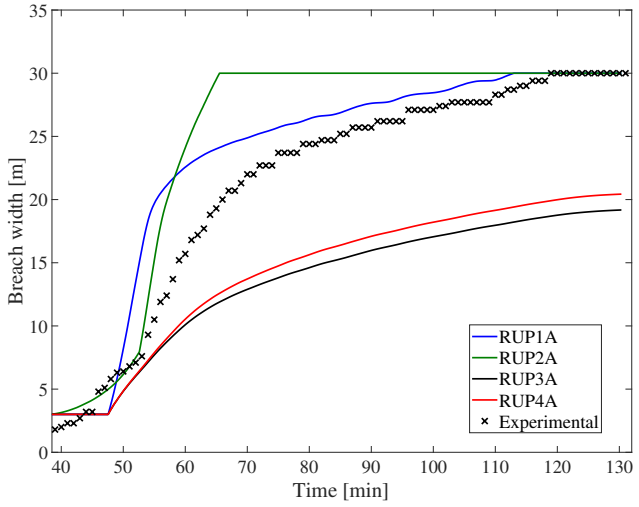

Figure 3.51: Comparison of computed breach width for different RUPRO model options for $K_d = 60$ (cm^3/(s Pa)) (Case 2).

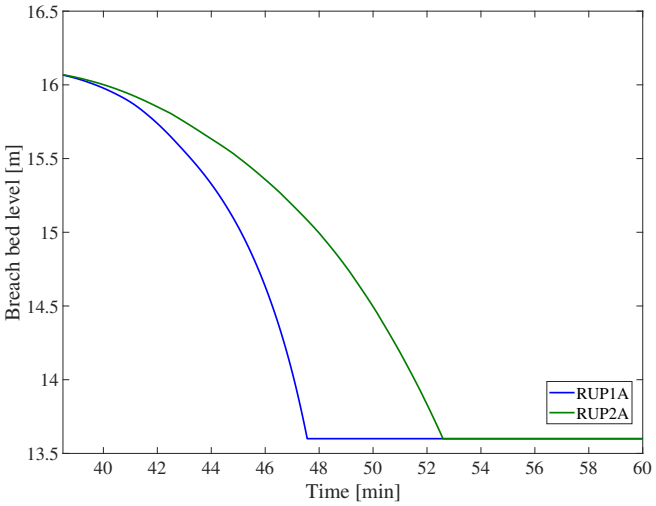

Figure 3.52: Comparison of computed breach bed level for different RUPRO model options for $K_d = 60$ (cm^3/(s Pa)) (Case 2).

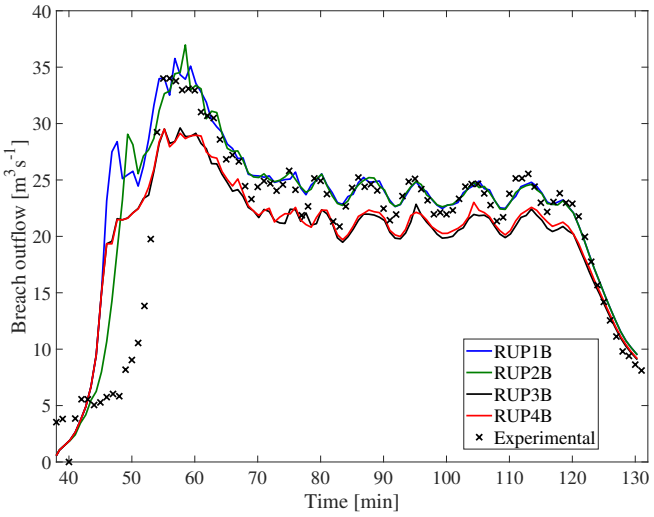

Figure 3.53: Comparison of computed breach discharge for different RUPRO model options for $K_d = 80$ (cm^3/(s Pa)) (Case 2).

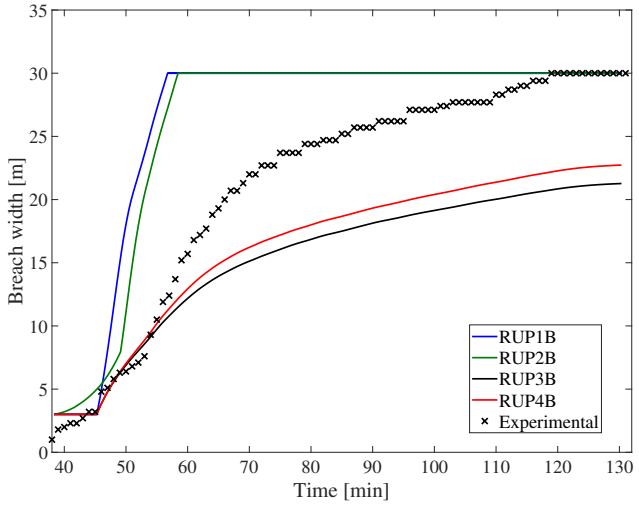

Figure 3.54: Comparison of computed breach width for different RUPRO model options for $K_d = 80$ (cm^3/(s Pa)) (Case 2).

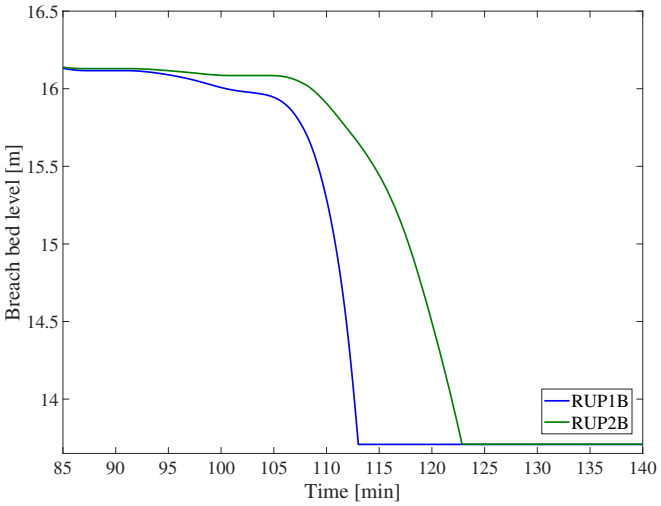

Figure 3.55: Comparison of computed breach bed level for different RUPRO model options for $K_d = 80$ (cm^3/(s Pa)) (Case 2).

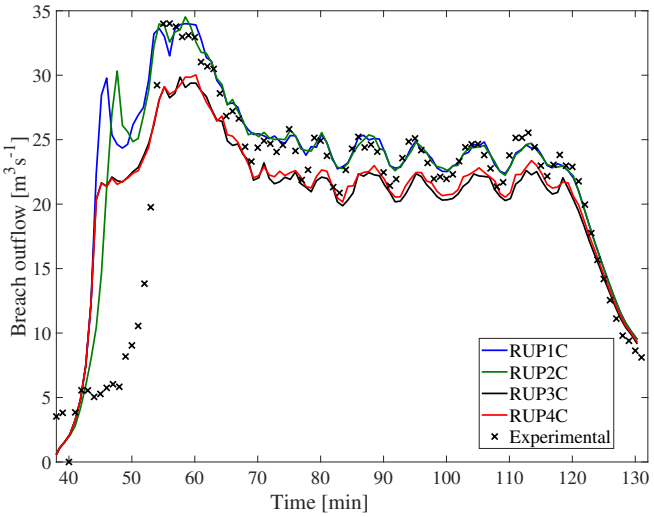

Figure 3.56: Comparison of computed breach discharge for different RUPRO model options for $K_d =$ 100 (cm^3/(s Pa)) (Case 2).

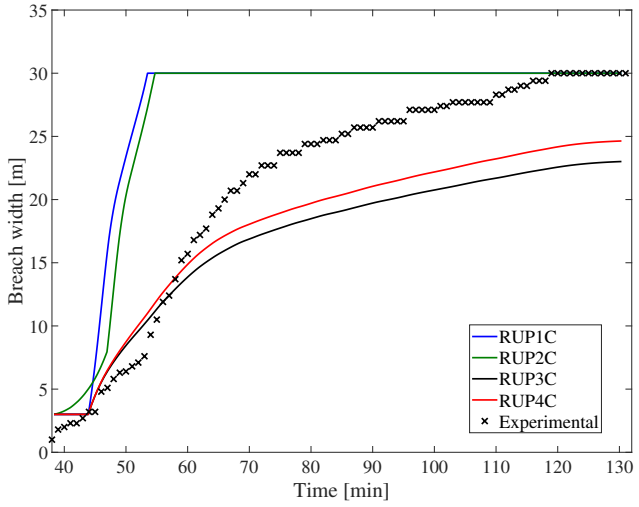

Figure 3.57: Comparison of computed breach width for different RUPRO model options for $K_d =$ 100 (cm^3/(s Pa)) (Case 2).

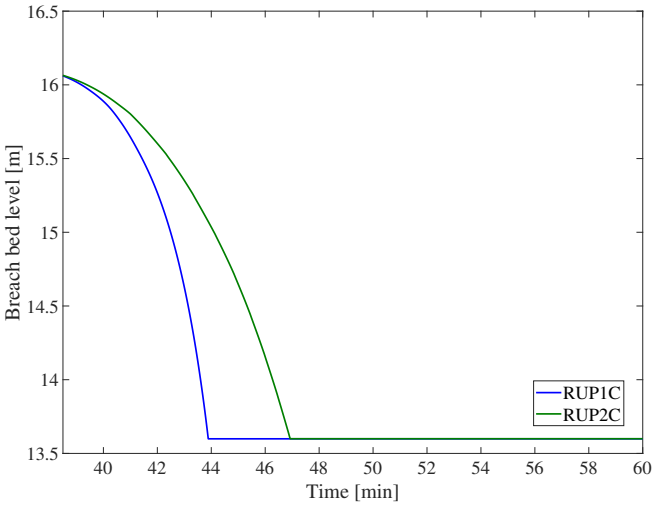

Figure 3.58: Comparison of computed breach bed level for different RUPRO model options for $K_d =$ 100 (cm^3/(s Pa)) (Case 2).

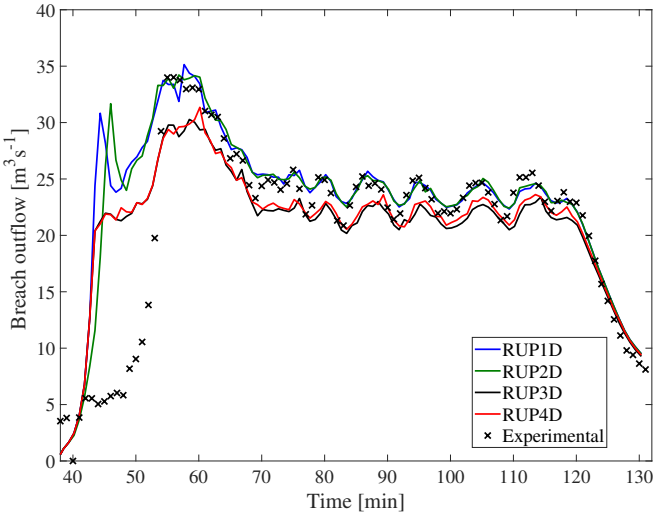

Figure 3.59: Comparison of computed breach discharge for different RUPRO model options for $K_d = 120$ (cm^3/(s Pa)).

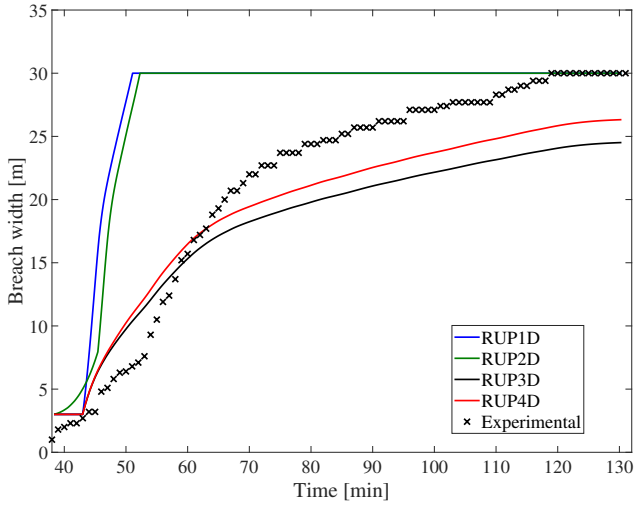

Figure 3.60: Comparison of computed breach width and bed level for different RUPRO model options for $K_d = 120$ (cm^3/(s Pa)).

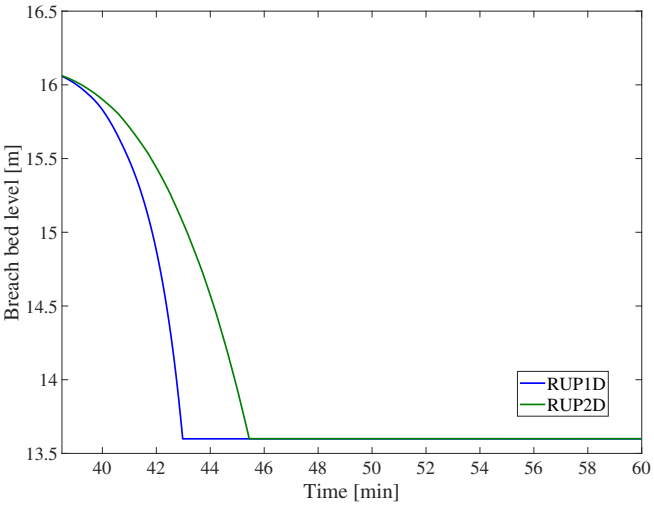

Figure 3.61: Comparison of computed breach bed level for different RUPRO model options for $K_d = 120$ (cm^3/(s Pa)).

3.5 Discussion

In section 3.4 an extensive analysis of the simplified breach models was performed and provided important insights about their capabilities to capture breach characteristics and the impact of their input parameters and assumptions on results accuracy.

The first part of the simulations focused on the effect of user-input erosion rates in the simple time-dependent linear breach model. Results highlighted model capabilities to predict breach discharge correctly when the user defines appropriate erosion rates. Although such information is not straightforward, some indications from the literature and historical levee failure cases can help identify the adequate range of breach opening rates.

Furthermore, simulation with two different phases of breach widening required an additional user-input erosion rate for the second stage. Still, it did not have a significant impact on breach discharge results. The second set of simulations addressed some questions regarding the definition of the hydrodynamic variable h_w in Von Thun and Gillette (1990) model for levee breach cases: both original formulation and adjusted ones managed to predict accurate and conservative breach discharge. It was also observed that the Verheij (2002) model results were differently appreciated for Case 4 and Case 2. In experimental Case 4, characterized by a higher main channel inflow discharge, breach width and outflow were significantly underestimated by the Verheij (2002) model. At the same time, the breach outflow was well predicted for Case 2. This highlights an explicit limitation of simple empirical breach models that do not account for the hydrodynamic forces that play a significant role in breach dynamics. Then, simulations with the modified version Verheij and Van der Knaap (2003) model using maximum hydraulic head difference performed better than the original formulation using water level difference on the simulated Case 4. While in Case 2, with lower flow velocities in the main channel, no significant improvement was observed with the new version. This model is an interesting option for levee breach modeling. It only requires a few input parameters, and it is not necessary to specify final breach width or widening duration, *a priori* as a natural balance can arise. However, a breach initiation criterion is still required to run this model, and the empirical parameters u_c, f_1, and f_2 can be calibrated to improve model predictions. When poor information is available about breach initiation, dimensions, and lateral expansion duration process, the RUPRO model is the most predictive and less user-dependent breach model as it is not mandatory to define the latter parameters. The model correctly captured breach start time while breach width was generally overestimated with options 1 and 2 and underestimated with options 3 and 4. The appreciations of model options performances differed between Case 4 and Case 2 as the levee geometry and main channel inflow were different in both cases. Additionally, we performed simulation with the option 1 of the RUPRO model using the Meyer-Peter and Müller (1948) formula for sediment discharge estimation but the optimal values of the coefficient α to get correct predictions of breach width and discharge, were much higher than conventional values used in hydro-morphodynamic models and conventional values of 8, 12 or 18 fell short to capture breach characteristics as shown in Figures 3.62, 3.63, 3.64 and 3.65. Among the tested values for α a value

of 100 and 18 best predicted breach width and discharge for Case 4 and Case 2, respectively.

It has been shown in Section 3.4.1.6 that the assumption of a symmetrical breach widening did not modify the computed breach discharge in comparison to tests with a non-symmetrical breach widening. However, assuming a symmetrical breach widening impacts the simulated breach location with respect to protected areas in the floodplain. Breach symmetry is expected to significantly impact flood risk assessment studies as shown by Tadesse and Fröhle (2020) for the 1996 levee breach flood event of Awash River at Wonji, Ethiopia. Additionally, the resulting breach outflow and dimensions from the RUPRO model were much higher in the case of an asymmetrical breach which is not surprising as breach dimensions were estimated from the sediment discharge directly linked to hydrodynamic forces through the excess shear stress equation. On the other hand, assuming a non-symmetrical breach widening implies the user to provide additional information quantifying the upstream and downstream breach portions. Wu et al. (2017) performed overtopping induced levee breach experiments in a U-bend flume and quantified the non-symmetrical breach lateral development with a coefficient representing breach downstream width to breach upstream width ratios. Coefficients of about 2.2–2.6 were estimated for non-cohesive levees and 2.7–3.3 for cohesive levees. However, field-scale experiments in a linear river channel by Kakinuma et al. (2013) showed coefficients of about 6.7-25.7. Zomorodi (2020) stated that for the sake of simplicity, one might also consider that the breach only expands in the downstream direction. Therefore, we performed additional simulations with the RUPRO model, where the breach only widens in the downstream direction. Indeed, the latter assumption provided similar results to the ones obtained with the non-symmetrical configuration without the need to define breach downstream width to breach upstream width ratios.

Regarding the empirical breach models that do not include a vertical erosion rate, it has been shown that a reasonable linear erosion duration could be defined within the very early breaching stage. Otherwise, the assumption of a quasi-instantaneous breach deepening can be used as a good simplifying approximation.

Fluvial dike breaches are generally observed with a trapezoidal-like longitudinal profile induced by material erosion by the water flow through the breach channel and failure of unstable sediment blocks. However, the longitudinal breach section is generally assumed rectangular in simplified breach models as levees are much longer than deeper this assumption does not significantly impact the breach section area as mentioned by Zomorodi (2020). The simulations presented in Section 3.4 with the Froehlich (2008) breach model were performed with a quasi-trapezoidal longitudinal breach section. However, the influence of breach section shape was not discussed since different erosion rates were used in the latter model compared to tests with a rectangular breach section. We perform simulations to verify the sensitivity of the estimated breach outflow to the shape of the breach longitudinal profile with fixed lateral and vertical erosion rates using the USBR (1988) formula. The results for a classical rectangular breach section and a trapezoidal-like section (as used for the Froehlichl (2008) model) are compared. Figures 3.66 and 3.67 show the evolution of breach discharge for both rectangular and trapezoidal breach longitudinal sections in cases 4 and

2, respectively. The results are very similar in both configurations for Case 4, characterized by an extensive breach. In contrast, breach section shape significantly impacted results in Case 2 with a relatively small breach width. One can conclude that the breach section shape has a greater impact in cases with small breach widths while it seems not to influence large breaches.

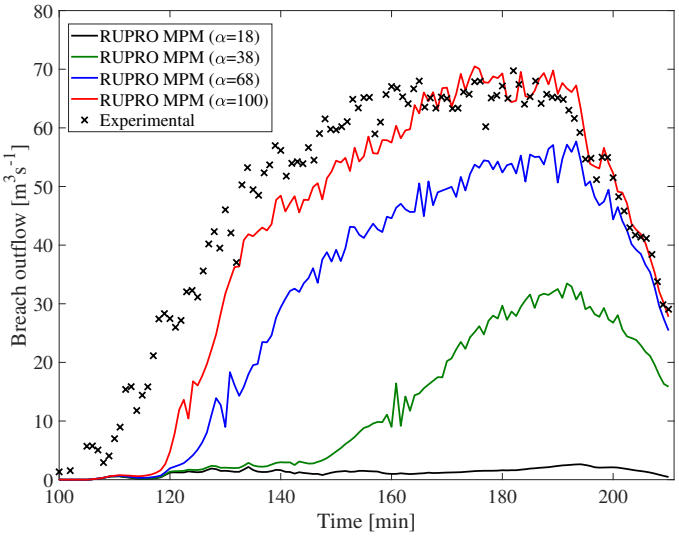

Figure 3.62: Comparison of computed breach discharge for different values of α in Case 2.

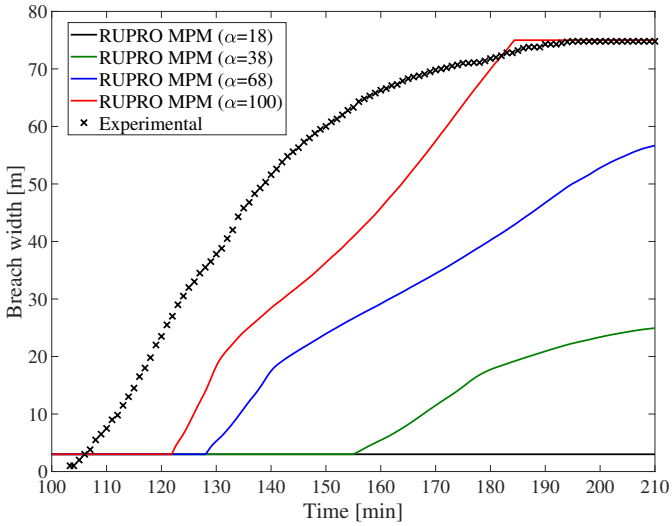

Figure 3.63: Comparison of computed breach width for different values of α in Case 4.

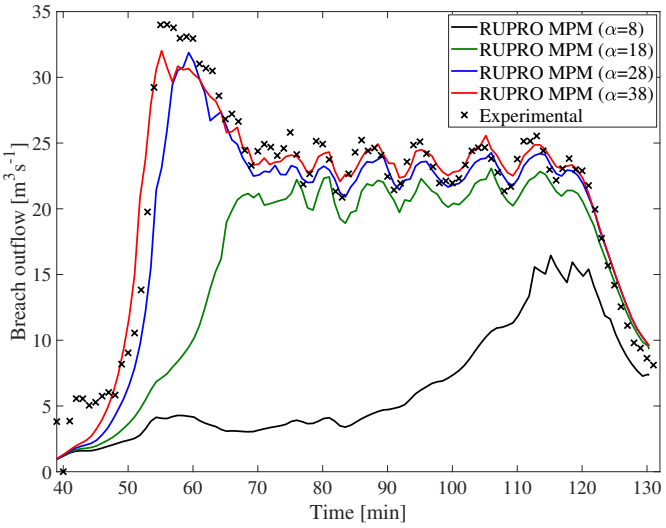

Figure 3.64: Comparison of computed breach discharge for different values of α in Case 2.

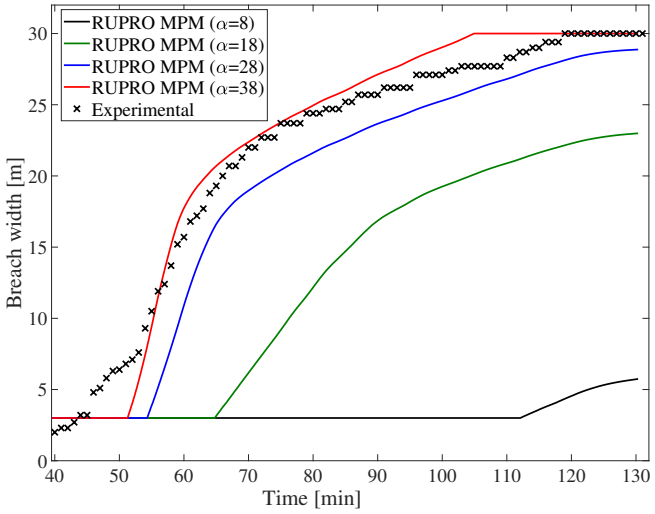

Figure 3.65: Comparison of computed breach width for different values of α in Case 2.

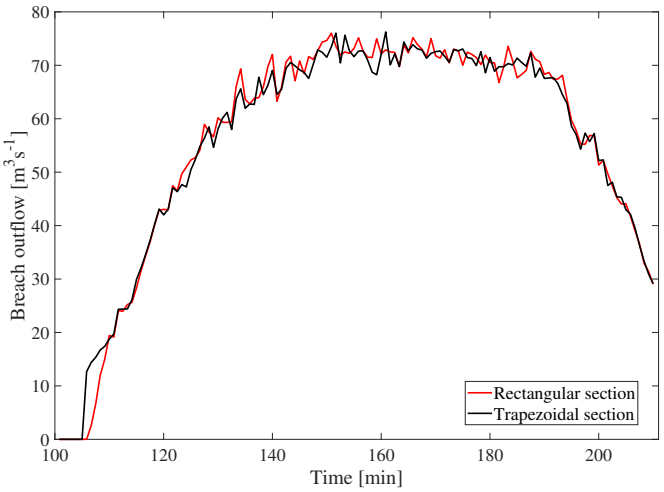

Figure 3.66: Influence of the longitudinal breach section shape on breach discharge for Case 4 (USBR (1988) formula).

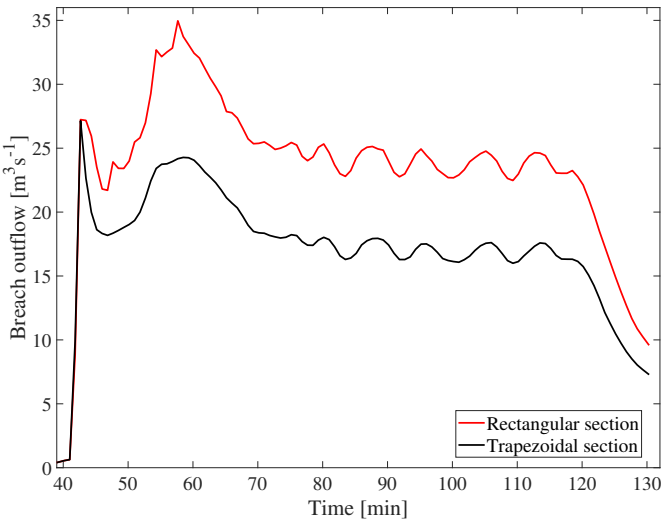

Figure 3.67: Influence of the longitudinal breach section shape on breach discharge for Case 2 (USBR (1988) formula).

3.6 Conclusion

In this Chapter, a set of parametric equations describing breach expansion and the RUPRO breach model were presented and implemented in the breach module of TELEMAC-2D. Numerical simulations of side-overflow levee failure field experiments were conducted to assess the performances and usability of the newly integrated breach models in TELEMAC-2D. The simplified modeling approach with asymmetrical breach widening and idealized breach longitudinal sectional profile (rectangular or trapezoidal shape) have been shown to predict consistent breach features with experimental data (breach dynamics and discharge). Table 3.15 summarizes the different breach models required user input parameters. Most tested breach models performed well during the breach formation stage and better during the quasi-stabilization stage provided they were well-calibrated. Finally, the analysis of various simple breach models provided the following primary outcomes :

- Parametric models are simple and time-efficient but include numerous assumptions for breach initiation, shape, and dimensions. The user expertise is essential to correctly choose the adequate breach model and set reasonable input parameters accounting for the simulated site specifications.
- Although some breach models underestimated breach width in the second stage, they provided reasonable estimations of breach outflow. Experimental investigations could explain this trend, which reported a dead water area formation at the upstream end of the breach. Thus, breach outflow is only conveyed through the downstream part of the breach section.
- For the studied parametric models, breach characteristics were directly influenced by user-

defined parameters such as the erosion rate for the simple linear widening formula or the empirical factors f_1, f_2 and u_c for the Verheij and Van der Knaap (2003) model. At the same time, it was less sensitive to breach asymmetry and vertical erosion duration as long it remained in a reasonable range within the very early breaching stage.

- The use of the original RUPRO model and its modified version within the IMPACT project provided satisfactory results for both tested cases. At the same time, option 3 with the reduced wetted perimeter in Step 3 and option 4 with the reduced lateral shear stress perform differently for different levee geometries and main channel inflow discharges.
- The asymmetry of lateral breach expansion significantly influenced the breach hydrograph and dimensions with the RUPRO model while assuming an exclusive widening in the downstream direction resulted in very similar results with asymmetrical configuration.
- The Verheij and Van der Knaap (2003) does not require information about the final breach width or widening duration. In addition, using the hydraulic head instead of the water level allows better prediction for cases with high main channel inflow discharge.
- The RUPRO model is the most predictive and less user-dependent breach model as there is no need to define an initiation criterion or a direct breach widening rate, and breach final width is not necessary.However, a good calibration of the erodibility coefficient K_d or the dimensionless coefficient α remains necessary.

Breach model	Start criterion	B_f or T_f	Other
Linear	YES	YES	NO
Two stages	YES	YES	NO
Von Thun and Gillette (1990)	YES	YES	NO
Verheij (2002)	YES	YES	NO
Verheij and Van der Knaap (2003)	YES	NOT NECESSARY	f_1, f_2, u_c
Froehlich (2008)	YES	YES	NO
RUPRO	NO	NOT NECESSARY	K_d / α

Table 3.15: Breach models required input parameters.

Chapter 4

Detailed physically-based approach for side-overflow levee breaching

La modélisation numérique détaillée de la rupture de digues fluviales est un sujet en plein développement et les modèles hydro-morphodynamiques bidimensionnels ont fait l'objet de nombreux progrès. Dans ce chapitre, le module hydrodynamique TELEMAC-2D est couplé au module morphodynamique SISYPHE/GAIA du système TELEMAC-MASCARET pour simuler des expériences de rupture de digues fluviales à échelles de laboratoire et de terrain. Le module de rupture de pente est amélioré afin de tenir compte de différents angles de repos des sédiments et de nouvelles formules pour le transport de sédiment par charriage ont été implémentées et testées. Les résultats des différentes simulations reproduisent de façon satisfaisante les caractéristiques de la brèche. Une analyse de sensibilité met également en évidence l'importance du calage des différents paramètres du modèle nécessaire pour améliorer la qualité des résultats.

4.1 Introduction

Understanding and predicting levee breach-induced floods is essential due to their potential human, environmental and economic damages. The different causes and mechanisms of fluvial dike breaching were detailed in Chapter 1. The literature review also highlighted a higher frequency of levee failure cases resulting from overtopping. Over the past few decades, significant advances have been made in research on levee breaching that differs from frontal embankment breaching (Elalfy et al. (2018), Islam (2012), Kakinuma et al. (2013), Michelazzo (2014), Rifai et al. (2017a)). Levee breaching under overtopping conditions involves complex interactions between the flow field, dike material, and geotechnical aspects. This results in complex physical processes, including different flow regimes (subcritical, critical, supercritical), surface erosion and sediment transport, sediment failure due to slope instability, and other effects depending on the embankment composition and site specifications. Parametric and simplified physically-based models do not explicitly compute breach morphodynamics (Chapter 1), while most hydrodynamic and sediment transport processes are implemented in detailed physically based models. In general, two-dimensional models solve the Shallow Water equations for the flow field and the Exner equation for bed morphodynamics. Only a few studies included suspended load transport (Wang and Bowles (2006), Chinnarasri et al. (2003)) as it is usually negligible for embankment failure application while bedload transport capacity is estimated using common formula such as the Meyer-Peter and Müller (1948) equation validated for laboratory experiments with bed slopes that do not exceed 2.4% and sediments of median diameters ranging from 0.4 to 29 mm, the Ashida and Michiue (1972) equation widely user in Japan, and Smart (1984) equations validated for steep bed slopes (that do not exceed 20%) and sediments of median diameters ranging from 2 to 10.5 mm. This is questionable as these empirical formulas were used for complex configurations like levee failure, including highly transient flow and steep bed slopes. However, their use can provide a reasonable representation of breach expansion in fluvial dikes induced by flow overtopping (Kakinuma and Shimizu (2014),Volz et al. (2017), Dazzi et al. (2019), Elalfy et al. (2018)). Another option consists in using the excess shear stress equation (Walder and O'Connor (1997)) to estimate the material erosion rate. Dazzi et al. (2019) compared the results of the bedload transport formula by Smart (1984) and that estimated with the linear excess shear stress equation. Results highlighted that both models' performances were equivalent, provided they are well calibrated. Some models also integrate the failure of unstable material by geometric methods with stability criteria based on sediment repose angles. However, the use of detailed physically-based models is still limited as they require further validation.

The main objective of this chapter is to investigate the performance of a detailed physically based modeling approach to predict overtopping induced breaching. This approach couples the hydrodynamic and morphodynamic components of the TELEMAC-MASCARET system TELEMAC-2D and SISYPHE/GAIA, respectively, to model interactions between hydrodynamics, sediment transport, and bank stability (El Kadi Abderrezzak et al. (2016)). The two-dimensional hydrodynamic module TELEMAC-2D solves shallow water equations using finite volume or finite element methods. The

morphodynamic module SISYPHE/GAIA is used, considering only bed load transport. It computes bed evolution by solving Exner's sediment continuity equation (Exner (1920)). Various equations are available to compute sediment flux; additional formulations were implemented and tested in the context of this thesis. The model incorporates a bank failure operator that we modified to account for three different repose angles ϕ_{wet}, ϕ_{dry} and ϕ_{dep} for submerged, emerged, and deposited sediments, respectively. Sediment transport magnitude and direction corrections for the bed slope effect and bottom shear stress direction correction for the secondary current effect are also available. The model is applied to simulate non-cohesive fluvial dike breaching induced by overtopping flows. A laboratory experiment conducted by Rifai et al. (2019) and two field scale experiments of levee failure due to overtopping presented by Kakinuma et al. (2013) were simulated. The numerical results are compared against measured breach outflow and water and reliable time-resolved, 3-D measurements of the evolving breach topography. A sensitivity analysis is carried out to highlight the most influencing parameters.

The chapter is organized as follows. Section 4.2 briefly describes the 2D hydro-morphodynamic model. The laboratory and field scale experiments are described in Section 4.3. The results of the simulations are presented in Sections 4.4, 4.5, and 4.6. In Section 4.7, an overall discussion is given followed by concluding remarks in Section 4.8.

4.2 Model description

4.2.1 Hydrodynamic component

To compute flow characteristics we use the hydrodynamic module TELEMAC-2D from TELEMAC-MASCARET system. It solves the two-dimensional Saint-Venant equations as described in Section 3.2.

4.2.2 Morphodynamic component

The morphodynamic module SISYPHE/GAIA simulates sediment transport (bedload and suspended load) and bed morphodynamics. It is based on the two-dimensional continuity equation of sediments; Exner equation (Exner, 1920) written hereafter in the case of bedload transport only, under quasi equilibrium flow conditions:

$$(1-p)\frac{\partial z_b}{\partial t} + \frac{\partial q_x}{\partial x} + \frac{\partial q_y}{\partial y} = 0 \tag{4.1}$$

with p bed porosity, z_b the bed elevation in (m) and q_x and q_y are bed load transport rates per unit width (m^2/s) in the x and y directions, respectively.

4.2.2.1 Equations for bedload transport

After solving the flow field equations, the sediment transport is estimated to compute the morphodynamic changes in the bed (Eq. 4.1). The morphodynamic module SISYPHE/GAIA incorporates the most commonly-used sediment transport equations to calculate the bedload transport rate relying on the Shields criterion for incipient motion, such as the Meyer-Peter and Müller (1948) formula (Eq. 4.2). In this research work, we implemented Ashida and Michiue (1972) (Eq. 4.3) and Smart (1984) (Eq. 4.4) bedload equations that were used in the literature to simulate embankment breaching (Dazzi et al. (2019), Tabrizi et al. (2015), Elalfy (2015)).

Meyer-Peter and Müller (1948) bedload transport formula

$$\begin{cases} \Phi = \alpha(\theta - \theta_c)^{1.5} & \theta > \theta_c \\ \Phi = 0 & \theta \leq \theta^c \end{cases} \tag{4.2}$$

Ashida and Michiue (1972) bedload transport formula:

$$\begin{cases} \Phi = 17\theta^{1.5}(1 - \frac{\theta_c}{\theta})(1 - \sqrt{\frac{\theta_c}{\theta}}) & \theta > \theta_c \\ \Phi = 0 & \theta \leq \theta_c \end{cases} \tag{4.3}$$

Smart (1984) bedload transport formula:

$$\begin{cases} \Phi = 4(\frac{d_{90}}{d_{30}})^{0.2} F S^{0.1} \theta^{0.5}(\theta - \theta_c^{sm}) & \theta > \theta_c^{sm} \\ \Phi = 0 & \theta \leq \theta_c^{sm} \end{cases} \tag{4.4}$$

With F the Froud number,d_{30} and d_{90} the grain sizes at which 30% and 90% of sediments are finer, S_e the energy slope, ($\theta_c^{sm} = \theta_c(1 - \frac{S_e}{\tan\phi_{wet}})$) the dimensionless critical shear stress by Smart (1984), θ_c the critical Shields (1936) parameter equal to 0.047 as suggested by Meyer-Peter and Müller (1948), θ and Φ are the dimensionless Shields parameter and sediment discharge, computed as follows :

$$\begin{cases} \theta = \frac{\tau_b}{g(\rho_s - \rho)d_{50}} \\ \Phi = \frac{q_b}{\sqrt{g(\frac{\rho_s - \rho}{\rho} d_{50}^3)}} \end{cases} \tag{4.5}$$

Where q_b is the bedload discharge per unit width (m^2/s) and τ_b the bed shear stress in (Pa).

4.2.2.2 Secondary currents effects on the direction of the bed shear stress

Secondary flow patterns (helical, spiral) are generally observed in curved and meandering channels. In such cases, the sediment transport direction deviates from the bed shear stress direction. These effects are directly captured by three-dimensional models, while two-dimensional models neglect

vertical velocities. Different authors proposed formulas to include the secondary flow effects in two-dimensional models. Engelund (1974) proposed a formula for the angle δ between the bedload transport direction and main flow direction as follows:

$$\tan\delta = 7\frac{h}{r} \tag{4.6}$$

Where h is the water depth and r the local radius of curvature of the streamline.

4.2.2.3 Bed slope effects on the magnitude and direction of sediment transport

As discussed above, most available bedload transport formulas were mainly fitted against laboratory data with smooth bed slopes (except for the Smart (1984) formula). Gravity can highly influence the bedload transport for cases with steep or mild slopes. In SISYPHE/GAIA, correction formulas are available to take into account the bed slope effect on both the magnitude (Koch and Flokstra (1980), Soulsby (1997)) and the direction of bedload transport (Koch and Flokstra (1980), Talmon et al. (1995)). Koch and Flokstra (1980) proposed a correction of the bedload magnitude by adding a diffusion factor in the Exner equation as follows :

$$q_{bnew} = q_b\Big[1 + \beta\big(\partial_x z_b \cos\alpha_b + \partial_y z_b \sin\alpha_b\big)\Big] \tag{4.7}$$

where q_{bnew} is the corrected bedload rate, β is an empirical coefficient accounting for the streamwise bed slope effect which default value is equal to 1.3 and α_b is the angle between the sediment transport direction and the x-axis direction. Another formula was also developed by Soulsby (1997) based on the modification of the critical Shields parameter as follows:

$$\theta_c^{ss} = \theta_c \frac{\cos\psi\sin\xi + \sqrt{\cos^2\xi\tan^2\phi - \sin^2\psi\sin^2\xi}}{\tan\phi} \tag{4.8}$$

where θ_c^{ss} is the corrected critical Shields parameter, ϕ is the angle of repose of the sediment, ξ is the bed slope angle with x-axi, and ψ is the angle between the flow and the bed slope directions.

The correction of bedload direction due to the combination of bed slope and secondary currents is given by the relation of Bendegom (1947):

$$\tan\alpha_b = \frac{\sin\delta - T\partial_y z_b}{\cos\delta - T_i\partial_x z_b} \tag{4.9}$$

where the coefficient T_i is calculated can be calculated according to Talmon et al. (1995) as follows:

$$T_i = \frac{1}{\beta_2\sqrt{\theta}} \tag{4.10}$$

Where β_2 is an empirical coefficient which default value is 0.85 but can be calibrated.

Koch and Flokstra (1980) also proposed a formula for T_i as follows:

$$T_i = \frac{2\theta}{3} \tag{4.11}$$

4.2.3 Bank failure algorithm

The bank failure algorithm compares the slope of each element in the grid with a stable slope that is assumed to be the tangent of the user-defined sediment repose angle ϕ. Whenever the slope of the element exceeds the stable slope, the element is rotated around a horizontal axis until it reaches a stable slope. In the presence of a non-erodible substrate, the rotation is limited so that the final bed elevation is not below the level of the substrate. Examples of similar slope failure algorithms can be found in the literature, and some studies (Elalfy et al. (2018), Evangelista (2015), Guan et al. (2014), Swartenbroekx et al. (2010)) define distinct stability criteria depending on the water content of sediments. In this context, we updated the original slope failure module of SISYPHE/GAIA to account for different wet (ϕ_{wet}) , dry (ϕ_{dry}) and deposited (ϕ_{dep}) sediments repose angles. Rotating the element around a horizontal axis is equivalent to considering that a specific volume of sediment material in the upper half of the element (the half higher than the axis) is instantaneously transported to the lower half of the element. The axis of rotation intersects the center of gravity of the element and is chosen so that the volume lost above the axis equals the volume gained below it. When the rotation is performed on all unstable elements (those with an angle steeper than ϕ_{wet}, ϕ_{dry} or ϕ_{dep}), this produces node height discontinuities in nodes shared by adjacent elements. Subsequently, the new height for each node is obtained by averaging the height discontinuities according to the adjacent element areas. It is, thus, performed in a mass conservative way.

The algorithm does not ensure a newly stable geometry after applying the bank failure module in one single iteration. It is possible to perform several iterations of the algorithm within each computational time step until all the elements forming the bank have a stable angle. However, this would result in significant computational times. Additionally, this simplified geometric approach is highly dependent on mesh size. A short analysis of a simple hypothetical case is presented in Appendix A to highlight this dependency.

The sediments' repose angle values can be measured in experimental tests but are usually not documented in real field cases. Al-Hashemi and Al-Amoudi (2018) presented an extensive review of the different measurement methods and factors influencing the angle of repose of granular material. Some typical gravel, sand,and clay repose angle values can be found in (http://www.geotechdata.info). The reference values can be varied by 3° or 6° to account for other parameters such as soil moisture, compaction, and other components (Wu et al. (2017)).

In the simulations presented hereafter, the bank slope operator is activated at each flow and sediment transport time step, and the number of sub-iterations is set to 1.

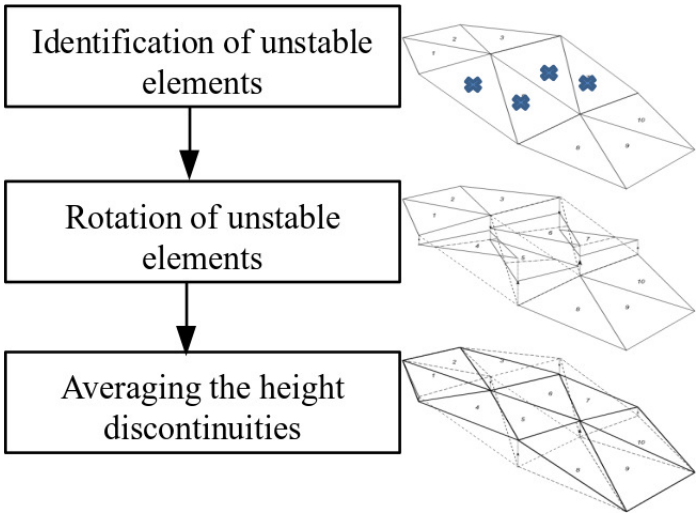

Figure 4.1: Representation of the sediment slide algorithm steps within a single iteration.

4.3 Validation cases

This section presents the laboratory and field experiments used to validate model improvements and evaluate its capacities to reproduce fluvial dikes breaching.

The laboratory dataset derives from the broader study of non-cohesive fluvial dike breaching undertaken by Rifai et al. (2019). Experiments consisted in provoking the overtopping of the main channel flow over the dike crest at a designated spot (i.e., initial notch) and observing subsequent dike erosion and breach expansion. Details about the experimental setup and measurements are given in Chapter 2 and by Rifai et al. (2017b). Test 36 conducted at the National Laboratory of Hydraulics and Environment of EDF-R&D was numerically simulated to validate newly implemented model improvements and discuss its performances. The experimental model was the same as in Chapter 2; it consisted of the main channel with a 7 m long side opening toward a 1 × 7 m floodplain. The main channel width l was set ton 1.8 m. The bottom of the main channel and the floodplain were at the same level and can be made of rigid material. The opening side was obstructed with sand to represent a fluvial dike of trapezoidal shape, as shown in Figure 4.2. The sand was uniform, with a median diameter d_{50} = 1 mm, a density ρ_s = 2470 kg/m^3, a porosity p = 0.37, a measured dry sediments repose angle of 55° and 28° for wet sediments. A perforated plane located at the downstream end regulated the flow so that, for a given inflow discharge Q_i, the water level in the main channel was at the dike crest level. In the selected Test 36, the flow across the breach was discharged freely from the floodplain without any storage change or tailwater effects (Figure 4.2) and the inflow discharge Q_i was equal to 0.072 (m^3/s).

The field-scale dataset comes from the Japanese Chiyoda flume experiments and two different configurations were simulated. Case 2 and Case 4 performed by Kakinuma et al. (2013) consisted in triggering levee breaching by overtopping at a specific location to observe breach dynamics and

outflow. The levee was built from gravel, sand, and a small fraction of silt and clay. The sediments median diameter (d_{50}) in the main channel was 4.9 mm for both cases while the levee material had a median diameter of 4.9 mm in Case 2 and 0.7 mm in Case 4 corresponding to a density ρ_s of 2667 kg/m^3 and 2034 kg/m^3, respectively. The erodible portion of the dike was 100 m long 3 m high, and its crown width was equal to 3 m in Case 2 and 6 m in Case 4 with 1:2 (V:H) side slopes. The inner slope of the levee was protected with material blocks to prevent a collapse due to the erosion by the lateral flow in the main channel. Finally, the main channel and floodplain were 8 m and 80 m wide, respectively. The inflow discharge to the main channel was gradually increased to reach the required water level for overtopping. Additional details on the experiments can be found in Section 3.3 of 3.

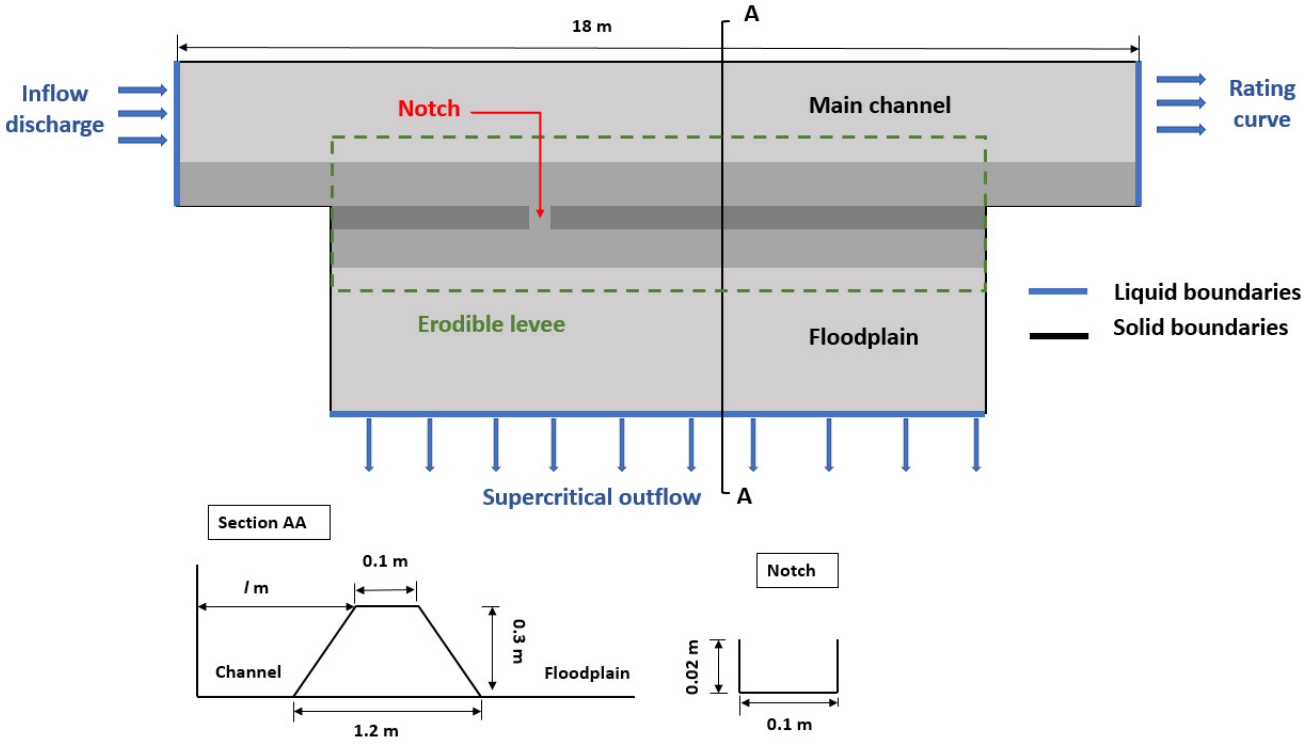

Figure 4.2: Sketch of the laboratory experiments configuration and model boundary conditions.

4.4 Simulation of the laboratory scale experiment Test 36

4.4.1 Computational parameters

For Test 36, the 2D computational domain was discretized into unstructured triangular elements with a typical size of 10 cm in the main channel and 4 cm in the dike and floodplain. It was selected after a mesh convergence analysis as displayed in Appendix B. As shown in Figure 4.2 the boundary conditions consisted of a constant inflow discharge in the main channel, a rating curve at the channel outflow, and a supercritical outflow in the floodplain, and solid boundaries were imposed elsewhere.

The time step was set to 0.01 s. The Strickler formula represented the energy loss due to bottom friction with a coefficient $K = 80$ (m $^{1/3}$ s^1) in the main channel and floodplain and $K = 66$ (m $^{1/3}$ s^1) in the dike area. A constant velocity diffusivity (molecular viscosity + turbulent viscosity) of 10^{-4} m^2/s was applied for the turbulence term closure. The characteristics advection scheme is used for velocity fields, and the PSI (Positive Streamwise Implicit) was selected for water depth.

TELEMAC-2D was coupled with SISYPHE, and only bedload transport was modeled using the Meyer-Peter and Müller (1948) formula with a multiplying coefficient set to 18. Both the magnitude and direction of bedload transport were corrected using the Koch and Flokstra (1980) formula with the empirical parameter β set to the default value (1.3). The slope failure module was modified to account for three different repose angles measured for the sediments with a value of ϕ_{wet}=28° for submerged sediments, ϕ_{dry}=55° for dry sediments and ϕ_{dep}=14° for deposited sediments. The correction for secondary currents proposed by Engelund (1974) was also activated.

4.4.2 Overview of the performed simulations

An extensive sensitivity analysis on hydrodynamic parameters in TELEMAC-2D was performed by Rifai (2018) to determine the best-fitted parameters for the flow field. Here, we focus on the morphodynamic parameters that are varied to achieve the best agreement with measurements. The parameters in TELEMAC-2D are the same as presented in Section 4.4.1 while bedload formula, repose angles and bedload transport direction correction formulas for bed slope and secondary currents effects were varied as detailed in Table 4.1. The magnitude correction of bedload transport was accounted for using the Koch and Flokstra (1980) formula with (β = 1.3) for all runs.

Finally, the resulting Normalized Root-Mean-Square Error values on breach width and discharge are listed in Table 4.2.

Run	Drainage discharge	Bedload formula	Repose angles	Additional options
Run 1 (Exp. 36)	No	MPM (α= 12)	ϕ=35°	Koch and Flokstra (1980) deviation formula for slope effect, and Engelund (1974) formula for secondary currents.
Run 2 (Exp. 36)	Yes	MPM (α= 12)	ϕ=35°	Same as Run 1.
Run 3 (Exp. 36)	Yes	MPM (α= 12)	ϕ_{wet}=28°, ϕ_{dry}=55°	Same as Run 1.
Run 4 (Exp. 36)	Yes	MPM (α= 12)	ϕ_{wet}=28°, ϕ_{dry}=55°, ϕ_{dep}=14°	Same as Run 1.
Run 5 (Exp. 36)	Yes	MPM (α= 8)	ϕ_{wet}=28°, ϕ_{dry}=55°, ϕ_{dep}=14°	Same as Run 1.
Run 6 (Exp. 36)	Yes	MPM (α= 18)	ϕ_{wet}=28°, ϕ_{dry}=55°, ϕ_{dep}=14°	Same as Run 1.
Run 7 (Exp. 36)	Yes	MPM (α= 9.64$\theta^{1/6}$)	ϕ_{wet}=28°, ϕ_{dry}=55°, ϕ_{dep}=14°	Same as Run 1.
Run 8 (Exp. 36)	Yes	Ashida and Michiue (1972)	ϕ_{wet}=28°, ϕ_{dry}=55°, ϕ_{dep}=14°	Same as Run 1.
Run 9 (Exp. 36)	Yes	Smart (1984)	ϕ_{wet}=28°, ϕ_{dry}=55°, ϕ_{dep}=14°	Same as Run 1.
Run 10 (Exp. 36)	Yes	Van Rijn (1984)	ϕ_{wet}=28°, ϕ_{dry}=55°, ϕ_{dep}=14°	Same as Run 1.
Run 11 (Exp. 36)	Yes	MPM (α= 18)	ϕ_{wet}=28°, ϕ_{dry}=55°, ϕ_{dep}=14°	Talmon et al. (1995) (β_2= 0.85) deviation formula for slope effect, and Engelund (1974) formula for secondary currents.
Run 12 (Exp. 36)	Yes	MPM (α= 18)	ϕ_{wet}=28°, ϕ_{dry}=55°, ϕ_{dep}=14°	Talmon et al. (1995) (β_2= 1.7) deviation formula for slope effect, and Engelund (1974) formula for secondary currents.
Run 13 (Exp. 36)	Yes	MPM (α= 18)	ϕ_{wet}=28°, ϕ_{dry}=55°, ϕ_{dep}=14°	Talmon et al. (1995) (β_2= 9.$(\frac{d_{50}}{h})^{0.3}$) deviation formula for slope effect, and Engelund (1974) formula for secondary currents.
Run 14 (Exp. 36)	Yes	MPM (α= 18)	ϕ_{wet}=28°, ϕ_{dry}=55°, ϕ_{dep}=14°	Koch and Flokstra (1980) deviation formula for slope effect, and Bernard and Schneider (1992) formula for secondary currents.
Run 15 (Exp. 36)	Yes	MPM (α= 18)	ϕ_{wet}=28°, ϕ_{dry}=55°, ϕ_{dep}=14°	Koch and Flokstra (1980) deviation formula for slope effect, without secondary currents effects.

Table 4.1: Test 36 simulations and corresponding numerical parameters.

4.4.3 General results

In this section, the resulting breach characteristics with the best fitted parameters (**Run 11**, Table 4.1) for Test 36 are presented and compared to experimental data. In order to define the best fitted numerical parameters, several preliminary simulations were carried out (some are explained below) prior to that shown in Figures 4.3 and 4.4.

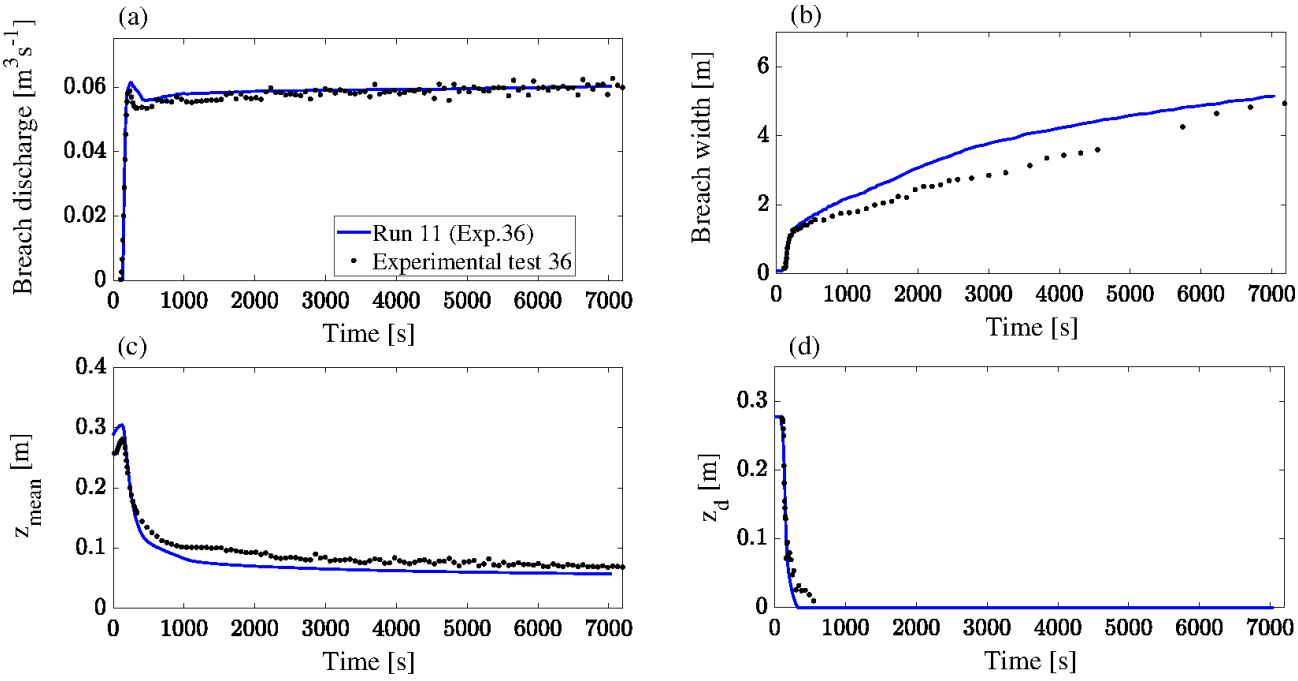

Figure 4.3: Comparison of simulations results and experimental data for Test 36 : (a) breach discharge, (b) breach width at the crest level (y=0.65 m), (c) average water level in the main channel and (d) Breach invert elevation.

Figure 4.3 compares the measured and calculated breach discharge, width at the crest level, the average water level in the main channel, and the breach invert elevation. The predicted breach discharge agrees reasonably with the measured one. It reproduces the rapid increase and the peak formation with a slightly higher magnitude and then reaches a stable value similar to that measured in the experiment. Breach width was well captured for time (< 300 s) but was then slightly overestimated by the model for the rest of the breaching period. This is mainly due to the over-predicted erosion of the inner dike slope by the parallel flow in the main channel. Figure 4.4 shows that the overall breaching process is well captured by the model, such as the progressive and asymmetrical erosion. However, one can see that the upstream dike portion (x< 2.55 m) is narrower in the simulation resulting than in measurements in slope failure on unstable blocks and an overestimated upstream widening, as is detailed by the representation of breach extremities location in Figure 4.5. Figure 4.3 also displays a good agreement between measured and computed breach deepening with slightly higher water levels in the main channel for the numerical results at a time (< 170 s), but then it decreased and stabilized at a slightly lower value.

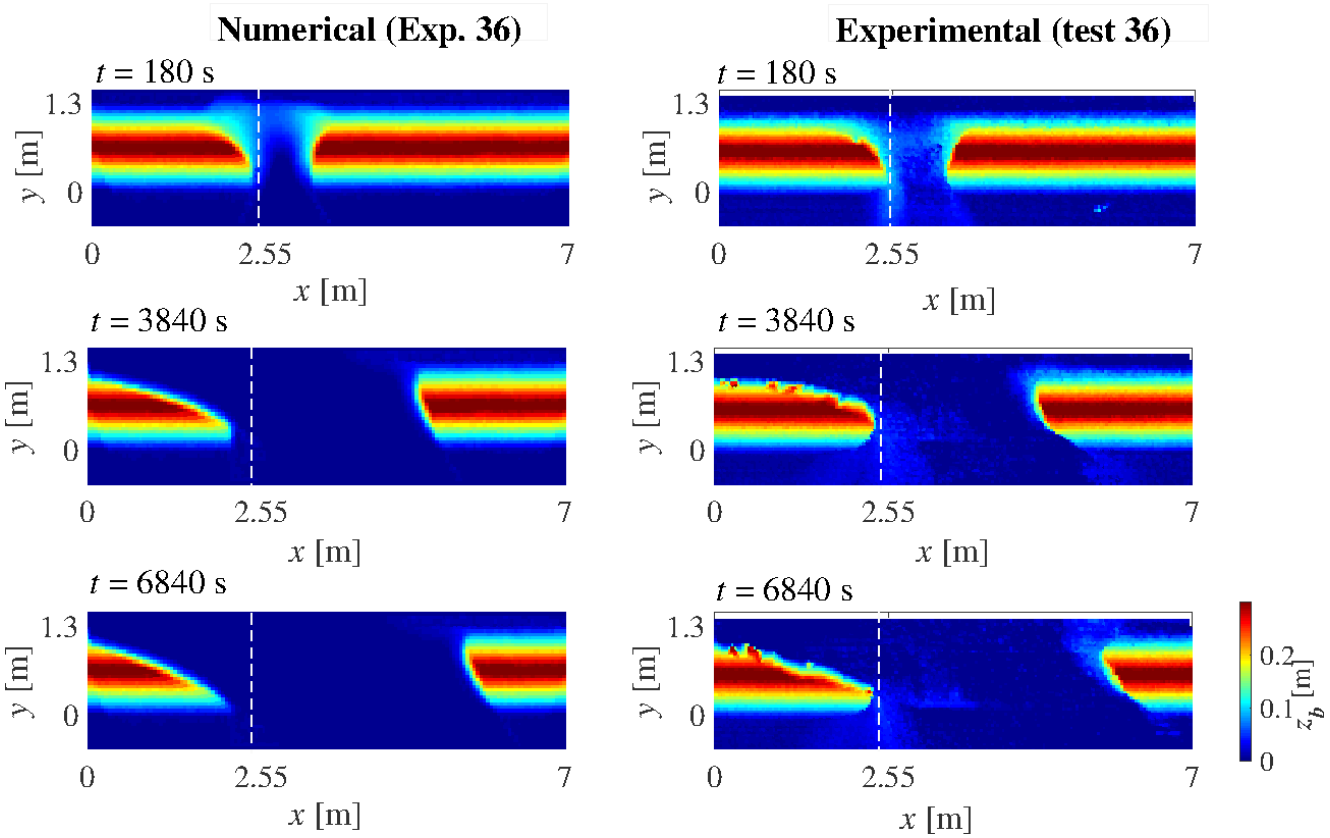

Figure 4.4: Simulated and measured 3D breach shapes for Test 36 (the dashed White lines indicate initial notch location).

4.4.4 Sensitivity analysis

4.4.4.1 Influence of drainage discharge

In this section, we investigate the influence of the drainage discharge on the resulting breach expansion and discharge in simulations. Two different runs were performed, and run 2 accounted for the drainage discharge using the evaporation option of the TELEMAC-2D module as shown in Table 4.1. The value assigned for drainage discharge was extracted from experimental data provided in Rifai et al. (2019).

Figure 4.5 shows that simulated breach discharge and width are overestimated by the numerical model in Run 1 that was performed with no drainage loss. Including the drainage discharge improves the agreement between numerical predictions and measurements for breach discharge. However, it has a limited effect on breach extremities expansion.

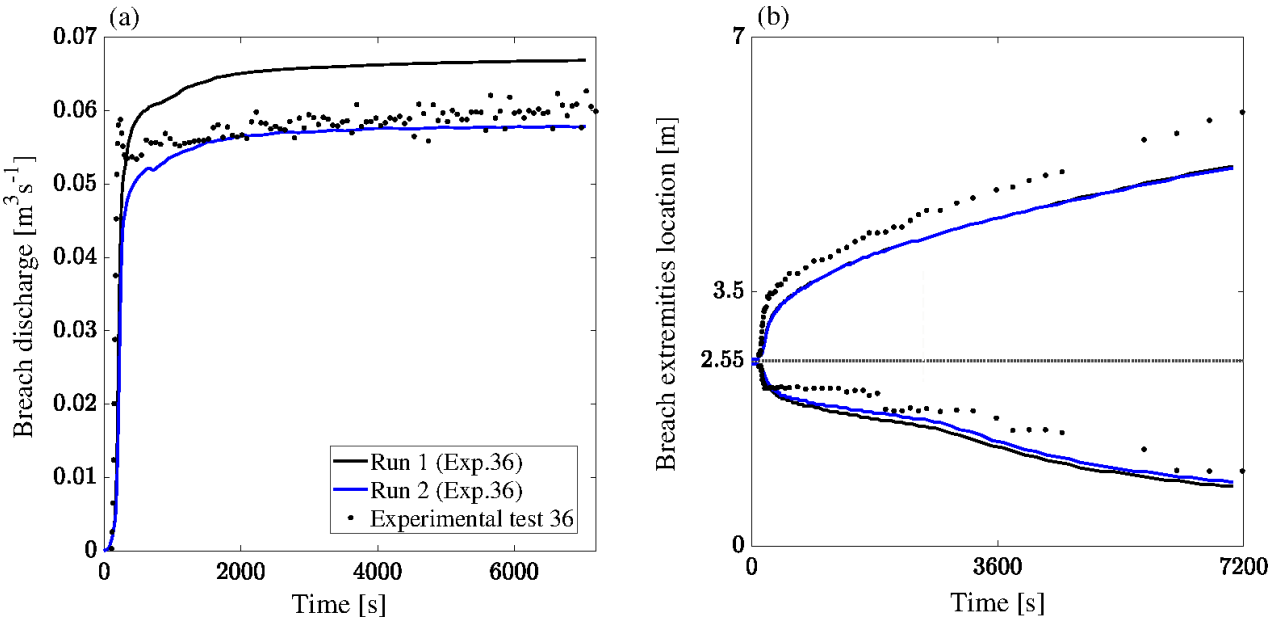

Figure 4.5: Influence of the drainage discharge in numerical simulations for Test 36 : (a) breach discharge and (b) breach extremities location along the longitudinal axis at the crest center line (y=0.65 m) and the dashed black line indicated initial notch location.

4.4.4.2 Adaptation of the slope failure module to multiple sediments repose angles

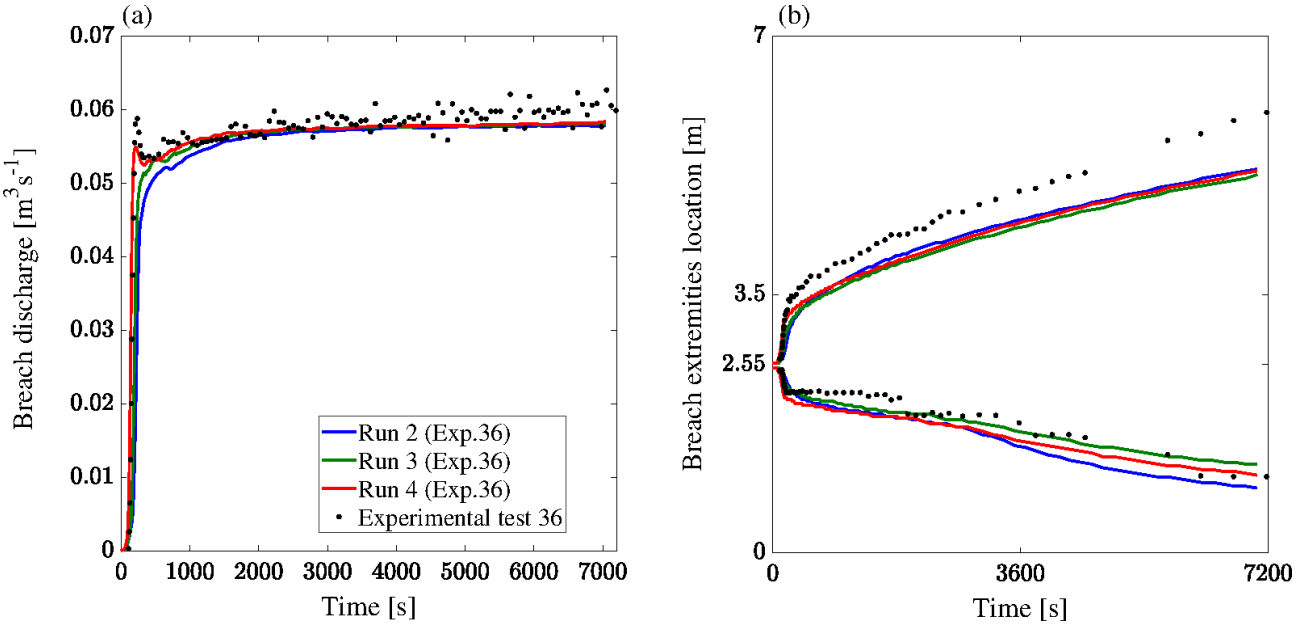

Figure 4.6: Comparison of Test 36 simulations with the original and modified slope failure module : (a) breach discharge and (b) breach extremities location along the longitudinal axis at the crest center line (y=0.65 m) and the dashed black line indicated initial notch location.

New developments were made in the slope failure module to improve the model capabilities to reproduce the multiple physical processes of levee breaching. Instead of using one repose angle for all sediments, three distinct repose angles can be specified to account for the different properties of submerged, dry, and deposited sediments. The values of ϕ_{wet} and ϕ_{dry} come from measurements while the value for deposited sediments ϕ_{dep} was set to half the angle of repose ϕ_{wet} as reported by Volz (2013) and Guan et al. (2014). For run 2 the value of ϕ was set to 35° as successfully calibrated for Test 36 by Rifai (2018).

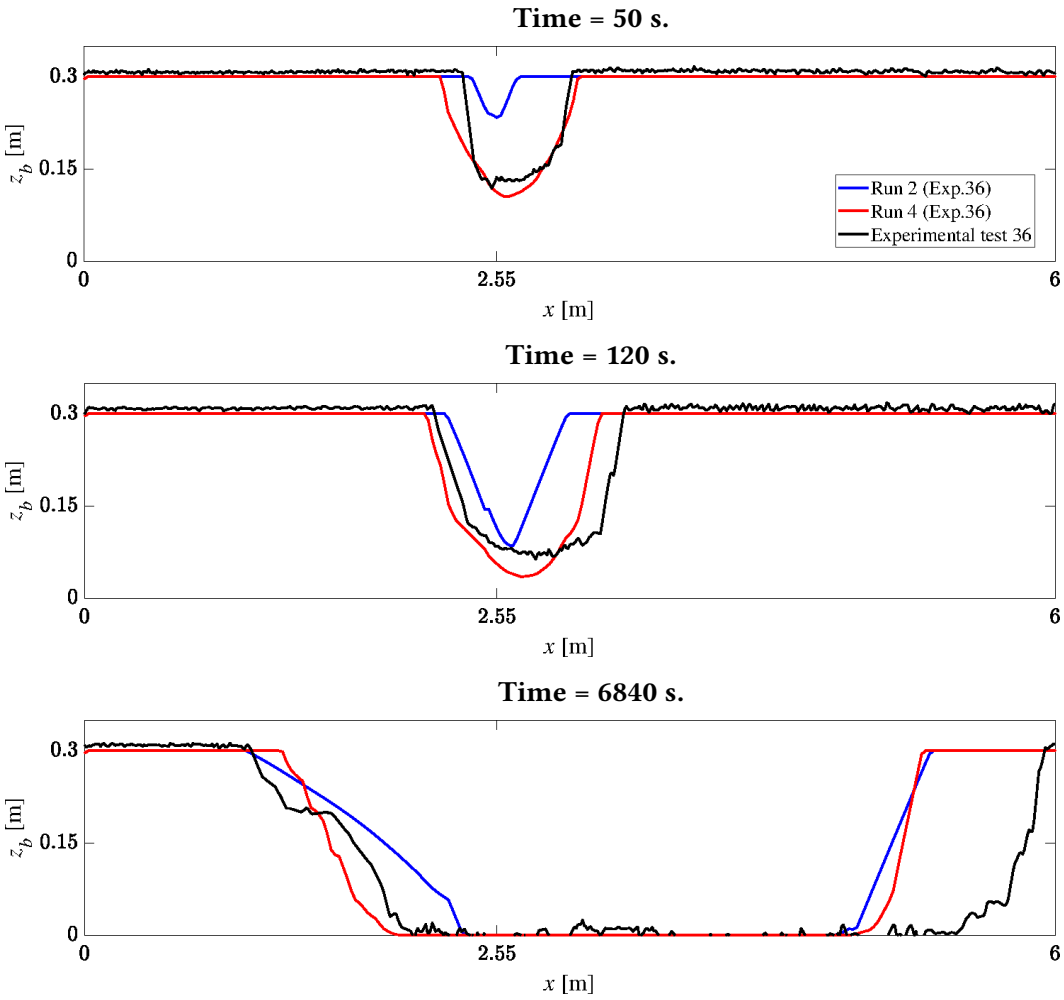

Figure 4.7: Influence of the sediment slide parameters on breach longitudinal profile at the crest center for Test 36.

Figure 4.6 illustrates computed and measured breach hydrographs and extremities location at the crest level. We can see that run 2 with a single repose angle and run 3 with two different repose angles failed to capture the peak in breach hydrograph and resulted in a slightly delayed increase of the breach discharge. The simulations with three repose angles performed better, although they estimated a lower peak magnitude in breach discharge. Breach extremities locations do not show significant differences between the three runs. Figure 4.7 also highlights improvements in the breach

longitudinal sections prediction with the multiple repose angles simulation. In simulations performed with one single repose angle for the entire erodible domain (run 2), breach longitudinal profiles are more triangular at 50 and 120 seconds of the breaching process than that observed in experiments, while the multiple repose angles simulation seems to result in better approximations of the longitudinal breach section. The breach side walls slopes at the end of the breach process (6840 seconds) were reasonably approximated by both approaches; however, the simulation with one repose angle for sediments showed milder slopes than experimental data. Finally, some discrepancies can still be observed and are related to the limits of the simple geometric approach used to mimic slope failure. Such methods can not reproduce complex geotechnical processes and failure modes.

4.4.4.3 Bedload transport formula

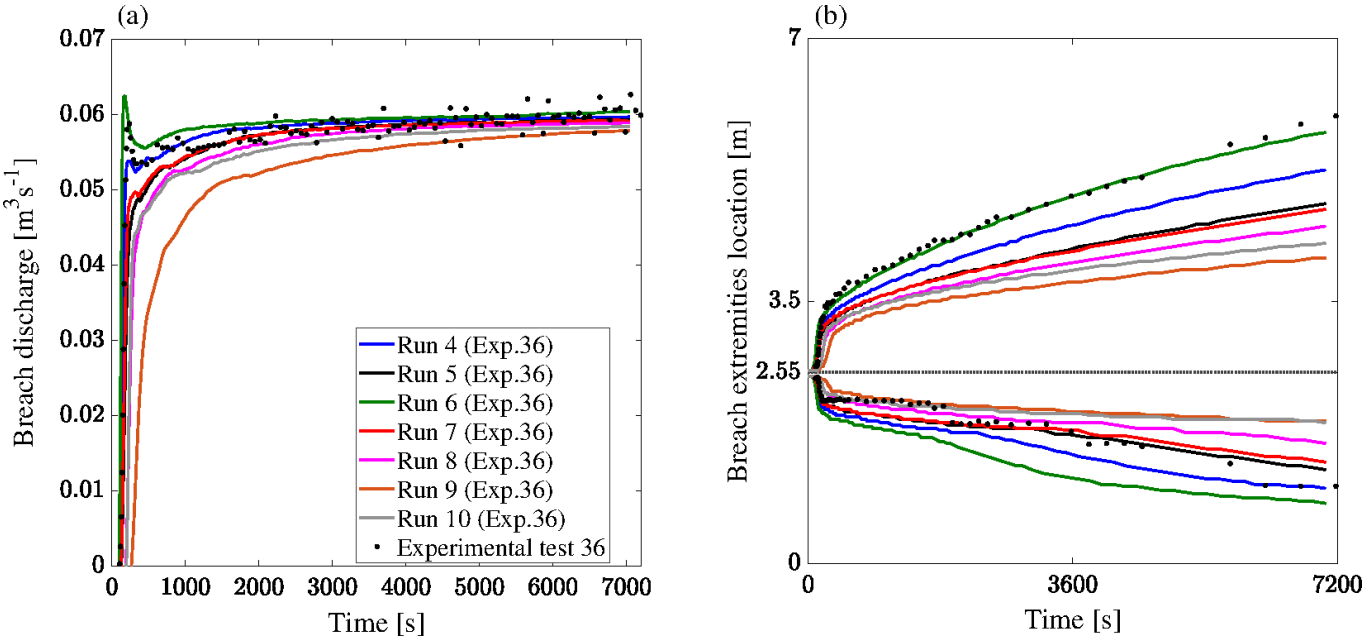

Figure 4.8: Comparison of Test 36 simulations with different bedload transport formulas: (a) breach discharge and (b) breach extremities location along the longitudinal axis at the crest center line (y=0.65 m) and the dashed black line indicated initial notch location.

This section evaluates four different empirical bedload transport formulas as shown in Table 4.1. Runs 4, 5, m, and 7 were performed with the Meyer-Peter and Müller (1948) equation with different values for the dimensionless coefficient α. The classical value of 8 that was originally suggested by Meyer-Peter and Müller (1948), El Kadi Abderrezzak and Paquier (2010) showed that for embankments failure, the value of 12 was more suitable, Kakinuma and Shimizu (2014) suggested a value of 18 based on data. Finally, the α coefficient was expressed as a function of the shields parameter as suggested by Wiberg and Smith (1989) and tested for dam break simulations by Clemens. Dorfmann (2014). The newly implemented Ashida and Michiue (1972) and Smart (1984) formulas were also

tested in addition to the Van Rijn (1984) bedload formula available in SISYPHE. The simulation with Smart (1984) formula was performed without correction for the bed slope effect as it is included in the formula itself, and the Koch and Flokstra (1980) correction for the bedload magnitude and direction was activated in the other simulations.

Figure 4.8 shows the effect of the bedload transport formula on predicted breach discharge and widening. The model results are generally below experimental measurements for both breach hydrograph and width except for the Meyer-Peter and Müller (1948) formula with a multiplying coefficient of 18. The underestimation of the breach erosion impacted breach discharge where the peak formation was not reproduced, and breach discharge increase was delayed, except for run 6, which resulted in good predictions. However, breach upstream widening was slightly overestimated due to the dike erosion from the channel side that was overpredicted in the model.

4.4.4.4 Corrections of bedload transport direction

Here a short parametric analysis is presented for the deviation of bedload transport. For that, the Koch and Flokstra (1980) formula for magnitude correction was adopted, and equations for bedload directions are varied as shown in Table 4.1. The β coefficient in the formula proposed by Talmon et al. (1995) was set to different values; 0.85, usually used for natural rivers, 1.7 was advised for laboratory conditions, and β expressed as a function of water depth and sediments median diameter.

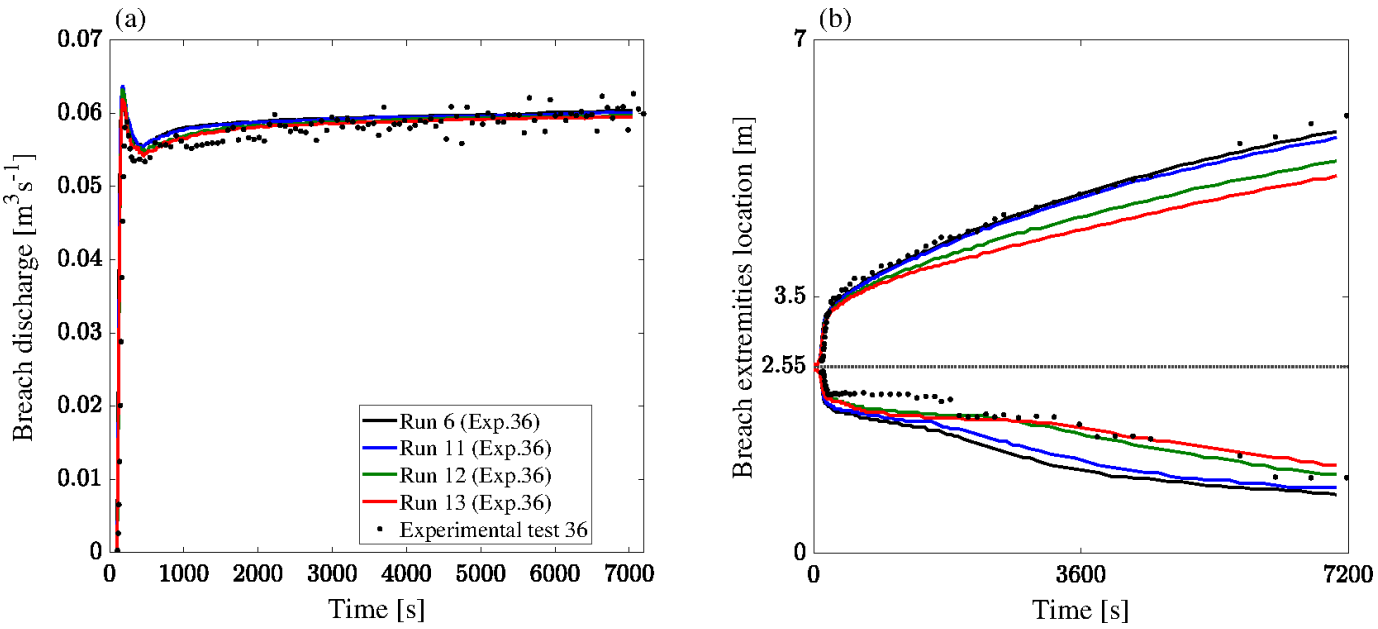

Figure 4.9: Comparison of Test 36 simulations with different corrections for bedload deviation formulas: (a) breach discharge and (b) breach extremities location along the longitudinal axis at the crest center line (y=0.65 m) and the dashed black line indicated initial notch location.

Figure 4.9 shows that breach width is much more sensitive to the deviation corrections than

breach outflow. A possible reason is that a dead water area forms towards the upstream breach extremity, and the flow is not conveyed through the entire breach section. Therefore, predicting a smaller breach width during an advanced breach stage time (> 500 s) does not significantly impact the estimated breach discharge. Finally, the best agreement between the model results and measurement is achieved with the Koch and Flokstra (1980) formula or using the Talmon et al. (1995) with β equal to 0.85.

4.4.4.5 Secondary currents effect

The secondary currents effect can be accounted in the hydrodynamic field using the stream-wise secondary currents correction model by Bernard and Schneider (1992). One can also use the correction on the bottom shear stress direction using the cross-wise secondary currents correction by Engelund (1974). In this section, we compare the model predictions for the different corrections and a simulation in which the secondary currents effect is not included (Table 4.1). In Figure 4.10 comparisons between observed and computed breach discharge and extremities evolution in time with and without the secondary flow correction are given. Run 15 performed without secondary currents resulted in overestimated breach discharge peak and widening. Clear improvements can be seen in simulations, including modifications for secondary currents. The results for run 6 with Engelund (1974) corrected model display the best agreement the breach hydrograph and its lateral expansion while the Bernard and Schneider (1992) correction slightly overpredicts the latter parameters.

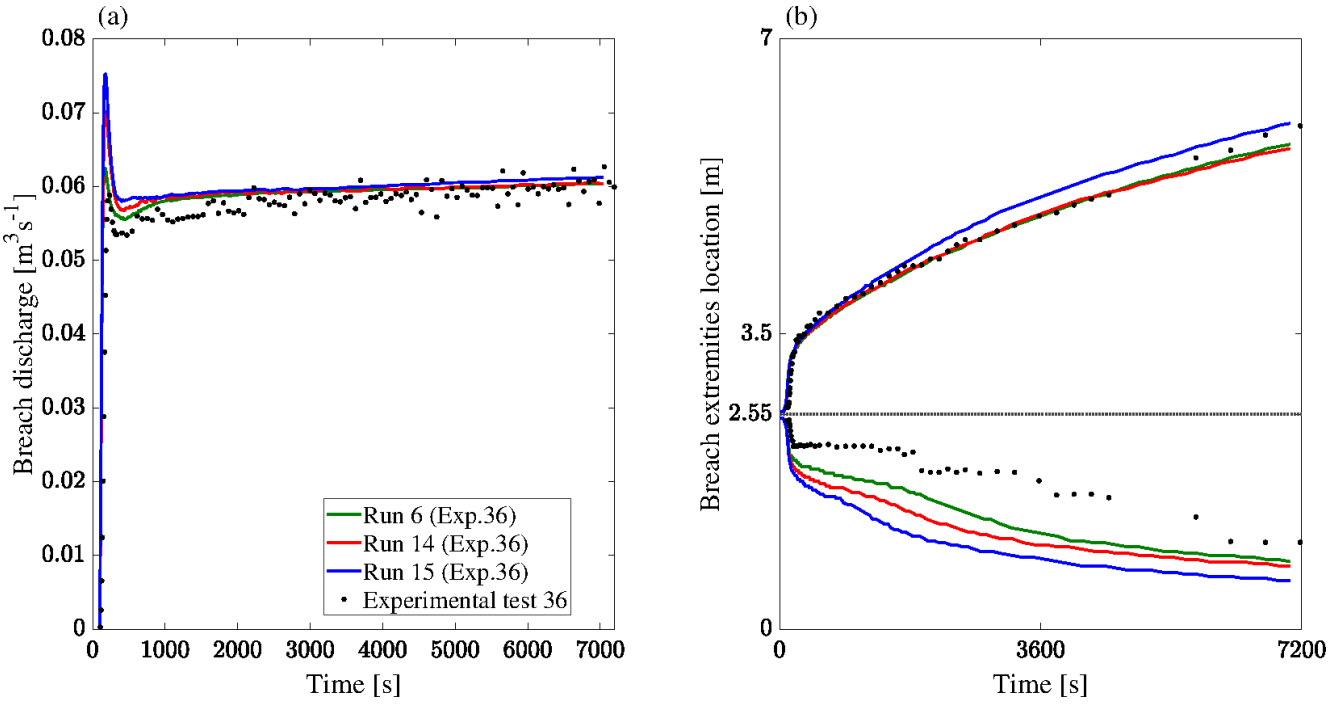

Figure 4.10: Comparison of Test 36 simulations with different corrections for secondary currents: (a) breach discharge and (b) breach extremities location along the longitudinal axis at the crest center line (y=0.65 m) and the dashed black line indicated initial notch location.

Run	NRMSE on breach discharge	NRMSE on breach width
Run 1 (Exp. 36)	21.4%	7.4%
Run 2 (Exp. 36)	15.8%	7%
Run 3 (Exp. 36)	7.2%	9.6%
Run 4 (Exp. 36)	6.5%	5.2%
Run 5 (Exp. 36)	17.3%	9.7%
Run 6 (Exp. 36)	4.6%	7.6%
Run 7 (Exp. 36)	16.4%	10.5%
Run 8 (Exp. 36)	17%	12.5%
Run 9 (Exp. 36)	24.8%	21.2%
Run 10 (Exp. 36)	16.5%	15.9%
Run 11 (Exp. 36)	5%	7.9%
Run 12 (Exp. 36)	4.5%	6.4%
Run 13 (Exp. 36)	4.3%	8%
Run 14 (Exp. 36)	7%	8.2%
Run 15 (Exp. 36)	8.5%	11%

Table 4.2: Simulations of Test 36 with resulting NRMSE on breach width and discharge.

4.5 Simulation of the field scale experiment Case 4

4.5.1 Computational parameters and boundary conditions

For the field scale experiment Case 4, the 2D computational domain was discretized into structured triangular elements with an edge of 0.5 m as recommended by Kakinuma and Shimizu (2014), and Dazzi et al. (2019) for hydro-morphodynamic simulations. Boundary conditions were the same as detailed in Chapter 3 (Fig.3.5). The measured inflow discharge was set at the main channel input (Fig.3.4) while a rating curve was used for the channel outflow boundary. A supercritical outflow was set in the floodplain output, and solid walls were used elsewhere. The Strickler coefficient was set to 43 ($m^{1/3}s^{-1}$). A constant velocity diffusivity of 10^{-3} (m^2 s^{-1}) was applied for turbulence closure and the time step was set to 0.1 s. Finally, Water depth and velocity advection were performed using the mass-conservative PSI and NERD schemes, respectively. The bed was initialized considering two sediments classes, the first class consisted in non-cohesive sediments of median diameter d_{50} of 4.9 mm in the main channel and floodplain. The second class represented the levee material with a median diameter d_{50} of 0.74 mm. Only bedload transport was modeled and allowed in the entire domain (except the non erodible portion of the dikes). The best fitted numerical parameters were defined after a sensitivity analysis (**Run 8** in Table 4.3). The Meyer-Peter and Müller (1948) formula was used with multiplying coefficients α_x (for bedload in the longitudinal direction) and α_y (for bedload in the transverse direction) set to α_x=4 and α_y=18 . Both the magnitude and direction

of bedload transport were corrected using the Koch and Flokstra (1980) formula with the empirical parameter β for bedload magnitude set to its default value (1.3). The slope failure module was modified to account for three different repose angles measured for the sediments with ϕ_{wet}=28°for submerged sediments, ϕ_{dry}=40°for dry sediments and ϕ_{dep}=14° for deposited sediments. The secondary currents effect was included with the correction proposed by Engelund (1974).

4.5.2 Overview of the performed simulations

In order to achieve the best agreement with measurement and identify relevant user-input parameters, a sensitivity analysis was carried-out focusing on the morphodynamic module parameters. The different runs and their corresponding parameters are listed in Table 4.3 and the resulting Normalized Root-Mean-Square Error values on breach width and discharge can be found in Table 4.4.

Run	Repose angles	α_x	α_y	Additional options
Run 1 (Case 4)	ϕ_{wet}=30°, ϕ_{dry}=40°, ϕ_{dep}=14°	12	12	Koch and Flokstra (1980) deviation formula for slope effect, and Engelund (1974) formula for secondary currents.
Run 2 (Case 4)	ϕ_{wet}=30°, ϕ_{dry}=40°, ϕ_{dep}=15°	6	12	Same as Run 1.
Run 3 (Case 4)	ϕ_{wet}=30°, ϕ_{dry}=40°, ϕ_{dep}=15°	3	12	Same as Run 1.
Run 4 (Case 4)	ϕ_{wet}=30°, ϕ_{dry}=40°, ϕ_{dep}=15°	18	18	Same as Run 1.
Run 5 (Case 4)	ϕ_{wet}=30°, ϕ_{dry}=40°, ϕ_{dep}=15°	9	18	Same as Run 1.
Run 6 (Case 4)	ϕ_{wet}=30°, ϕ_{dry}=40°, ϕ_{dep}=15°	4	18	Same as Run 1.
Run 7 (Case 4)	ϕ_{wet}=30°, ϕ_{dry}=35°, ϕ_{dep}=15°	4	18	Same as Run 1.
Run 8 (Case 4)	ϕ_{wet}=28°, ϕ_{dry}=40°, ϕ_{dep}=14°	4	18	Same as Run 1.
Run 9 (Case 4)	ϕ_{wet}=28°, ϕ_{dry}=40°, ϕ_{dep}=14°	4	18	Talmon et al. (1995) (β_2= 0.85) deviation formula for slope effect, and Engelund (1974) formula for secondary currents.
Run 10 (Case 4)	ϕ_{wet}=28°, ϕ_{dry}=40°, ϕ_{dep}=14°	4	18	Talmon et al. (1995) (β_2= 1.7) deviation formula for slope effect, and Engelund (1974) formula for secondary currents.

Table 4.3: Case 4 simulations and corresponding numerical parameters.

4.5.3 General results

In this section the capabilities of the coupled hydro-morphodynamic model (TELEMAC-2D/GAIA) to predict the levee breaching process for the field scale experiment Case 4 performed by Kakinuma et al. (2013) are discussed. Here we present the general results obtained after a preliminary analysis to determine the best-fitted parameters (**Run 8**, Table 4.3) listed in Section 4.5.1.

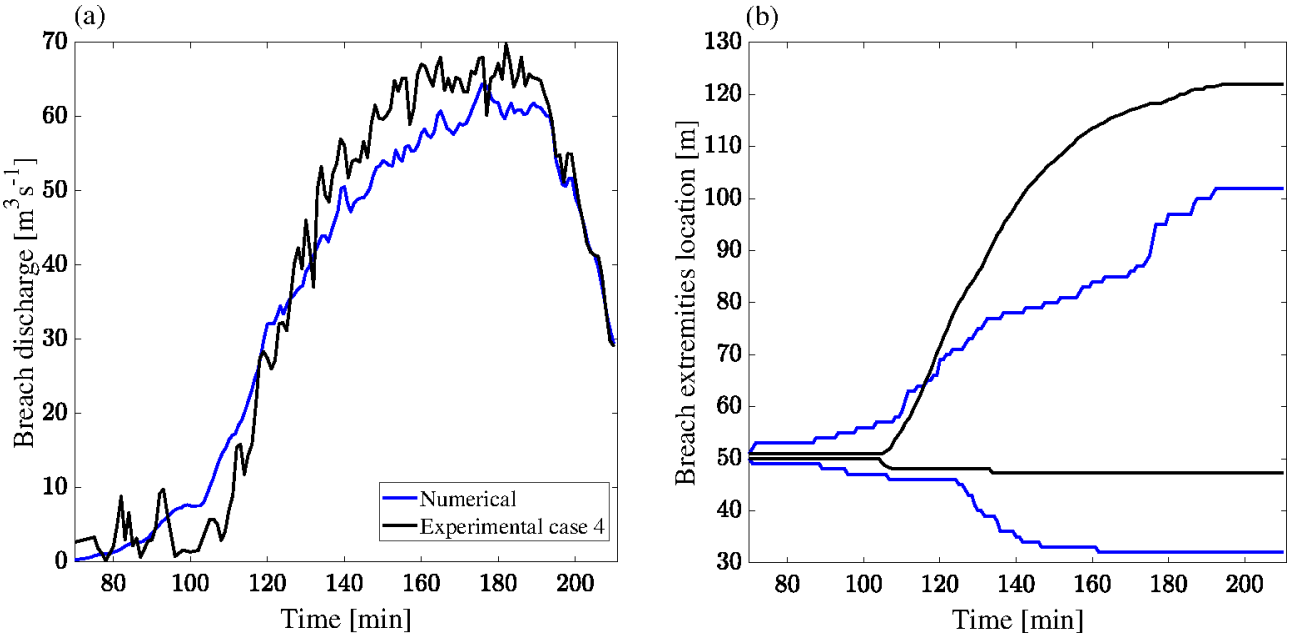

Figure 4.11: Comparison of Case 4 simulated and measured : (a) breach discharge and (b) breach extremities location along the longitudinal axis at the crest center line (y= 89 m), the notch center was located at x= 50 m.

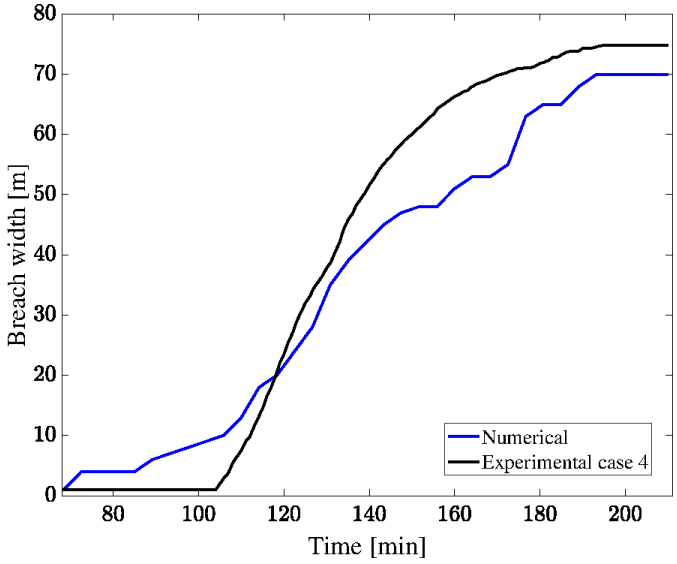

Figure 4.12: Comparison of simulated and measured breach width at the crest center line (y= 89 m) for Case 4.

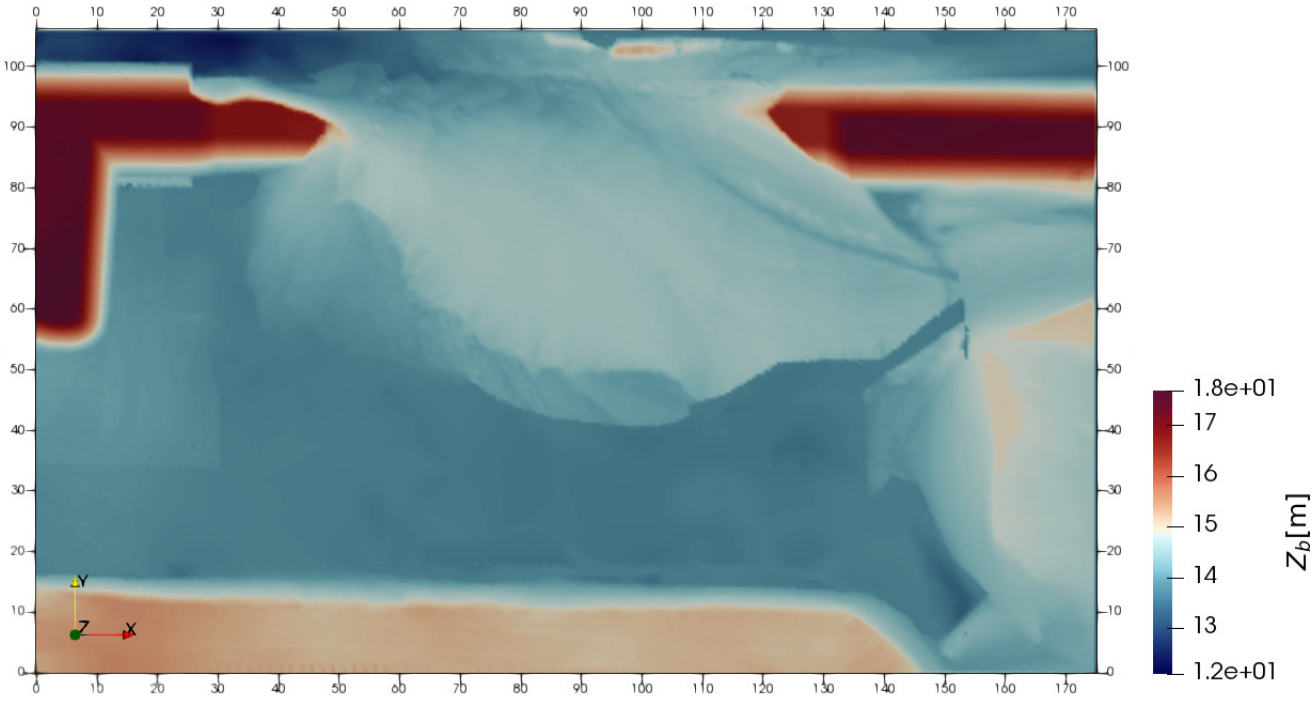

Figure 4.13: Laser scan of the test channel bed at the end of the breaching process for Case 4 (the water flows from the left to the right).

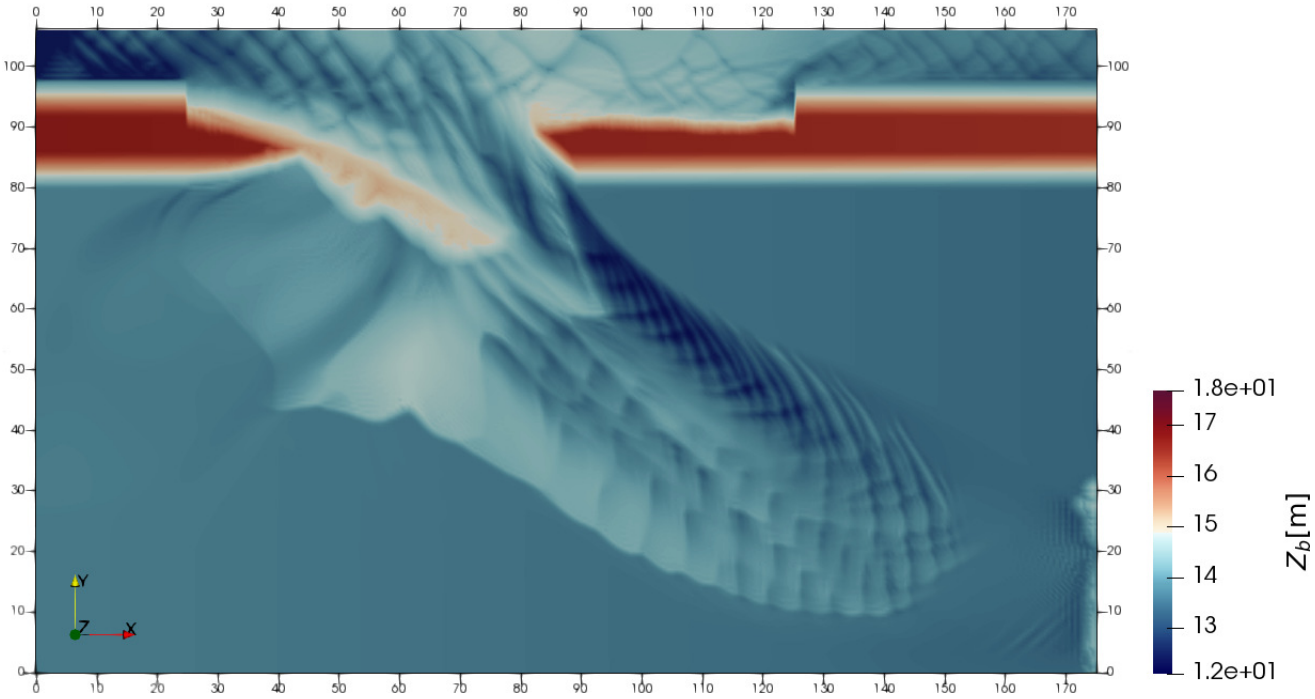

Figure 4.14: Simulated test channel bed at the end of the breaching process for Case 4 (the water flows from the left to the right).

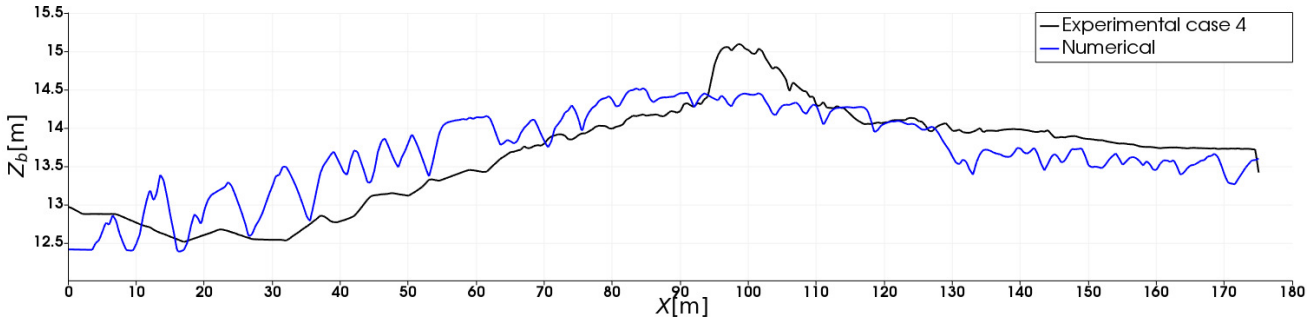

Figure 4.15: Simulated and measured bed longitudinal profile at the main channel center (y= 102 m) at the end of the breaching process for Case 4.

Figure 4.11 displays the measured and computed breach outflow hydrograph and breach extremities location along the crest center line. It can be seen that the hydro-morphodynamic model reasonably predicts the breach discharge fast increase and quasi-stabilization with a slightly lower magnitude at (time >130 minutes). This can be explained by the simulated breach extremities location evolution below measured ones downstream the notch and overestimated at the upstream . In addition, the breach width magnitude was also underestimated by the model, as shown in Figure 4.12 for time (>120 minutes). One should also note that breach widening and discharge increase were slightly anticipated in the numerical model. Still, the asymmetrical and preferential breaching widening towards the downstream end on the dike (x > 50 m) was also observed in calculated results. Different user input parameters were modified to improve the results further. Still, the main difficulty was representing the protection user by experiments on the inner levee slope to prevent its erosion from the channel side by the strong lateral velocities of the flow. Figures 4.13 and 4.14 comparing the measured and simulated test channel bed after the test end highlight the excessive erosion of the dike inner slope (from the channel side) in the simulation, which probably allowed a lower portion of the flow in the breach channel. Therefore, levee erosion in the downstream direction (x > 50 m) was clearly impacted and underestimated. Figure 4.14 also shows the formation of bedforms that were not observed in the experiment bed However, Figure 4.15 of the modeled and measured longitudinal profile at the main channel center line indicates that besides bedforms formation and some discrepancies, the bed erosion and deposition processes were well captured in the main channel.

4.5.4 Sensitivity analysis

4.5.4.1 Bedload transport formula

The sensitivity analysis in this section focuses on the dimensionless parameter α of the Meyer-Peter and Müller (1948) formula. Kakinuma and Shimizu (2014) calibrated the latter coefficient from experimental data and defined a reference value of 18. The simulations included tests with a Meyer-Peter and Müller (1948) coefficient of 12 as advised by El Kadi Abderrezzak and Paquier (2010) and

18 as recommenced by Kakinuma and Shimizu (2014). Simulations with distinct coefficients in the longitudinal (α_x) and transverse (α_y) directions are also introduced to mimic the protections used in experiments that avoid excessive erosion of the inner dike slope (Table 4.3). As a start for the sensitivity analysis, the sediment repose angles were set at 30°and 40° for ϕ_{wet} and ϕ_{dry} as recommended by Dazzi et al. (2019) while the deposited sediments were characterized with a repose angle ϕ_{dep} of 14° (half ϕ_{wet}).

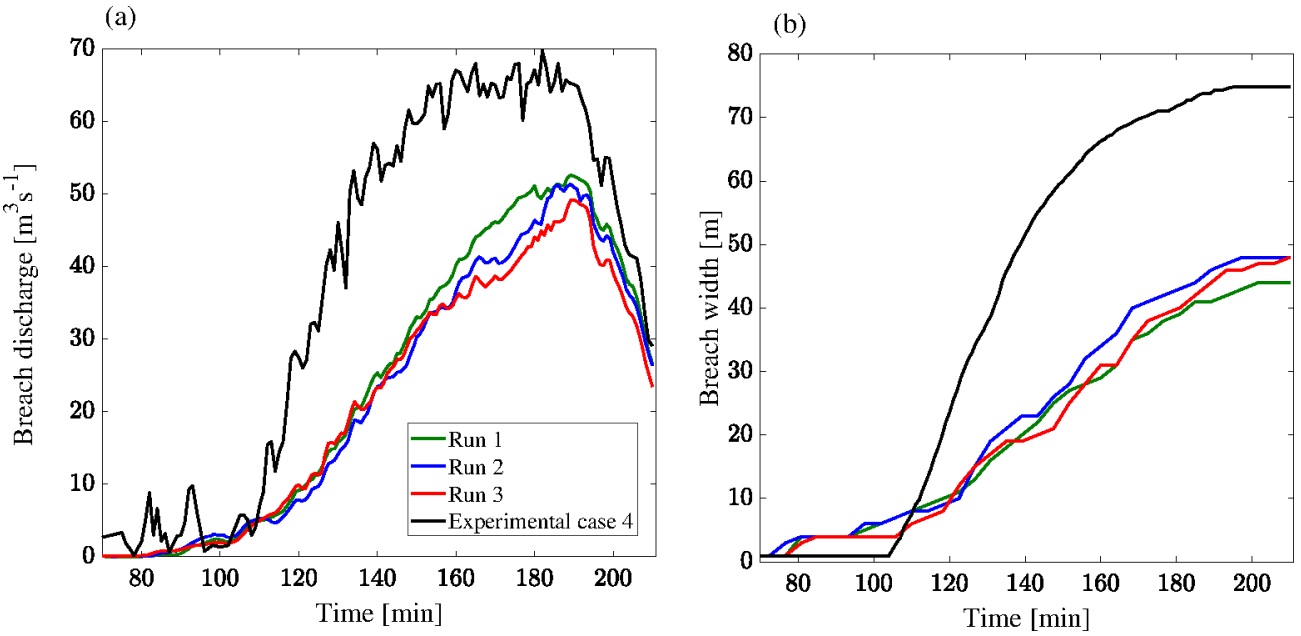

Figure 4.16: Comparison of Case 4 simulations with α_y= 12 and different α_x values : (a) breach discharge and (b) breach width at the crest level (y= 89 m).

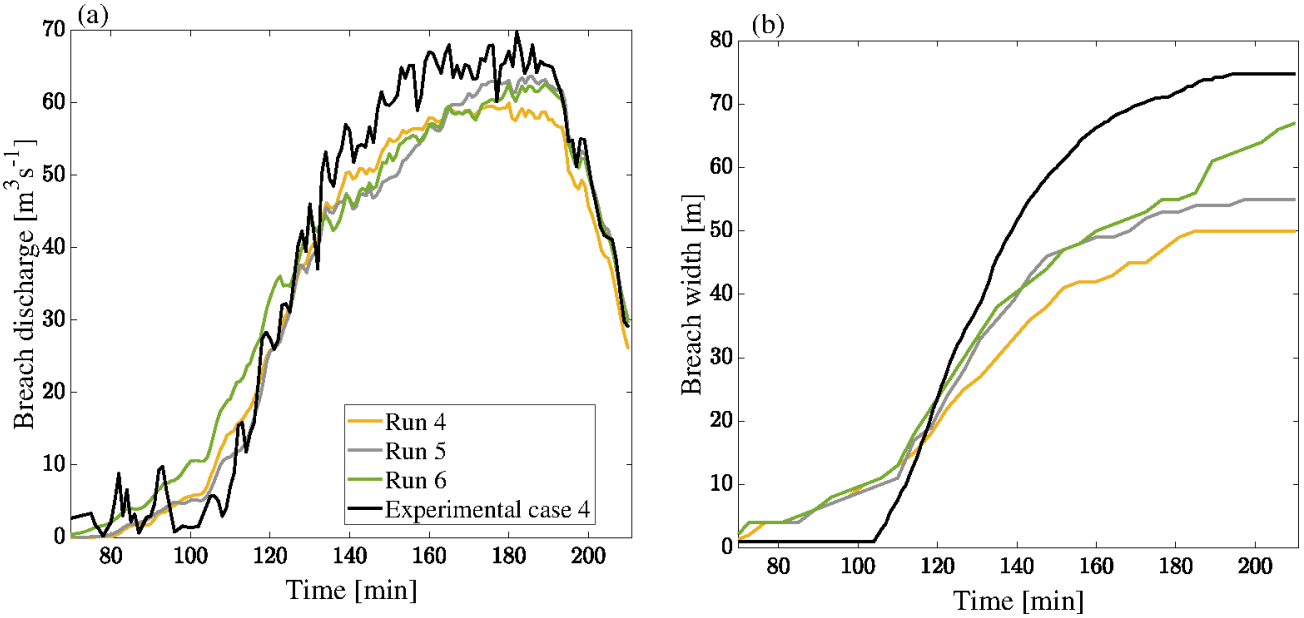

Figure 4.17: Comparison of Case 4 simulations with α_y= 18 and different α_x values : (a) breach discharge and (b) breach width at the crest level (y= 89 m).

Figures 4.16 and 4.17 depict simulated and measured breach width and discharge. The model generally underpredicted breach width and discharge for simulations with α_y set to 12 compared to runs performed with a coefficient α_y set to 18. The latter coefficient was advised by Kakinuma and Shimizu (2014) and allowed a better estimation of breach width and discharge. Regarding the effect of the Meyer-Peter and Müller (1948) coefficient in the longitudinal direction (α_x), it results in a slightly higher breach width, while its effect on breach discharge is not straightforward. For runs with α_x= 12, breach discharge is marginally higher for run 3 with the lowest α_x value before 140 minutes; however, it is lower than that estimated in runs 1 and 2 for advanced breach stages (time > 160 minutes). A possible reason is that the total bedload rate is reduced when lowering α_x values. This resulted in a lower breach width, section area (Figure 4.18), and discharge for run 3 compared to run 1. For run series with α_y equal 18, the breach width and section area increase when the Meyer-Peter and Müller (1948) coefficient in the longitudinal direction α_x is decreased. In the early breaching phase, the predicted values are very similar for runs 4, 5, and 6, while significant differences can be observed for time (> 120 minutes). Therefore, breach discharge was less sensitive and quite similar for the three runs as it is more likely to vary if significant changes in the breach dynamics area are observed during the early breaching stage. One should note that breach discharge increases earlier for run 6 with α_x equal 4 as the breach section is higher than it is for other runs (Figure 4.18). Figures 4.19 and 4.20 illustrate the position of breach extremities location along the longitudinal crest center line (y = 89 m). One can see that reducing the value of α_x influences the overall breach width but does not improve the location of the breach that is shifted towards the upstream end of the dike in the numerical model. Finally, the best fit for breach width is obtained for run 6 with α_x = 4 and α_y = 18, and breach discharge was also reasonably predicted and overall more conservative than other runs.

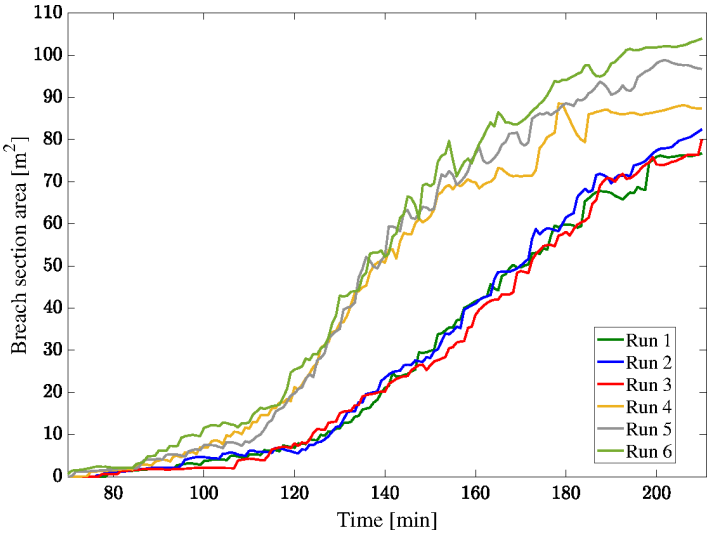

Figure 4.18: Comparison of resulting section breach area at the crest center line for Case 4 simulations with α_x= 12, α_x= 18 and different α_y values.

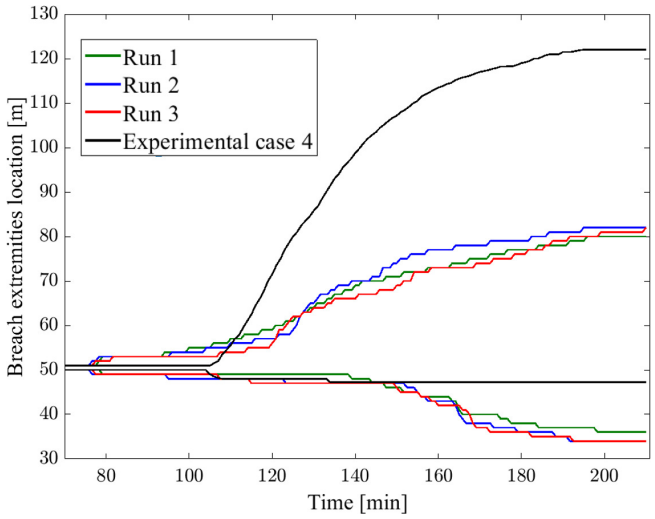

Figure 4.19: Comparison of Case 4 simulations with α_y= 12 and different α_x values : breach extremities location at the crest center line (y= 89 m) with initial notch located at x = 50 m.

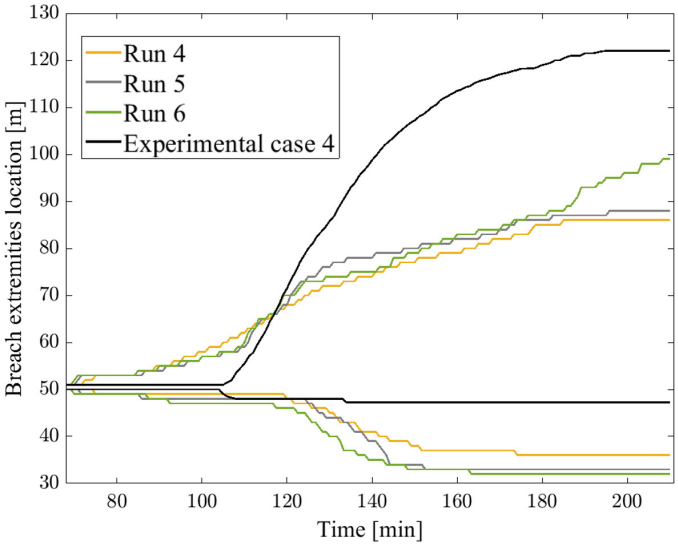

Figure 4.20: Comparison of Case 4 simulations with α_y= 18 and different α_x values : breach extremities location at the crest center line (y= 89 m) with initial notch located at x = 50 m.

4.5.4.2 Sediment repose angle

This section presents a short sensitivity analysis of breach dynamics to the user input repose angles and their possible improvement in predicting breach hydrograph that could result from the calibration of the different repose angles values with ϕ_{dep} for sediments deposition always defined as half the submerged sediments repose angle ϕ_{wet}. The details of the different runs are displayed in Table 4.3.

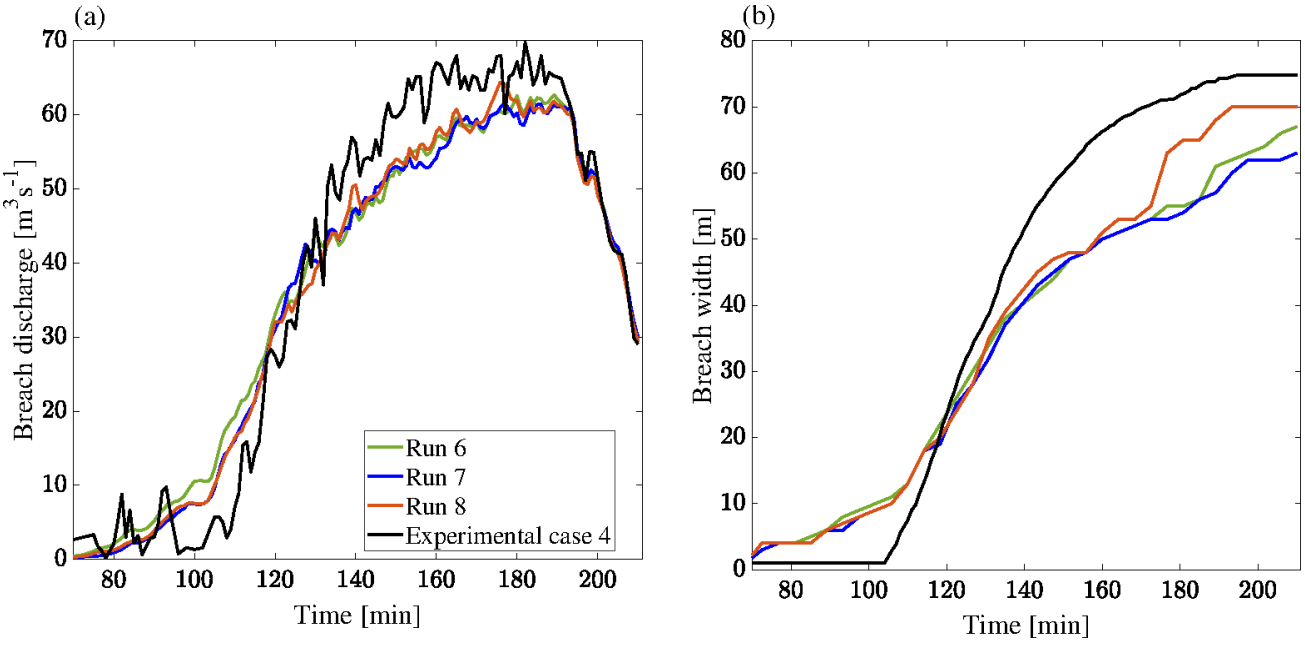

Figure 4.21: Comparison of resulting breach area for Case 4 simulations with different repose angles values.

It is clearly shown in Figure 4.21 that the resulting breach width is more impacted by changes in the wetted sediments repose angle values than its value for dry sediments. However, decreasing ϕ_{wet} in run 7 only increased breach width in the quasi-stabilization stage and thus did not allow any significant improvement of breach discharge prediction. The latter parameter could not be further decreased to respect the levee side slopes and avoid its collapse. Decreasing the value of ϕ_{dry} by 5° results in a similar prediction to that observed in run 6 over the entire duration of the breaching process.

4.5.4.3 Correction of bedload transport direction

Bedload deviation due to bed slope and bed forms effect was also included and compared with the Koch and Flokstra (1980) and Talmon et al. (1995) formulas as shown in Table 4.3.

Figure 4.22 presents the comparison of breach hydrographs and breach width for the different bedload deviation formulas. As it can be seen, the best agreement is achieved when using the Koch and Flokstra (1980) correction. Run 10 with Talmon et al. (1995) formula and a coefficient β_2 of 1.7 also provided good predictions, while 0.85 for β_2 estimated a lower breach width and discharge. These tendencies are relatively similar to that seen in the sensitivity analysis of the experimental Test 36 above.

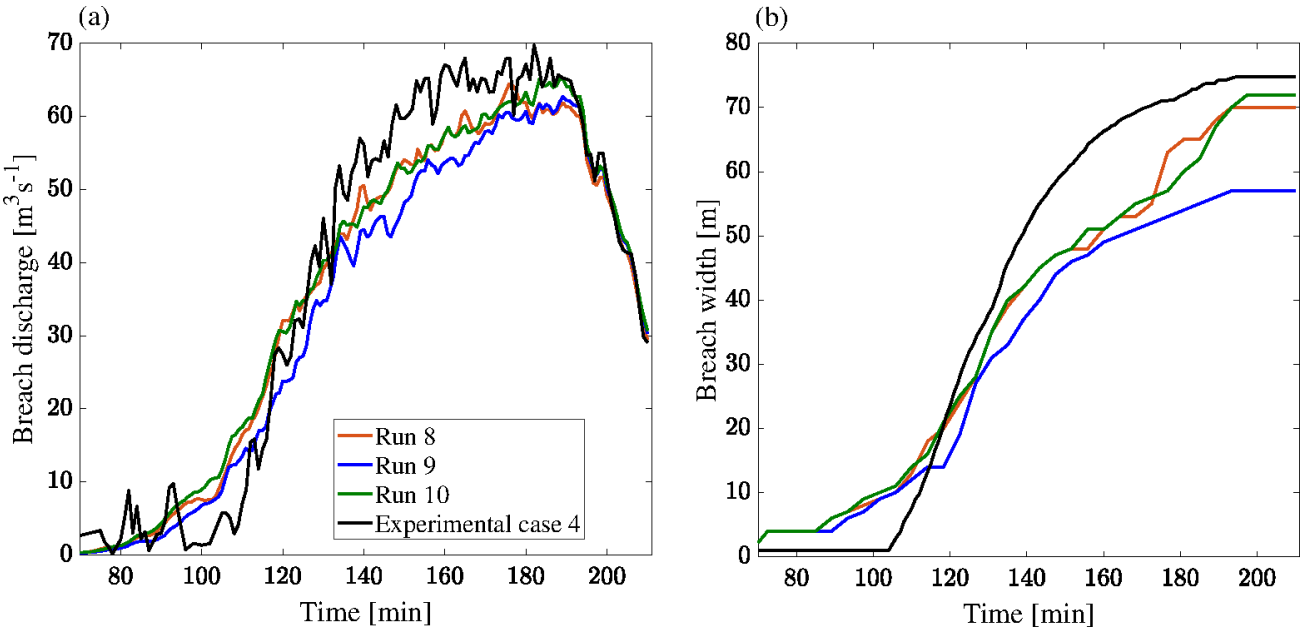

Figure 4.22: Comparison of Case 4 simulations with different corrections for the slope effect : (a) breach discharge and (b) breach width at the crest level (y= 89 m).

Run	NRMSE on breach discharge	NRMSE on breach width
Run 1 (Case 4)	23.9%	33.34%
Run 2 (Case 4)	26.6%	29.6%
Run 3 (Case 4)	27%	32.4%
Run 4 (Case 4)	7.2%	22.8%
Run 5 (Case 4)	7.1%	17.4%
Run 6 (Case 4)	8.1%	14.4%
Run 7 (Case 4)	7.9%	15.1%
Run 8 (Case 4)	7.2%	11.2%
Run 9 (Case 4)	9.4%	17.1%
Run 10 (Case 4)	7.5%	11.2%

Table 4.4: simulations of Case 4 with resulting NRMSE on breach width and discharge.

4.6 Simulation of the field experiment Case 2

4.6.1 Computational parameters and boundary conditions

The 2D computational domain for Case 2 consisted in structured triangular elements with an edge of 0.5 m as for Case 4. The same boundary conditions were used as in Chapter 3 (Fig.3.5). The Strickler coefficient was set to 38 ($m^{1/3}s^{-1}$) and a constant velocity diffusivity of 10^{-3} (m^2 s^{-1}) was adopted. Water depth and velocity advection were performed using the mass-conservative PSI and NERD schemes, respectively. Finlay, the time step was set to 0.1 s. Two sediments in the main channel, floodplain and levee beds consisted in non-cohesive sediments of median diameter d_{50} of 4.9 mm. The best results (**Run 6**, Table 4.5) were obtained with the Meyer-Peter and Müller (1948) formula and multiplying coefficients α_x and α_y set to 18. The magnitude of bedload transport was corrected using the Koch and Flokstra (1980) formula while bedload deviation was included by the Talmon et al. (1995) formula with an empirical coefficient β_2 set to 1.7. The sediments repose angles were: ϕ_{wet}=28° for submerged sediments , ϕ_{dry}=40°for dry sediments and ϕ_{dep}=14° for deposited sediments. The secondary currents option with the Engelund (1974) formula was also activated.

4.6.2 Overview of the performed simulations

Different runs were performed (Table 4.5) varying the morphodynamic module parameters, in order to obtain predictions closer to measurements. The resulting Normalized Root-Mean-Square Error values on breach width and discharge are also listed in Table 4.6.

Run	Repose angles	α_x	α_y	Additional options
Run 1 (Case 2)	ϕ_{wet}=30°, ϕ_{dry}=40°, ϕ_{dep}=14°	12	12	Koch and Flokstra (1980) deviation formula for slope effect, and Engelund (1974) formula for secondary currents.
Run 2 (Case 2)	ϕ_{wet}=30°, ϕ_{dry}=40°, ϕ_{dep}=15°	6	12	Same as Run 1.
Run 3 (Case 2)	ϕ_{wet}=30°, ϕ_{dry}=40°, ϕ_{dep}=15°	18	18	Same as Run 1.
Run 4 (Case 2)	ϕ_{wet}=30°, ϕ_{dry}=40°, ϕ_{dep}=15°	9	18	Same as Run 1.
Run 5 (Case 2)	ϕ_{wet}=28°, ϕ_{dry}=40°, ϕ_{dep}=14°	4	18	Same as Run 1.
Run 6 (Case 2)	ϕ_{wet}=28°, ϕ_{dry}=40°, ϕ_{dep}=14°	4	18	Talmon et al. (1995) (β_2= 1.7) deviation formula for slope effect, and Engelund (1974) formula for secondary currents.

Table 4.5: Case 2 simulations and corresponding numerical parameters.

4.6.3 General results

This section addresses the capabilities of the hydro-morphodynamic (TELEMAC-2D/GAIA) model to capture the main features of non-cohesive levee breaching for an additional field scale experiment with a lower inflow discharge and tighter levee crest than that of Case 4. The results presented in this section were the best achieved after a sensitivity analysis (**Run 6**, Table 4.5).

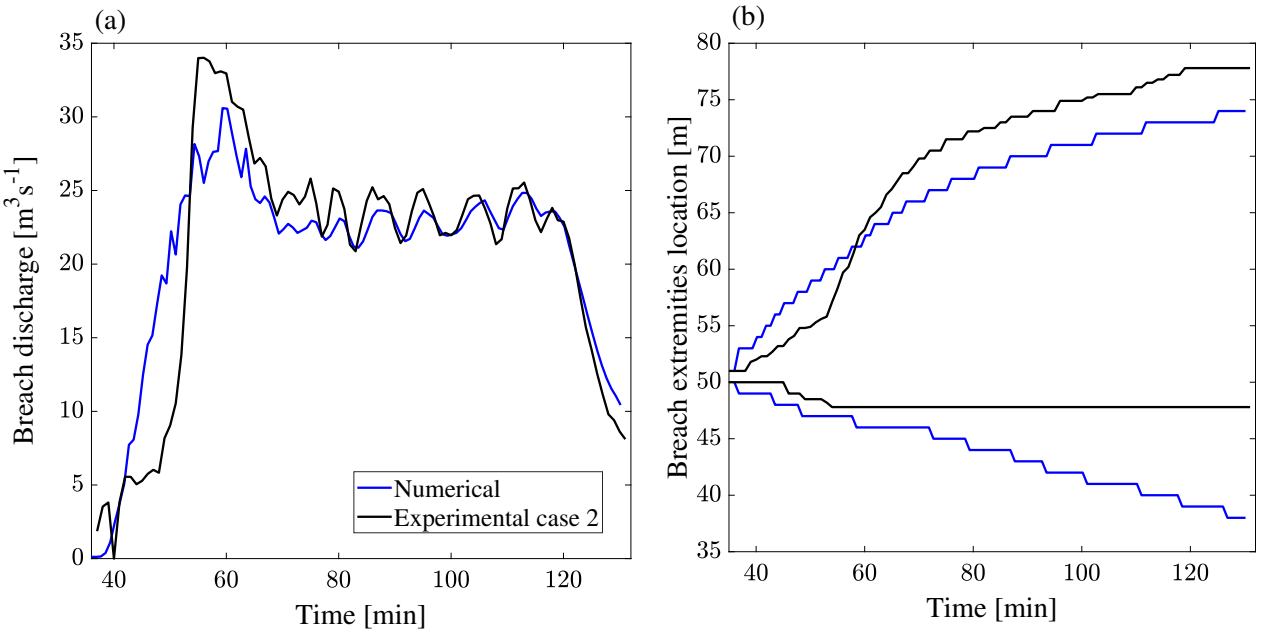

Figure 4.23: Comparison of Case 2 simulated and measured : (a) breach discharge and (b) breach extremities location along the longitudinal axis at the crest center line (y= 90.5 m), the notch center was located at x= 50 m.

Figures 4.23 and 4.24 compare the simulated and calculated breach outflow hydrographs, breach extremities evolution over the crest center line, and the total breach widths. The hydro-morphodynamic model reproduces these parameters well; the general trend of a rapid increase in the breach discharge and peak formation is well captured with a slightly lower magnitude. The model also reproduces an asymmetrical and progressive lateral breach expansion with a higher erosion of the downstream end of the breach due to the lateral arriving flow in the main channel. However, the calculated results exhibit a slightly anticipated breach widening and discharge increase. Additionally, breach extremities evolution in time at the crest center line is slightly underestimated downstream the notch (x > 50 m) while the upstream end was more eroded (x < 50 m). This is also visible in Figures 4.25 and 4.26 comparing the measured final bed laser scan to modeled bed at the end of the simulation. It shows that the upstream part of the dike is more eroded from the channel side and has a narrower shape in calculated results. This could partly explain the model's lower predicted magnitude for breach discharge.

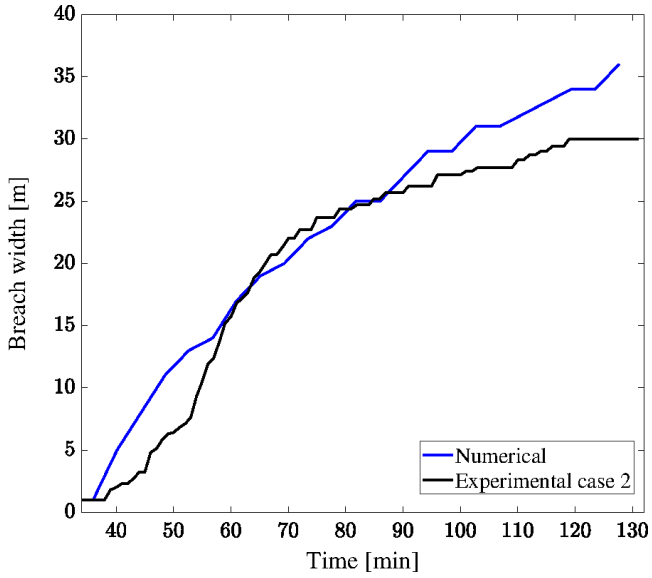

Figure 4.24: Comparison of simulated and measured breach width at the crest center line (y= 90.5 m) for Case 2.

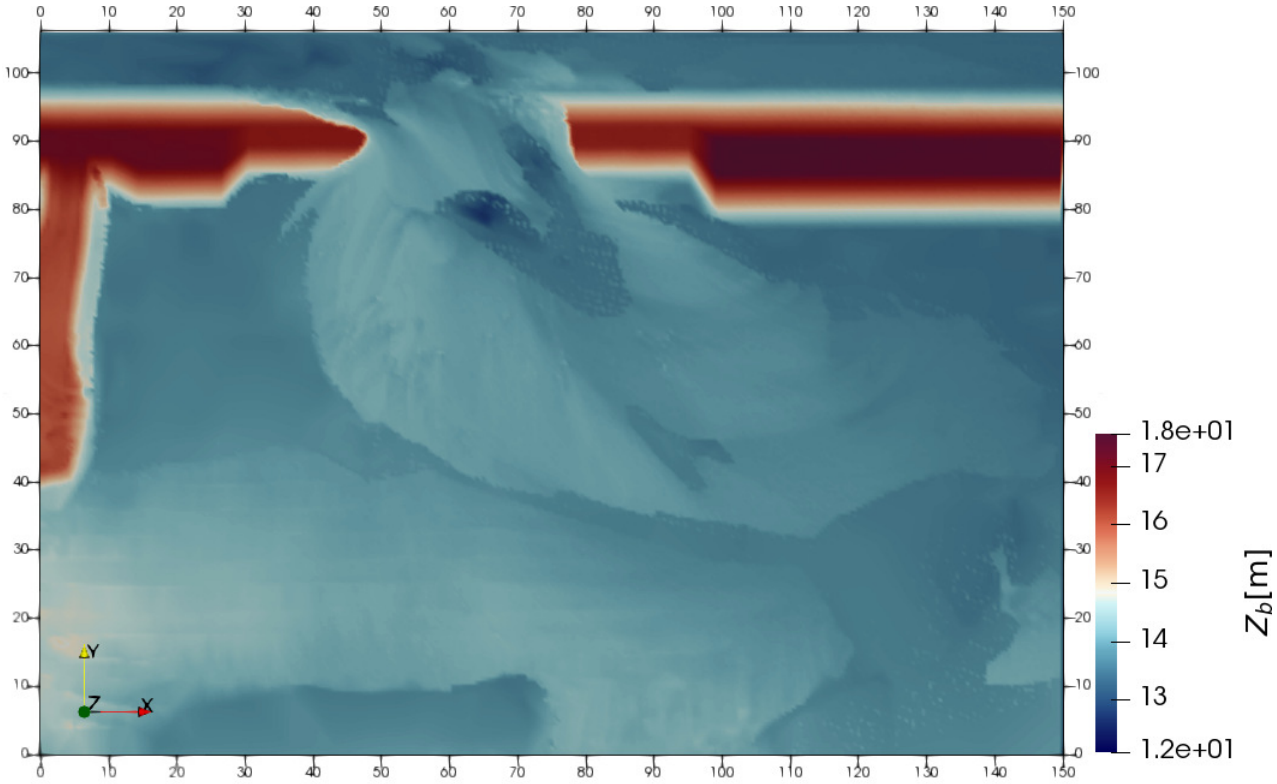

Figure 4.25: Laser scan of the test channel bed at the end of the breaching process for Case 2 (the water flows from the left to the right).

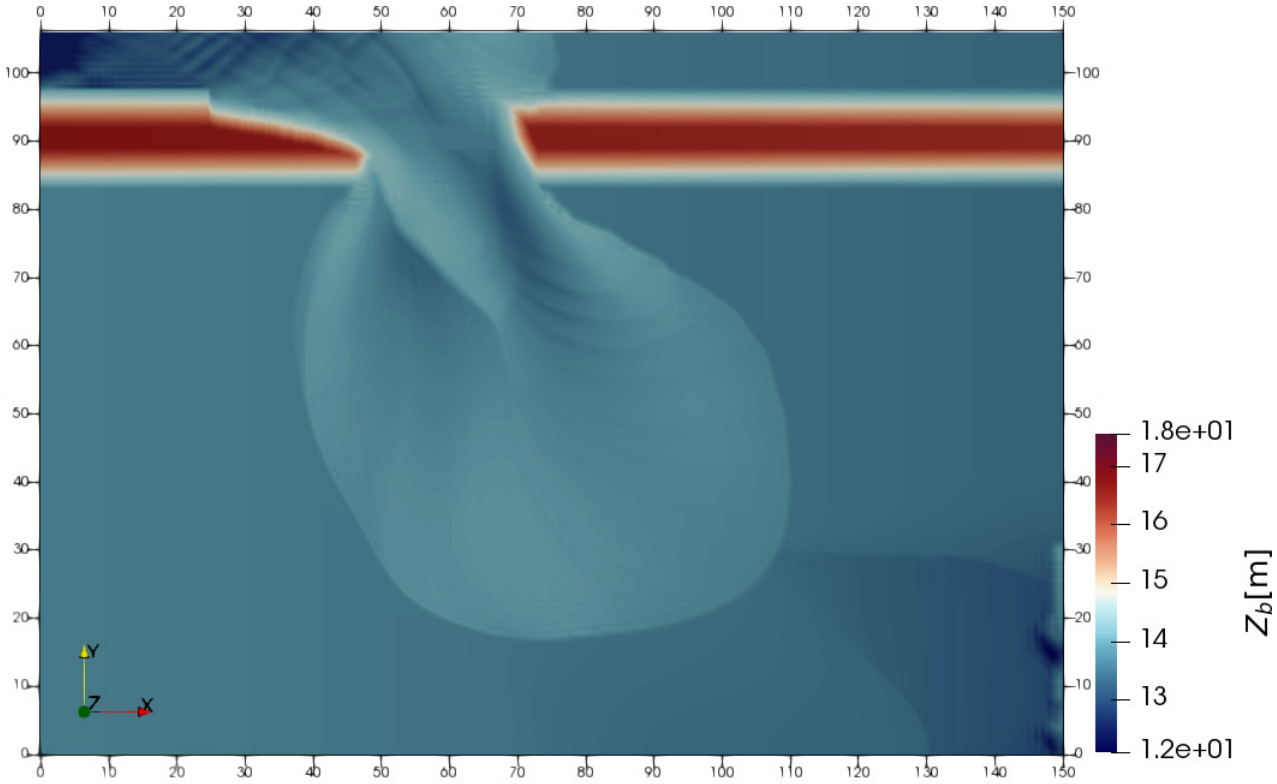

Figure 4.26: Simulated test channel bed at the end of the breaching process for Case 2 (the water flows from the left to the right).

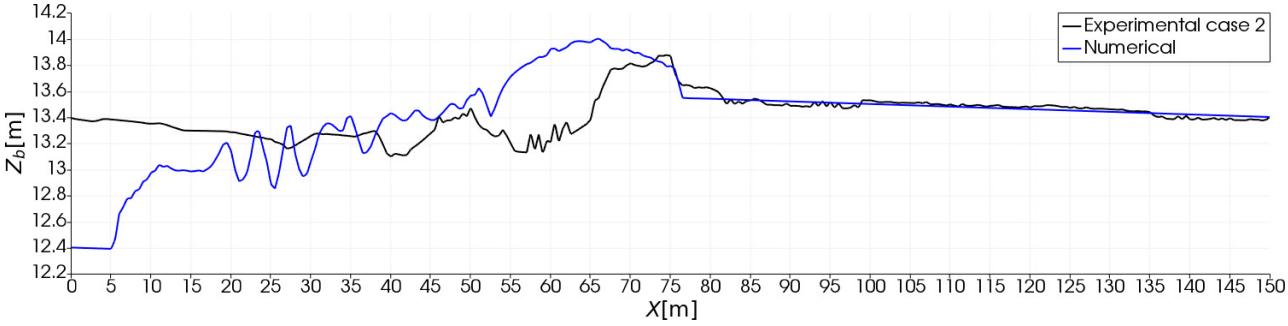

Figure 4.27: Simulated and measured bed longitudinal profile at the main channel center (y= 102 m) at the end of the breaching process for Case 2.

The main channel inflow discharge in this test was lower than in Case 4. Therefore levee erosion from the channel side was lower and the simulations with no reduction of the longitudinal bedload rate provided reasonable predictions. The levee's upstream part was eroded due to the parallel flow acceleration in the channel upstream when the breach expanded. On the other hand, one can see in Figure 4.27 that the main channel bed erosion was overpredicted at the inlet, which led to a higher amount of sediments deposited right after (x > 50 m). In this case, no significant bedforms had formed in the numerical results as the longitudinal bedload rate was not reduced as in Case 4.

4.6.4 Sensitivity analysis

4.6.4.1 Bedload transport formula

Comparisons between observed and computed breach width and discharge are shown in Figure 4.28 for different values of the Meyer-Peter and Müller (1948) dimensionless coefficients α_x and α_y shown in Table 4.5. The sediment repose angles were set at 30° and 40° for ϕ_{wet} and ϕ_{dry} and 14° for ϕ_{dep} (half ϕ_{wet}). The Koch and Flokstra (1980) corrections for the magnitude and deviation of bedload transport were used along with Engelund (1974) correction for secondary currents.

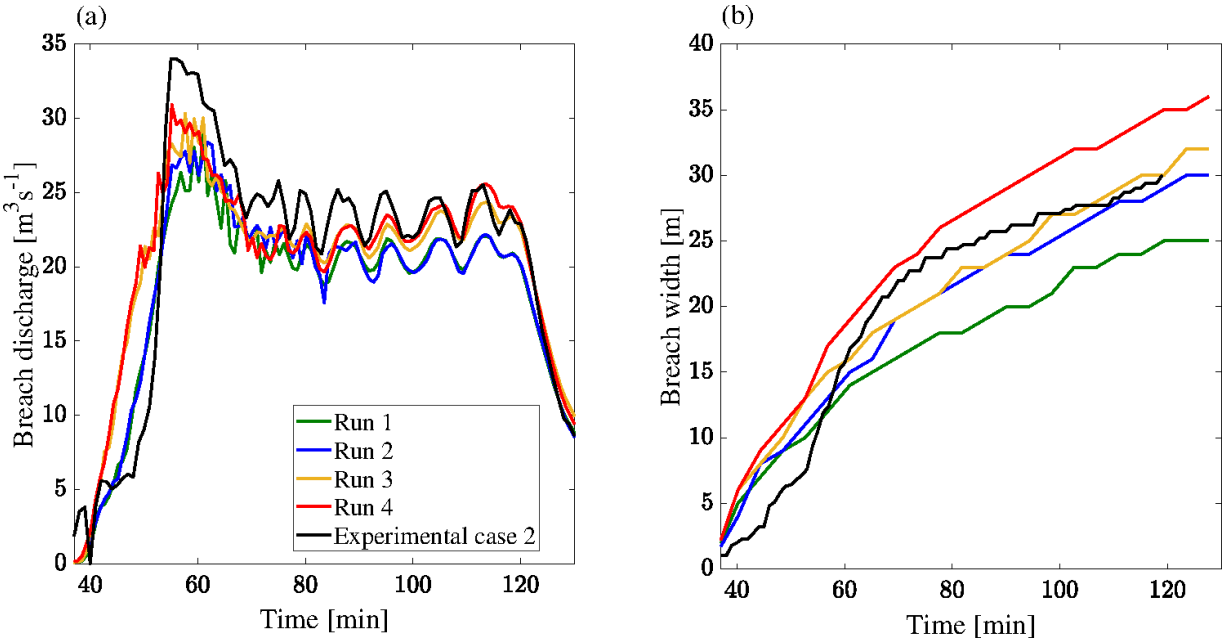

Figure 4.28: Comparison of Case 2 simulations with different α_x an α_y values : (a) breach discharge and (b) breach width at the crest level (y= 90.5 m).

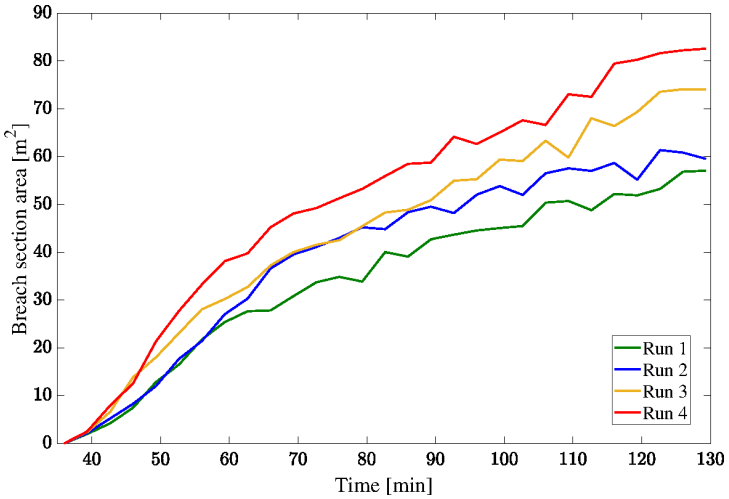

Figure 4.29: Comparison of Case 2 simulations with α_y= 18 and different α_x values : breach section area at the crest center line (y= 90.5 m).

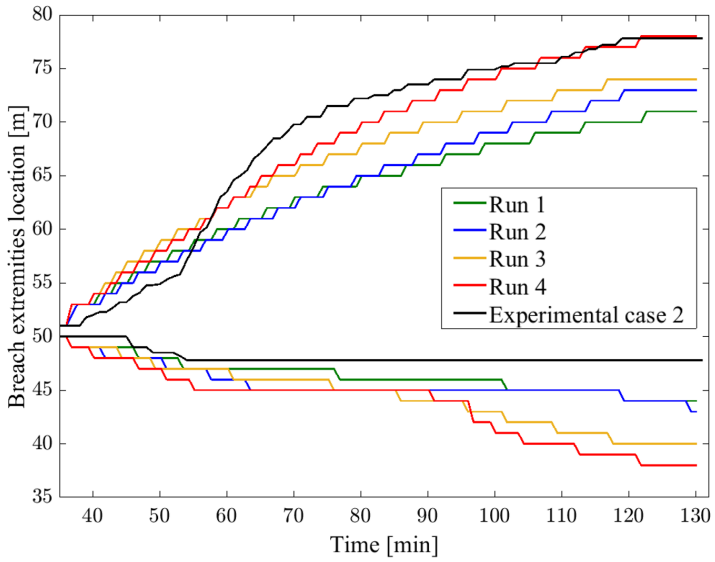

Figure 4.30: Comparison of Case 2 simulations with α_y= 18 and different α_x values : breach extremities location at the crest center line (y= 90.5 m) with initial notch located at x = 50 m.

Figure 4.28 compares simulated and measured breach width and discharge with different α_y and α_x values . The model results in lower breach widths and discharges with α_y set to 12 compared to runs performed with a coefficient α_y set to 18. In addition, reducing the Meyer-Peter and Müller (1948) coefficient in the longitudinal direction α_x results in a higher breach width and section area (Figure 4.29) but does not significantly affect breach discharge. In run 4 with α_y set to 18 and α_x reduced to 9, the breach width and section area significantly increase compared to run 3, especially for time (> 60 minutes). This did not improve the magnitude of breach discharge as it is less impacted after the rapid increase stage. Figure 4.30 illustrates the simulated and measured breach extremities location along the longitudinal crest center line (y = 90.5 m) as seen for Case 4, reducing the value of α_x influences the overall breach width but does not improve the location of the breach upstream end. Although run 2 provided slightly better NRMSE values (Table 4.6), the results for run 3 with α_x = 18 and α_y = 18 are selected to pursue the sensitivity analysis as breach width was reasonably predicted and breach discharge more conservative than in run 2.

4.6.4.2 Sediment repose angle

In order to compare the resulting breach lateral widening for a different slope stability criterion, an additional run was performed with a lower value for submerged sediments repose angle (Table 4.5). The latter parameter has been shown to impact the results more significantly than dry sediments repose angle. The stability of deposited sediments was defined as previously by half ϕ_{wet}. No significant difference is observed in Figure 4.31 between the simulated breach discharge and width when using the wetted sediments repose angle of 30° and 28°, with the other parameters being the same.

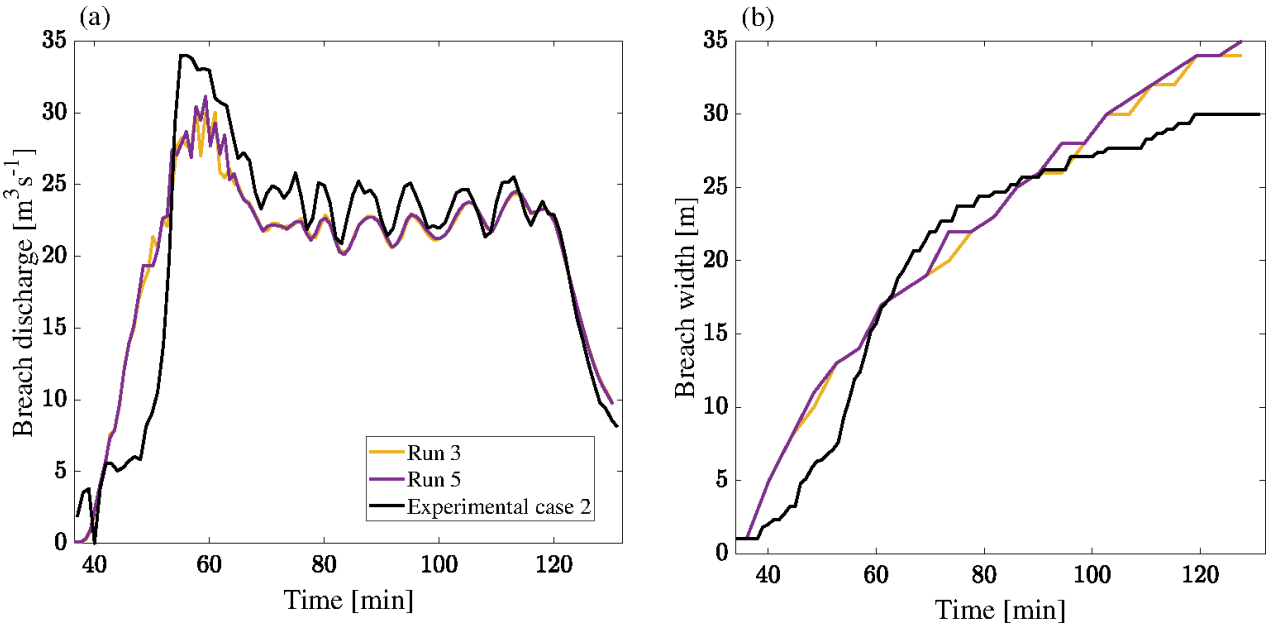

Figure 4.31: Comparison of Case 2 simulations with different repose angles values : (a) breach discharge and (b) breach width at the crest level (y= 90.5 m).

4.6.4.3 Correction of bedload transport direction

Regarding the influence of bedload transport deviation correction, an additional run was performed using the Talmon et al. (1995) equation with β_2 set to 1.7 (Table 4.5) as it provided better results for Test 36 and Case 4 than the 0.85 default value.

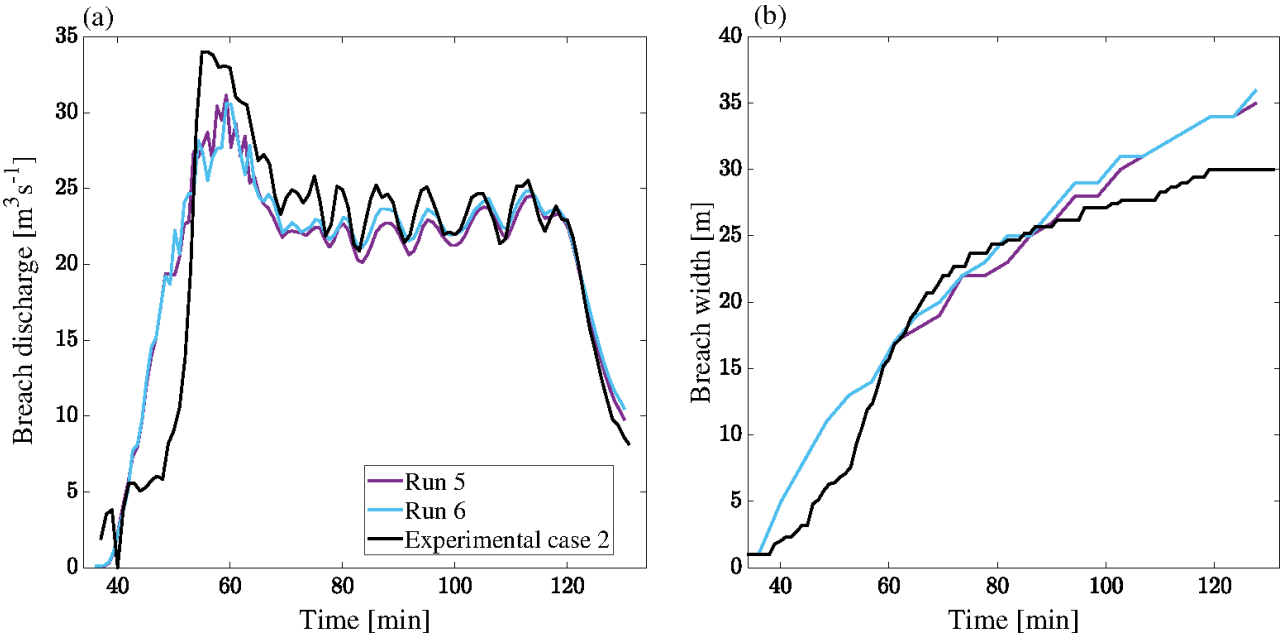

Figure 4.32: Comparison of Case 2 simulations with different bedload transport deviation formulas : (a) breach discharge and (b) breach width at the crest level (y= 90.5 m).

Figure 4.32 displays similar resulting breach discharge and width for both the Koch and Flokstra (1980) and Talmon et al. (1995) formulas. Still, run 6 provided slightly higher NRMSE values on breach width and discharge than run 5 (Table 4.6). However, it was retained as the best fit because it predicted breach discharge in a more conservative way.

Run	NRMSE on breach discharge	NRMSE on breach width
Run 1 (Case 2)	10.3%	16.8%
Run 2 (Case 2)	9%	7.8%
Run 3 (Case 2)	10.43%	8.7%
Run 4 (Case 2)	10.6%	14.06%
Run 5 (Case 2)	10.3%	10%
Run 6 (Case 2)	10.7%	10.5%

Table 4.6: Simulations of Case 2 with resulting NRMSE on breach width and discharge.

4.7 Discussion

The main advantage of detailed-physically based models is predicting breach characteristics without user-defined breach location, final dimensions, or start time. However, the simulations carried out in this chapter showed that results accuracy is variable and depends on the calibration of some model's parameters. Indeed, detailed-physically-based models also include empirical and semi-empirical models to compute bedload, bed slope, and secondary currents effects. Such equations include empirical coefficients that require careful calibration. Additionally, the number of possible choices and parameters combined in a sensitivity analysis can be significant. Each selected parameter can also influence the selection of the following one. For example, in the simulations presented for Test 36, the values of the repose angles were fixed to the measured values, and the bedload formula was varied. Figure 4.33 shows another possible choice consisting in decreasing the dry sediments repose angle ϕ_{dry} to 50° or 45° that can also lead to satisfactory results for the Meyer-Peter and Müller (1948) formula with a coefficient α=12.

The newly implementAshida and Michiue (1972) and Smart (1984) sediment transport formulas did not correctly predict breach dynamics. This was also verified by simulating test 38 from Rifai et al. (2019) performed in a similar configuration to that of Test 36 and a higher inflow discharge of 0.099 (m^3/s) and test 34 with a smaller main channel width (1.4 m) as shown in Figures 4.35 and 4.34. The discrepancies observed between the numerical and experimental breach characteristics for all the tests can also be due to the simplifications in the hydrodynamic component (hydrostatic pressure, negligible vertical velocity, mild bed slopes). An extensive analysis of the hydrodynamic parameters in TELEMAC-2D was performed by Rifai (2018) by updating the bottom with experimental data (3D breach geometry from Laser Profilometry Technique), including turbulence models, numerical schemes for advection, and secondary currents effect. However, the simulated velocity field

showed a more perpendicular deviation angle than experimental observations. In addition, Elalfy (2015) investigated the impact of non-hydrostatic pressure and bed slope on levee breach modeling and compared simulations with the classical shallow water equations to simulations performed with the Boussinesq equations and other simulations with a modified version of the Saint-Venant equations. However, no significant improvements were observed in the numerical results. This points to the limits of 2D numerical models that can not capture complex 3D flow structures.

Simulations of the field scale experiments Case 2 and Case 4 reasonably reproduced breach width and discharge. The sensitivity analysis performed for each field case highlighted the improvements in results quality when using a Meyer-Peter and Müller (1948) coefficient set to 18 as observed for laboratory experiments. Still, some details and features were not precisely captured, probably due to the model's simplifications. In addition, some specific experimental features could not be correctly reproduced, such as the blocks used to prevent erosion of the levee before breach expansion by the parallel flow in the main channel. Highly reducing the longitudinal bedload rate also impacts the total bedload rate and underestimated breach dimensions. Attempts to include this effect by increasing the critical shields for the inner levee slope did not allow breach opening at the initial notch location. This further resulted in the levee crest overtopping at different locations.

Finally, although using conventional bedload transport equations for levee breach modeling can be questionable, it provided good predictions compared to the linear excess shear stress equation used by Dazzi et al. (2019) to simulate Case 4. In addition, the sediment deposition was also predicted in the simulations presented in this Chapter, while it was not allowed in the model presented by Dazzi et al. (2019).

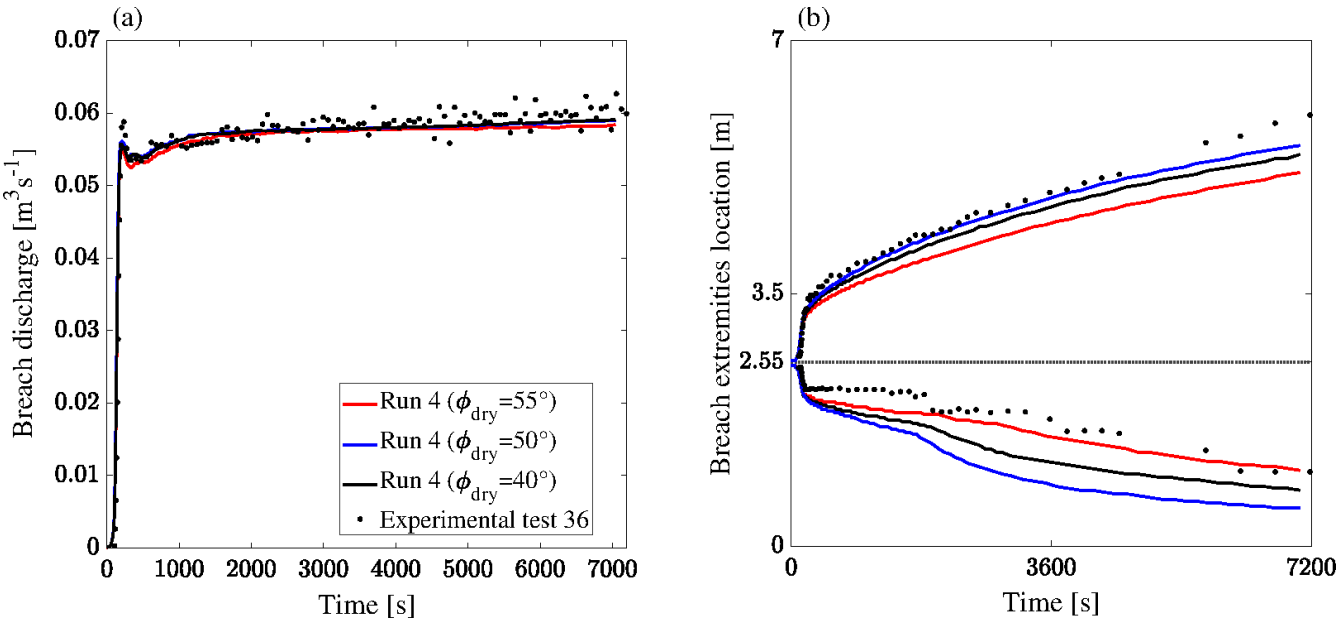

Figure 4.33: Comparison of Test 36 simulations with different repose angles values : (a) breach discharge and (b) breach extremities location along the longitudinal axis at the crest center line (y=0.65 m) and the dashed black line indicated initial notch location.

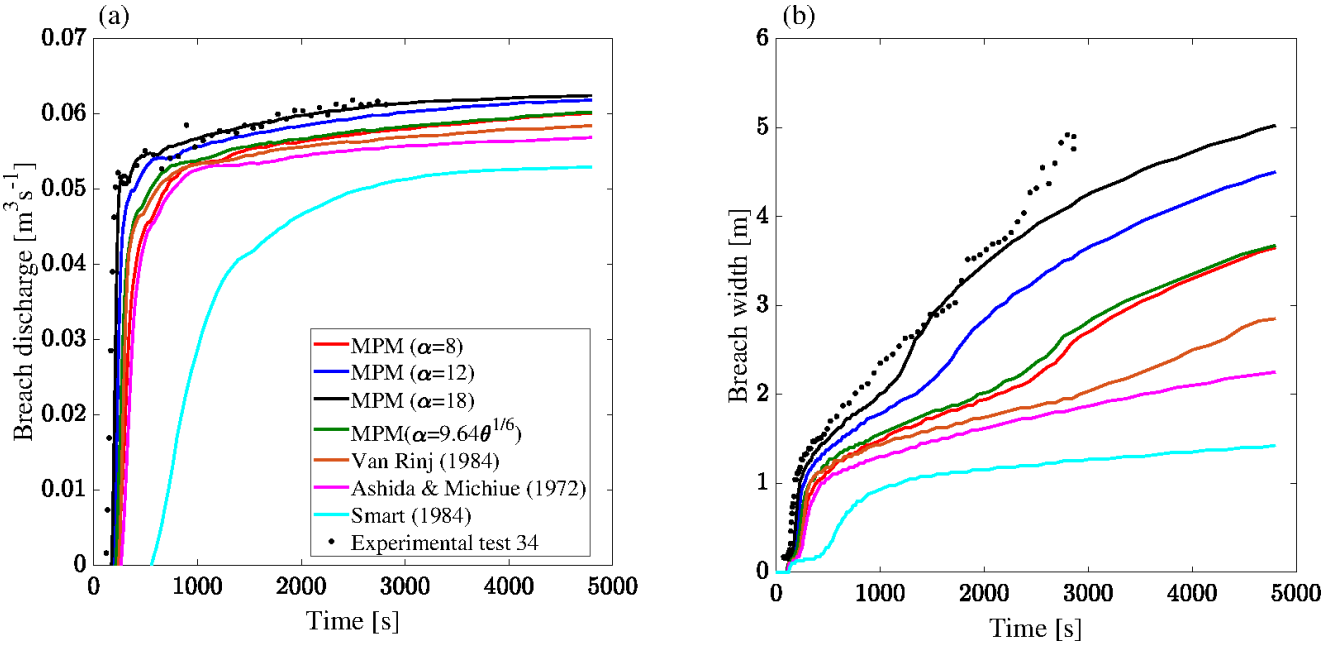

Figure 4.34: Comparison of test 34 simulations with different bedload transport equations : (a) breach discharge and (b) breach extremities location along the longitudinal axis at the crest center line (y=0.65 m) and the dashed black line indicated initial notch location.

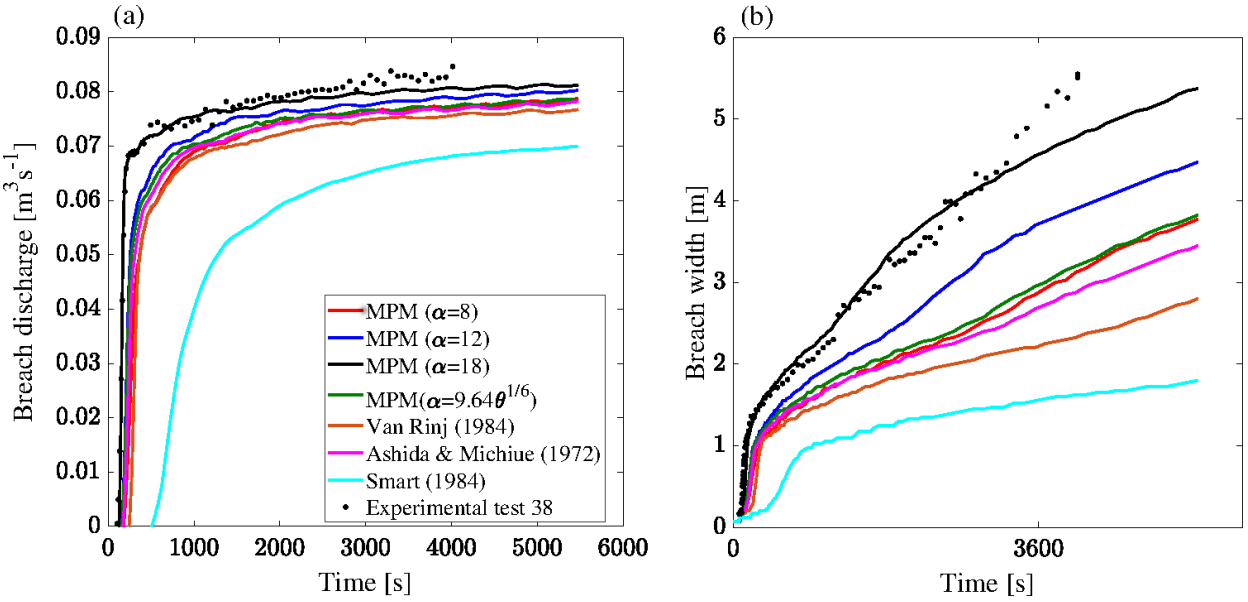

Figure 4.35: Comparison of test 38 simulations with different bedload transport equations : (a) breach discharge and (b) breach extremities location along the longitudinal axis at the crest center line (y=0.65 m) and the dashed black line indicated initial notch location.

4.8 Conclusion

In this Chapter, the capabilities of the hydro-morphodynamic (TELEMAC-2D with SISYPHE/GAIA) model to capture the main features of overtopping induced levee breaching were investigated through simulations of a laboratory case from the series of experiments presented by Rifai et al. (2019) and two field scale experiments performed in the Chiyoda test channel (Japan) by Kakinuma et al. (2013).

First, the qualitative and quantitative comparisons of simulated and measured hydrodynamic and morphodynamic breach characteristics for the laboratory experiment Test 36 (Rifai et al. (2019)) allowed the validation and evaluation of additional sediment transport equations implemented in SISYPHE/GAIA. The sensitivity analysis to the choice of bedload equation showed that the newly implemented Ashida and Michiue (1972) and Smart (1984) formulas did not perform as well as the Meyer-Peter and Müller (1948) formula with a dimensionless coefficient of 18 that, seems to be the best-fitted value for non-cohesive dikes surface erosion as suggested by Kakinuma and Shimizu (2014). Second, improving the slope failure module to state-of-the-art clearly improved simulated breach longitudinal profiles and resulted in a better agreement with measured breach width and discharge. Finally, the different corrections proposed in the numerical model to mimic the impact of some physical processes that are not explicitly computed were tested. The formulas for bedload direction correction by Koch and Flokstra (1980) and Talmon et al. (1995) with a coefficient of 1.7 had similar results, and the Engelund (1974) correction for secondary currents significantly improved the model predictions.

The lessons from the detailed numerical analysis with the laboratory experiment Test 36 were adopted to simulate the field scale cases 2 and 4. The model reasonably predicted the main breach characteristics for well-calibrated input parameters without specifying breach location, final dimensions, or initiation time. The levee erosion was also directly estimated with bedload transport capacity empirical Meyer-Peter and Müller (1948) equation that provided the best results with an α coefficient set to 18 (noting that in Case 4 the longitudinal bedload coefficient was reduced to 4 to avoid levee collapse before breaching). In addition, the influence of the user-defined repose angles values was investigated and highlighted a higher sensitivity of the results to the submerged sediments repose angle values rather than dry sediments repose angle. One should note that some details of the breaching process were not captured by the numerical model, such as breach extremities location along the crest center line and the breach initiation time that was slightly anticipated for field scale cases 2 and 4. This is not surprising if we recall all the simplifications included in the numerical model. In the hydrodynamic module, the Shallow Water equations are solved with the assumption of hydrostatic pressure distribution and neglected vertical velocities. In addition, the sediment transport module simulates surface erosion based on empirical bedload equations. It includes unstable slope failure with a simple geometric approach that makes it difficult to accurately reproduce specific field site features such as the presence of additional material layers (the blocks used in field-scale experiments to avoid excessive levee erosion by lateral channel flow) and complex geotechnical slope failure modes.

Chapter 5

Conclusions and perspectives

5.1 General conclusions

Numerical models can improve flood risk management and enhance the resilience of protected areas with adapted counter-measures. In the case of levee failure, the resulting inundations are aggravated, and predicting resulting flood maps requires an accurate estimate of breach dynamics and discharge. However, levee breaching mechanisms are still poorly understood, and available modeling approaches require further validation to assess their advantages and limitations. The primary purpose of this thesis work was to enrich the current knowledge about levee breaching mechanisms and improve the performances of the breach modeling tools in TELEMAC-MASCARET.

The first part of the thesis elucidated the physical mechanisms of non-cohesive levees breaching due to overtopping flows through laboratory experiments performed at the National Laboratory for Hydraulics and Environment (LNHE) of EDF-R&D. The experimental set-up and measurement techniques presented by Rifai (2018) were used. Additional experiments were carried out with a movable bed in the main channel, floodplain, and dike foundation. Both main channel width and input discharge were varied through test series to investigate their possible influence on breach dynamics. The results were analyzed and discussed considering the previous experimental data (with a rigid bottom in the main channel, floodplain, and dike foundations) performed by Rifai et al. (2019). The analysis of 3D breach expansion data from the Laser Profilometry Technique and water level measurements allowed a detailed comparison of breach dimensions and outflow hydrographs for the different tested configurations.

The hydrodynamic regime (initial Froude number) in the main channel had a dominant effect on breach dynamics compared to the main channel width. A higher Froude number in the main channel induced deeper and wider breaches with a higher erosion of the downstream end of the breach. Regarding the influence of the main channel width, experiments indicated that decreasing the main channel width enhances the portion of the flow deviated to the breach channel and results in higher breach discharge to main channel inflow ratios with a peak formation in breach hydrograph for most tests with low input discharges in the main channel. The same trends were also reported in experiments with a rigid channel bed presented by Rifai et al. (2019). Finally, the experiments with an erodible layer in the channel and dike foundation displayed larger and deeper breaches and thus conveyed higher breaches than rigid bed equivalent configurations.

In the second part, numerical developments of empirical breach laws and the RUPRO model (Paquier and Recking (2004)) were made in the BREACH module of TELEMAC-2D. The capabilities of each breach parametric law and of RUPRO model to reproduce main breach characteristics for field scale levee breaching experiments were investigated in the context of a simplified physically based approach. In such approaches, breach dimensions are parametrically estimated as surface erosion processes are not explicitly modeled, while the two-dimensional Shallow Water equations

are solved for the flow field.

The model can capture breach outflow if well calibrated, as the results strongly depend on user-defined parameters. Besides the intrinsic empirical parameters specific to each breach model (erosion rate for the simple linear widening formula or the empirical factors f_1, f_2 and u_c for the Verheij and Van der Knaap (2003) and erodibility coefficient in the RUPRO model), all models require a user-defined breach location, breach final bed elevation, breach ultimate width (except the Verheij and Van der Knaap (2003) breach law and RUPRO model) and a breach initiation criterion (except for the RUPRO model). Among all tested breach models, the RUPRO model is the most predictive and does not require breach initiation criterion nor breach final width, it is then followed by the Verheij and Van der Knaap (2003) model which can achieve an equilibrium state for equivalent hydrodynamic conditions in the channel and floodplain.

Field observations and experimental investigations proved that levee lateral breaching mainly occurs downstream from the initial location. Most empirical laws provided similar results when using a symmetrical or asymmetrical breach widening for the tested configurations. At the same time, the RUPRO model was clearly more sensitive as the erosion rate is directly estimated from the hydrodynamic forces applied on the levee bed. However, defining an asymmetry coefficient for breach widening is not straightforward forwards, and different values can be found in the literature. Additional simulations showed that one could assume levee widening only in the downstream direction and predict equivalent results with the asymmetrical upstream and downstream widening configuration. On the other hand, it was demonstrated that using a quasi-instantaneous breach vertical erosion was valid in the context of a progressive lateral opening. Still, the latter conclusions need further analysis and tests with different configurations.

Regarding the Verheij and Van der Knaap (2003) breach widening law, we proposed the use of the hydraulic head instead of the water level (original formula), and simulations demonstrated that the modified version better predicts breach width and discharge, especially for high river channel inflow discharges in which the flow velocity is significant.

We also investigated different options for the use of the RUPRO model. Its original and modified versions (in the IMPACT project) performed well for both field cases. However, the options, including a reduced wetted perimeter during the widening step and reduced lateral shear stress, did not capture breach dynamics for case 4.

In the third part of the thesis, the hydro-morphodynamic (TELEMAC-2D with SISYPHE/GAIA) model was enriched with additional bedload transport equations, and its slope failure module was improved to state of the art in order to differentiate submerged, emerged, and deposited levee material. The developments were validated by simulating a laboratory experiment from test series presented by Rifai et al. (2019). Then, a sensitivity analysis was carried out and highlighted improvements in modeled breach discharge and width for the multiple repose angles version of the bank failure module. On the other hand, the newly implemented Smart (1984) and Ashida and Michiue (1972) formulas did not result in accurate predictions. Two field-scale experiments performed in the

Chiyoda test channel (Japan) by Kakinuma et al. (2013) were also simulated. Comparing model predictions to experimental measurements comforted that the Meyer-Peter and Müller (1948) bedload formula with a dimensionless coefficient of 18 is particularly adapted to model levee surface erosion as suggested by Kakinuma and Shimizu (2014). In addition, the corrections for bedload direction by Koch and Flokstra (1980) and Talmon et al. (1995) with a coefficient of 1.7 provided satisfactory and similar predictions. The Engelund (1974) correction for secondary currents also displayed more accurate results.

Although the model well predicted general breach features, one should note that input parameters calibration was still necessary to achieve the best agreement with experimental measurements. In addition, the discrepancies observed between measured and computed parameters pointed to some limitations of the hydro-morphodynamic model. First, the hydrodynamic model simplifications include a hydrostatic pressure distribution and a negligible vertical velocity, while field observations highlighted complex 3D flow structures in the vicinity of the breach. Second, the morphodynamic module relies on a simple geometric slope failure approach that can not account for complex geotechnical processes such as levee erosion at the dike toe and advanced geotechnical slope failure modes. Additionally, it is not adapted for abrupt block failure as observed in cohesive embankments.

In conclusion, both modeling approaches showed sensitivity to user input parameters and choices. Therefore, a sensitivity analysis was necessary to achieve good predictions. Such analysis should also be performed for future real-field uses. The simplified physically-based approach is less time-consuming than the physically-based approach and performs well in predicting general breach parameters. It seems to be an interesting tool to support flood risk management where the model usability on extended computational domains is necessary. Regarding the user-defined parameters, lessons from the present work, historical levee failure accidents, and experiments can be used to guide the modeler for the different input parameters choices.

5.2 Perspectives

Looking back at the scientific needs presented in the introduction of this research work and the conclusions described above, possible further experimental investigations and numerical developments are presented in this section.

Physical modeling

- The impact of the main channel width on breach dynamics was not clearly elucidated and requires further investigations with a wider range of main channel widths.
- Although important advances were made in the field of experimental investigation of levee failure there is still a need to extend experiments to more complex configurations with realistic

stratified levees containing various materials, including sand-gravel material or cohesive-sand material.

- Relevant parameters were identified to impact breach dynamics and resulting discharge however in most experiments the parameters were varied one at a time. Studying the interaction of multiple parameters would improve our knowledge of the physics in levee failure.
- After overtopping, piping is the second cause for levee failure. However, experimental investigations on this subject are scarce. Therefore, physical modeling of levee failure due to piping is called.

Numerical modeling

- The different models presented in this thesis were validated and investigated in laboratory and field scale experiments. Additional investigations on real field cases with complex topographies and levees would bring more information about their performances in complex configurations.
- Simplified physically based models represent an interesting alternative to purely empirical approaches and complex physically-based models. However, further analysis of the uncertainties related to user-defined parameters is needed. This would allow an appreciation of the performances of each model based on its capabilities to predict breach characteristics taking into account the required inputs and their uncertainties.
- In the detailed hydro-morphodynamic model, we pointed out an important mesh dependence of the slope failure algorithm. Additionally, it is not adapted for applications on cohesive embankments failures as it does not ensure stable elements in a single iteration. At the same time, attempts to increase the sub-iterations of this module resulted in very high computational times (Die Moran (2012)), making it inapplicable on extensive real field cases. Therefore, we performed a literature review on existing slope failure algorithms and several studies were found interesting (Volz (2013),Elalfy et al. (2018), Evangelista et al. (2015)). A possible way to improve this module would be to compute the volume or mass of sediments at each node of the computational domain required to stabilize the element and add this quantity as a source term directly in the Exner equation Exner (1920) as it is done for bedload transport. The results presented in Chapter 4 also highlighted the limitations of simple geometric slope failure models that can not reproduce complex geotechnical processes such as the headcut erosion and erosion at dike toe. Possible further developments by coupling the hydromorphodynamic module with a geotechnical erosion module such as MEANDER from the CONCEPTS model (Langendoen et al. (2016)) would enrich the modeled physical processes. The eventual improvements in results quality would then be discussed against possible computational resources required to couple the three codes (hydrodynamic, sediment transport, and geotechnical erosion modules).

- The limitations of the Shallow Water equations were addressed in the present work, and studies in the literature based on the Boussinesq equations and modified Saint-Venant equations to account for bed slope did not perform better. Therefore, further investigation of levee breaching with full 3D hydro-morphodynamic models would help discuss the possible improvements in the accuracy of the results compared to 2D models, considering the required computational times and resources.

- Conclusions above highlighted a strong dependency of numerical results to user-input parameters. Therefore, in future simulations the models need to be combined with advanced tools for the sensitivity analysis and uncertainties quantification.

Appendix A

Appendix A

A.1 Mesh dependency of the slope failure module

In this section, we present simulations performed with SISYPHE in a standalone mode with no bedload or suspended load transport; only the slope failure module is activated. The study case consists of a 1 m wide and 16 m long rectangular channel. The bed consisted of three sediments classes with different sizes and fractions (2 mm, 3 mm and 4 mm median diameters with associated fractions 0.1, 0.2 and 0.7, respectively). The sediment repose angle was set to 30° leading to a lower critical slope than the initial bed slope (Figure A.1) to trigger sediment sliding. In order to see how the computational mesh size influences the results of sediment sliding, we performed four different simulations with four mesh sizes ranging from the coarser with 1600 elements to the finer with 102400 elements as show in Table A.1. The mesh refinement was performed by splitting each element by four with the STBTEL tool of TELEMAC-MASCARET as shown in Figure A.2.

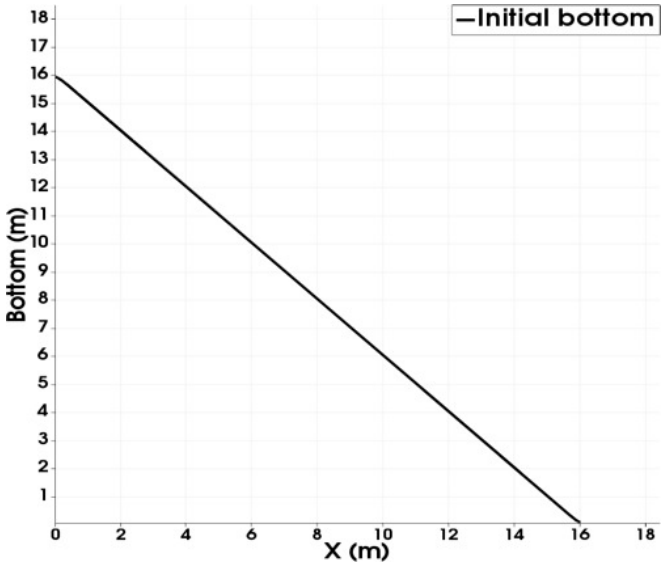

Figure A.1: Initialed slope

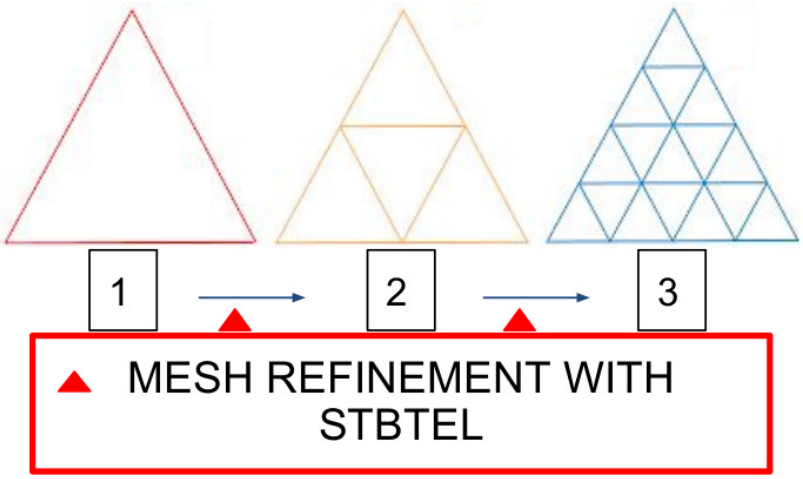

Figure A.2: Initialed slope

Mesh	Mesh 1	Mesh 2	Mesh 3	Mesh 4
Elements	1600	6400	25600	102400

Table A.1: Computational meshes characteristics.

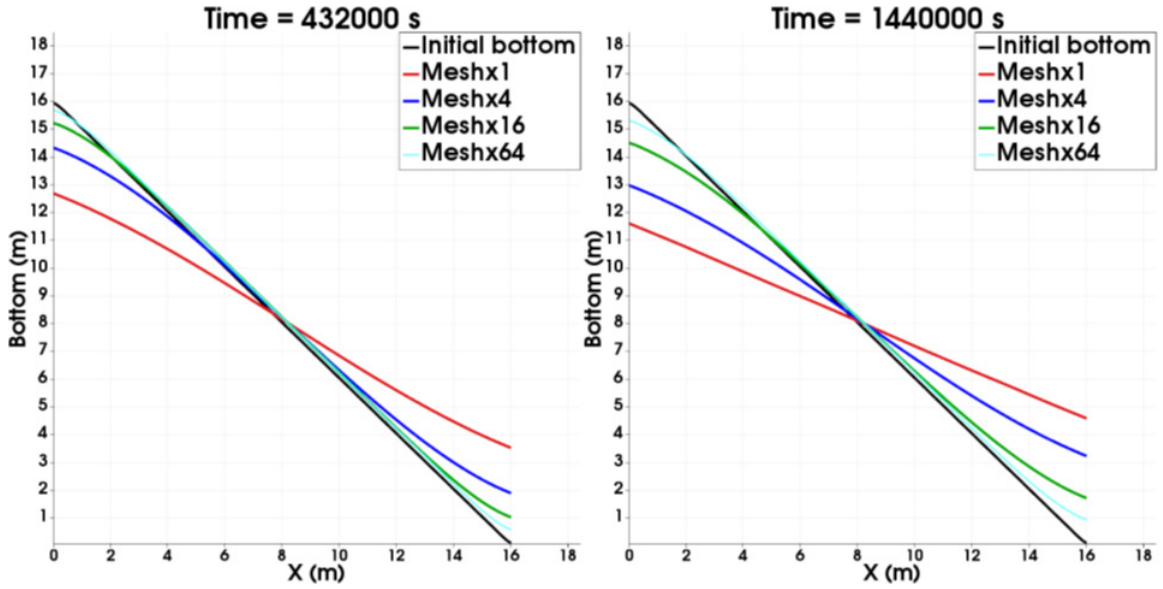

Figure A.3: Bed evolution for different mesh sizes and constant CFL.

Figures A.3 show a clear dependence of the resulting bed slope evolution on mesh size . No convergence could be achieved and one can see that the less unstable slopes are obtained for coarser meshes while finer ones show a very slow evolution towards a stable slope This is mainly due to the algorithm that performs rotations element per element making the module highly dependent on mesh size.

Appendix B

Appendix B

B.1 Influence of mesh size

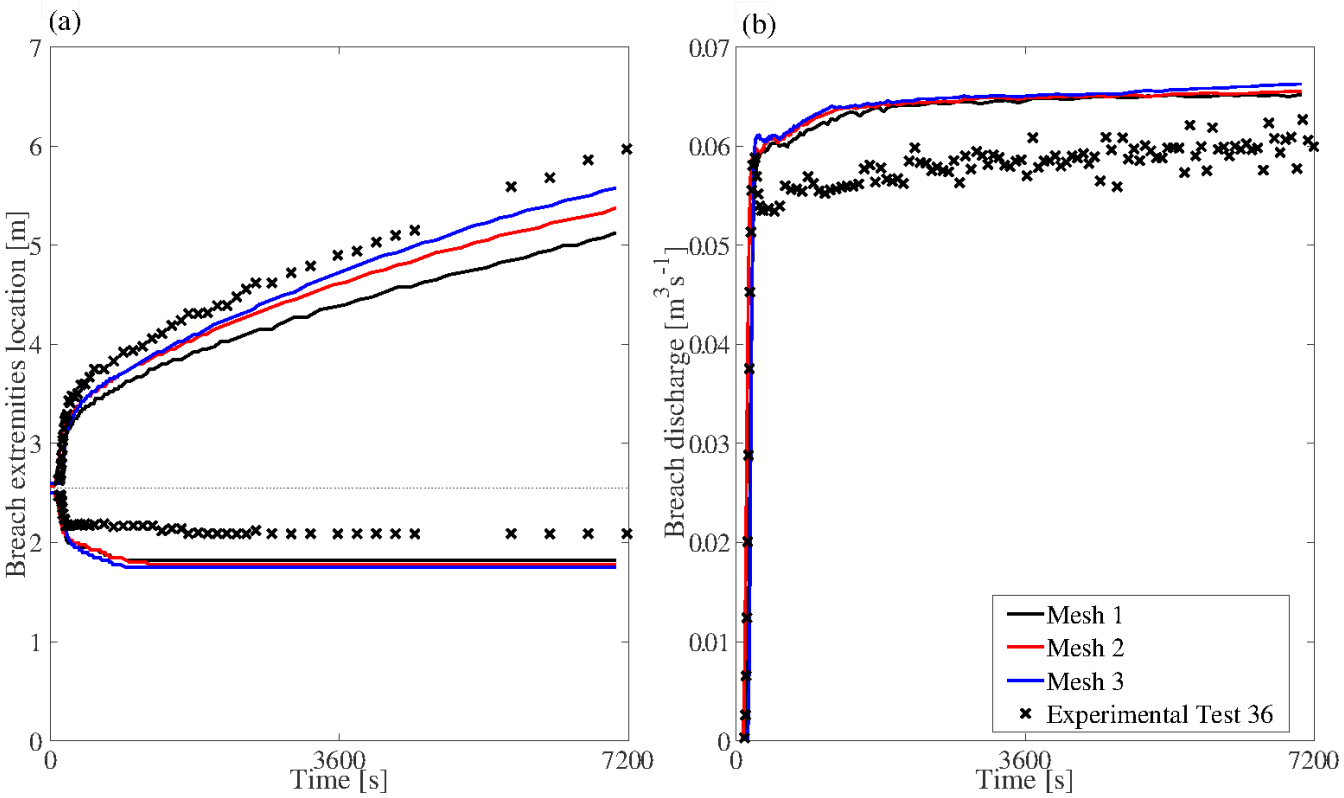

Figure B.1: Comparison of Test 36 simulations with different meshes: (a) breach extremities location along the longitudinal axis at the crest center line (y=0.65 m) and (b) breach discharge.

Run	Number of elements	NRMSE on breach discharge	NRMSE on breach total width
Mesh 1	15575	17.4%	6.3%
Mesh 2	27110	15.8%	6.2%
Mesh 3	62459	16.9%	6.4%

Table B.1: Simulations of Test 36 with different meshes and resulting NRMSE on breach width and discharge.

In simulations presented by Rifai (2018) the influence of mesh size was investigated for 2D hydrodynamic simulations only. In this section a similar sensitivity analysis is performed using a 2D hydro-morphodynamic model. The experimental case 36 was represented with unstructured triangular elements with a varying size evolving from coarse elements in the main channel and floodplain to finer elements in the dike region. We used three different mesh sizes as shown in Table B.1. To start the sensitivity analysis the energy loss was due to bottom friction was represented with the Strickler formula and a coefficient $K = 80$ (m $^{1/3}$ s^1). A constant velocity diffusivity of 10^{-4} m^2/s was applied for the turbulence term closure. The characteristics advection scheme is used for velocity fields and the PSI scheme was selected for water depth. Only bedload transport was modeled using the Meyer-Peter and Müller (1948) formula with a multiplying coefficient set to 12, both the magnitude and direction of bedload were corrected using the Koch and Flokstra (1980) formula with empirical parameters set to default values (β = 1.3). Figure B.1 shows slight differences between the computed breach discharge for the three tested mesh sizes while breach widening seems more sensitive to the mesh size. A possible explanation for that is the highly mesh dependent module user to simulate sediment slide as shown in A. Mesh 2 was therefore retained as it resulted in satisfactory estimation of breach width and discharge.

Bibliography

Aerts, J. C., Botzen, W. J., Clarke, K. C., Cutter, S. L., Hall, J. W., Merz, B., Michel-Kerjan, E., Mysiak, J., Surminski, S., and Kunreuther, H. Integrating human behaviour dynamics into flood disaster risk assessment. *Nature Climate Change*, 8(3):193–199, 2018.

Ahadiyan, J., Bahmanpouri, F., Adeli, A., Gualtieri, C., and Khoshkonesh, A. Riprap effect on hydraulic fracturing process of cohesive and non-cohesive protective levees. *Water Resources Management*, 36, 01 2022. doi: 10.1007/s11269-021-03044-6.

Al-Hafidh, I. A. I., Calamak, M., LaRocque, L. A., Chaudhry, M. H., and Imran, J. Experimental investigation of flood management by an instantaneous levee breach. *Journal of Hydraulic Engineering*, 148(2):04021056, 2022. doi: 10.1061/(ASCE)HY.1943-7900.0001960.

Al-Hashemi, H. and Al-Amoudi, O. A review on the angle of repose of granular materials. *Powder Technology*, 330:397–417, 05 2018. doi: 10.1016/j.powtec.2018.02.003.

Al-Riffai, M. Experimental study of breach mechanics in overtopped noncohesive earthen embankments. 2014.

Amaral, S., Viseu, T., and Ferreira, R. Estimates of breach effluent flow from the failure by overtopping of homogeneous earthfill dams based on non-local measurments. *E-proceedings of the 38th IAHR World Congress*, pages 1411–1425, 2019. doi: 10.3850/38WC092019-5557.

Amaral, S., Caldeira, L., Viseu, T., and Ferreira, R. M. L. Designing experiments to study dam breach hydraulic phenomena. *Journal of Hydraulic Engineering*, 146(4):04020014, 2020. doi: 10.1061/(ASCE)HY.1943-7900.0001678.

Apel, H., Merz, B., and Thieken, A. Influence of dike breaches on flood frequency estimation. *Computers Geosciences*, 35(5):907–923, 2009. ISSN 0098-3004. doi: https://doi.org/10.1016/j.cageo.2007.11.003. Modelling and Simulation of Dangerous Phenomena for Hazard Mapping.

Ashida, K. and Michiue, M. Studies on bed load transportation for nonuniform sediment and river bed variation. *Disaster Prevention Research Institute Annuals*, 14, 1972.

ASCE/EWRI task committee . Earthen Embankment Breaching. *Journal of Hydraulic Engineering*, 137(12):1549–1564, 2011. doi: 10.1061/(ASCE)HY.1943-7900.0000498.

Bendegom, L. V. Some considerations on river morphology and river improvement, De Ingenieur vol. 59–4, pp. B1–11. *Dutch. English translation: Nat. Res. Council of Canada, Technical Translation*, 1054:1963, 1947.

Bernard, R. and Schneider, M. Depth-averaged numerical modeling for curved channels. page 48, 09 1992.

Bhattarai, P. K., Nakagawa, H., Kawaike, K., and Zhang, H. Study of breach characteristics and scour pattern for overtopping induced river dyke breach. *E-roceedings of the 36th IAHR World Congress*, pages 1–11, 2015.

Brunner, G. L. HEC RAS - River analysis system user's manual, version 3.1." Rep. No. CPD- 68U.S. Army Corps of Engineers, Hydrologic Engineering Center, Davis, CA. 2002.

Cestero, J. A. F., Imran, J., and Chaudhry, M. H. Experimental investigation of the effects of soil properties on levee breach by overtopping. *Journal of Hydraulic Engineering*, 141(4):04014085, 2015. doi: 10.1061/(ASCE)HY.1943-7900.0000964.

Charrier, G. *Etude expérimentale des ruptures de digues fluviales par surverse.* PhD thesis, Aix-Marseille Université, 2015.

Chinnarasri, C., Tingsanchali, T., Weesakul, S., and Wongwises, S. Flow patterns and damage of dike overtopping. *International Journal of Sediment Research*, 18(4):301–309, 2003.

Clemens. Dorfmann, Konrad. Moser, G. Z. 2D Numerical Simulations of Embankment Dam Failure Due To Overtopping. In *XXIst TELEMAC-MASCARET User Conference Proceedings*, 2014.

Coleman, S. E., Andrews, D. P., and Webby, M. G. Overtopping Breaching of Noncohesive Homogeneous Embankments. *Journal of Hydraulic Engineering*, 128:829–838, 2002. doi: 10.1061/(ASCE) 0733-9429(2002)128:9(829).

Danka, J. and Zhang, L. M. Dike Failure Mechanisms and Breaching Parameters. *Journal of Geotechnical and Geoenvironmental Engineering*, 141(9):04015039, 2015. ISSN 1090-0241. doi: 10.1061/(ASCE)GT.1943-5606.0001335.

Dazzi, S., Vacondio, R., and Mignosa, P. Integration of a levee breach erosion model in a gpu-accelerated 2d shallow water equations code. *Water Resources Research*, 55(1):682–702, 2019. doi: https://doi.org/10.1029/2018WR023826.

Dhiman, S. and Patra, K. C. Experimental study of embankment breach based on its soil properties. *ISH Journal of Hydraulic Engineering*, 26(3):247–257, 2020. doi: 10.1080/09715010.2018.1474500.

Di Baldassarre, G., Kreibich, H., Vorogushyn, S., Aerts, J., Arnbjerg-Nielsen, K., Barendrecht, M., Bates, P., Borga, M., Botzen, W., Bubeck, P., Marchi, B. D., Llasat, C., Mazzoleni, M., Molinari, D., Mondino, E., Mard, J., Petrucci, O., Scolobig, A., Viglione, A., , and Ward, P. J. Hess opinions:

An interdisciplinary research agenda to explore the unintended consequences of structural flood protection. *Hydrology and Earth System Sciences*, 22(11):5629–5637, 2018a.

Di Baldassarre, G., Kreibich, H., Vorogushyn, S., Aerts, J., Arnbjerg-Nielsen, K., Barendrecht, M., Bates, P., Borga, M., Botzen, W., Bubeck, P., Marchi, B. D., Llasat, C., Mazzoleni, M., Molinari, D., Mondino, E., Mard, J., Petrucci, O., Scolobig, A., Viglione, A., , and Ward, P. J. Hess opinions: An interdisciplinary research agenda to explore the unintended consequences of structural flood protection. *Hydrology and Earth System Sciences*, 22(11):5629–5637, 2018b.

Die Moran, A. *Physical and numerical modelling investigation of induced bank erosion as a sediment transport restoration strategy for trained rivers*. PhD thesis, 2012.

Dou, S. T., Wang, D. W., Yu, M. H., and Liang, Y. J. Numerical modeling of the lateral widening of levee breach by overtopping in a flume with 180 bend. *Natural Hazards and Earth System Sciences*, 14(1):11–20, 2014. doi: 10.5194/nhess-14-11-2014.

El Kadi Abderrezzak, K. and Paquier, A. Applicability of sediment transport capacity formulas to dam-break flows over movable beds. *Journal of Hydraulic Engineering*, 137(2):209–221, 2010. ISSN 0733-9429. doi: 10.1061/(ASCE)HY.1943-7900.0000298.

El Kadi Abderrezzak, K., Die Moran, A., Tassi, P., Ata, R., and Hervouet, J.-M. Modelling river bank erosion using a 2d depth-averaged numerical model of flow and non-cohesive, non-uniform sediment transport. *Advances in Water Resources*, 93:75–88, 2016. ISSN 0309-1708. doi: https://doi.org/10.1016/j.advwatres.2015.11.004. Numerical modelling of river morphodynamics.

Elalfy, E., Tabrizi, A. A., Asce, A. M., Chaudhry, M. H., and Asce, D. M. Numerical and Experimental Modeling of Levee Breach Including Slumping Failure of Breach Sides. 144(2):1–18, 2018. doi: 10.1061/(ASCE)HY.1943-7900.0001406.

Elalfy, E. Y. E. M. Numerical and experimental investigations of dam and levee failure. (October), 2015. doi: 10.1115/1.4002035.

Engelund, F. Flow and bed topography in channel bends. *Journal of the Hydraulics Division*, 100(11): 1631–1648, 1974.

Evangelista, S. Experiments and numerical simulations of dike erosion due to a wave impact. *Water (Switzerland)*, 7(10):5831–5848, 2015. ISSN 20734441. doi: 10.3390/w7105831.

Evangelista, S., Greco, M., Iervolino, M., Leopardi, A., and Vacca, A. A new algorithm for bank-failure mechanisms in 2D morphodynamic models with unstructured grids. *International Journal of Sediment Research*, 30(4):382–391, 2015. ISSN 10016279. doi: 10.1016/j.ijsrc.2014.11.003.

Exner, F. M. *Zur physik der dünen*. Hölder, 1920.

Faeh, R. Numerical Modeling of Breach Erosion of River Embankments. *Journal of Hydraulic Engineering*, 133(9):1000–1009, 2007. ISSN 0733-9429. doi: 10.1061/(ASCE)0733-9429(2007)133:9(1000).

Fell, R., Hanson, G., Herrier, G., Marot, D., and Wahl, T. Relationship between the erosion properties of soils and other parameters. In *Erosion in Geomechanics Applied to Dams and Levees*, pages –. 2013. doi: 10.1002/9781118577165.ch5.

Ferrari, A., Dazzi, S., Vacondio, R., and Mignosa, P. Enhancing the resilience to flooding induced by levee breaches in lowland areas: a methodology based on numerical modelling. *Natural Hazards and Earth System Sciences*, 20(1):59–72, 2020. doi: 10.5194/nhess-20-59-2020.

Flynn, S., Vahedifard, F., and Schaaf, D. *A Dataset of Levee Overtopping Incidents*, pages 99–108. doi: 10.1061/9780784483701.010.

Foster, M., F. R. and Spannagle, M. A method for assessing the relative likelihood of failure of 20 embankment dams by piping. *Canadian Geotechnical Journal*, 37(5):1025–1061, 2020.

Frank, P.-j. R. *HYDRAULICS OF SPATIAL DIKE BREACHEFrank, P. R. (2016). HYDRAULICS OF SPATIAL DIKE BREACHES presented by. https://doi.org/10.3929/ethz-a-010803310S presented by.* PhD thesis, 2016.

Fredlund, D. and Rahardjo, H. Soil mechanics for unsatured soils. xxiv, 01 1993. doi: 10.1002/9780470172759.

Froehlich, D. C. Embankment Dam Breach Parameters and Their Uncertainties. *Journal of Hydraulic Engineering*, 134(12):1708–1721, 2008.

Froehlichl, D. C. Embankment dam breach parameters revisited. *Water Resources Engineering, Proceedings of the ASCE Conference on Water Resource Engineering*, pages 887 – 891, 1995.

Froehlichl, D. C. Embankment dam breach parameters and their uncertainties. *Journal of Hydraulic Engineering*, 134(12):1708–1721, 2008.

Fry, J.-j., Vogel, A., Royet, P., and Courivaud, J.-r. Dam failures by erosion : lessons from ERINOH data bases Key words. In *6th International Conference on Scour and Erosion*, pages 273–280, Paris, 2012.

Guan, M., Wright, N. G., and Sleigh, P. A. 2D Process-Based Morphodynamic Model for Flooding by Noncohesive Dyke Breach. *Journal of Hydraulic Engineering*, 140(7):04014022, 2014. ISSN 0733-9429. doi: 10.1061/(ASCE)HY.1943-7900.0000861.

Hanson, G. and Hunt, S. Lessons learned using laboratory jet method to measure soil erodibility of compacted soils. *Applied Engineering in Agriculture*, 23, 05 2007. doi: 10.13031/2013.22686.

Hanson, G. J., Wahl, T., Temple, D., Hunt, S., and Tejral, R. *ERODIBILITY CHARACTERISTICS OF EMBANKMENT MATERIALS.* 2010.

Hirabayashi, Y., Roobavannan, M., Koirala, S., Konoshima, L., Yamazaki, D., Watanabe, S., Kim, H., and Kanae, S. Global flood risk under climate change. *Nature Climate Change*, 3:816–821, 09 2013. doi: 10.1038/nclimate1911.

Hui, R., Jachens, E., and Lund, J. Risk-based planning analysis for a single levee. *Water Resources Research*, 52(4):2513–2528, 2016. doi: https://doi.org/10.1002/2014WR016478.

ICOLD. Internal erosion of existing dams, levees and dikes, and their foundations. Volume 1: Internal erosion processes and engineering assessment. Technical report, 2015.

IPCC. Impacts, adaptation and vulnerability: Regional aspects. Technical Report 688 pp, Cambridge Univ. Press, United Kingdom and New York, 2014.

Islam, M. Experimental investigation on failure behavior of levee based on its bed material and river bed height relative to floodplain level. *Journal of Agriculture Rural Development*, 10:65–74, 06 2018.

Islam, S. *Study on Levee Breach and Successive Disasters in Low-Land Through Numerical and Experimental.* PhD thesis, Nagoya University, 2012.

Jandora, J. and Říha, J. *The failure of embankment dams due to overtopping*. VUTIUM, 2008. ISBN 8021435275.

Jüpner, R.and Henning, B. Deichbruch fischbeck–zwei jahre danach. *Wasser und Abfall*, 2015.

Kakinuma, T. and Shimizu, Y. Large-Scale Experiment and Numerical Modeling of a Riverine Levee Breach. *Journal of Hydraulic Engineering*, 140(9):04014039, 2014. doi: 10.1061/(ASCE)HY.1943-7900.0000902.

Kakinuma, T., Tobita, D., Yokoyama, H., and Takeda, A. Levee breach observation at Chiyoda experimental flume. In *Advances in River Sediment Research*, pages 1013–1020, Kyoto, 2013. ISBN 9781138000629.

Kheirkhah Gildeh, H., Hosseini, P., Zhang, H., Riaz, M., and Acharya, M. *Canal embankment failure mechanism, breach parameters and outflow predictions*, pages 61–74. 08 2019. ISBN 9780429319778. doi: 10.1201/9780429319778-6.

Knight, D.W., D. J. and Hamed, M. Boundary shear in smooth rectangular channels. *Journal of Hydraulic Engineering*, 110(4):405–422, 1984.

Koch, F. and Flokstra, C. *Bed Level Computations for Curved Alluvial Channels: Prepared for the 19th IAHR Congress, New Delhi, India, February 1981.* Waterloopkundig Laboratorium, 1980.

Langendoen, E. J., Mendoza, A., Abad, J. D., Tassi, P., Wang, D., Ata, R., El kadi Abderrezzak, K., and Hervouet, J.-M. Improved numerical modeling of morphodynamics of rivers with steep banks. *Advances in Water Resources*, 93:4–14, 2016. ISSN 0309-1708. doi: https://doi.org/10.1016/j.advwatres.2015.04.002. Numerical modelling of river morphodynamics.

MacDonald, T. and Langridge-Monopolis., J. Breaching Characteristics of Dam Failures. *Journal of Hydraulic Engineering*, 110(5):567–586, 1984.

Madsen, H., Lawrence, D., Lang, M., Martinkova, M., and Kjeldsen, T. R. Review of trend analysis and climate change projections of extreme precipitation and floods in Europe. *Journal of Hydrology*, 519(PD):3634–3650, 2014. doi: 10.1016/j.jhydrol.2014.11.003.

Meyer-Peter, E. and Müller, R. Formulas for bed-load transport. In *International Association for Hydraulic Structures Research*. IAHR, 1948.

Michelazzo, G. *Breaching of river levees : analytical flow modelling and experimental hydro-morphodynamic investigations*. PhD thesis, University of Florence, 2014.

Michelazzo, G., Oumeraci, H., and Paris, E. Laboratory Study on 3D Flow Structures Induced by Zero-Height Side Weir and Implications for 1D Modeling. *Journal of Hydraulic Engineering*, 141 (10):04015023, oct 2015. doi: 10.1061/(ASCE)HY.1943-7900.0001027.

Michelazzo, G., Oumeraci, H., and Paris, E. New hypothesis for the final equilibrium stage of a river levee breach due to overflow. *Water Resources Research*, 7(54):4277–4293, 2018.

Montalvo-Bartolomei, A. and Robbins, B. Laboratory evaluation of lightweight sand boil filters. *Proceedings of the ASDSO Dam Safety*, Orlando, Florida, 2019.

Morris, M. Breaching Processes: A state of the art review. *FLOODsite*, page 1 to 70, 2009.

Morris, M., Hassan, M., and Vaskinn, K. Breach formation: Field test and laboratory experiments. *Journal of Hydraulic Research*, 45(sup1):9–17, 2007. ISSN 0022-1686. doi: 10.1080/00221686.2007.9521828.

Morris, M., Hassan, M., Kortenhaus, A., and Visser, P. Breaching processes: A state of the art review. *FLOOD site Project Report, T06-06-03*, 01 2009.

Morris, M. W. *CADAM: A European Concerted Action Project on Dambreak Modelling*, pages 42–53. 2000. doi: 10.1680/d2000.28708.0006.

Müller, C., Frank, P.-J., and Hager, W. H. Dyke overtopping: effects of shape and headwater elevation. *Journal of Hydraulic Research*, 54(4):410–422, 2016. doi: 10.1080/00221686.2016.1170072.

Nagy, L. Estimating dike breach length from historical data. *Periodica Polytechnica Civil Engineering*, 50(2):125–138, 2006. ISSN 15873773.

OCDE. *The Economic Consequences of Climate Change*. 2015. doi: https://doi.org/https://doi.org/10.1787/9789264235410-en.

Onda, S., Hosoda, T., Jaćimović, N. M., and Kimura, I. Numerical modelling of simultaneous overtopping and seepage flows with application to dike breaching. *Journal of Hydraulic Research*, 57 (1):13–25, 2019. doi: 10.1080/00221686.2018.1442882.

Orendorff, B., Al-Riffai, M., Nistor, I., and Rennie, C. D. Breach outflow characteristics of non-cohesive embankment dams subject to blast. *Canadian Journal of Civil Engineering*, 40(3):243–253, 2013. doi: 10.1139/cjce-2012-0303.

Orlandini, S., Moretti, G., and Albertson, J. D. Evidence of an emerging levee failure mechanism causing disastrous floods in Italy. *Water Resources Research*, 51(10):7995–8011, 2015. doi: 10.1002/2015WR017426.

Özer, I. E., van Damme, M., Schweckendiek, T., and Jonkman, S. N. On the importance of analyzing flood defense failures. In *E3S Web of Conferences*, volume 7, page 03013. EDP Sciences, 2016.

Paquier, A. Dam-breakwave: validating Cemagref's numerical models during CADAM. *Ingénieries EAT*, pages 11–12, 2001.

Paquier, A. Testing a simplified breach model on impact project test cases. *32nd congress of IAHR*, n/a, 2007.

Paquier, A. and Béraud, c. Validating a simplified model for flood hazard downstream levees. *Proceedings of River Flow Conference*, pages 591–597, 2010.

Paquier, A. and Recking, A. Advances on breach models by Cemagref during impact project. *4th IMPACT Workshop*, n/a, 2004.

Peeters, P., Zhao, G., de Vos, L., and Visser, P. J. Large-scale dike breaching experiments at Lillo in Belgium. *Proceedings of the 7th International Conference on Scour and Erosion - ICSE 2014, The University of Western Australia, Perth, Australia, 2-4 December 2014*, page 289, 2014.

Peeters, P., Heredia Gomez, M., van Damme, M., and Visser, P. Unveiling the consequences of your breach growth model choice. *E3S Web of Conferences*, 7:03005, 2016. ISSN 2267-1242. doi: 10.1051/e3sconf/20160703005.

Pickert, G., Weitbrecht, V., and Bieberstein, A. Beaching of overtopped river embankments controlled by apparent cohesion. *Journal of Hydraulic Research*, 49(2):143–156, 2011. doi: 10.1080/00221686.2011.552468.

Pierce, M. W., Thornton, C. I., and Abt, S. R. Predicting peak outflow from breached embankment dams. *Journal of Hydrologic Engineering*, 15(5):338–349, 2010. doi: 10.1061/(ASCE)HE.1943-5584.0000197.

Rentschler, J. and Salhab, M. Flood Exposure and Poverty in 189 Countries. *Climate Change Group and Global Facility for Disaster Reduction and Recovery*, 2020.

Resio, D., Boc, S., Maynord, S., Wal, D.and Abraham, D. D. D., and Welsh, B. Development and Deployment of Rapid Repair of Levee Breaching Technology. Technical report, Southeastern Regional Research Initiative, Department of Homeland Security, 2009.

Rifai, I. *Physical and numerical modelling of overtopping induced fluvial dike failure.* PhD thesis, University of Paris-Est and University of Liège, 2018.

Rifai, I., Erpicum, S., Archambeau, P., Violeau, D., Dewals, B., El, K., and Abderrezzak, K. Physical Modeling of Overtopping Induced Fluvial Dike Failure : Effects of Main Channel Flow and Floodplain Innundation. 6865(1):1573–1579, 2017a.

Rifai, I., Erpicum, S., Archambeau, P., Violeau, D., Pirotton, M., El Kadi Abderrezzak, K., and Dewals, B. J. Overtopping induced failure of noncohesive, homogeneous fluvial dikes. *Water Resources Research*, pages 3373–3386, 2017b. doi: 10.1002/2017WR020840.

Rifai, I., El Kadi Abderrezzak, K., Erpicum, S., Archambeau, P., Violeau, D., Pirotton, M., , and Dewals, B. J. Floodplain Backwater Effect on Overtopping Induced Fluvial Dike Failure . *Water Resources Research*, 54(11):9060–9073, 2018.

Rifai, I., El Kadi Abderrezzak, K., Erpicum, S., Archambeau, P., Violeau, D., Pirotton, M., , and Dewals, B. J. Flow and detailed 3D morphodynamic data from laboratory experiments of fluvial dike breaching. *Nature/Scientific Data*, 53(6), 2019.

Rifai, I., Schmitz, V., Erpicum, S., Archambeau, P., Violeau, D., Pirotton, M., Dewals, B., and el Kadi Abderrezzak, K. Continuous monitoring of fluvial dike breaching by a laser profilometry technique. *Water Resources Research*, 56, 10 2020a. doi: 10.1029/2019WR026941.

Rifai, I., Schmitz, V., Erpicum, S., Archambeau, P., Violeau, D., Pirotton, M., Dewals, B., and El Kadi Abderrezzak, K. Continuous monitoring of fluvial dike breaching by a laser profilometry technique. *Water Resources Research*, 56(10):e2019WR026941, 2020b. doi: https://doi.org/10.1029/2019WR026941. e2019WR026941 2019WR026941.

Rifai, I., El Kadi Abderrezzak, K., Hager, W., Erpicum, S., Archambeau, P., Violeau, D., Pirotton, M., , and Dewals, B. J. Apparent cohesion effects on overtopping-induced fluvial dike breaching . *Journal of Hydraulic Research*, 59(1):75–87, 2021.

Riha, J., Alhasan, Z., Petrula, L., Popielski, P., Dąbska, A., Fry, J.-J., Solski, S., Perevoshchikova, N., and Landstorfer, F. *Harmonisation of Terminology and Definitions on Soil Deformation Due to Seepage*, pages 347–366. 09 2019. doi: 10.1007/978-3-319-99423-9_31.

Risher, P. and Gibson, S. Applying mechanistic dam breach models to historic levee breaches. *3^{rd} European Conference on Flood Risk Management*, 2016.

Roger, S., Dewals, B., Erpicum, S., Schwanenberg, D., Schuttrumpf, H., Kongeter, J., and Pirotton, M. Experimental and numerical investigations of dike- break induced flows. *Journal of Hydraulic Research*, 47:349–359, 2009. doi: 10.1080/00221686.2009.9522006.

Saucier, C. L., Howard, I. L., and Tom, J. G. Levee breach geometries and algorithms to simulate breach closure. Technical report, OAK RIDGE NATIONAL LABORATORY, Oak Ridge, Tennessee, 2009.

Savitzky, A. and Golay, M. J. E. Smoothing and differentiation of data by simplified least squares procedures. *Analytical Chemistry*, 36(8):1627–1639, 1964.

Schmitz, V., Erpicum, S., El Kadi Abderrezzak, K., Rifai, I., Archambeau, Pierre aand Pirotton, M., , and Dewals, B. J. Overtopping-induced failure of non-cohesive homogeneous fluvial dikes: effect of dike geometry on breach discharge and widening . *Water Resources Research*, 57(7): e2021WR029660, 2021.

Schmocker, L. and Hager, W. H. Plane dike-breach due to overtopping: effects of sediment, dike height and discharge. *Journal of Hydraulic Research*, 50(6):576–586, 2012. ISSN 0022-1686. doi: 10.1080/00221686.2012.713034.

Sharp, M., Wallis, M., Deniaud, F., Hersch-Burdick, R., Tourment, R., Matheu, E., Seda-Sanabria, Y., Wersching, S., Veylon, G., Durand, E., Smith, P., Forbis, J., Spliethoff, C., Hemert, H., Igigabel, M., Pohl, R., Royet, P., and Simm, J. *The International Levee Handbook*. 01 2013.

Shields, A. *Anwendung der Aehnlichkeitsmechanik und der Turbulenzforschung auf die Geschiebebewegung*. PhD thesis, 1936.

Shimada, T., Watanabe, Y., Yokoyama, H., and Tsuji, T. Levee Breach Experiment by Lateral Overflow at the Chiyoda Experimental Flume. *Journal of Japan Society of Civil Engineers*, Ser. B1 (Hydraulic Engineering), 2009.

Shustikova, I., N. J. D. A. B. P. V. S. C. A. Levee Breaching: A New Extension to the LISFLOOD-FP Model. *Journal of Hydraulic Research*, (942), 2020. doi: 10.1080/00221680309506889.

Singh, V. *Dam breach modeling technology*, volume 17. Springer Science & Business Media, 1996. ISBN 0792339258.

Smart, G. M. Sediment Transport Formula for Steep Channels. *Journal of Hydraulic Engineering*, 110(3):267–276, 1984. ISSN 0733-9429. doi: 10.1061/(ASCE)0733-9429(1984)110:3(267).

Sofia, G., Masin, R., and Tarolli, P. Prospects for crowdsourced information on the geomorphic 'engineering' by the invasive coypu (myocastor coypus). *Earth Surface Processes and Landforms*, 42(2):365–377, 2017. doi: https://doi.org/10.1002/esp.4081.

Soulsby, R. *Dynamics of marine sands: a manual for practical applications*. Thomas Telford, 1997. ISBN 072772584X.

Swartenbroekx, C., Soares-Frazão, S., Staquet, R., and Zech, Y. Two-dimensional operator for bank failures induced by water-level rise in dam-break flows. *Journal of Hydraulic Research*, 48(3): 302–314, 2010. doi: 10.1080/00221686.2010.481856.

Tabrizi, A. A., E. Elalfy, L. Ann LaRocque, M. H. C., and Imran, J. Experimental Modeling of Levee Failure Process due to Overtopping. (August 2016), 2015.

Tadesse, Y. and Fröhle, P. Modelling of flood inundation due to levee breaches: Sensitivity of flood inundation against breach process parameters. *Water*, 12:3566, 12 2020. doi: 10.3390/w12123566.

Talmon, A., Struiksma, N., and Van Mierlo, M. Laboratory measurements of the direction of sediment transport on transverse alluvial-bed slopes. *Journal of Hydraulic Research*, 33(4):495–517, 1995.

Tellman, B., Sullivan, J., Kuhn, C., Kettner, A., Doyle, C., Brakenridge, R., Erikson, T., and Slayback, D. Satellite observations indicate increasing proportion of population exposed to floods, 08 2020.

Tobita, D., Kakinuma, T., Yokoyama, H., and Takeda, A. Quantification of levee breach volume based on levee breach at the chiyoda experimental flume. *Journal of Japan Society of Civil Engineers*, 2: 136–143, 2014.

USACE. Hydrologic engineering center river analysis system (hec-ras). Technical report, US Army Corps of Engineers, Washing DC, USA, 2011.

USBR, U. S. B. o. R. Guidelines for defining inundated areas downstream from Bureau of Reclamation dams. *Reclamation Planning Instruction No. 82-11*, 1982.

USBR, U. S. B. o. R. Downstream hazard classification guidelines. *ACER Technical Memorandum No. 11, United States Department of the Interior*, 1988.

Vacondio, R., Aureli, F., Ferrari, A., Mignosa, P., and Palù, A. Simulation of the January 2014 flood on the Secchia River using a fast and high-resolution 2D parallel shallow-water numerical scheme. *Natural Hazards*, 80:1–23, 01 2016. doi: 10.1007/s11069-015-1959-4.

Van Damme, M. Morris, M. H. M. A new approach to rapid assessment of breach driven embankment failures. Technical Report WP4.4, FRMRC Research Report, Washing DC, USA, 2012.

Van Rijn, L. C. Sediment transport, part III: bed forms and alluvial roughness. *Journal of hydraulic engineering*, 110(12):1733–1754, 1984.

Vannucchi, G., Gottardi, G., Madiai, C., Marchi, M., and Tonni, L. Analisi della probabilità di collasso arginale dei grandi fiumi. *Proceedings of the XXV Convegno Nazionale di Geotecnica, Baveno, Italy*, pages 4–6, 2014.

Vardon, P.J., W. B. . H. M. Slope failure simulations with MPM. *Journal of Hydrodynamics*, 29, 2017. doi: 10.1016/S1001-6058(16)60755-2.

Ventini, R., Dodaro, E., Gragnano, C. G., Giretti, D., and Pirone, M. Experimental and numerical investigations of a river embankment model under transient seepage conditions. *Geosciences*, 11 (5), 2021. doi: 10.3390/geosciences11050192.

Verheij, H. Time dependent breach development in cohesive material. Technical report, Internal Technical Memorandum, United States Bureau of Reclamation, 2002.

Verheij, H. and Van der Knaap, F. Time dependent breach development in cohesive material. Technical report, Internal Technical Memorandum, United States Bureau of Reclamation, 2003.

Visser, P. Breach growth in sand-dikes, 1998. ISSN 01696548.

Volz, C. *Numerical Simulation of Embankment Breaching Due to Overtopping*. PhD thesis, ETH Z´rich, 2013.

Volz, C., Frank, P.-J., Vetsch, D. F., Hager, W. H., and Boes, R. M. Numerical embankment breach modelling including seepage flow effects. *Journal of Hydraulic Research*, 1686(February):1–11, 2017. doi: 10.1080/00221686.2016.1276104.

Von Thun, J. L. and Gillette, D. R. Guidance on breach parameters. Technical report, Internal Technical Memorandum, United States Bureau of Reclamation, 1990.

Vorogushyn, S., Merz, B., Lindenschmidt, K. E., and Apel, H. A new methodology for flood hazard assessment considering dike breaches. *Water Resources Research*, 46(8):1–17, 2010. doi: 10.1029/2009WR008475.

Wahl, T. L. and Lentz, D. J. Experimental methods for studying canal breach processes. *2012 Hydraulic Measurements & Experimental Methods Conference - EWRI / ASCE August 12-15, 2012*, page 6, 2012.

Walder, J. S. and O'Connor, J. E. Methods for predicting peak discharge of floods caused by failure of natural and constructed earthen dams. *Water Resources Research*, 33(10):2337, 1997. doi: 10.1029/97WR01616.

Wang, Z. and Bowles, D. Three-dimensional non-cohesive earthen dam breach model. part 1: Theory and methodology. *Advances in Water Resources*, 29:1528–1545, 2006. doi: 10.1016/j.advwatres.2005.11.009.

Wei, H., Yu, M., Wang, D., and Li, Y. Overtopping breaching of river levees constructed with cohesive sediments. *Natural Hazards and Earth System Sciences*, 16(7):1541–1551, 2016. doi: 10.5194/nhess-16-1541-2016.

West, M., Morris, M., and Hassan, M. A guide to breach prediction. *FLOODsite Project Report, HR Wallingford,Wallingford, U. K.*, 2018.

Wiberg, P. L. and Smith, J. D. Model for calculating bed load transport of sediment. *Journal of Hydraulic Engineering*, 115(1):101–123, 1989. doi: 10.1061/(ASCE)0733-9429(1989)115:1(101).

Winz, E. *Einuss der Kornverteilung auf den zweidimensionalen Deichbruch. Master thesis,*. PhD thesis, ETH Zurich, 2012.

Wu, F.-C., Shao, Y.-C., and Chen, Y.-C. Quantifying the forcing effect of channel width variations on free bars: Morphodynamic modeling based on characteristic dissipative Galerkin scheme. *Journal of Geophysical Research: Earth Surface*, 116(F3):5717–5734, 2011. doi: 10.1029/2010JF001941.

Wu, S., Yu, M., Wei, H., Liang, Y., and Zeng, J. Non-symmetrical levee breaching processes in a channel bend due to overtopping. *International Journal of Sediment Research*, 09 2017. doi: 10.1016/j.ijsrc.2017.09.007.

Wu, W. Simplified Physically Based Model of Earthen Embankment Breaching. *Journal of Hydraulic Engineering*, 137(12):837–851, 2013. doi: 10.1061/(ASCE)HY.1943-7900.0000741.

Wu, W. Introduction to DLBreach – A Simplified Physically-Based Dam / Levee Breach Model, Department of Civil and Environmental Engineering. 2016.

Wu, W. and Li, H. A simplified physically-based model for coastal dike and barrier breaching by overtopping flow and waves. *Coastal Engineering*, 130(September 2016):1–13, 2017. ISSN 03783839. doi: 10.1016/j.coastaleng.2017.09.007.

Xu, Y. and Zhang, L. M. Breaching Parameters for Earth and Rockfill Dams. *Journal of Geotechnical and Geoenvironmental Engineering*, 135(12):1957–1970, 2009. doi: 10.1061/(ASCE)GT.1943-5606.0000162.

Yu, M. H., Wei, H. Y., Liang, Y. J., and Zhao, Y. Investigation of non-cohesive levee breach by overtopping flow. *Journal of Hydrodynamics*, 25(4):572–579, 2013. doi: 10.1016/S1001-6058(11)60398-4.

Zhong, Q., Chen, S.-s., and Deng, Z. Numerical model for homogeneous cohesive dam breaching due to overtopping failure. *Journal of Mountain Science*, 14:571–580, 2017. doi: 10.1007/s11629-016-3907-5.

Zhou, G., Mingjun, Z., Shrestha, M., Song, D., Choi, C., Cui, K. F., Peng, M., Shi, Z., Zhu, X., and Chen, H. Experimental investigation on the longitudinal evolution of landslide dam breaching and outburst floods. *Geomorphology*, 334, 02 2019. doi: 10.1016/j.geomorph.2019.02.035.

Zhu, Y. *Breach Growth in Clay-Dikes*. 2006. ISBN 9789090209647.

Zomorodi, K. Empirical equations for levee breach parameters based on reliable international data. *Proceedings of the Dam Safety 2020 conference*, 2020.

Özer, I. E., van Damme, M., and Jonkman, S. N. Towards an international levee performance database (ilpd) and its use for macro-scale analysis of levee breaches and failures. *Water*, 12(1), 2020. ISSN 2073-4441. doi: 10.3390/w12010119.